
LIDAR MEASUREMENTS AND ENGINEERING
MODELLING OF WIND TURBINE WAKES

Davide Trabucchi

Von der Fakultät für Mathematik und Naturwissenschaften
der Carl von Ossietzky Universität Oldenburg
zur Erlangung des Grades und Titels eines

DOKTORS DER INGENIEURWISSENSCHAFTEN

DR.-ING.

angenommene Dissertation

von Herrn Davide Trabucchi
geboren in Sondalo, Italien

Gutachter : Prof. Dr. Martin Kühn
Zweitgutachterin : Prof. Dr. Laura Lukassen
Tag der Disputation : 27. August 2019

Abstract

Wind turbines extract energy from the wind. Consequently, wakes with lower wind speed and higher turbulence than in the upstream flow propagate downstream. For this reason, in a wind farm, different energy budgets are generally available to downstream turbines even under steady and homogeneous inflow conditions.

Several models with different orders of detail can estimate the wind deficit in the wake. Engineering wake models – i.e. models implementing simplified equations to describe the fluid mechanics of the wind flow at a low computational cost – are applied in the initial planning phase of a wind farm to predict its annual energy yield. Common simplifications are for instance the assumption of axisymmetric wakes and the possibility to assess the wakes of single turbines independently in a first step and then to combine arithmetically their wind speed deficits.

The main objective of this thesis is to suggest an alternative engineering model to solve the flow equations considering all turbines at once. This research was supported by full-field measurements realised with scanning lidars (remote sensing instruments based on infra-red laser) for the calibration and verification of the model. For this reason, the first part of the thesis is dedicated to lidar experiments for the assessment of wakes and the second one to the novel engineering model.

Lidars can scan the wind speed in a range from tens of metres to ten or more kilometres. However, they have two major limitations: (i) They measure only the projection of the wind vector on the radial direction of the laser beam; hence, wind field reconstruction models are needed to estimate the local wind vector. (ii) They average the wind projection over long (from tens to hundreds of metres) and thin (in the order of ten centimetres) volumes along the radial direction.

In this respect, the first part of the thesis is dedicated to answering the question: How to overcome the limitations of lidar technology when being applied to wake measurements?

A lidar simulator was applied to test several experimental layouts, on the one hand for measurements of the average wind speed profile in wakes and, on the other hand, to study the dynamic path of a single wake (wake meandering). The results indicate that the accuracy of the measurement is sensitive to the experimental configuration (lidar position, scanning trajectory and wind field reconstruction method). In the test cases analysed, the faster trajectories with the lower misalignment with respect to the average flow direction provided better results.

The experimental activities dealt first with wake meandering. Onshore and offshore lidar measurements demonstrate that the effects of wake meandering can be identified in lidar measurements

along a fixed radial direction. The spectral analysis of these measurements suggests that the increased low-frequency turbulent fluctuations at the flanks of the wake can be associated with wake meandering. This result was also confirmed by lidar simulations.

Another offshore campaign was conducted to measure the wake with a nacelle-based lidar. The main goal was to estimate the average wind speed profile in the wake. The measurements compare well with an analytical wake model; however, the results in terms of the initial wake width deviate from the theoretical expectations.

The second part of the thesis deals with the implementation of a three-dimensional shear-layer (3DSL) wake model which is based on the same assumptions as of other engineering wake models, but it is extended to simulate non-axisymmetric flows as the multiple wakes given by the mutual interaction of wind turbines and wakes in wind farms.

The development of the model is presented in two main steps. The first one provides the skeleton of the model with a rough approximation of pressure effects in the downstream induction range of the rotor. A comparison between multiple wakes simulated with the 3DSL model and extracted from large-eddy simulations (LES) highlights the advantages of the 3DSL model in relation to an axisymmetric wake model.

In the second step, a mixing-length model of the turbulent diffusion in the wake and a model for the streamwise pressure gradient within the rotor induction range are implemented into the 3DSL model. These two modules were calibrated and verified for single wakes by means of the aforementioned nacelle-based lidar measurements and LES. The comparison with multiple wakes extracted again from LES confirmed the results obtained with the first development. A detailed analysis of the wind field on selected wake cross-sections indicates that the deviations between the results of the LES and the 3DSL model are partly due to upstream initial conditions and to non-homogeneous convective turbulent structures present in the LES but not included in the 3DSL model.

In the end, the 3DSL model could be seen as a "patchwork wake model" which combines modules taken from other engineering models in order to reproduce in a simple way the complexity of the wind flow in wakes. In this regard, it makes sense to ask: How far is it possible to conveniently improve the physics of engineering wake models? A general answer to this question is suggested in the final remarks of the thesis.

Zusammenfassung

Windenergielagen entziehen dem Wind Energie. Daher breiten sich Nachläufe mit geringerer Windgeschwindigkeit und höherer Turbulenz stromabwärts aus. Aus diesem Grund steht Turbinen, die in Windschatten in einem Windpark operieren, generell ein niedrigerer Energiegehalt zur Verfügung, selbst unter stationären und homogenen Bedingungen. Mehrere Modelle mit unterschiedlichen Detailanforderungen können das Winddefizit im Nachlauf abschätzen. In der ersten Planungsphase von Windenergieprojekten werden Modelle zur Vorhersage des jährlichen Energieertrags zukünftiger Windparks angewendet, d. h. Modelle mit vereinfachten strömungsmechanischen Gleichungen, die die Strömung mit geringem Rechenaufwand beschreiben können.

Übliche Vereinfachungen sind beispielsweise die Annahme von achsensymmetrischen Nachläufen und die Möglichkeit, in einem ersten Schritt die Nachläufe einzelner Turbinen unabhängig voneinander zu bewerten und dann deren Winddefizite rechnerisch zu kombinieren.

Das Hauptziel dieser Arbeit ist es, ein alternatives Modell vorzuschlagen, um die Strömungsgleichungen unter Berücksichtigung aller Turbinen zu lösen. Diese Forschungsarbeit wurde durch Messungen mit scannenden Lidar-Geräten (auf Laserstrahlen basierende Fernerkundungsmessinstrumente) unterstützt. Aus diesem Grund befasst sich der erste Teil dieser Arbeit mit Lidar-Experimenten zur Bewertung von Nachläufen und der zweite Teil mit den Nachlaufmodellen.

Lidar-Geräte können den Wind in einem Bereich von zehn Metern bis zu zehn oder mehr Kilometern erfassen. Sie haben jedoch zwei Hauptbeschränkungen: (i) Sie messen nur die Projektion des Windvektors auf der radialen Richtung des Laserstrahls; aus diesem Grund werden Windfeldmodelle benötigt, um den lokalen Windvektor abzuschätzen. (ii) Sie mitteln die Windprojektion über lange (von zehn bis Hunderten von Metern) und dünne (in der Größenordnung von zehn Zentimetern) Volumina entlang der radialen Richtung.

In diesem Zusammenhang widmet sich der erste Teil der vorliegenden Arbeit der Beantwortung der Frage: Wie kann mit den Einschränkungen von Lidar-Geräten umgegangen werden, die für Nachlaufströmungsmessungen verwendet werden? Die Antwort wird indirekt durch einige beispielhafte Anwendungen und einige Kommentare in der Schlussfolgerung am Ende der Arbeit gegeben.

Mit einem Lidar-Simulator wurden mehrere Versuchsanordnungen zur Messung des gemittelten Windprofils im Nachlauf und des dynamischen Verlaufs eines einzelnen Nachlaufs (Nachlaufmäanderströmung) getestet. Die Ergebnisse zeigen, dass die Genauigkeit der Messung von der

experimentellen Konfiguration abhängt (Lidarposition, Abtasttrajektorien und Windfeldrekonstruktionsmethode). In den analysierten Testfällen lieferten die schnelleren Trajektorien mit der geringeren Fehlaustrichtung in Bezug auf die durchschnittliche Strömungsrichtung bessere Ergebnisse.

Die experimentellen Untersuchungen befassten sich zunächst mit der Nachlaufmäanderströmung. Onshore- und Offshore-Lidar-Messungen haben gezeigt, dass der dynamische Verlauf der Nachläufe in Lidar-Messungen identifiziert werden kann, die entlang einer festen radialen Strahlrichtung abgetastet wurden. Die Spektralanalyse der Messungen legt nahe, dass die erhöhten niederfrequenten turbulenten Fluktuationen an den Flanken des Nachlaufs teilweise auf das Mäandern zurückzuführen sind. Dieses Ergebnis wurde auch durch Lidar-Simulationen bestätigt.

Eine weitere Offshore-Kampagne wurde durchgeführt, um den Nachlauf mit einem gondelbasierten Lidar zu messen. Das Hauptziel war die Messung des mittleren Windprofils im Nachlauf. Im Allgemeinen lassen sich die gemessenen Profile gut mit einem analytischen Nachlaufmodell vergleichen. Die Ergebnisse in Bezug auf die anfängliche Nachlaufbreite weichen jedoch von den theoretischen Erwartungen ab.

Der zweite Teil der Arbeit befasst sich mit der Implementierung eines dreidimensionalen Scherungsgrenzschicht-Nachlaufmodells (3DSL), das auf den gleichen Annahmen wie die anderen technischen Nachlaufmodelle basiert, jedoch erweitert wurde, um nicht-achsensymmetrische Strömungen zu simulieren, die durch die Wechselwirkung von Windenergieanlagen und Nachläufen in Windparks entstehen.

Die Entwicklung des Modells wird in zwei Schritten vorgestellt. Der erste liefert das Gerüst des Modells mit einer groben Näherung der Druckwirkungen im stromabwärts gelegenen Gebiete hinter dem Rotor. Ein Vergleich zwischen mehreren mit dem 3DSL-Modell simulierten und aus Large-Eddy-Simulationen (LES) extrahierten Nachläufen zeigt die Vorteile des 3DSL-Modells gegenüber einem axialsymmetrischen Nachlauf-Modell.

Im zweiten Schritt werden ein Mischungs-Längenmodell der turbulenten Nachlaufdiffusion und ein Modell für den Druckgradienten entlang der Strömung im Rotorinduktionsbereich vorgestellt. Diese beiden Module werden mit den oben genannten gondelbasierten Lidar-Messungen und LES anhand von Einzelnachläufen kalibriert und verifiziert. In einem Vergleich mit mehreren Nachläufen, die erneut aus LES extrahiert wurden, wurden die Ergebnisse des ersten Arbeitsschnitts bestätigt. Eine detaillierte Analyse des Windfeldes an ausgewählten Nachlaufquerschnitten zeigt, dass die Abweichungen zwischen LES- und 3DSL-Modellsimulation teilweise auf vorgelagerte Anfangsbedingungen und auf inhomogene konvektive turbulente Strukturen zurückzuführen sind, die in LES vorhanden, aber nicht im 3DSL-Modell enthalten sind.

Am Ende könnte das 3DSL-Modell als "Patchwork Wake-Modell" anzusehen sein, bei dem Module aus anderen technischen Modellen kombiniert werden, um die Komplexität des Windfeldes im Nachlauf auf einfache Weise zu reproduzieren. In diesem Zusammenhang ist es sinnvoll zu fragen: Inwieweit ist es möglich, die physikalische Beschreibung von Nachlauf-Modellen zu verbessern? Eine allgemeine Antwort auf diese Frage wird in den Schlussbemerkungen am Ende der Arbeit gegeben.

Preface

During my years as a university student, I would have never thought to do academic research after my graduation. The decision of writing my master thesis at the Stiftungslehrstuhl Wind Energy at the University of Stuttgart gave me the opportunity to start my adventure in the wind energy research which brought me to pursue a PhD at Oldenburg University.

The main objective of this manuscript is the conclusion of my journey as a PhD candidate. Furthermore, it aims to disseminate the results of my research project. Some of them have been already published as papers, which are also included in the dissertation as stand-alone chapters. I tried to write also the other chapters in a stand-alone form to facilitate the consultation by readers not interested in the entire work. This means that sometimes there are repetitions through the chapters. Eventually, the dissertation has also a personal meaning: Collecting all the results and formatting them in the manuscript acted as self-acknowledgement of the achievements.

Completing a research project is never the work of a sole person. My results were only possible thanks to all the colleagues and friends at Forwind - Oldenburg University. In particular, I am grateful to Jörg Schneemann, Juan-Josè Trujillo and Stephan Voss for the close collaboration; to Björn Witha, Gerald Steinfeld and Lukas Vollmer for providing the wind fields based on large-eddy simulations; thanks also to David Bastine and Matthias Wächter for the enlightening discussion about turbulence. I also would like to thank all my co-authors and the many people who discussed with me intermediate results or reviewed my research results and manuscripts before their publication. I thank the students who helped with experimental campaigns, data analysis and investigation of alternative ideas too. For what concerns this manuscript, Elia Daniele, Jonas Schmit, Jörg-Hendrik Bach, Klaus Franke, Martin Dörenkämper and Simon Stokes receive my acknowledgement for their comments and suggestions.

I owe my supervisor, Prof. Martin Kühn, a debt of gratitude. Beyond acquiring the funds for this long-lasting research, he trusted my work, dedicated time to fruitful discussions, guided my intuitions and kept me focused.

Many thanks go also to Prof. Laura Lukassen who took part with enthusiasm to the examination of the PhD.

Part of this research was based on experimental measurements. Concerning the offshore campaigns, I would like to thank the former DEWI institute (now part of UL International) and the Fachhochschule Kiel for their friendly and uncomplicated support during the deployments in alpha ventus; for the same reason, I would like to acknowledge Niko Mittelmeier, who facilitated the

sharing of data by Senvion GmbH and provided the information needed to analyse those data. With respect to the measurement equipment – the scanning lidars – many thanks for the constructive collaboration go to the staff of DTU-Wind Energy and particularly to Nikola Vasiljevic who shared the struggle of working with prototypes.

The research reported in this dissertation was mainly funded by the projects GW-Wakes (grant no. 0325397A by the German Federal Ministry for Economic Affairs and Energy) and CLUSTERDESIGN (project no. 283145; FP7 Energy). I acknowledge all project partners, specially the ones of the research initiative RAVE Offshore (Research at alpha ventus) and Senvion GmbH for providing access to part of the data analysed in the present study.

Last but not least, I would like to thank my great wife Marina for her patience and unconditional support during the last years.

Contents

Abstract	vii
Zusammenfassung	ix
Preface	xi
Nomenclature	xvii
List of figures	xxv
List of tables	xxvii
1 Introduction	1
1.1 Motivation	1
1.2 State of art	3
1.2.1 Wind turbine wakes	3
1.2.2 Wake models	5
1.2.3 Doppler wind lidar for wake measurements	7
1.3 Objectives and structure of the thesis	10
2 Lidar simulations for the design of wake measurement campaigns	13
2.1 Introduction	13
2.2 Wind speed and wake profiles from lidar measurements	14
2.2.1 Wind field reconstruction	14
2.2.2 Wake characterisation	17
2.3 LIdar SCanner SIMulator (LiXim)	18
2.4 Lidar simulations of wake measurements	20
2.4.1 Wind field: unsteady wake simulations	21

2.4.2	Measuring the average vertical profile of the wind speed in the wake of a wind turbine	21
2.4.3	Dynamic tracking of the wake centre position	25
2.5	Summary	31
3	Application of staring lidars to study the dynamics of wind turbine wakes	33
3.1	Introduction	35
3.2	Experimental realization	36
3.3	Wake identification	38
3.4	Wake identification	39
3.5	Wake dynamics	40
3.6	Conclusions	41
3.7	List of symbols	42
3.8	Acknowledgements	42
3.9	References	42
4	Study of wake meandering by means of fixed point lidar measurements: Spectral analysis of line of sight wind component	43
4.1	Introduction	45
4.2	Influence of the lidar beam inclination	46
4.3	Application of fixed point lidar measurements to the study of the wake meandering	47
4.4	Offshore lidar measurements of the wake meandering	48
4.5	Conclusion	52
4.6	Acknowledgements	53
4.7	References	53
5	Nacelle-based lidar measurements for the calibration of a wake model at different offshore operating conditions	55
5.1	Introduction	57
5.2	Measurements	58
5.3	Measurements	60
5.4	Wake model description and fit	61
5.5	Results and discussion	62
5.6	Conclusions	66
5.7	Aknowledgements	67
5.8	References	67

6	3-D shear-layer model for the simulation of multiple wind turbine wakes: Description and first assessment	69
6.1	Introduction	71
6.2	Model description	72
6.3	Wake simulations	76
6.4	Results	77
6.5	Discussion	83
6.6	Conclusions	83
6.7	Appendix A	85
6.8	Acknowledgements	88
6.9	References	88
7	3-D shear-layer model for the simulation of multiple wind turbine wakes: Further development, calibration and assessment	89
7.1	Introduction	89
7.1.1	Basic formulation of the 3DSL model	89
7.1.2	Objectives	90
7.2	Model of the streamwise pressure gradient	91
7.3	Numerical implementation	93
7.4	Calibration of the turbulence length scale in a single wake	96
7.4.1	Profiles of the wind deficit in the wake from nacelle-based lidar measurements	96
7.4.2	Turbulence length scale of a single wake	97
7.5	Parameter assessment for the pressure gradient model	99
7.6	Evaluation of the 3DSL model: Simulation of multiple wakes	101
7.7	Summary and discussion of the results	103
8	Conclusion	109
8.1	Summary and final remarks	109
8.2	Outlook	111
	References	113
	Publications	121
	List of peer-reviewed publications on which this thesis is based	121
	Further peer-reviewed publications	122
	Conferences and colloquia	122
	Curriculum vitae	125
	Declaration of authorship	127

Nomenclature

Greek letters

ΔQ	overall variation of the mass flow between two consecutive cross-sections
$\Delta\alpha$	difference between the wind direction V_{dir} and the azimuth angle χ
Δp	spatial extension of the laser pulse emitted by a lidar
Δr	spatial extension of the range gate processed by the lidar
Δu	difference between the simulated and the reference streamwise wind speed components u_{sim} and u_{ref} , respectively
Δv	difference between the simulated and the reference cross-stream wind speed components v_{sim} and v_{ref} , respectively
Δw	difference between the simulated and the reference vertical wind speed components w_{sim} and w_{ref} , respectively
Γ_b	bound vortex of a vortex-cylinder wake model
Γ_l	longitudinal vortex of a vortex-cylinder wake model
Γ_r	root vortex of a vortex-cylinder wake model
Γ_t	tangential vortex of a vortex-cylinder wake model
Π	complete elliptic integral of the third kind
Φ	potential function of the cross-stream and vertical wind speed components
Φ_M	non-dimensional shear profile
γ_t	intensity of the tangential vortex Γ_t
ϵ_{inc}	incoming eddy-viscosity implemented in the definition of the aerodynamic correction factor C_{aero}
ϵ'	initial radius of the wake implemented in the model of the turbulence mixing-length σ_r
ϵ_y	eddy-viscosity along the cross-stream direction
ϵ_z	eddy-viscosity along the vertical direction
ζ	elevation angle of the radial direction
η	weighting function applied to the radial wind speed in the convolution of the laser pulse and the range gate
η_F	weighting function applied to the radial wind speed in the convolution of the laser pulse and the range gate if the laser is focused

κ	von Karman constant
λ_L	wave length of the laser
ρ	air density
σ_r	parameter defining the wake radius in the bivariate Gaussian function f_G and in the horizontal function W_{DF} describing the wind speed deficit in a wind turbine wake; turbulence mixing-length in the eddy-viscosity model
χ	azimuth angle of the radial direction
χ_{max}	phase shift applied to the sinusoidal function in the visual azimuth display wind field reconstruction method

Symbols

A	area of the the lidar telescope aperture
A_G	difference between the maximum and the minimum values of the bivariate Gaussian function f_G
D	rotor diameter
C_{aero}	aerodynamic correction factor applied to model the aerodynamic under-performance of rotors operating in wakes
C_T	thrust coefficient
D	rotor diameter
D	non-dimensional unit of length representing the number of rotor diameters from a reference turbine
D_M	difference between the maximum and the minimum values of the horizontal function W_{DF} describing the wind speed deficit in a wind turbine wake
E	complete elliptic integral of the second kind
F_1	filter function implemented in the eddy-viscosity model to modulate the contribution of the wake in the near-wake range
F_2	filter function implemented in the eddy-viscosity model to modulate the contribution of ambient turbulence in the near-wake range
G_γ	scaling factor of the streamwise pressure gradient implemented in the 3-D shear-layer model
I_F	Lorentzian shape used to approximate the energy distribution of a focused lidar
I_p	Gaussian shape used to approximate the laser pulse of a lidar
L1 to L5	test cases simulated with LiXim in Chapter 2
K	complete elliptic integral of the first kind
L_{MO}	Monin-Obukon length
\mathbf{M}_{eR}	matrix collecting the unity vectors \mathbf{e}_{R1} , \mathbf{e}_{R2} and \mathbf{e}_{R3} of three radial directions
P_0	centre of the Lissajous trajectory applied to lidar wind measurements in the wake of a wind turbine
R_V	radius of the rotor in the vortex-cylinder wake model
S_F	focal length

S_R	Rayleigh length
TI	turbulence intensity
\mathbf{V}	wind vector
\mathbf{V}_i	wind vector $[u_{Di} \ v_i \ w_i]$ at the i^{th} cross-section downstream
\mathbf{V}_H	horizontal wind vector
V_R	radial wind component measured by a lidar scanning
V_{RE}	radial wind component measured during a Doppler beam swinging trajectory with the azimuth angle aligned with the East direction
V_{RN}	radial wind component measured during a Doppler beam swinging trajectory with the azimuth angle of the North direction
V_{RS}	radial wind component measured during a Doppler beam swinging trajectory with the azimuth angle of the South direction
V_{RV}	radial wind component measured during a Doppler beam swinging trajectory with the the elevation angle of with the vertical direction
V_{RW}	radial wind component measured during a Doppler beam swinging trajectory with the azimuth angle of West direction
V_{dir}	wind direction
W_{DF}	function describing the shape of the horizontal wind deficit in the wake of a wind turbine
Z	physical height above the ground/see level
a_{aero}	parameter implemented in the definition of the aerodynamic correction factor C_{aero}
a_{VAD}	offset added to the sinusoidal function in the visual azimuth display wind field reconstruction method
b_{VAD}	amplitude of the sinusoidal function in the visual azimuth display wind field reconstruction method
b_{aero}	parameter implemented in the definition of the aerodynamic correction factor C_{aero}
d_{aero}	parameter implemented in the definition of the aerodynamic correction factor C_{aero}
\mathbf{e}_R	unitary vector defining a radial direction
f_0	offset defining the minimum value of the bivariate Gaussian function f_G
f_G	bivariate Gaussian function applied to model the shape of the wake
k	empirical parameter implemented in the eddy-viscosity model
k'	wake expansion rate implemented in the model of the turbulence mixing-length σ_r
m	elliptic parameter
p	pressure
q^2	elliptic parameter
r_V	radial distance from the rotor axis in the vortex-cylinder wake model and in the horizontal wake deficit function W_{DF}
s	radial coordinate in the lidar volume average model
u	streamwise wind speed component; horizontal wind component pointing to North
u_*	friction velocity

u_0	difference between the maximum and the minimum values of the function W_{DF} describing the shape of the horizontal wind speed deficit in the wake of a wind turbine
u_D	difference of the normalized wind speed deficit in the wake of a wind turbine from 1
\tilde{u}_D	iteration variable implemented in the numerical solution of the 3-D shear-layer model
u_{HH}	streamwise wind speed component at hub height in the free-flow
$u_{a y}$	turbulence velocity scale in the cross-stream direction
$u_{a z}$	turbulence velocity scale in the vertical direction
u_{lidar}	streamwise wind speed component resulting from the simulation of lidar measurements in a wind field generated with large-eddy simulations
u_{r,γ_t}	radial wind speed component induced by the tangential vortex
u_{ref}	streamwise wind speed component extracted from a wind field generated with large-eddy simulations and implemented as domain of lidar simulations
u_{x,γ_t}	streamwise wind speed components induced by the tangential vortex Γ_t
v	cross-stream wind speed component; horizontal wind component pointing to East
v_r	local radial wind component implemented in the volume average model of lidar measurements
w	vertical wind component
x	streamwise/North axis of a Cartesian frame of reference; downstream distance from the rotor centre in the vortex-cylinder wake model
x_{F_2}	parameter of the filter function F_2 implemented in the eddy-viscosity model
y	cross-stream/East axis of a Cartesian frame reference;
y_μ	cross-stream coordinate of the maximum value of the bivariate Gaussian function f_G
z	vertical axis of a Cartesian frame reference
z_0	roughness length
z_{HH}	hub height
z_μ	vertical coordinate of the maximum value of the bivariate Gaussian function f_G

Abbreviations

3DSL	three-dimensional shear-layer model
CFD	computational fluid dynamics
CNR	carrier to noise ratio
DBS	Doppler beam swinging
DWM	dynamic wake meandering model
FFT	fast Fourier transform
FINO	Forschungsplattformen in Nord- und Ostsee
FLaP	farm layout program
FWHM	full width half maximum
IEA	International Energy Agency
IEC	International Electrotechnical Commission
LES	large-eddy simulations
LiXim	lidar scanner simulator
LOS	line of sight
PALM	parallelised large-eddy simulation model for atmospheric and oceanic flows
PPI	plan position indicator
RANS	Reynolds averaged-Navier-Stokes
RHI	range height indicator
RMSE	root-mean-square error
SCADA	supervisory control and data acquisition
VAD	visual azimuth display
avg	average
cw	continuous wave
max	maximum
min	minimum
st. dev	standard deviation

List of Figures

1.1	Development of the wind speed vertical profile in the wake of a wind turbine . . .	4
1.2	Turbulence development in a wind turbine wake (a). Idealised sketch of the vertical wake meandering (b)	4
1.3	Meandering of smoke plumes released by a chimney in the atmosphere (a). Dynamic wake meandering pictured as a train of disc particles meandering like smoke plumes (b)	7
1.4	Illustration of the volume average and radial projection of lidar measurements . .	8
1.5	Position of the radial wind speed measurements for different lidar measuring strategies: Doppler beam swinging, DBS (a); visual azimuth display, VAD (b); plan position indicator, PPI (c); range height indicator, RHI (d)	10
2.1	Sketch of the radial direction of the laser beam defined by the azimuth and elevation angles	15
2.2	Comparison of the radial wind speed measurements simulated with LiXim and Simulid with respect to eight reference cases	20
2.3	Possible approaches for lidar measurements of a wind turbine wake profile at the reference points: Doppler beam swinging (DBS) (a) ; concurring, synchronised measurements (multi-lidar) with lidars near to the target and with low elevation angles (b) and further away from it with high elevation angles (c)	22
2.4	Measurements of a wind turbine mean wake profile simulated with the approaches of Fig. 2.3 and compared to the corresponding reference values	23
2.5	Absolute deviation from the reference of the wind speed components calculated implementing the approaches of Fig. 2.3 into lidar wake measurements simulations	24
2.6	Three-dimensional view of the experiment simulated with LiXim	26
2.7	Comparison of the reference streamwise wind component with the simulated radial measurements averaged over time	28
2.8	Comparison of normalised average wind speed deficit of the reference with the normalised average radial wind speed deficit evaluated from the lidar simulations. In both cases, the corresponding fit of the wake model is also included	29

2.9	Results from different wake tracking approaches applied to simulations of lidar measurements with a variable offset between the radial and the wind directions . . .	30
7.1	Helicoidal vortex system of a wind turbine wake (a) decomposed into its linear components (b), i.e. the bound, root and trailing edge longitudinal vortices and its tangential component (c)	91
7.2	Wind field induced by a semi-infinite vortex-cylinder	92
7.3	Flowchart of the algorithm implemented in the 3DSL model to solve the wind field on the next downstream vertical cross-section	95
7.4	Number of 10 min intervals available classified according to the thrust coefficient C_T and the turbulence intensity TI (a). Exemplary wake profile W_D obtained for the C_T class 0.6 at the cross-section $x_i = 3D$ (b)	97
7.5	Downstream evolution of the wake width σ_r evaluated from the profile function of the wind speed deficit fitted to full-field wake measurements	98
7.6	Horizontal (a) and vertical (b) profiles of the normalised streamwise wind component simulated with the 3DSL model applying $x_{F2}=5.5$ in combination with $G_\gamma=1.15$ and $G_\gamma=1.25$. The results are compared to the reference profiles from the large-eddy simulation (LES) wind field at different downstream position	100
7.7	Horizontal profiles of the normalised streamwise wind component simulated with the 3DSL model applying $x_{F2}=5.5$ in combination with $G_\gamma=1.15$ or $G_\gamma=1.25$. The results are compared to the reference profiles measured with a nacelle-based lidar at different downstream positions	101
7.8	Layout of the simulated turbines with the rotor in different wake conditions: full-wake (a), partial-wake (b) and alongside-wake (c) rotor conditions	101
7.9	Scatter plot and corresponding regression line and root-mean-square error of the streamwise wind component derived from the 3DSL model in relation to the reference field calculated with large-eddy simulations for (a) full-wake, (b) partial-wake and (c) alongside-wake rotor conditions	102
7.10	Juxtaposition and difference of the results from large-eddy and 3DSL model simulations with respect to the normalised streamwise wind speed component estimated on nine downstream cross-sections for the full-wake rotor conditions.	104
7.11	Juxtaposition and difference of the results from large-eddy and 3DSL model simulations with respect to the normalised streamwise wind speed component estimated on nine downstream cross-sections for the partial-wake rotor conditions	105
7.12	Juxtaposition and difference of the results from large-eddy and 3DSL model simulations with respect to the normalised streamwise wind speed component estimated on nine downstream cross-sections for the alongside-wake rotor conditions	106
7.13	Juxtaposition and difference of the results from large-eddy and 3DSL model simulations with respect to the normalised cross-stream wind speed component estimated on nine downstream cross-sections for the full-wake rotor conditions	107

7.14	Juxtaposition and difference of the results from large-eddy and 3DSL model simulations with respect to the normalised vertical wind speed component estimated on nine downstream cross-sections for full-wake rotor conditions	108
------	--	-----

List of Tables

2.1	Statistics of the deviation from the reference of the wind speed components calculated from lidar measurements simulated for different approaches within a wind turbine wake	24
2.2	Limits of the parameters implemented for the fit of Eq. 2.14 to the average wind speed deficit and corresponding results for the simulated layouts	27
2.3	Results from the fit of Eq. 2.14 to the average wind speed deficit in the wake of a wind turbine for the simulated layouts and the reference case	30
7.1	Average atmospheric conditions and data availability for the thrust coefficient classes, considering the corresponding interval of the hub-height wind speed and the turbulence intensity range from 5% to 6%	97
7.2	Expansion rate k' and initial wake width ϵ' evaluated from the profile function of the wind deficit fitted to full-field wake measurements	98
7.3	Main characteristics of the reference datasets used for the assessment of the parameters of the pressure gradient model	99

Introduction

1.1 Motivation

In the last decades, the earth has been subject to climate mutations which can be generally attributed to global warming. Specifically, worldwide average temperatures have already increased by 1° from pre-industrial time, at a rate of 0.2° per decade in the last years. As a consequence of higher temperatures, polar ice caps are melting, glaciers are retreating, sea levels are rising, seasonal and rainfall patterns are changing and extreme weather events are becoming more frequent. The Intergovernmental Panel on Climate Change, (2018) warned that these conditions are not sustainable and will lead to dramatic changes to the world if global warming is not contained.

Energy production based on the combustion of fossil fuels is one of the main causes of increasing temperatures. In fact, their carbon emissions into the atmosphere are responsible for the greenhouse effect, i.e. on the one side the exhaust fumes let the sun's radiation into the atmosphere which gets warmer, but on the other side they are an obstacle to the release of the heat accumulated into the atmosphere itself. In this respect, global warming can be limited reducing carbon emissions.

In 2018, 68 % of the global primary energy demand was fulfilled by fossil fuels. Renewable energies had a share of 25 % and the remaining part was provided by nuclear plants. Very similar figures describe also the electricity generation mix (IEA, 2018). Considering Europe only, 32 % of the electric energy was produced from renewable sources, in particular, wind had the largest share with about 12 % (Jones et al., 2019).

National governments are together discussing possible solutions to limit carbon emissions and global warming. The European Commission compiled a strategic long-term vision (European Union, 2019) with the main goal of limiting to 1.5° the temperature increase with respect to pre-industrial time. According to the calculations by the European Commission, renewable electricity must rise to 57 % by 2030 to achieve this goal. In this scenario, wind energy has still the largest share in the renewable energy mix with 26 % of the overall production. Focusing on wind energy, the installed capacity should rise to 350 GW by 2030. This is a challenge considering the 189 GW capacity installed at the end of 2018 WindEurope, (2019) and the average growth rate of 17.4 GW a year expected for the next five years WindEurope, (2018).

These figures point out the importance of wind energy as a renewable source to limit global warming. In this respect, research should support the development of new technologies to reduce the cost of wind energy and facilitate its use. This could be achieved for instance by developing technologies to improve the efficiency of wind power plants, optimising their construction process, or investigating wind physics to improve the accuracy of prediction models implemented in the design and development of wind projects.

Proper wind farm planning is a key point for the success of wind projects because it brings major economic benefits to both investors and developers. This complex task comes with technological challenges and is subject to many sources of uncertainties which can undermine the profitability of the project during its expected life-time. This is the reason why accurate planning, modelling and optimisation are required for the technical feasibility and competitiveness of wind projects.

Wake losses are one of the adverse factors affecting the energy yield of a wind farm and need to be assessed already at the beginning of a wind project. A wake is the region behind an obstacle – such as the turbine rotor – characterised by slower wind, increased vorticity and higher turbulence levels. As a result, a wind turbine exposed to a wake has less kinetic energy available to convert into mechanical and then electric energy. Because of the increased turbulence, a waked turbine experiences higher load fluctuations that could reduce the lifetime of turbine components or increase their operation and maintenance costs due to increased fatigue loading.

The width and intensity of a wind turbine's wake depend on the wind conditions defining the operating point of the turbine but have opposite behaviours: Whilst the former grows with the downstream distance, the latter decreases. Accordingly, wake effects can be reduced by increasing the space between the turbines in a wind farm. In this respect, wake losses depend on the wind resource at the site and on the layout of the wind farm; e.g. a wind farm with closely packed turbines in line with the prevailing wind direction is not going to be economically viable in terms of wake effects.

Wake models are often applied to estimate the reduction of the wind resources caused by wakes at a wind farm site. They are implemented in automatic optimisation tools (Schmidt et al., 2014; Thøgersen et al., 2011) to test different layouts, predict their wake losses and choose an optimal solution. Also the effects of the higher turbulence levels expected in wakes can be predicted by wake models and included into the optimisation of the wind farm design (Réthoré et al., 2013), however, this is not common practice (Herbert-Acero et al., 2014).

The development of wake models is supported by experimental activity in order to reveal specific physical aspects of the wake or to validate their implementation. Scaled wind turbine models (Medici et al., 2008; Rockel et al., 2016) or porous discs are installed in wind tunnels for measurements in wakes. Typical instruments for these measurements are based on laser Doppler velocimetry (García et al., 2017), hot wire anemometry (España et al., 2012; Muller et al., 2015) or particle image velocimetry (España et al., 2011). Wind tunnel experiments have the advantage of a controlled environment where the flow parameters (Hancock et al., 2014) and the turbine characteristics (Schepers, 2012) are well defined.

In full-field measurements, mast-mounted instruments can be implemented to measure the free-stream atmospheric conditions and the wind velocity in the wake (Lange et al., 2003; Troldborg et al., 2010). In an indirect manner, the wind speed deficit in the wake can be estimated in terms of the difference between the power of a front-row turbine and the turbines downstream (Archer et al., 2018).

Remote sensing is another more recent option for wake measurements. Its technology is based on sound, radio or light waves emitted into the atmosphere and enables to scan the wind within a range from tens of metres to kilometres. Depending on the wave source, remote sensing instruments are indicated differently; namely, sodar, radar or lidar devices are based on sound, radio and light waves, respectively.

The application of lidars to wind energy research projects has been growing fast in recent years (Aitken et al., 2014; García et al., 2017; Herges et al., 2018; Iungo et al., 2014; Smalikho et al., 2013; Trujillo et al., 2011; van Dooren et al., 2016). Still, lidars measurements are a subject of research because they have reduced spatial and temporal resolution and rely on flow models which might be not always representative of real conditions.

Understanding the complexity of the non-linear phenomena dominating wakes and minimising wake losses – in particular for offshore wind farms – is still an open challenge. This thesis is a contribution to the development of wake models using modern lidar technology. Following this purpose, on the one hand, it studies full-field lidar experiments for wake measurements. On the other hand, it suggests an engineering simplification for the simulation of the wakes in a wind farm. The following sections provide background about wind turbine wakes, lidar measurements, and outline the structure of this thesis.

1.2 State of art

This section focuses on the structure and development of the airflow in the wake of a wind turbine, shortly describes the most important models for numerical simulations of wakes and introduces remote wind speed measurements in wakes by means of lidars.

1.2.1 Wind turbine wakes

The wake flow is generally divided into the near- and far-wake regions: In the former, the flow expands and its shape is defined by the geometry and action of the rotor; in the latter, the development of the flow is driven by turbulent diffusion. Figures 1.1 and 1.2a sketch the downstream development of the wind speed and turbulence vertical profiles, respectively.

Not only does the rotor affect the downstream region, but it also influences the upstream airflow, which expands and increases in pressure while approaching the rotor in the so-called upstream induction zone. The extent of this region can vary between 2 and 4 rotor diameters. At the rotor, a complex system of vortices is shed by the blades and the aerodynamic energy is converted into mechanical energy by the rotor, causing the pressure to drop below the value in the free-stream.

The near wake development starts behind the rotor where the pressure of the airflow recovers at the expense of the kinetic energy with a consequent wind speed reduction. At the same time, the velocity gradients at the flanks of the wake give rise to an annular shear-layer. The large scale turbulence generated in this annular layer results in two peaks in the turbulence radial profile. At the end of the expansion region – between one and two rotor diameters downstream – the wake has the lowest centre-line wind speed. Due to turbulent mixing, diffusion of momentum becomes the dominating process in the flow, the peaks in the turbulence profile gradually converge and the shear-layer grows while moving downstream until it covers the full wake cross-section between 2

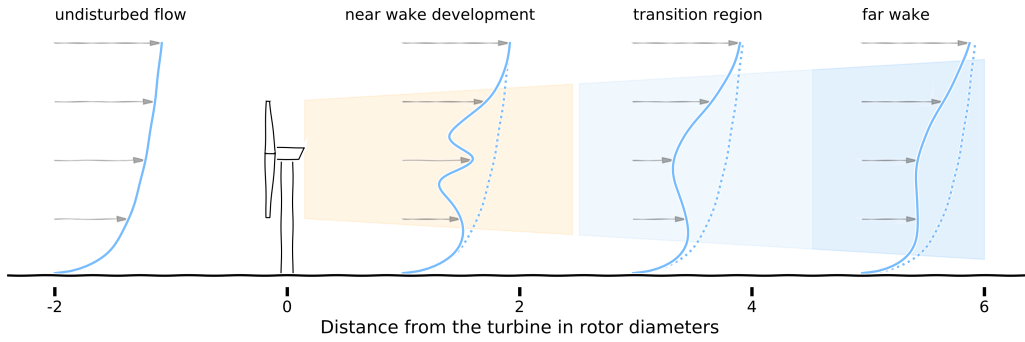


Figure 1.1: Development of the wind speed vertical profile in the wake of a wind turbine. The blue lines indicate the vertical profile of the stationary wind velocity. The wake region is shaded with different colours, namely orange where the near wake develops itself and dark blue in the far wake region. Light blue is the colour of the transition range in between.

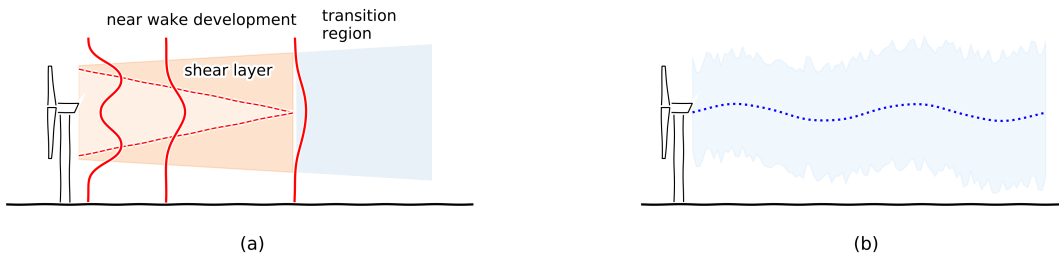


Figure 1.2: Turbulence development in a wind turbine wake (a). The solid red lines represent the vertical profile of the turbulence level in the wake. The shaded area (orange and blue) indicate the wake region; the shear-layer (darker orange) gets thicker until it reaches the core of the wake as shown by the dashed red lines. Idealised sketch of the vertical wake meandering (b).

and 5 rotor diameters downstream. At this point, the near wake is fully developed (Crespo et al., 1999).

Downstream of the near-wake development, the tip-vortices break down; in the far wake region further downstream only the overall rotor thrust and the total turbulent kinetic energy produced by the rotor influence the wake profiles which can be assumed self-similar if the ground and the ambient shear are disregarded.

The above description applies to the case of stationary wakes and implies a wake propagation along a straight line. In reality, wakes could follow a winding and dynamic path known as wake meandering. In fact, the interaction between the rotor and the large scale turbulent structures of the atmospheric boundary layer could make the wake centre oscillate around the axis of the stationary wake (see Fig. 1.2b).

In wind farms, wakes are not always as simple as their steady-state or dynamic description. Each turbine sheds a wake which can interact with other turbines or other wakes depending on turbine positions in relation to the wind direction. Considering the case of two turbines aligned with the wind direction, the wake of the upstream turbine will cover the entire rotor of the one downstream which then will be operating in full-wake conditions. If the wind direction changes in a way that the misalignment between the turbines and the wind direction grows gradually, at a certain point only part of the rotor will be within the wake (partial-wake conditions). Eventually, the wake will

not go through the rotor any more, but just pass by and interact with the wake shed by the rotor (alongside-wake conditions). The wake-wake and the wake-turbine interaction are often indicated as merging or multiple wakes.

1.2.2 Wake models

Wake models are essential for the estimation of the energy yield of a wind farm. Their main application is the prediction of the wind conditions downstream of a turbine rotor. With this information, one can estimate the energy available to the downstream turbines. Extending the application of wake models to the entire wind farm, it is possible to estimate its annual energy yield or optimise its layout. In the following, an introduction is given about the main aspects of wake simulations including an overview of different models and information about their application within a wind farm.

Kinematic analytical models

Kinematic analytical wake models are steady-state models commonly used for engineering applications because they are robust, fast, and easy to apply. Models of this family assume a self-similar velocity deficit profile, an assumption corroborated by experimental and theoretical research on co-flowing jets. The first kinematic models started appearing along with the first operating wind farms towards the end of the 1970s. The models by Jensen, (1983), Katic et al., (1986), and Lissaman, (1979) belong to this category and are based on the conservation of mass and momentum assuming an axisymmetric linear expansion of the wake. Larsen, (1988) derived a different analytical model from the turbulent boundary layer equations, assuming self-similarity of the wake profile and applying the mixing-length theory to describe the turbulent stresses. Another example of analytical models is the one proposed by Frandsen et al., (2006) who considered a simplified momentum balance between the undisturbed flow and the wind turbine wake applied to a cylindrical control volume with the same axis as the rotor and constant cross-sectional area equal to the area of the expanded wake. Archer et al., (2018) provide a review of analytical models commonly used for wind farm planning.

Field models

In contrast to kinematic models, field models calculate the flow quantities at each point of the flow field. Following this approach, several steady wake models have been developed with a very broad range in terms of computational requirements. The eddy-viscosity model by Ainslie, (1988) is one of the first field models; it implements the simplified shear-layer formulation of the axisymmetric Navier-Stokes equations with an eddy-viscosity closure, disregarding viscous and gravitational forces. A Gaussian-shaped wind velocity deficit defines the initial conditions at a rotor distance where pressure gradients can be neglected, i.e. at approximately 2.5 rotor diameters downstream of the turbine. The width of the Gaussian profile was scaled in order to satisfy the momentum balance between the free-flow and the wake, while its amplitude was calibrated on the basis of wind tunnel experiments realised at different turbulence intensity and rotor thrust conditions.

Reynolds averaged Navier-Stokes (RANS) simulations and large-eddy simulations (LES) rely on field models applied to computational fluid dynamics (CFD); they provide the highest level of

physical accuracy and are often applied to investigate the physics of wakes. While RANS can be implemented for engineering applications, LES are rarely implemented because of their high computational cost. Sanderse et al., (2011) provide a good overview of CFD models of the wake aerodynamics.

In RANS simulations, the instantaneous Navier-Stokes equations are averaged over time decomposing the main variables into an average and a fluctuating value. The averaged equation equals the instantaneous equations with the additional contribution of the so-called Reynolds stress tensor, which results from the non-linearity of the convective terms and describes the mean momentum transfer given by turbulent fluctuations. Several models have been developed to estimate the Reynolds stress tensor and the viscous effects of turbulence. Simplified RANS models for wake simulations are based on a linearised (Ott et al., 2011; Segalini, 2017) or parabolic (Crespo et al., 1985; Iungo et al., 2018; Schepers, 2003) formulation of the Navier-Stokes equations.

In LES, the airflow is decomposed depending on the scales of eddies, i.e. the turbulent structures in the airflow. For large scale eddies, the Navier-Stokes equations are solved directly; small scales eddies are approximated with a sub-grid-scale model. To model the wind turbine, body forces are imposed on the wind field. The actuator disc model estimates these forces considering a uniformly loaded rotor and disregarding rotational effects. Thanks to its simplicity, it can be applied with reasonable results to simulate the flow of large wind farms (Witha et al., 2014). The rotating actuator line model (Martinez-Tossas et al., 2016; Troldborg et al., 2010) is a much more complex and accurate model, but also more demanding in terms of computational time. A solution in between is an enhanced actuator disk model with rotation (Dörenkämper et al., 2015).

Wake added turbulence and dynamic wake models

Not only does a turbine in wake face lower wind speeds than the undisturbed flow, but it experiences increased load fluctuations because of the wake added turbulence, the wake meandering and the load imbalances given by possible partial-wake conditions of the rotor. Prediction of these effects is required in the design of wind turbines to estimate fatigue loads and the life-time of their components.

On the basis of wind tunnel experiments, Hassan, (1992) and Quarton et al., (1989) proposed empirical expressions to model the wake added turbulence as a function of the free-stream turbulence intensity and the rotor thrust coefficient. Frandsen, (2007) suggested an alternative method based on the geostrophic drag law and considering the effect of wind farms as additional surface roughness. This model is also included in the international standard for the design of wind turbines (IEC, 2005) as an informative annex. In a recent study, Gerke et al., (2018) compared the mentioned as well as other models with data from the supervisory control and data acquisition (SCADA) system; they found that the investigated models for wake added turbulence generally overestimate turbulence and recommend to recalibrate the parameters of the models for multi-megawatt wind turbines.

The wake meandering, i.e. dynamic vertical and lateral movement of wake, is accounted for in the dynamic wake meandering model (DWM) (Larsen et al., 2008) in which an analogy associates wakes to smoke plumes or passive tracers transported through the atmosphere as depicted in Fig. 1.3. Accordingly, the wake is imagined as a train of discrete particles emitted by the rotor, and moving downstream driven by vertical and lateral large scale turbulent structures. The contribution by

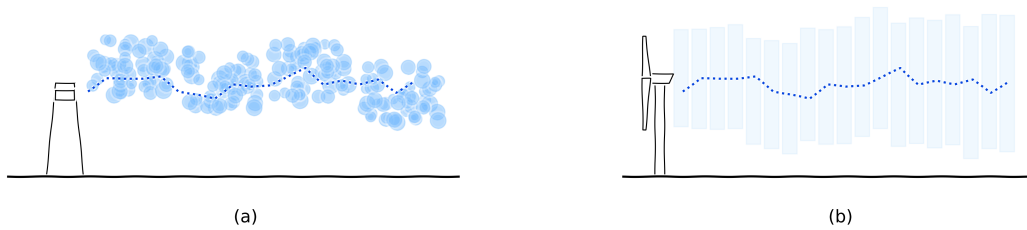


Figure 1.3: Meandering of smoke plumes released by a chimney in the atmosphere (a). Dynamic wake meandering pictured as a train of disc particles meandering like smoke plumes (b).

turbulent structures with smaller scales is assumed to be averaged out by the rotor action. In practice, a low pass filter is applied to fluctuations of the lateral and vertical wind speed components (the cut-off frequency is estimated by the mean free-flow wind speed divided by two rotor diameters) and the turbulent wind field is advected through the rotor applying Taylor's hypothesis of frozen turbulence (Panofsky et al., n.d.). Next, the profile of the wind speed deficit calculated at each time step is transported downstream considering the advection speed of the wake along with the filtered lateral and vertical wind speed components.

Lately, wake stochastic models have been proposed to predict loads on a waked turbine. Doubrawa et al., (2017) based their model on the wake of an LES wind field defining the spectral characteristics of the wake shape in terms of wake radius and azimuthal position. Bastine et al., (2018) developed a dynamic wake model based on a reduced number of modes from proper orthogonal decomposition of the wind speed deficit weighted by stochastic coefficients describing their dynamics. Moon et al., (2018) presented a wake model in which the stochastic parameters of the wake are calculated with multivariate multiple linear regression with respect to a reference wind field.

Wakes in a wind farm

Most of the mentioned models are generally applied to simulate single wakes. To reproduce the flow in a wind farm, merging and multiple wakes are modelled with the superposition of the effects estimated independently for every single wake beforehand. For instance, while Lissaman, (1979) suggested to cumulate linearly the wind reduction of individual wakes, Katic et al., (1986) proposed their quadratic superposition. In more recent work, Macheaux, (2015) proposed a combination of the linear and quadratic addition methods weighted depending on the thrust conditions on the rotor.

1.2.3 Doppler wind lidar for wake measurements

Doppler wind lidar systems (hereinafter indicated simply as lidars) are remote sensing instruments which use the light emitted by a laser into the atmosphere to estimate the wind speed. They are based on technology developed in the end of the 1980s. First applications dealt for example with airborne wind speed measurements (Bilbro et al., 1984) or airport weather studies (Rothermel et al., 1985). However, lidar popularity has increased in the last decades thanks to the development of telecommunication laser in the infra-red frequency range. This development reduced costs and dimensions of lidars, which have often become a convenient alternative to tall meteorological towers.

Lidars send infra-red laser beams into the atmosphere and sample the wind. When the aerosol particles transported by the wind backscatter the light emitted by the lidar, the frequency of the reflected light is shifted because of the Doppler effect. This frequency variation can be measured and is proportional to the relative movement between the light and the aerosol, i.e. to the projection of the aerosol velocity on the radial direction (see Fig. 1.4).

The underlying assumptions of the lidar working principle are (i) the presence of aerosol in the atmosphere, (ii) the equality between the speed of the aerosol and of the wind and (iii) the possibility of the lidar to "see" the aerosol, i.e. the possibility of the light to reach the aerosol and come back without being absorbed along the way. As a consequence, the environmental conditions fail the first point in a very clean atmosphere or above the atmospheric boundary layer. Similarly, the presence of low clouds or fog may fail the third point because of low visibility along the laser path. In such conditions, lidars do not work properly and have low availability of data.

Depending on the laser source, lidars can sample a single distance for each beam emitted, or at several ranges from the telescope lens. In the former case, the lidar has a continuous-wave (cw) laser which is focused on the measurement target and the sampling frequency varies from ~ 50 Hz to ~ 400 Hz.

In the latter, the laser is collimated and emits light pulses at a frequency between 10 kHz and 20 kHz. While a pulse propagates through the atmosphere, its light is continuously reflected and sampled by the lidar until the next pulse is emitted. This means that the light collected between two pulses comes from different distances along the radial direction. Hence, analysing the backscatter signal in windows (usually called range-gates) and averaging thousands of pulses it is possible to calculate the radial wind component simultaneously at several distances. These distances are then estimated from the time-of-flight of the light collected during the range-gate windows. Due to the averaging time (also known as accumulation time), the highest sampling frequency is in the range from ~ 0.1 Hz to ~ 10 Hz.

The pulse of the laser illuminates a volume in the atmosphere which mainly depends on the shape and duration of the pulse. The intensity of the pulse can be well approximated by a Gaussian shape with a full-width half-maximum in the range from 100 ns to 800 ns. For this reason, the radial wind speed measured by lidars is not representative of a specific point, but of the weighted

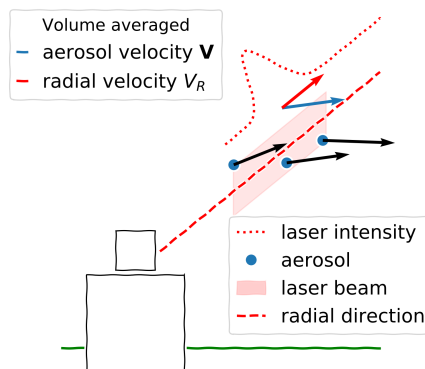


Figure 1.4: Illustration of the volume average and radial projection of lidar measurements.

average over a finite volume which resembles a thin cylinder with a diameter equal to the aperture of the lidar telescope and extension up to 150 m (see Fig. 1.4).

To retrieve the three components of the wind vector, lidar measurements in at least three linearly independent radial directions need to be combined with a wind reconstruction model including some necessary assumptions about the wind flow. The so-called Doppler-beam swinging (DBS) and the visual-azimuth display (VAD) methods are two common techniques applied to calculate the full wind vector from lidar measurements over an upside-down conical surface (Peña et al., 2015). Figure 1.5a-b sketch the scanning patterns suitable for the DBS and VAD wind reconstruction methods.

Lidars are often used to measure the vertical profile of the horizontal wind speed as completion or often even as replacement of wind sensors installed on meteorological masts (IEC, 2017; MEASNET, 2016). Pulsed lidars commonly apply the DBS method and measure the wind vector simultaneously at several heights and a sample rate of around 1 Hz. Continuous-wave lidars operate differently: They need to change the focus distance after completing a full azimuthal scan of 360° which takes about 1 s. The two approaches provide similar results in terms of 10 min averaged quantities. A less complicated and more flexible installation and the possibility to reach the upper tip height of current multi-megawatt wind turbines are the advantages of lidars in relation to mast mounted anemometry.

As a consequence of the spatial and temporal averaging over the sample volume and the multiple radial directions, the wind vector measured with a lidar is not the same as the one measured for instance with a sonic anemometer which can sample the wind at a single point in space with a rate of 100 Hz. For the same reasons, in flows dominated by shear or dynamic turbulent structures uncorrelated wind speeds from different positions could be erroneously averaged by the lidar and the measurements could be inaccurate or imprecise and misleading. In these situations, it is recommended practice to verify the measurement strategy by means of lidar simulations within a synthetic wind field representative of the expected atmospheric conditions (Clifton et al., 2018).

If a hemispherical scanner is incorporated into a pulsed lidar and if the power of the laser enables long-range measurements, it is possible to map the radial wind speed component with plan position indicator (PPI) scans over a sector of a shallow cone (see Fig. 1.5c) or with range height indicator (RHI) scans over vertical slices (see Fig. 1.5d) obtained by varying the azimuth angle at a low and constant elevation angle in the former case, or keeping the azimuth angle constant while changing the elevation angle in the latter. Also in these cases, assumptions on the wind flow and a wind field reconstruction model are necessary to calculate the map of the wind vector from the radial measurements. These scanning strategies are suitable to study non-homogeneous wind fields, e.g. wakes, canopies, non-flat terrain or low-level jets.

Analysing the wake of a multi-megawatt turbine on the basis of lidar measurements, Käsler et al., (2010) demonstrated that long-range scanning lidars are convenient tools to investigate wakes. In fact, they enable sampling of the wind field in the wake with reasonable time and space resolution. In similar works, Iungo et al., (2014) and Smalikho et al., (2013) studied the downstream development of the wind speed deficit in the wake of a wind turbine under different atmospheric conditions.

To study wake meandering, Trujillo et al., (2011) developed a wake tracking method capable of identifying the centre-line of a two-dimensional far-wake deficit; the method fits a Gaussian shape

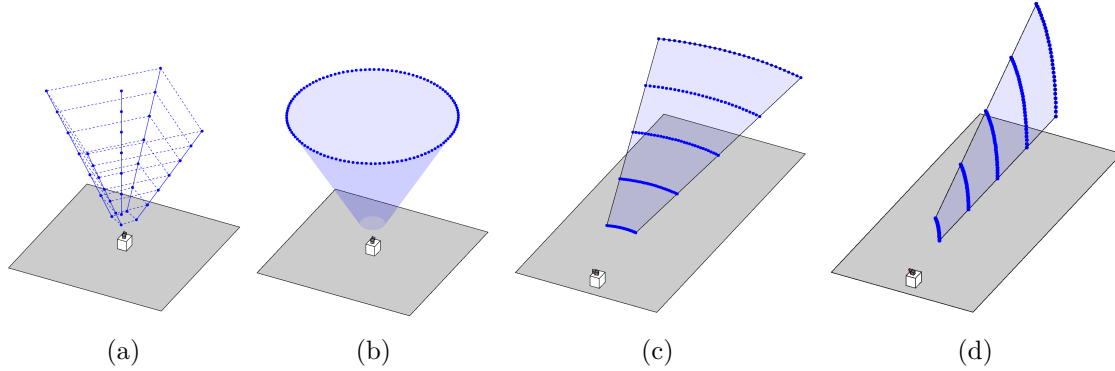


Figure 1.5: Position of the radial wind speed measurements (blue dots) for different lidar measuring strategies: Doppler beam swinging, DBS (a); visual azimuth display, VAD (b); plan position indicator, PPI (c); (d) range height indicator, RHI (d).

to the radial wind speed measured from the nacelle of a wind turbine to find the centre position of the wake, its width and maximum wind speed deficit. Different variants of this method can be applied to identify stationary properties of wakes (Aitken et al., 2014; Barthelmie et al., 2016; Bodini et al., 2017; Carbaajo Fuertes et al., 2018; García et al., 2017; Raach et al., 2017; Trujillo et al., 2016).

1.3 Objectives and structure of the thesis

As mentioned in Section 1.1, it is of fundamental importance to be able to accurately predict the annual energy yield of a wind farm already at the beginning of its planning phase. In this respect, lower uncertainties mean lower risks of investment, better financial conditions and in the end a lower cost of energy. For this reason, enhancing wake models to reduce the uncertainty of the annual energy yield predictions is among the primary objectives of wind energy research.

Wakes are generally accountable for power losses with respect to wind turbines facing the undisturbed flow. Higher wake losses can be expected in wind farms with closely packed turbines because of the mutual interaction among wakes and turbines.

The wake models adopted to estimate the annual energy yield of a wind farm, address wakes interaction pragmatically: Each wake is considered individually and their deficits are combined where the wakes overlap. This approach enables fast computation, but it is not supported by any solid physical background. Furthermore, the interaction among wakes and turbines is modelled considering wakes as isolated entities and not as part of the continuous flow streaming through the wind farm.

In this respect, the first objective of the present work is to develop an engineering wake model which abandons the idea of single wakes to consider multiple wakes as a whole, with the ambition to reduce the uncertainty affecting the estimation of wake losses.

Wake models are based on parameters that need to be calibrated. Lidar data can be adopted for this purpose, but the complexity of the wake flow might invalidate the measurements. On this ground, the second objective of the thesis is to develop methodologies for the assessment of wakes with lidar measurements.

In order to serve both objectives, the wake model will only look at the interaction of steady wakes. More complex modelling such as wake meandering of multiple wakes does not lend itself to be validated by lidar due to the latter's limited spatial and temporal resolution when it comes to scanning large sectors within a wind farm.

The two objectives are addressed in reverse order, beginning with the application of lidar to wake measurements from Chapters 2 to 5. The new wake model is then described in Chapters 6 and 7. Finally, Chapter 8 gives an account with respect to the objectives and the achievements. These chapters are briefly outlined in the following paragraphs.

Chapter 2

The present research started when knowledge and experience of wind speed measurements in the wake of a wind turbine with lidars was still limited. To fill this gap, Chapter 2 deals with a lidar simulator which enables testing of measurement strategies and estimation of their error in a virtual environment. The chapter also introduces basic concepts applied in the following chapters for lidar measurements in wakes.

Chapter 3

Wake meandering has often been studied with lidar measurements. In fact, the centre position of the wind deficit can be identified from horizontal or vertical scans of the wake. However, it is not always possible to achieve a sufficient repetition rate of the scanning trajectory. The journal article "Application of staring lidars to study the dynamics of wind turbine wakes" (Trabucchi et al., 2015b) included in this chapter suggests how a sufficient repetition rate can be achieved with an atypical approach and it also shows how insight about wake meandering can be gained from these measurements.

Chapter 4

In Chapter 3 lidar measurements along a fixed direction were analysed in the frequency domain, assuming that the spectral characteristics of the wind could be measured with lidar measurements along a direction. This assumption is verified in the paper "Study of wake meandering by means of fixed point lidar measurements: Spectral analysis of line of sight wind component" (Trabucchi et al., 2015a) included here. In the publication, the results of the full-field experiment of Chapter 3 are confirmed on the one hand by virtual measurements synthesised with the lidar simulator introduced in Chapter 2 and on the other hand by new offshore measurements.

Chapter 5

While the two previous chapters are focused on measurements of the wake meandering, the research of this chapter aims to study 10 min averaged wake profiles obtained from lidar measurements. The work is reported here in the form of the paper "Nacelle-based Lidar Measurements for the Calibration of a Wake Model at Different Offshore Operating Conditions" (Trabucchi et al., 2017b). This work describes the experimental setup of the lidar measurements and the methodology applied to calculate the profiles of the wind speed deficit used in the calibration of an analytical wake model.

Chapter 6

As explained in Section 1.2.2, most engineering wake models are not suitable for dealing with multiple wakes directly because they solve a two-dimensional, axisymmetric flow. This chapter introduces a three-dimensional model which is applicable also to non-axisymmetric, single or multiple wakes. The development and evaluation of the model are explained by the paper entitled "3-D shear-layer model for the simulation of multiple wind turbine wakes: description and first assessment" Trabucchi et al., 2017a which is the last paper incorporated into the thesis.

Chapter 7

In this chapter, the 3-D shear-layer model introduced in Chapter 6 is further developed to include the previously excluded induction zone into the domain of the model. Furthermore, Chapter 7 closes the circle between the two main objectives of the thesis comparing the new wake model with the lidar measurements of Chapter 5.

Chapter 8

This chapter closes the thesis with a twofold conclusion: On the one hand, it compares the objective with the achievements. On the other hand, it deals with two questions that are hidden behind the main objectives of the present research:

1. How to deal with the limitations of lidar technology when being applied to wake measurements?
2. How far is it possible to conveniently improve the physics of engineering wake models?

Lidar simulations for the design of wake measurement campaigns

2.1 Introduction

Doppler wind lidars cannot measure the wind vector at a specific point of interest as wind vanes, cup and sonic anemometers. They measure the component of the wind vector parallel to their pointing direction as a weighted average over a thin (tens of centimetres), but long volume (ten to hundred or more metres) illuminated by their laser.

Nevertheless, they can be implemented for wake measurements. In fact, they can retrieve the wind vector over large surfaces in a relatively short time interval. In the most optimistic scenario, three simultaneous lidar measurements with linearly independent pointing directions and intersecting at – or being representative of – the same point in space are available and can be combined to reconstruct the wind vector. If such configuration cannot be implemented, a wind field reconstruction method based on reasonable assumptions on the wind field (e.g. horizontal homogeneity of wind speed and wind direction, or negligible influence of the vertical flow on the radial wind speed measurements) is applied to estimate the wind vector at the point of interest.

During full-field measurements, it is not easy to identify all the environmental variables defining the actual atmospheric conditions. Hence, it is not always possible to define an accurate model corresponding to the actual situation and, for this reason, also the estimation of the lidar volume average effects might be a cumbersome task.

Lidar simulations provide a practicable alternative to full-field experiments for the verification of the wind field reconstruction methodologies. Lidar measurements are simulated in a well-known wind field and the results of the wind vector reconstruction method are compared to the original wind field which is a perfect reference.

Lidar simulations have been used often in the past, for instance, to investigate the performances of wind lidars (Frehlich, 1996) and to assess the accuracy of turbulence measurements with lidars (Banakh et al., 2005). Lidar simulators have been developed for wind energy applications too, e.g. in order to support the development of scanning strategies for predictive wind turbine control (Raach

et al., 2017; Schlipf et al., 2015, 2009). Lidar simulations have also been applied in the research field of wind turbine wakes, for example, to estimate errors due to the wind field reconstruction algorithm (Lundquist et al., 2015), to optimise the installation layout for wake measurements from the nacelle of a wind turbine operating in yaw misalignment conditions (Churchfield et al., 2016) and to estimate the effects of the lidar sampling volume (Meyer Forsting et al., 2017).

The research of this chapter is based on – and partly extends – results I presented at international scientific conferences (Trabucchi et al., 2015a, 2011). These works might be surpassed, but they belong to the learning process necessary for the success of the experimental campaigns that followed. For this reason, they are proposed again here with the aim to provide an example of how the strategy of a measuring campaign (lidar setting and scanning pattern, device layout, wind field reconstruction model) can be investigated in a virtual environment by means of lidar simulations.

The chapter starts with a general description of methods for wind field reconstruction and wake characterization based on lidar measurements (Section 2.2); this overview is followed by the description of the lidar simulator developed for the present research (Section 2.3). Next, two exemplary applications of the lidar simulator are presented (Section 2.4). The first one is about the estimation of the average vertical profile of the wind speed in the middle of a wind turbine wake; the second one about the measurement of dynamic wake meandering. Finally, the chapter is concluded with a short summary (Section 2.5).

2.2 Wind speed and wake profiles from lidar measurements

When wakes are measured with lidars, the wind speed is derived from measurement at different positions in space and time. For this purpose, wind field reconstruction models are applied to combine different radial speed measured under different directions considering reasonable assumptions about the wind flow. Some approaches for wind field reconstructions and wake characterisation are explained in the next sections.

2.2.1 Wind field reconstruction

Lidar can measure only one component of the local wind vector at once, precisely its projection on the radial direction \mathbf{e}_R of the laser beam defined by the azimuth angle χ and the elevation angle ζ of the lidar optics (see Fig. 2.1). From a frequency shift in the power spectral density of the backscatter signal, lidars can measure the radial component of the wind

$$V_R = \mathbf{V}^T \cdot \mathbf{e}_R = [u \ v \ w] \begin{bmatrix} \cos(\zeta) \sin(\chi) \\ \cos(\zeta) \cos(\chi) \\ \sin(\zeta) \end{bmatrix} = u \cos(\zeta) \sin(\chi) + v \cos(\zeta) \cos(\chi) + w \sin(\zeta) \quad (2.1)$$

where u , v , w are the North, East and vertical components of the wind vector \mathbf{V} , respectively.

The following methods can be applied to estimate two or three-dimensional wind vectors from lidar measurements.

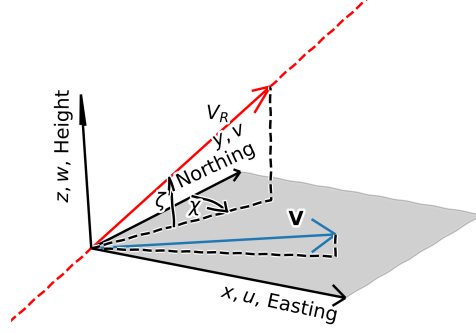


Figure 2.1: Sketch of the radial direction of the laser beam defined by the azimuth and elevation angles χ and ζ , respectively. V_R denotes the radial component of the wind velocity vector \mathbf{V} .

Inverse projection

If the wind direction V_{dir} is known, a simple approach to calculate the magnitude of the horizontal wind vector $|\mathbf{V}_H|$ assumes no vertical wind ($w = 0$) to rewrite Eq. 2.1 as

$$V_R = |V_H| \cos(\Delta\alpha) \cos(\zeta) \quad (2.2)$$

where $\Delta\alpha = V_{dir} - \chi$ is the difference between the wind direction and azimuth angle. This formulation of the radial wind component can be directly inverted to calculate the horizontal wind speed:

$$|V_H| = \frac{V_R}{\cos(\Delta\alpha) \cos(\zeta)}. \quad (2.3)$$

Doppler beam swinging (DBS) method

The DBS technique (Werner, 2005) can be applied to lidar measurements as the ones exemplified in Fig. 1.5a. In the basic form, the lidar sequentially scan three radial directions: one oriented vertically and two at a fixed elevation angle (for instance $\zeta = 60^\circ$) with a mutual offset of 90° between their azimuth angles. The corresponding radial wind speed components can be written as

$$\begin{aligned} V_{RV} &= w \\ V_{RN} &= u \sin(\zeta) + w \cos(\zeta) \\ V_{RE} &= v \sin(\zeta) + w \cos(\zeta) \end{aligned} \quad (2.4)$$

considering, for instance, the vertical beam for V_{RV} and the azimuth angle corresponding to the North and East directions for V_{RN} and V_{RE} , respectively.

Working on these equations, it is possible to obtain the two horizontal components of the wind vector:

$$\begin{aligned} u &= \frac{V_{RN} - V_{RV} \cos(\zeta)}{\sin(\zeta)} \\ v &= \frac{V_{RE} - V_{RV} \cos(\zeta)}{\sin(\zeta)} \end{aligned} \quad (2.5)$$

If additionally the radial wind speed components V_{RS} and V_{RW} with the azimuth angle of the remaining South and West directions, respectively, it is possible to write the horizontal components

of the wind vector as

$$\begin{aligned} u &= \frac{V_{RN} - V_{RS}}{2 \sin(\zeta)} \\ v &= \frac{V_{RE} - V_{RW}}{2 \sin(\zeta)} \\ w &= \frac{V_{RN} + V_{RE} + V_{RS} + V_{RW}}{4 \cos(\zeta)} \end{aligned} \quad . \quad (2.6)$$

This approach is commonly implemented in lidar by cycling the azimuth angle over the four cardinal directions under the assumption that the wind field is horizontally homogeneous and does not vary during the measurement along the different directions.

Visual azimuth display (VAD)

To apply the VAD method (Werner, 2005), the lidar measures along a 360° azimuthal scan with closely separated radial directions as drafted in Fig. 1.5b. The corresponding radial wind component varies as a sinusoidal function of the azimuth angle:

$$V_R = a_{VAD} + b_{VAD} \cos(\chi - \chi_{max}) \quad (2.7)$$

where the offset a_{VAD} , amplitude b_{VAD} and phase shift χ_{max} . The parameter of V_R can be estimated by means of a least-square-fit to the radial measurements of a complete azimuthal scan. Under the assumption that the wind field is horizontally homogeneous and does not vary during the measurement along the different directions, the results can be related to the wind vector components by

$$\begin{aligned} u &= -b_{VAD} \sin(\chi_{max}) / \cos(\zeta) \\ v &= -b_{VAD} \cos(\chi_{max}) / \cos(\zeta) \\ w &= -a_{VAD} / \sin(\zeta) \end{aligned} \quad . \quad (2.8)$$

Dual-Doppler techniques

If two or more synchronised lidars measure simultaneously at the same target position and the corresponding radial directions are linearly independent, the temporal and spatial averaging implied by the DBS and VAD methods could be avoided applying the matrix inversion method: If three radial wind speed components V_{Ri} and the corresponding radial directions are collected into the vector $\mathbf{V}_R^T = [V_{R1} \ V_{R2} \ V_{R3}]$ and into the matrix $\mathbf{M}_{e_R} = [\mathbf{e}_{R1} \ \mathbf{e}_{R2} \ \mathbf{e}_{R3}]$, respectively, it is possible to write and solve a linear system to find the components of the wind vector:

$$\mathbf{V}^T = [u \ v \ w] = \mathbf{V}_R^T \cdot \mathbf{M}_{e_R}^{-1} \quad (2.9)$$

This system has a solution only if the matrix \mathbf{M}_{e_R} is invertible, which means that the three radial directions need to be linearly independent. Dual-Doppler algorithms (Drechsel et al., 2010) could be applied to relax this limitation. Similar approaches were applied for instance in the works by Cherukuru et al., (2017) and van Dooren et al., (2016) to resolve the wake wind field inside an offshore wind farm from azimuthal scans (plan position indicator, PPI) at low and zero elevation, respectively. Dual-Doppler measurements are very convenient also in complex terrain where wind field inhomogeneity due to the site topography adds up to the one of the wake. For example, Wildmann et al., (2018) analysed how a wake runs over a ridge using the dual-Doppler method and coplanar vertical scans (range height indicator, RHI) of the wake.

2.2.2 Wake characterisation

Procedures applied to identify the overall properties of the wind velocity deficit at a downstream section of the wake are commonly indicated as wake tracking methods. Different approaches have been applied to lidar measurements during the last years. Some representative examples are described in the following¹; the reader interested in an evaluation of common wake tracking approaches is invited to consult Doubrava et al., (2017) and Vollmer et al., (2016).

Direct fit of Gaussian surfaces

This method was first introduced by Trujillo et al., (2011) for lidar wake measurements from the nacelle of a wind turbine. The goal was to estimate the centre position of the wake at a fast repetition rate and to qualitatively describe the corresponding steady wake. The measurements covered a two-dimensional cross-section of the wake. First, the wind deficit was isolated from the wake flow subtracting an estimation of the shear profile from the radial wind speed measurements. Then a Gaussian surface was fit to the wind deficit in order to track the centre of the position of the wake.

Fit of projected Gaussian profiles

To fully characterise the wake and its meandering path (centre position, width and amplitude of the wind speed deficit) within a PPI or RHI scan by means of ground-based lidars, Aitken et al., (2014) modelled the wind deficit measured in the wake at each range-gate with a one-dimensional Gaussian profile. Slightly different models were applied to take into consideration (i) the scanner strategy, (ii) measurements in the free-flow, (iii) measurements in the near-wake or (iv) measurements in the far-wake.

The free-flow model dealt only with the projection of the wind vector on the radial direction of the measurements; in PPI measurements the elevation was disregarded; in the RHI measurements, the vertical profile of the wind speed was incorporated into the wind model as a logarithmic profile.

A double or a single Gaussian profile was added to the free-flow wind model in the near- or far-wake region, respectively.

To characterise the average development of wind speed deficit in the wake (i.e. wake direction, recovery and expansion rates), Aitken et al., (2014) fitted the model of PPI measurements in the far-wake region considering for each sweep all the range-gates at once. First, they rotated the model into the rotor frame of reference; then, they imposed a power law to describe the expansion and recovery of the wind deficit.

Centroid methods

The centroid method can be applied to detect the centre of the wake deficit at a certain downstream cross-section and to study the meandering path of the wake. Herges et al., (2018) applied this

¹Please note that, depending on the scanning pattern and on the availability of the measurements, interpolation of the data might be required before starting the analysis of the wake. These interpolation methods are out of the scope of this section.

method to high resolution, nacelle-based lidar measurements. The deficit area used to evaluate the centroid is defined iteratively reducing progressively the threshold of the deficit amplitude until the deficit area equals the area of the rotor. Similarly as in the work by Trujillo et al., (2011), the deficit was isolated from the wake shape considering the vertical shear profile in the un-waked region of the measurements.

García et al., (2017) investigated the average path of two nearly parallel wakes with a different variant of the centroid method. The study was based on PPI scans from which the horizontal wind speed was estimated with the inverse projection method using a wind direction calculated from measurements not affected by wakes. The centroids at constant downstream distances were calculated after the application of an exponential function to wind deficits extracted separately from each PPI scan. Differently from the methods previously described, here the deficit was defined as the difference between the local the maximum wind speed values at the considered downstream distance.

Wake tracking for control application

Two methods developed for control applications are briefly explained in the following paragraphs. The first one focuses on identifying the centre position of the wake by means of the so-called available power tracking method (Vollmer et al., 2016). The method considers a hypothetical turbine at a fixed downstream distance in the wake of another turbine with the same hub-height and rotor diameter. The available power of the downstream hypothetical turbine is estimated from the cube of the mean flow in wind direction, integrated on the rotor surface assuming uniform air density. Varying the position of the hypothetical turbine along the cross-stream coordinate, the wake centre position can be associated with the position with the lowest available power.

The second one aims to get information about the wake and on the operating conditions of the wind turbine. In this case, the wake model and the tracking method are part of an optimisation process implemented in a control application software (Raach et al., 2017). This method includes the vertical shear, assumes a mono-dimensional wind field and defines the wake with an initial profile. The downstream development of the wake is then obtained with a two-dimensional Gaussian filter which smooths the initial profile according to the dissipation rate of the wake; furthermore, the model estimates the lateral deflection of the wake with respect to the yaw offset between the rotor axis and the wind direction.

2.3 LIdar SCanner SIMulator (LiXim)

As explained in Section 2.2, a heterogeneous wind field with dynamic turbulent structures might degrade the quality of the wind velocity vector estimated from lidar measurements because of the lidar sample volume and the spatial/temporal averaging implied by the wind field reconstruction model.

To evaluate the performance of a long-range pulsed lidar with a flexible scanner, a lidar scanner simulator (LiXim) was developed. In LiXim, the kinematics of a hemispheric scanner and a simplified model describing the physics of lidar measurements are implemented such that trajectories can be defined and scanned in a synthetic wind field where the volume average and the radial projection can be simulated.

In LiXim, the sample volume is defined along a linear coordinate s , which represents the radial distance from the lidar to the target point. The volume average of lidar measurements depends on the shape of the laser pulse² and by the duration of the range-gate. Their extension in space Δp and Δr , respectively, can be estimated along the radial distance s considering their time duration and the speed of light. Then, the normalised intensity of the laser pulse can be approximated with a Gaussian pulse:

$$I_p(s) = \frac{1}{\sqrt{\pi}\Delta r} \exp\left(-\frac{s^2}{\Delta r^2}\right). \quad (2.10)$$

Finally, the volume-averaged wind radial component $V_R(s)$ can be modelled with the convolution of the local radial wind component v_R with the weighting function η as

$$\begin{aligned} V_R(s) &= \frac{1}{\Delta p} \int_{-\frac{\Delta p}{2}}^{\frac{\Delta p}{2}} v_p(s) ds \quad \text{with} \quad v_p(s) = \int_{-\frac{\Delta r}{2}}^{\frac{\Delta r}{2}} v_r(s') \eta(s' - s) ds' \\ &\quad \text{and} \quad \eta(s) = \frac{I_p(s)}{\int_{-\infty}^{+\infty} I_p(s) ds}. \end{aligned} \quad (2.11)$$

where the primes denote the variable of integration along s (Frehlich, 2001).

In LiXim $V_R(s)$ is evaluated numerically considering fifteen points equally spaced within the sample volume and linearly interpolated from the input wind field. These parameters avoid an unnecessary oversampling of the wind field.

If pulsed lidars are not collimated, i.e. the focal length S_F of their telescope is not infinite, the weighting function η in Eq. 2.11 should be replaced by

$$\begin{aligned} \eta_F(t) &= \frac{I_p(s)I_F(t)}{\int_{-\infty}^{+\infty} I_p(s)I_F(s)ds} \quad \text{with} \quad I_F(s) = \frac{1}{\pi} \left(\frac{S_R}{S_R^2 + (S_F - s)^2} \right) \\ &\quad \text{and} \quad S_R = \frac{\lambda_L S_F^2}{\pi A^2}. \end{aligned} \quad (2.12)$$

where the Rayleigh length S_R is defined by the laser wavelength λ_L and the diameter A of the output lens (Pitter et al., 2015).

Figure 2.2 compares LiXim with an early implementation of Simulid, the lidar simulator developed by the lidar manufacturer Leosphere (Boquet et al., 2016) and made available for this validation. For seven ranges and ten radial directions, the two simulators calculated the volume-averaged radial wind speed component V_R from the corresponding reference series. The simulations reproduce the volume average effect of a pulsed lidar with a laser wavelength of 1.56 μm , a pulse duration of 200 ns in terms of full width half maximum (FWHM), a range gate of 200 ns and an emitting length with a radius of 1.5 cm, focused at 80 m. With these settings, the averaging volume is ~ 40 m long and filters spatial turbulent fluctuations with a smaller length scale. The averaging effect can be recognised in the simulations, for instance in the bottom right panel of Fig. 2.2.

The comparison shows a fair agreement between the two lidar simulators which have an average absolute difference of 0.14 m s^{-1} . However, with the average absolute deviation from the reference of 0.14 m s^{-1} , LiXim slightly underestimates the effect of the volume average in relation to Simulid whose average absolute error is 0.20 m s^{-1} . Assuming Simulid to implement a more realistic model of the volume averaging than LiXim this means that larger deviations between the radial wind component at specific positions and the corresponding values simulated with LiXim are to be expected when dealing with real measurements.

²The pulse can be well approximated by a Gaussian function and its duration is commonly indicated as full width half maximum (FWHM).

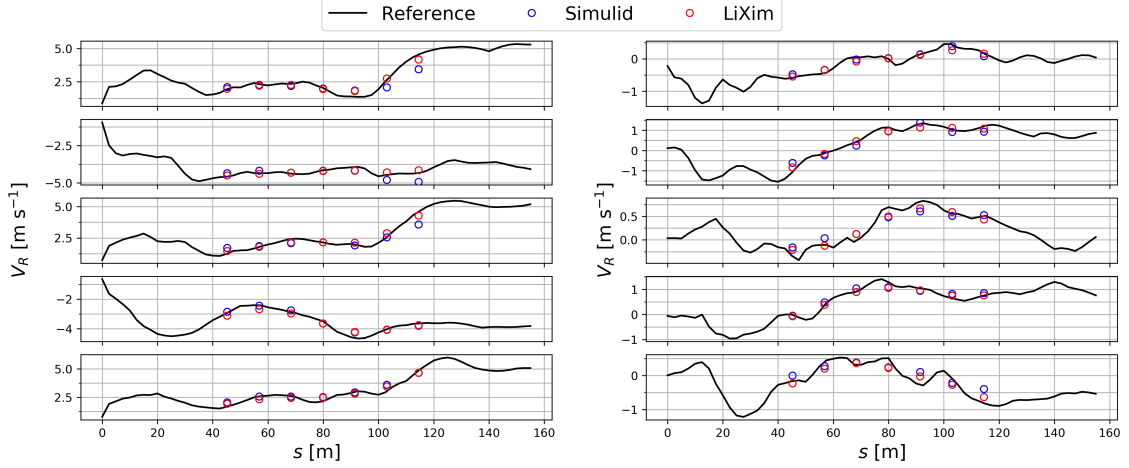


Figure 2.2: Comparison of the radial wind speed measurements simulated with LiXim and Simulid with respect to eight reference cases. The comparison includes seven range-gates along the radial coordinate s .

The kinematics of the scanner implemented in LiXim consists of an all-sky scanner with two rotational degrees of freedom. By default, the scanner follows the assigned trajectories moving continuously and as fast as possible between consecutive target points: Approaching a point, the scanner slows down to 0°s^{-1} at the maximal negative angular acceleration of the device; then, moving away from the point, speeds up at the maximal positive acceleration, up to the maximal angular speed if needed. In LiXim, the absolute angular acceleration and speed are $\sim 100^\circ \text{s}^{-2}$ and $\sim 50^\circ \text{s}^{-2}$, respectively. These settings reproduce the behaviour of the devices Leosphere Windcube WLS400S available for experimental campaigns at Forwind - Oldenburg University.

2.4 Lidar simulations of wake measurements

Lidars have several possible applications in the research about wind turbine wakes, but there are very few guidelines about the interpretation of the measurement results and the corresponding uncertainty estimation. Furthermore, there is not an obvious choice of the setup³ to be implemented in lidar experimental campaigns.

With lidar simulations, one can assess the possible combinations of setup variables and optimize them already in the preparatory phase of an experimental campaign. Moreover, simulations can give insight into the results to be expected and can be repeated also after the campaign applying the actual setup and environmental conditions to support the interpretation of the full-field lidar measurements.

In this regard, two cases are presented, in which lidar measurements of the wind speed in wakes are simulated with LiXim to investigate possible configurations to be implemented into actual measurement campaigns. In both cases, the unsteady large-eddy simulations (LES) wind field described in Section 2.4.1 is the domain of the simulations.

³Here *setup* means the combination of lidar position, measurement points and scanning strategy.

The objective of the two virtual experiments described below is to assess different strategies for lidar measurements applied, in the first test case, to the estimation of the average vertical profile of the wind speed in the wake of a wind turbine (Section 2.4.2) and, in the second case, to track the centre position of the wake (Section 2.4.3). In both cases, the scanning speed and the volume averaging effect applied in the simulation correspond to the lidar specifications described in Section 2.3.

2.4.1 Wind field: unsteady wake simulations

The wind field used for the test cases of this chapter reproduces the wake of a wind turbine with a rotor diameter D of 62 m and a hub-height z_{HH} of 62 m. To run the simulations, an unsteady wind field is calculated with the Parallelised LES Model (PALM) (Raasch et al., 2001). An actuator line approach (Troldborg, 2008) is included to simulate the wind turbine. For the experiments, a ten-minute wind field is generated on a 4 m resolved grid with a temporal resolution of 0.4 s.

The boundary conditions were chosen in order to simulate a neutral atmosphere with a roughness length $z_0 = 0.05$ m and a friction velocity $u_* = 0.5$ m s⁻¹. Considering the hub-height, this setting generated an average inflow wind speed $u_{HH} = 9$ m s⁻¹, a wind direction of 270° and a turbulence intensity TI of 8%.

The profiles of the wind speed deficit in the wake used in the following exercises were calculated subtracting the streamwise wind component u downstream of the wind turbine from the corresponding mean values on the cross-section at the inlet of the LES domain.

2.4.2 Measuring the average vertical profile of the wind speed in the wake of a wind turbine

The features of lidar measurements (volume averaging of the laser beam and the projection of the wind speed vector on its radial wind component) are a source of error in non-homogeneous flows (Clifton et al., 2018). Wind turbine wakes belong to this category of flow. In this section, simulations of lidar wind speed measurements in the wake of a wind turbine show how the effects of the lidar measuring principle can be influenced by varying the experimental approach. The results provide also an indication about which strategy should be preferred to minimise the errors.

Simulation setup

The objective of the first simulated experiment is to measure the vertical profile of the mean wind velocity in the wake of a wind turbine. The wind field described in Section 2.4.1 is the virtual environment of the simulations. The profile includes nine heights from 40 m to 120 m every 10 m and is aligned to the centre line of the turbine rotor at a downstream distance of 2.5 D .

Four cases are considered in the simulations:

- **Reference** The three wind speed components u , v and w along the streamwise, cross-stream and vertical directions x , y and z , respectively, are interpolated at the target points from the simulated wind field.

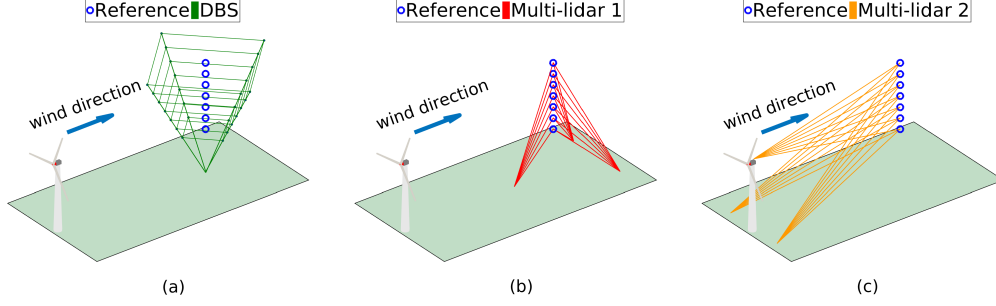


Figure 2.3: Possible approaches for lidar measurements of a wind turbine wake profile at the reference points: Doppler beam swinging (DBS) (a); concurring, synchronised measurements (multi-lidar) with lidars near to the target (b) and further away from it (c).

- **Doppler beam swinging (DBS)** A lidar is installed on the ground beneath the target points. The wind vector is evaluated by applying Eq. 2.6 to the radial wind speed component measured on conical scans composed by four radial wind speed components. The elevation angle of the beams is 60° ; the azimuth angle varies with 90° steps and is alternatively parallel to u and v . This configuration minimises the heterogeneity of the wind field sampled by the four beams. The scanning pattern is plotted in Fig. 2.3a.
- **Multi-lidar 1** Three lidars are installed near the target profile and perform concurrent, synchronised measurements with high elevation angles: Two lidars are $\sim 0.67 D$ downstream of the profile, at opposite sides, separated by $2 D$ in the cross-stream direction; the third lidar is between the turbine and the profile, $\sim 1.83 D$ downstream of the former and $\sim 0.64 D$ upstream of the latter. The wind vector is calculated with the matrix inversion method of Eq. 2.9. Figure 2.3b represents schematically this measurement strategy.
- **Multi-lidar 2** Three lidars are installed near the turbine and, as in the previous case, perform concurrent, synchronised measurements with low elevation angles: Two lidars are at opposite sides of the turbine separated by $2 D$ in the cross-stream direction; the third lidar is on the nacelle of the turbine. The wind vector is calculated again with the matrix inversion method of Eq. 2.9. The trajectory of these measurements is illustrated in Fig. 2.3c.

To isolate and study the effect of the volume and spatial average, the measurement of the full profile is simulated every 2.3 s for all the four cases.

Results

The four approaches are compared in relation to the vertical profiles of mean components of the wind velocity vector (see Fig. 2.4). In this respect, Fig. 2.5 displays the deviations

$$\begin{aligned}
 \Delta u &= u_{lidar} - u_{ref} \\
 \Delta v &= v_{lidar} - v_{ref} \\
 \Delta w &= w_{lidar} - w_{ref}
 \end{aligned} \tag{2.13}$$

where the reference and the lidar simulated wind velocity components are indicated with the subscripts ref and $lidar$, respectively. The statistics of these deviations are collected in Table 2.1 to provide an overview of the results.

When the streamwise wind component is addressed, the results of the simulations for the DBS and Multi-lidar 1 configurations look very similar (see Fig. 2.4). The former has a slightly smaller deviation from the reference case. Differently, simulations with the approach Multi-lidar 2 have results much closer to the reference. These points can be better quantified in Fig. 2.5a, where the deviation of the different approaches from the reference is represented.

The orientation and the position of the sample volumes in the simulated measurements are a reasonable explanation of the different results provided by the considered approaches. These two factors have a relevant influence on the volume average in wind fields with high spatial gradients as wakes. In the DBS, the wind field is calculated from radial wind speed components averaged over sample volumes centred at different positions in space (e.g. at opposite directions the volumes have a ~ 104 m distance at the height $z \sim 90$ m). This is not the case for the multi-lidar measurements, in which the sample volumes of the radial wind speed components concur at the same position eliminating the influence of the spatial averaging and reducing the deviation from the reference.

Another aspect to consider is that, in the multi-lidar configurations, the vertical extension of the sample volumes depends on the elevation angle, while the sample volumes of the DBS approach have it fixed. This fact is particularly important considering that significant vertical gradients of the streamwise wind component are expected at the target points. In the DBS and Multi-lidar 1 simulations, the vertical extension of the sample volume is very similar (~ 26 m for the first one and in average ~ 25 m for the second one); differently, the vertical extension of the sample volumes in the Multi-lidar 2 simulations is less than a half of the one in the other two cases (~ 11 m in average). In this respect, the aforementioned similar deviation from the reference could be due to the vertical extension of the probe volume.

Concerning the cross-stream wind speed component v (see Fig. 2.4b and Fig. 2.5b), the two multi-lidar configurations can resolve very well the variation from positive to negative values given by the rotation of the wake. This is not the case for the simulation of the DBS measurements, which capture this trend only at the lower heights, nevertheless with a larger deviation from the reference. In fact, v reaches fast the free-stream level (0 m s^{-1}) without changing sign because the sample volumes of the cross-stream beams of the DBS cone move towards and eventually cross the edges of the wake for increasing heights.

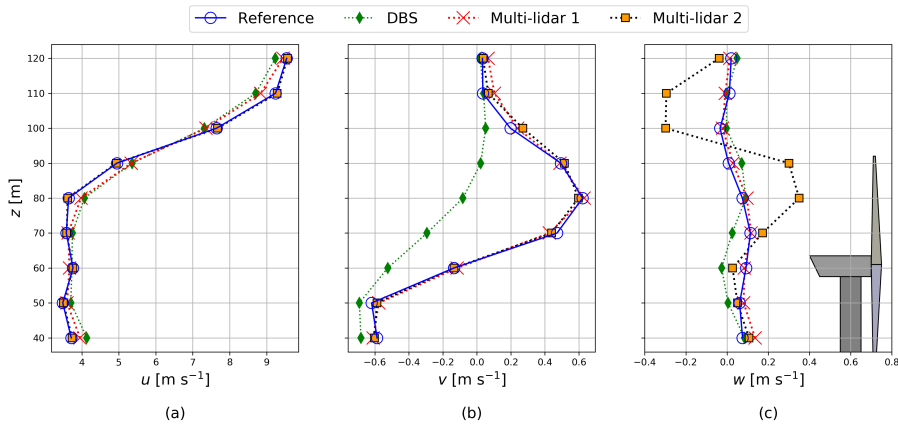


Figure 2.4: Measurements of a wind turbine mean wake profile simulated with the approaches of Fig. 2.3 and compared to the corresponding reference values.

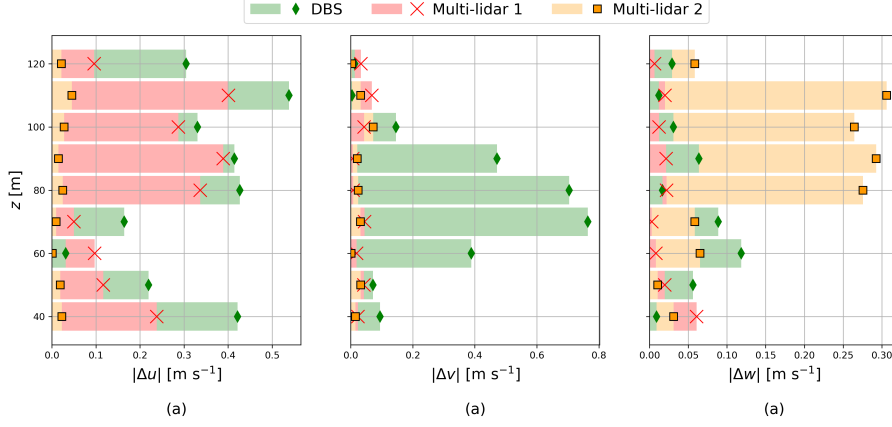


Figure 2.5: Absolute deviation from the reference of the wind speed components calculated implementing the approaches of Fig. 2.3 into lidar wake measurements simulations.

Table 2.1: Statistics of the deviation from the reference of the wind speed components calculated from lidar measurements simulated for different approaches within a wind turbine wake.

	$ \Delta u $ [m s ⁻¹]		Δu [m s ⁻¹]		$ \Delta v $ [m s ⁻¹]		Δv [m s ⁻¹]	
	avg	st. dev	min	max	avg	st. dev	min	max
DBS	0.32	0.15	-0.54	0.43	0.30	0.28	-0.76	0.00
Multi-lidar 1	0.22	0.13	-0.40	0.39	0.03	0.02	-0.04	0.07
Multi-lidar 2	0.02	0.01	-0.02	0.05	0.03	0.02	-0.03	0.07

Approach	$ \Delta w $ [m s ⁻¹]		Δw [m s ⁻¹]	
	avg	st. dev	min	max
DBS	0.05	0.04	-0.12	0.06
Multi-lidar 1	0.02	0.02	-0.02	0.06
Multi-lidar 2	0.15	0.12	-0.31	0.29

The profiles of the vertical wind speed component w in Fig. 2.4b provide another example of how the orientation and the position of lidar the sample volume affects the reconstruction of the wind vector. In this case, the Multi-lidar 2 simulations have the worst match with the reference because the difference between the elevations of the concurring beams is relatively small (especially above hub-height) and the system matrix \mathbf{M}_{e_R} of the wind field reconstruction model is almost singular. In relation to the Multi-lidar 2 approach, the DBS has lower deviations from the reference, but Fig. 2.4 shows that it still does not correlate with the reference very well. The Multi-lidar 1 configuration mitigates best the limits of lidar measurements for the vertical wind component and has results very close to the reference.

Given the low contribution of the vertical wind component to the line of sight wind speed measured by the lidar at very low elevations in the configuration Multi-lidar 2, it is reasonable to assume that similar results in term of precision could be achieved also with two lidars only.

Conclusions

The measurement principles of wind lidar limit their use in non-homogeneous flows. Three different measurement approaches have been investigated with lidar simulations in the wake of a wind turbine to find out their advantages and disadvantages.

The common DBS approach has the highest average absolute error with respect to the reference because of the average over steep volumes with strong spatial variation of the wind field. The error is also a consequence of combining radial measurements in the free-flow and in the wake. Concurrent sample volumes have better performances which vary depending on the inclination of the radial direction. The horizontal wind speed can be estimated better from small elevation angles. However, larger deviations of the vertical wind component from the reference are observed for such configurations.

From these results, a multi-lidar configuration with the devices located at a large distance from the target points should be chosen for measurements of the vertical profile of the average horizontal wind speed at the centre of the wake. In this situation, two devices could probably achieve similar results as three and might reduce the campaign efforts.

2.4.3 Dynamic tracking of the wake centre position

Engineering wake models such as the dynamic wake meandering model (DWM) (Madsen et al., 2010) estimate the shape and position of the wind deficit in the wake with respect to the large scale turbulence fluctuations within the atmospheric boundary layer. Nacelle-based lidars have been proved to be a valid tool for the direct verification of such models (Trujillo et al., 2011). Section 2.2.2 provides an overview of the different wake tracking methods developed for ground- or nacelle-based lidar measurements.

The wake measurements simulated for this section aim to verify whether the fit of Gaussian surfaces to the wind speed deficit measured at high resolution by a short-range nacelle-based lidar (Trujillo et al., 2011) could be applied to slower measurements performed with long-range lidars installed on the nacelle or on the ground.

Differently from the reference work by Trujillo et al., (2011), the radial directions scanned by a ground-based lidar aiming at the wake are fixed and the wind direction is variable (measurements from nacelle-based lidars are supposed to be centred along the mean wind direction); the difference between the two directions could be large and lead to inaccurate results of the Gaussian fit directly applied to the radial wind speed values.

To evaluate the application of the methodology by Trujillo et al., (2011) to long-range scanning lidars, five simulation layouts are analysed here.

Simulation setup

In the simulations, a Lissajous trajectory is approximated with a 7×7 points rectangular grid generated following the suggestion by Rettenmeier, (2015). A similar scanning pattern was also applied in the work by Trujillo et al., (2016). The measuring area covers $3.00 D \times 1.33 D$ and is centred at P_0 , $2.5 D$ downstream of the turbine, along its rotor axis. A sketch of the trajectory is depicted in Fig. 2.6a.

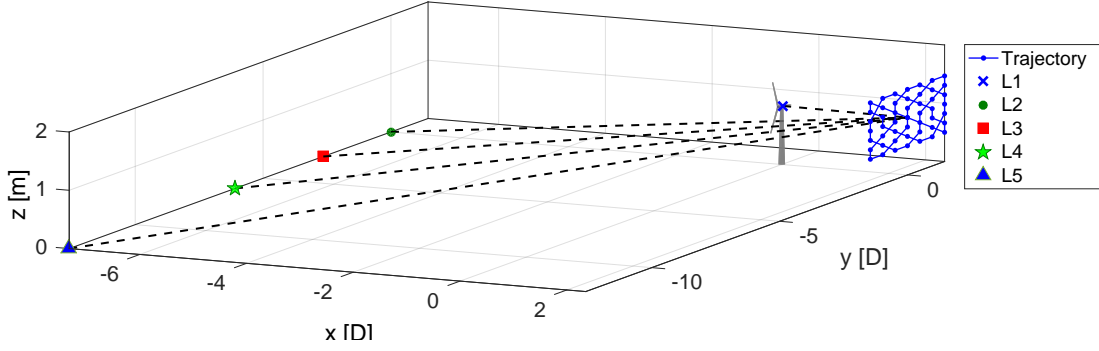


Figure 2.6: Three-dimensional view of the experiment simulated with LiXim.

The lidar measurements are simulated in the wind field introduced in Section 2.4.1. In the first layout L1, the lidar scans the wake from the nacelle of the wind turbine. The further layouts L2 through L5, are considered for a ground-based lidar. Each of them tests a different alignment of the lidar beams with the wind direction. For this purpose, the lidar is placed upstream of the wind turbine at a distance of about $7.3D$ along the x -axis. First, it is aligned with the rotor axis and there is no angular offset between the wind direction and lidar beam aiming at the trajectory centre P_0 located in the wake at a downstream distance of $2.5D$. This case is indicated as L1. In the remaining cases, namely L3, L4 and L5, the angular offset is increased to about 15° , 30° and 50° , respectively, by moving the lidar to negative values of the y -axis keeping the same coordinate x . Figure 2.6 provides a schematic illustration of the simulation layouts.

The same technical specifications as those of the long-range scanning lidar introduced in Section 2.3 are implemented in the simulations. With these settings, the trajectory repetition time might be too long to capture the fastest dynamics of wake meandering. In fact, the nacelle-mounted lidar (L1) takes about 31 s to scan a full trajectory. In case L2 to L5, the ground-based lidar can scan smaller arcs to follow the trajectory pattern thanks to the larger distance to the trajectory plane. As a result, the ground-based lidar completes a full trajectory in nearly half of the time needed by the nacelle-based unit. In the wind field used for the lidar simulations, the time scale of the wake meandering estimated as $2D/u_{HH}$ (Madsen et al., 2010) is around 14 s. According to Nyquist's theorem (Bendat et al., 2000), fluctuations with time scales shorter than twice the sample time cannot be resolved. It means that, in the most convenient configuration, this issue could affect meandering scales faster than about 30 s.

Wake tracking

The methodology applied to detect the wake meandering from the lidar measurements simulated in the LES wind field consists of three steps:

1. Identifying the average wind speed deficit in the wake.

First, the measurements of each complete and independent trajectory are collected as successive "snapshots" of the wake; then, the vertical profile of the radial wind speed in the free-flow is approximated averaging the profiles measured outside of the wake, at the lateral boundaries of the trajectory; next, the radial wake deficit is calculated subtracting

the measurements of each snapshot from the free-flow radial wind speed; finally the deficit of the radial wind speed is divided by the maximum values of the free-flow profile to obtain non-dimensional values between 0 and 1.

2. Identifying the average shape of the wake.

The simulated radial wind speed measurements are averaged over time; the radial wind deficit in the wake is modelled with the bivariate Gaussian function

$$f_G = f_0 + A_G \exp\left(-\frac{(y - y_\mu)^2 + (z - z_\mu)^2}{\sigma_r^2}\right) \quad (2.14)$$

centred at the coordinates y_μ, z_μ . The shape of this function is defined by the scale factor A_G and the parameter σ_r denotes the wake radius; the variable f_0 is an offset that compensates for possible inhomogeneity of the vertical profile used for the free-flow. To find the wakes mean features, f_G is fitted to the average deficit profiles. Table 2.2 reports the boundaries applied to the parameters of f_G in the fit to the profiles.

3. Identifying the instantaneous centre position of the wake.

The Gaussian profile of Eq. 2.14 is fitted to the successive wake deficit "snapshots" keeping all the parameters but the coordinates y_μ, z_μ of the wake centre fixed to the values of the average wind speed deficit.

The different experimental layouts are evaluated in relation to the reference values of horizontal meandering of the wake centre. For this purpose, the wake tracking method is applied to the streamwise wind speed component on the cross-section 2.5 D downstream of the turbine; the wind speed deficit in the wake is calculated every 0.4s from the vertical profile of the free-flow wind speed, 2 D in front of the rotor and is normalised as mentioned above.

Results

The first analysis is dedicated to the average characterisation of the wake. Starting with Fig. 2.7 and Fig. 2.8, the wind speed deficit profiles in the wake from the simulations are compared to the corresponding reference from the LES wind field. In both figures, panels are organised in rows and columns according to the vertical offset of the wake profile from the rotor centre and the lidar layout, respectively.

In Figure 2.7, the lidar simulations result (green circles) of case L1 to L3 (angular offset up to 15°) follow accurately the reference profiles (blue solid line). In cases L4 and L5 (angular offset 30° and 50°) the effect of the radial projection of the wind speed is recognisable from lower wind speed values of the lidar simulations with respect to the reference ones.

Table 2.2: Limits of the parameters implemented for the fit of Eq. 2.14 to the average wind speed deficit and corresponding results for the simulated layouts.

	y_μ [D]	z_μ [D]	σ_r [D]	A_G [-]	f_0 [-]
minimum	-3.0	-0.5	0.25	0.0	-0.5
maximum	+3.0	+3.0	0.70	1.0	+0.5

As it can be observed in Fig. 2.8, the deviation between the reference (blue solid line) and the lidar is lower if evaluated in terms of the normalised radial wind speed deficit (green circles). This result indicates that the normalisation of the lidar simulations can partly compensate for the effect of the radial projection. On the other hand, the normalisation introduces a little overestimation by the lidar at heights around the rotor centre and higher (see panels in the first four rows from the top), and a little overestimation in the lowest area of the rotor (see panels in the last two rows from the top).

The results of the fit to the deficit profiles of the reference (blue diamond) and the results of the fit to the deficit profiles from the lidar simulations (dark green crosses) are close in all the measurement layouts, with almost coinciding results apart from the case L5.

At the height around the centre of the rotor, the deficit profile of the reference has a plateau which comes from the diffusion of the double-peak profile expected in the near-wake. In none of the cases – simulated as well as reference – this signature is captured by the fit of the Gaussian profile, f_G . However, this issue does not affect the current analysis because the focus here is on the centre position and not on the exact shape of the deficit.

The fair agreement between the results from the lidar simulations and the reference qualitatively exposed above is confirmed by the parameters found fitting f_G to the data and collected in Table 2.3.

The second part of the analysis deals with the detection of horizontal wake meandering. Figure 2.9 juxtaposes the paths of the wake identified from the lidar simulations (green circles) and the

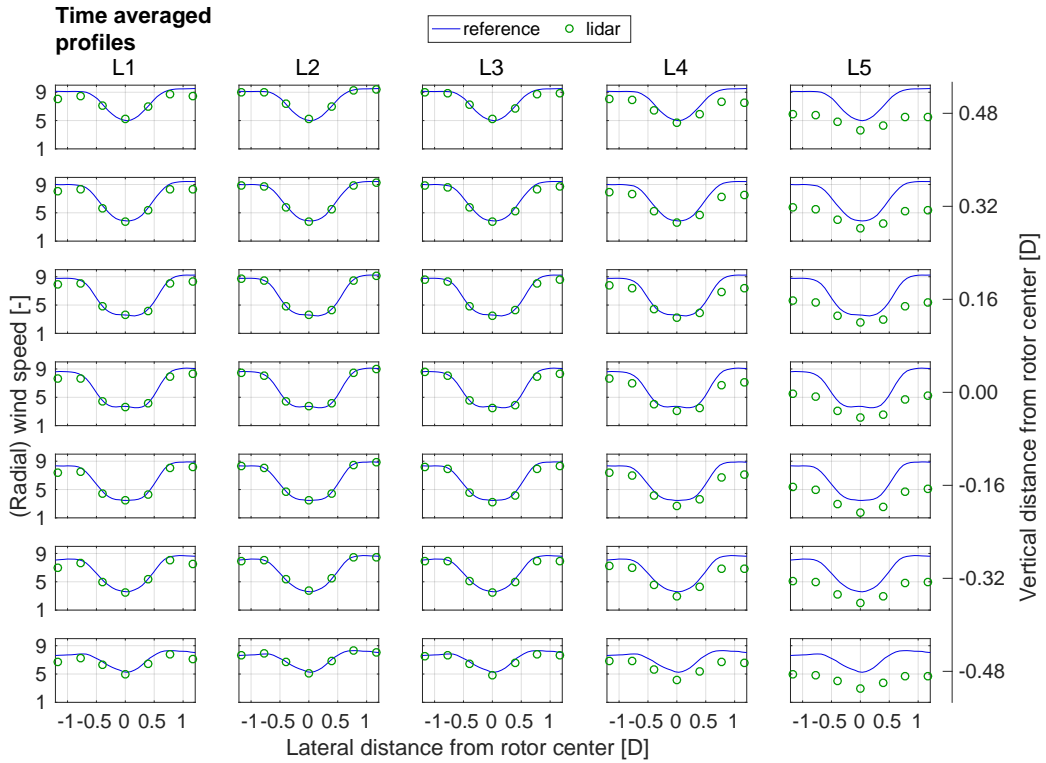


Figure 2.7: Comparison of the reference streamwise wind component with the simulated radial measurements averaged over time. The panels are organised in rows and columns according to the vertical offset of the wake profile from the rotor centre and the lidar layout, respectively.

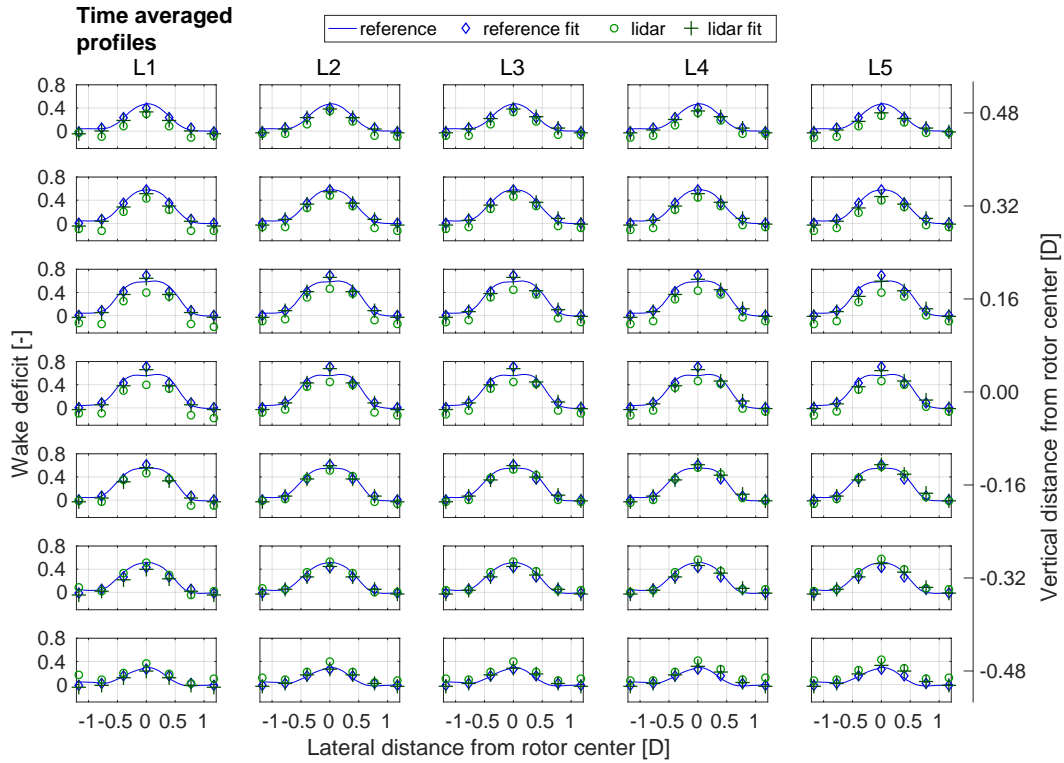


Figure 2.8: Comparison of normalised average wind speed deficit of the reference (solid blue line) with the normalised average radial wind speed deficit evaluated from the lidar simulations (green circles). In both cases, the corresponding fit of the wake model (blue diamonds and dark green crosses, respectively) is also included. The panels are organised in rows and columns according to the vertical offset of the wake profile from the rotor centre and the lidar layout, respectively.

reference data (solid blue line); additionally, the top-right panel summarises their overall mutual difference in terms of root-mean-square error (RMSE).

The paths detected from the lidar and the reference oscillate within $\pm 0.2D$ around the rotor centre position and shows an overall fair correlation, however with increasing deviations for larger angular offsets between the beams scanned by the lidar and the wind direction. The RMSE well represents this result. It also reveals that the longer trajectory repetition time of case L1 affects negatively the comparison. In this respect, examples of the low-pass filter effect due to the sampling time of the full trajectory can be observed in case L1 (e.g. between 50 s to 150 s); in cases L2 and L3, they are not so evident but still noticeable (for instance short before 400 s); in the remaining cases, they are hardly recognisable because of the fluctuating deviation from the reference.

Conclusions

Specific methods are available to study the wake meandering with the implementation of highly resolved lidar measurement from the nacelle of a wind turbine. Also long-range scanning lidar can be applied to investigate the wake meandering. From the nacelle of a wind turbine, the radial directions of the lidar are generally oriented with a small deviation from the mean wind direction; hence, the radial wind speed components measured along the trajectory have enough information

Table 2.3: Results from the fit of Eq. 2.14 to the average wind speed deficit in the wake of a wind turbine for the simulated layouts and the reference case.

	y_μ [D]	z_μ [D]	σ_r [D]	A_G [-]	f_0 [-]
reference	0.000	0.062	0.388	0.73	0.01
L1	0.002	0.052	0.386	0.71	-0.04
L2	0.002	0.055	0.415	0.72	-0.04
L3	0.024	0.046	0.416	0.72	-0.03
L4	0.041	0.022	0.422	0.70	-0.03
L5	0.051	-0.010	0.422	0.69	-0.03

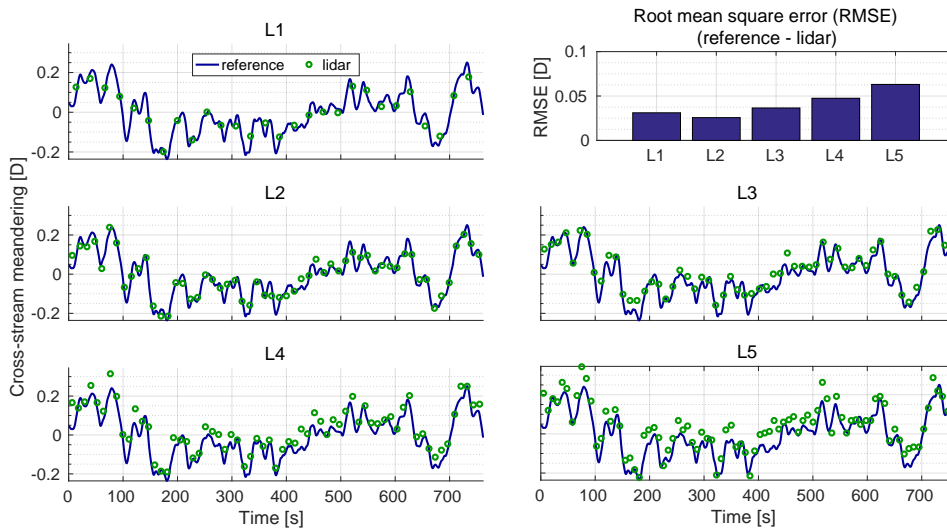


Figure 2.9: Results from different wake tracking approaches applied to simulations of lidar measurements with a variable offset between the radial and the wind directions.

to capture the main features of the wake; however, the trajectory would be located at a relatively close distance from the rotor and might require a long scanning time. This could be a limitation when the measurements are supposed to resolve the short time scales of the wake meandering. A remarkably shorter scanning time can be achieved with long-range scanning lidars deployed on the ground, at a large distance from the measurement points. In this case, the drawback is that, at specific wind directions, the projection of the wind speed along the radial direction has not enough information to capture the main features of the wake.

Lidar simulations of wind speed measurements in wake under different configurations indicate that the wake tracking approach developed by Trujillo et al., (2011) is very robust applied to ground- and nacelle-based scanning lidar measurements averaged over time. Here, effects due to possible angular offsets between the wind direction and the lidar measurement sector are compensated by the method.

In the time-resolved domain, the results point out the importance of the repetition rate of a full trajectory: Slower trajectory patterns act as a low-pass filter and cannot resolve the fastest meandering fluctuations. Also the angular offset between the wind direction and the lidar measurement sector deteriorate the quality of the wake tracking: For an angular offset increasing from 0° to 50° , the root-mean-square error in the simulations grows from about 12% to 31% of the largest separation observed between the rotor axis and the wake centre.

This research suggests that experimental campaigns for the study of wake meandering based on long-range scanning lidar need to be carefully planned. In particular, the measurement layout should be optimised considering the wind rose at the site and minimising the time to complete a full trajectory. In the presence of high angular offsets between the wind direction and the lidar measurement sector a methodology modelling the radial projection of the measurements is expected to be more appropriate.

2.5 Summary

This chapter gave the opportunity to review some fundamental points regarding lidar measurements:

- Flow models are needed to reconstruct the wind vector from lidar measurements or to characterise the wake of a wind turbine from lidar measurements.
- Flow models and reconstruction methods need to be validated.
- The same measurement objective can be measured by applying different approaches.

A lidar simulator was introduced to deal with these matters. It enables to reproduce lidar measurements in dynamic wind fields considering their sampling volume and the radial projection of the wind vector. The simulator was positively evaluated with respect to a more sophisticated implementation developed by a lidar manufacturer.

The focus was given here to wind speed measurements in the wake of a wind turbine and lidar simulations served to investigate two exemplary cases. The first one pointed out that concurring measurements with low elevation angles are the best option – among those analysed – for measurements in wakes: They minimise the mutual dislocation of the sampling volumes of the

measurements used to reconstruct the wind vector. For this reason, concurring measurements provide more precise results. Another advantage of this configuration is to reduce the effect of the lidar volume average over the sheared flow of the wake. The second case proved that wake meandering can be detected by fitting a Gaussian profile to the deficit derived directly from lidar wind measurements, at the condition that the offset between the wind direction and the lidar measuring sector is below 30° .

These examples demonstrated that lidar simulations allow to deal with conceptional issues ahead of the experimental campaign, support the assessment of wind and wake models applied to analyse lidar measurements and inform about the accuracy to be expected. Lidar measurements can also help to prevent data losses due to the late identification of possible inconvenient situations. In fact, lidar measurements are often analysed when the experimental campaign is already over and there is no simple remedy for those situations. With lidar simulations, it is possible to foresee inconvenient situations and develop dedicated measurement strategies to mitigate their effects. In conclusion, lidar simulations are an indispensable tool to full-field wake measurements.

Chapter 3

Application of staring lidars to study the dynamics of wind turbine wakes

The content of this chapter consists of the

JOURNAL ARTICLE

Meteorologische Zeitschrift Vol. 24 No. 6 (2015) 557-564

Main Author

©2014 The Authors

Reproduced under the Creative Commons Attributions-NonCommercial-ShareAlike 3.0 Unported ([link](#))

included in the special issue dedicated to the 17th International Symposium for the Advancement of Boundary Layer Remote Sensing hold in Auckland, New Zeland, January 2014.



Application of staring lidars to study the dynamics of wind turbine wakes

DAVIDE TRABUCCHI*, JUAN-JOSÉ TRUJILLO, JÖRGE SCHNEEMANN, MARTIN BITTER and MARTIN KÜHN

ForWind – University of Oldenburg, Germany

(Manuscript received April 16, 2014; in revised form September 17, 2014; accepted October 16, 2014)

Abstract

Standard anemometry or vertical profiling remote sensing are not always a convenient approach to study the dynamics of wind turbines wake. One or more lidar windscanner can be applied for this purpose. In this paper a measurement strategy is presented, which permits the characterization of the wake dynamics using two long range wind lidars operated in a stationary mode. In this approach two pulsed devices are staring with low elevation obliquely across the wake. The lidar beams are supposed to cross each other on the downstream axis of the wake to perform simultaneous measurements in the wake field from side to side. The deflection of the wake is identified fitting a model to the average data. Spectral analysis provide the frequency content of the measurements at different distances from the wake center. This setup was implemented in a full-field measurement campaign where the wake of a multi-MW wind turbine was analysed. The tracking of the wake centre was applied successfully to this measurement. Moreover the spectral analysis showed increased energy content close to the wake lateral edges. This can be connected both to the higher turbulence level due to the tip vortices and to the large scale dynamics of the wake.

Keywords: wind turbine wake, meandering, lidar

1 Introduction

A wind turbine extracts kinetic energy from the wind. As a consequence, a wake is generated downstream the rotor where the wind speed is generally lower and the turbulence intensity is higher in relation to the undisturbed flow upwind. In a wind farm, turbines often operate downstream other turbines. For this reason, a solid knowledge about wind turbine wakes is extremely relevant in order to have reliable models able to predict the energy yield of a wind farm, to optimize its layout or to be applied in the design phase of a wind turbine in the evaluation of the fatigue load increase due to wake added turbulence.

Several engineering models have been developed since the 80s, which describe the wind and turbulence intensity profiles as well as their development downstream in steady conditions. The N.O. Jensen wake model (KATIC et al., 1986) and the Ainslie wake model, also known as Eddy Viscosity Model (AINSLIE, 1988), are just two possible examples. The first one is based on the conservation of the mass flow in a control volume where the wake diameter is assumed to expand linearly starting directly from the rotor plane. The second one describes the far wake, i.e. starting from about 2.5 rotor diameters D , and it is based on the analytical solution of the axis-symmetric formulation of the steady Navier Stokes equations for a thin shear layer. In this formulation the pressure gradient as well as swirl are neglected and an eddy-viscosity closure is applied.

Empirical models for turbulence in the wake of a wind turbine have been also developed to estimate loads on turbines operating in wake conditions, e.g. in FRANDSEN and THØGERSEN (1999). A more sophisticated approach considers the wake as a series of deficit disks released at the turbine rotor and moving downstream driven by the atmospheric turbulence structures with scales comparable with the rotor diameter D . The Dynamic Wake Meandering (DWM) model (LARSEN et al., 2008) and the Disk Particle Model (DPM) (TRUJILLO and KÜHN, 2009) are based on this idea.

In order to validate wake models, full-field measurements of wind turbine wakes represent one of the best solutions. Meteorological mast mounted wind vanes, cups and/or sonic anemometers, are commonly applied for the measurement of the wind deficit (MACHIELSE et al., 2007) or the turbulence intensity in wakes. This approach has the limitation of a fixed layout which, combined with the wind direction and the distance between the mast and the available turbines, allows to study a restricted number of cases.

Remote sensing and in particular Doppler wind lidar has become a flexible and reliable technology to be adopted for wind energy. A Doppler wind lidar, hereinafter simply lidar, emits laser beams to the atmosphere which are back-scattered by the aerosols naturally present in the atmosphere. Assuming that the aerosols have the same velocity of the wind, the lidar measures the Doppler shift in the back-scattered light and calculates the so-called line of sight (LOS) velocity component, V_{LOS} , which is the projection of the wind vector on the LOS direction, i.e. the direction of laser beam (WERNER, 2005).

*Corresponding author: Davide Trabucchi, ForWind – University of Oldenburg, Ammerländer Heer-Str. 136, 26129 Oldenburg, Germany, e-mail: davide.trabucchi@uni-oldenburg.de

Mainly, lidars are applied as vertical profilers in site resource assessment and, supported by the upcoming second edition of the IEC 61400-12-1 standard, in the measurement of wind turbine power curves too. These devices scan a vertical cone, usually with an aperture angle of 30° , to evaluate the wind vector at the desired heights. This approach assumes the homogeneity of the wind field over the scanned area, which is not given, e.g. in complex terrain, in a convective layer or in the wake of a wind turbine. Whilst for the first two situations models have been developed to account for the inhomogeneity of the wind field in the evaluation of the wind vector, the application of vertical profilers in wake is still questionable.

When a scanning lidar is available, the laser beam can be steered freely changing the azimuth and the elevation of the scanner head. Moreover, when the lidar is a pulsed system device, the radial wind speed can be sampled simultaneously at several distances along the laser beam by using the knowledge of the propagation of light and the time-of-flight of the back-scatter signal. Each sampled distance is commonly referred as range gate.

Early application of scanning lidars to wake measurements are presented by KÄSLER et al. (2010), while in AITKEN et al. (2014) a scanning lidar is applied to study the downstream evolution of vertical and horizontal wake profiles of a utility wind turbine. Moreover, volumetric measurements of a wind turbine wake are analyzed by IUNGO and PORTÉ-AGEL (2014). In the mentioned papers mainly range height indicator (RHI) and plan position indicator (PPI) measurements were performed varying the elevation angle of the scanner keeping the azimuth angle constant in the first case and vice versa in the second one. A different type of research based on lidar measurements and focused on the turbulence characteristics in the wake of a wind turbine can be found in SMALIKHO et al. (2013). Two or more scanning lidars can be operated in a so-called windscanner configuration where the lidars are networked and synchronized in order to measure at the same spot in space at the same time. This approach enables to solve a geometrical system and retrieve two or all of the three components of the wind vector. Experiments applying this technique starting at a fixed point in space have been done in order to compare the wind measurements provided by the windscanner system and mast mounted anemometers (MANN et al., 2008, SCHNEEMANN et al., 2012).

This paper shows how measurements by two long-range scanning lidars concurrently staring in the wake of a multi-MW wind turbine can be used on the one hand to identify the steady wake in space and, on the other hand, to study the downstream and cross-sectional evolution of the low frequency dynamics of the wake.

2 Experimental realization

2.1 Layout

The experiments took place in a wind farm located in the countryside at the border between Germany and Den-

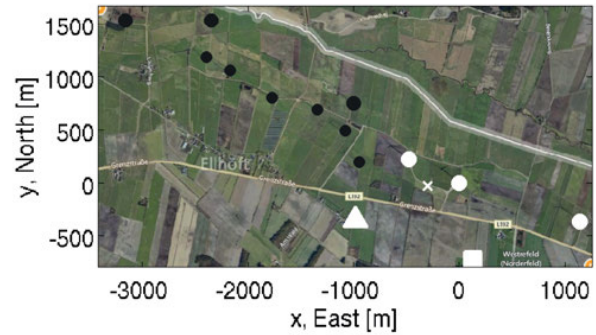


Figure 1: Aerial view of the experimental field. Lidar 1 and Lidar 2 are represented with a triangle and a square respectively. White circles indicate the considered wind farm while the dark ones other turbines in the vicinity. The position of the instrumented mast can be identified by a white cross.

Table 1: Technical sheet of the Windcube WLS200S.

Properties	
Wave length	1.54 μm
Pulse length (FWHM)	0.1–0.4 μs
Max laser power	5 mW
Pulse repetition rate	10–20 kHz
Max range	6500 m
Acquisition	
Photodiode sampling rate	250 MHz
FFT length	64–128–256 points
LOS component accuracy	0.2 ms^{-1}
max n. of range gates	240
Scanner	
Type	2 degrees of freedom
Angular resolution	0.01 $^\circ$
Pointing resolution	0.1 $^\circ$
Max angular speed	30 $^\circ\text{s}^{-1}$

mark. The wind farm consists of three 6 MW turbines with a 126 m rotor diameter D mounted on a 100 m high tower. They are indicated with white circles in Fig. 1, while dark circles are adopted for other turbines in the area.

Two long range scanning lidars of type Windcube WLS200S, manufactured by Leosphere and specified in Table 1 were deployed to this wind farm. They are indicated as Lidar 1 and Lidar 2 and can be identified in Fig. 1 by a triangle and a square respectively. The former is located at about 1040 m from the central turbine of the considered wind farm, the latter at about 740 m.

The two devices were operated by a control unit, the so-called master, which communicated with the lidars over a cable-WiFi network. The master included an NTP time-server which kept the clocks of the lidars synchronized. Due to limitation in the lidar operating system,

Table 2: Technical details of the instrumentation on the meteorological mast.

	Cup anemometer	Wind vane
Type	Thies First Class	Thies First Class
Measurement range	0.3–75.0 ms ⁻¹	0–360 °
Uncertainty	1 % in the range 0.3–50.0 ms ⁻¹ 0.2 ms ⁻¹ otherwise	1 °
Sampling frequency	20 kHz	20 kHz

the accuracy of the time synchronization is estimated in the order of 1 s.

The position of the turbines and of the lidars was measured with a GPS device embedded in a laptop (Dell Wireless 5550 Single-Mode HSPA + Mobile Broadband Mini-Card with A-GPS). The GPS data was recorded for 20 min at each position and then averaged to reduce the uncertainty. The lidars were levelled on the basis of the internal inclinometer of the lidar, which provided a resolution of 0.1 ° for the pitch and roll axis. The heading of the lidars was checked mapping the turbines using the lidar as hard-target detector (VASILJEVIC et al., 2013). Mainly, during a horizontal scan the tower of the wind turbines can be identified by a stronger back-scattered signal than the surrounding flow. The scanner head azimuth at which the strongest signal is retrieved is eventually compared to the reference azimuth between the lidar scanner and the turbine obtained from the GPS measurement. This method is expected to provide an uncertainty in the order of $\pm 1^\circ$ for the data acquired during this measurement campaign. In the wind farm, marked as a white cross in Fig. 1, a 100 m high meteorological mast was available too. Its instrumentation included a top cup-anemometer, a series of four cup anemometers and three wind vanes. In this research only the top anemometer and the wind vane mounted on the boom at 95.9 m directed to 103 ° from North were applied. A detailed description of these instruments is provided in Table 2.

2.2 Measurements

The main objective of this experiment was to study the wake dynamics on the basis of lidar measurements or, in other words, to analyse the influence on the turbulent fluctuations downstream a wind turbine produced by the low frequency varying displacement of the wake center from the rotor axis. In order to avoid loss of time due to a complex scan scenario, it was chosen to intersect the laser beams of the two lidars in the region-of-interest (ROI) at about $3D$ downstream a wind turbine at the hub height and to stare at that fixed point. In this way, it was possible to reach an acquisition rate of 2 Hz. As already mentioned in section 1, pulsed lidars measure the LOS component of the wind simultaneously at several range gates along the LOS. In this experiment 59 range gates were measured by each lidar symmetrically distributed

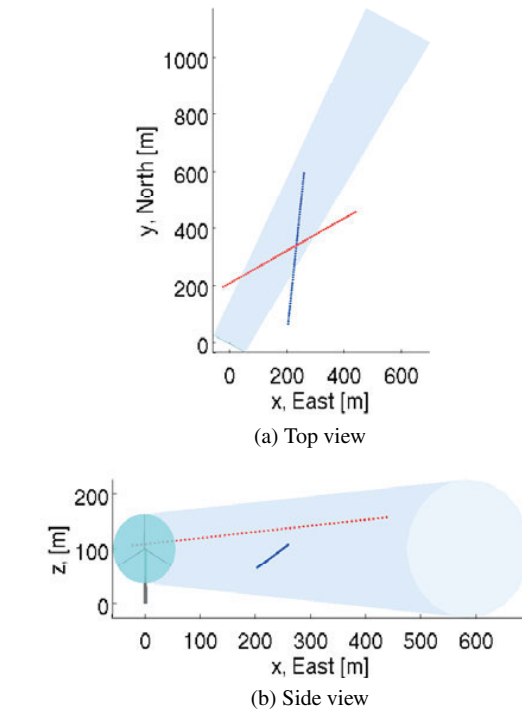


Figure 2: Layout of the measurement points in relation to the turbine position and the correspondent wake for a downstream wind direction of 25 °. The red dots represent the measurement points of Lidar 1, the blue ones those of Lidar 2.

every 10 m about the ROI. This configuration is thought to achieve optimal results when the two laser beams have a similar inclination with respect to the wind direction. Moreover, this inclination should guarantee on the one hand to uniformly distribute the range gates across the wake section, on the other hand to have a meaningful projection of the wind vector on the LOS direction, i.e. an accurate LOS component.

The experimental campaign covered the period from 20/03/2012 to 25/06/2012. Only the last week was dedicated to this experiment and this led to only one hour of data suitable for this study. This one was recorded during the night between the 24/06/2012 and 25/06/2012. In order to realize the described measurement scheme, the central turbine of the wind farm was chosen and a

Table 3: Measurement setup.

	Lidar 1	Lidar 2
Gauß-Krüger coordinates (left/right values) [meter]	3498161/6083860	3499262/6083468
Azimuth/Elevation angle [°]	60.5/5.5	6.0/4.6
Range [meter]	1100–1630	796–1329
Pulse length (FWHM) [μs]		0.2
FFT points [#]		64
Accumulation time [s]		0.5
Range gate spatial resolution [meter]		~ 30
Range gates [#]		59

downstream wind direction¹ of 20° was considered. The setup of the measurement is reported in Table 3. A top and a side view of the points measured by Lidar 1 and Lidar 2 are represented in Fig. 2, where the central turbine as well as the trace of its hypothetical wake for a downstream wind direction of 25° are also included. As can be seen from the figure, the laser beams of the two lidars are actually not intersecting each other. This occurred as consequence of the limitation of the leveling system, which required a recalculation of the position of the measurement points in the post-processing of the data.

All the LOS data recorded by Lidar 1 and Lidar 2 are reported in colors in Fig. 3a where it is possible to identify wake evolution in the region with a lower LOS component. The windy trace of the wake which appears here is due to the very low frequency variation of the wind direction. In order to make a consistent analysis of the wake, only time intervals where the variability of the wind direction did not affect the position of the wake downstream the turbine were considered. Three intervals of about 10 min were finally selected from the full dataset. The quality of the data was checked discarding all lidar measurements with a carrier-to-noise ratio (CNR) lower than -20 dB as well as the outliers not matching the Chauvenet criterion (TAYLOR, 1997). Details about these datasets can be found in Table 4. For sake of concision, only results from the second interval (see Fig. 3b) will be presented in detail in this study.

3 Wake identification

Apparently it might seem easy to identify the wake in the measurements presented in Fig. 3a, but an accurate identification of the wake is more complex since the measurement points of the lidars are on two lines directed across the wake and at the same time moving downstream. In this study it is proposed to fit a model of the lidar measurements inside a wake to the dataset presented in the previous section.

¹Usually the meteorological wind direction is indicated as the clockwise direction from which the wind is blowing. Here, in order to facilitate the comparisons with the direction of the wake axis, the so-called downstream direction is considered, i.e. direction towards the wind blows.

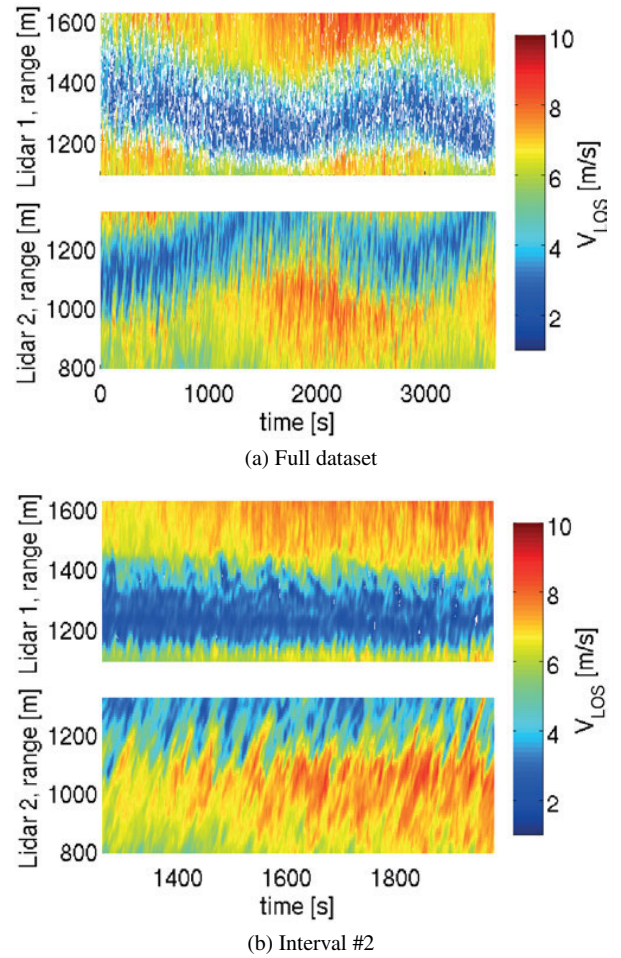


Figure 3: LOS measurements as a function of the time (horizontal axis) and of the range (vertical axis) including the full dataset (a) and considering only the second interval of data available (b).

3.1 The vertical profile of the LOS deficit

To describe the wake profile as a deficit, it is common to subtract the horizontal wind speed at a cross-section in the wake from the horizontal wind speed of the undisturbed flow. In analogy to the mentioned approach, here the LOS deficit, LOS_{def} , is evaluated from the lidar measurements averaged over the time in the considered interval. Thanks to the elevation applied in the measure-

Table 4: Details about the dataset measured with Lidar 1 and Lidar 2 from 12:00 AM UTC on 25/06/2012. The average wind data refers to the top anemometer mounted on the mast and the wind vane installed at 95.9 m at 103 °.

Time interval	Hor. wind speed [m/s]	Turbulence intensity [%]	Downstream wind direction (av./st. dev.) [°]	Availability (Lidar 1/2) [%]
0–550	7.82	8.1	25/6.6	98.6/99.9
1260–1980	8.21	7.4	17/6.7	100.0/100.0
2520–3070	8.30	6.4	22/6.5	100.0/100.0

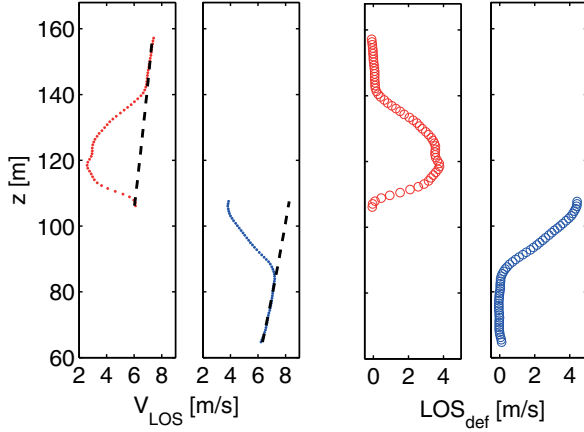


Figure 4: On the left: Average LOS measurements represented in the graphic as red and blue dots for Lidar 1 and Lidar 2 respectively. The dashed black line indicates vertical profile of LOS in the free stream evaluated fitting a power law curve to the data in the undisturbed flow. On the right: LOS deficit calculated subtracting the average LOS measurements from the evaluated LOS in the free stream. Lidar 1 is indicated again in red, Lidar 2 in blue.

ments, a vertical profile of V_{LOS} in the undisturbed flow can be estimated for each lidar fitting a power law curve to the range gates outside the wake. The measured profile of V_{LOS} is eventually subtracted from the fitted curve in order to estimate the LOS_{def} vertical profile. The results concerning this method are shown in Fig. 4.

3.2 The model of the LOS deficit

At this point it is possible to fit a model of LOS_{def} to the evaluated profile and to identify the wake. The model applied describes the wake in its own reference system, defined by the axes x' , y' and z' and centered at the turbine hub height. The first one follows the rotor axis downstream, the last one is vertical, pointing upwards and the remaining one is given accordingly to form a Cartesian frame of reference. A representation of the wake coordinate system can be found in Fig. 5. The global one, identified by the axes x , y , z aligned with the North, East and vertical direction respectively is included in the figure too.

In the model, lengths are normalized by the rotor diameter D and seven parameters are applied to describe the wake with an axisymmetric bivariate Gaussian function. A fundamental parameter is α , i.e. the direction of

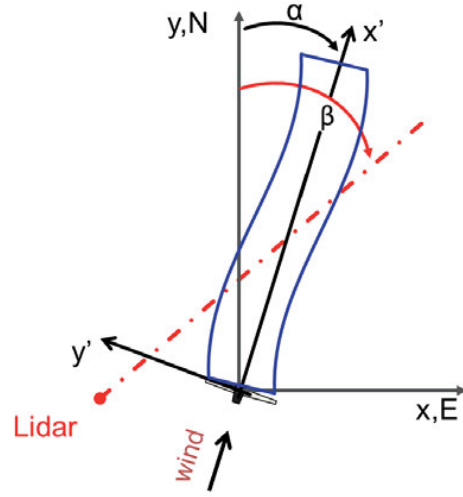


Figure 5: Schematic representation of the coordinate systems applied in the model of the LOS deficit. The reference frame of the wake, the global one and lidar measurements are included in the figure.

the wake axis. In the model it is used to define the rotation of the wake coordinate system in relation to the global one. Moreover, it is necessary along with the azimuth angle β of the lidar pointing direction to evaluate the LOS projection of the wind vector. The amplitude of the deficit is modulated by A_1 and decays exponentially with A_2 . The width of the wake at the rotor is controlled by A_3 , while a linear expansion of the wake downstream is given by A_4 . The remaining two parameters A_5 and A_6 define the offset of the wake center in y' and z' respectively. However, in this study the fit of the model was forced to center the wake about the rotor hub. The described model is summarized in Eq. 3.1 which includes also the relations between the reference system of the wake and the global one, where LOS_{def} is defined.

$$LOS_{def} = \cos(\alpha - \beta) \left[A_1 \exp\left(-\frac{x'}{A_2}\right) \exp\left(-\frac{z'^2 + y'^2}{2(A_3 + A_4 x')^2}\right) \right] \quad (3.1a)$$

where

$$\begin{aligned} x' &= x \sin(\alpha) + y \cos(\alpha) \\ y' &= -x \cos(\alpha) + y \sin(\alpha) - A_5 \\ z' &= z - A_6 \end{aligned} \quad (3.1b)$$

3.3 Fit of LOS deficit model and measurements

A least-square-fit of the model to the data was performed, applying to the parameters the constraints listed in Table 5 along with the correspondent results. It is interesting to note that some parameters saturate to one of their constrains, in particular A_2 which tends to retard the recovery of the deficit². The fitted curves show a reasonable agreement to LOS_{def} as shown in Fig. 6a. Some degrees of difference are found between the downstream wind direction measured at the metmast and the evaluated axis of the wake. Possible reasons for that are to be found in the combined uncertainty of the vane measurements and the limitations in the accuracy of the lidar levelling. Nevertheless, the operating wind turbine might deviate the axis of the wake from the wind direction. The direction of the wake axis found with the fit was applied in Fig. 6b to visualize the evaluated wake deficit at hub height along with the measurement points in the frame of reference of the wake.

4 Wake dynamics

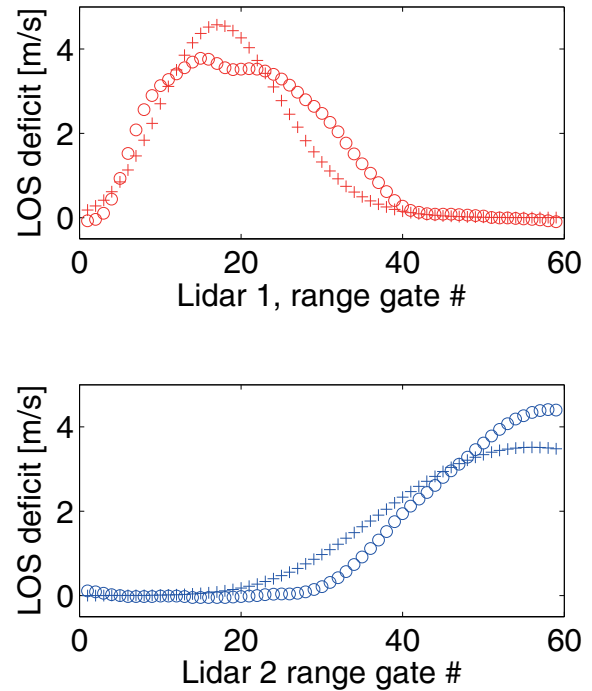
As it has been shown for instance in TRUJILLO et al. (2011), the center of the wake of a wind turbine has an offset around the mean wake axis varying dynamically along its way downstream. This behavior is commonly known as wake meandering and it is related to the interaction between the turbulent structures moving in the atmospheric boundary layer (ABL) (LARSEN et al., 2008). From all the scales included in the spectrum of turbulence, only the one comparable to the dimension of the rotor diameter is supposed to drive the wake meandering (ESPAÑA et al., 2012). Under this assumption, the highest frequency to be considered in meandering models f_m is estimated by means of Eq. 4.1, where the average horizontal wind speed V_{av} and the rotor diameters D are applied (LARSEN et al., 2008).

$$f_m = \frac{V_{av}}{2D} \quad (4.1)$$

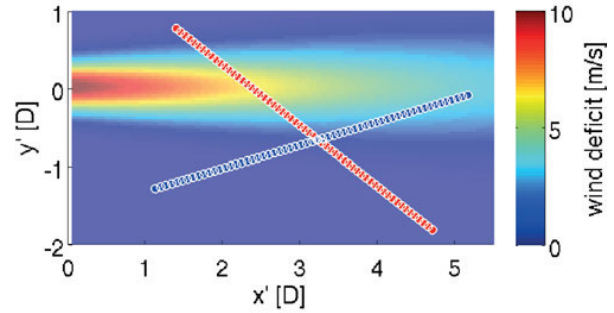
The effect of meandering can be observed in the measurements represented in Fig. 3b too, particularly at the interface between the wake and the undisturbed flow where, according to the position of the wake, the measurement point lies inside or outside the wind deficit. From this observation, it is reasonable to assume that part of the increased turbulence intensity observed in the wake region in relation to the undisturbed flow can be addressed to the wake meandering. This section points out the effect of meandering on the turbulence fluctuations in the flow of a wind turbine wake by means of spectral analysis.

The meandering was studied analyzing the frequency content of V_{LOS} downstream and across the wake. To

²according to the proposed model, the deficit recovers to the 99 % only 23 D downstream when $A_2 = 5$



(a) Comparison between the LOS deficit calculated with the model and evaluated from the lidar measurements.



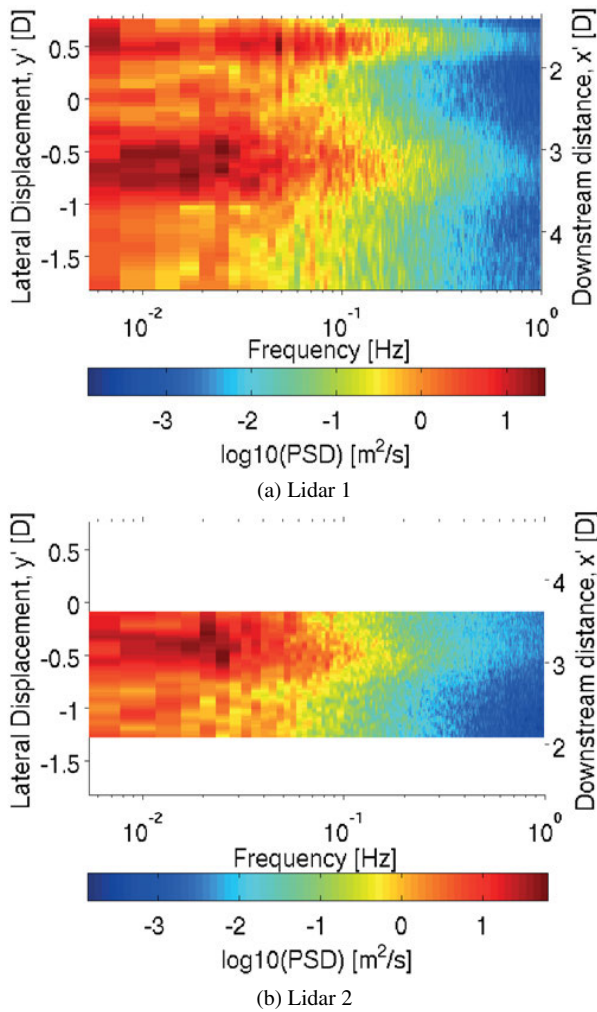
(b) Measurement points and evaluated wind deficit in the frame of reference of the wake. Lidar 1 is indicated in red, Lidar 2 in blue.

Figure 6: Results of the wake identification.

evaluate the power spectral density (PSD) of V_{LOS} the Welch algorithm was applied to the available datasets with 90 % overlapping intervals of about 3 min. No windowing was applied. The results are presented in Fig. 7 where, to simplify the interpretation, the position of the measurement points is transformed to the coordinate system of the wake evaluated in the previous section as indicated by the left and right vertical axis x' and y' in the graphics (cmp. Fig. 6b). As to be seen in Fig. 7a, an enhancement of the power at the lateral edges of the rotor characterizes the PSD both in the near and far wake. The enhancement related to the far wake appears also in Fig. 7b. The presented feature can be seen as the reflection to the frequency domain of the alternation inside-outside deficit observed in the time domain. This

Table 5: Constrains applied to the parameters of the LOS deficit model and correspondent results from the fit to the data.

	α [°]	A_1 [ms ⁻¹]	A_2 [D]	A_3 [D]	A_4 [-]	Norm-2 residual [m ² s ⁻²]
Lower/Upper constrain	14/40	2/15	1/5	0.2/0.3	0.05/0.25	–
Interval 1	33.5	9.9	5	0.20	0.010	143
Interval 2	22.5	10.4	5	0.22	0.050	30
Interval 3	28.1	10.7	5	0.20	0.068	50

**Figure 7:** Power spectral density of the LOS wind component as a function of the frequency (horizontal axis), of the lateral displacement y' from the wake axis (left vertical axis) and of the downstream position x' (right vertical axis).

interpretation links the enhanced regions of V_{LOS} PSD at the edges of the rotor to the wake meandering.

From a closer look at the graphics of Fig. 7, it can be noticed that the mentioned enhancement of the turbulence frequency content starts decaying at about 0.05 Hz. This observation is comparable to the f_m , evaluated to be around 0.03 Hz applying Eq. 4.1.

It is also interesting to observe the morphology of the region covered by the enhancement of the V_{LOS}

PSD in relation to the downstream position of the measured points: in the near wake this area appears slenderer than in the far wake. This characteristic can also be linked to the wake meandering. In the time series presented in Fig. 3b it is possible to see how the alternation inside-outside deficit at the measurement point of Lidar 1 is characterized by more refined structures at shorter ranges, i.e. in the near wake (less than $2D$ downstream), than at ranges located further in the wake (about $4D$ downstream). The available measurements leave space to different interpretations of this result. On one hand, this could suggest that the amplitude of the wake meandering increases while the wake propagates downstream. This is in agreement with the passive tracer hypothesis on which present meandering models such as the DWM and DPM are based (LARSEN et al., 2008; TRUJILLO and KÜHN, 2009). Considering that a wake volume, i.e. the so-called passive tracer, is transported downstream with a transversal velocity component, the transversal displacement has to increase downstream. Therefore, an observer positioned at a further distance downstream should observe larger displacements of the wind speed deficit. On the other hand, the shear layer at the wake edge as well as tip-vortices could provide reasonable explanations for the observed evolution of the turbulent structures downstream. However, it is not expected that the lidar adopted in this research can resolve the spatial scales of these turbulent phenomena considering the sample volume of about 30 m applied to the measurements. This is partially confirmed by the absence of a periodic signature in the PSD which could be associated with the tip-vortex frequency expected for the considered datasets which is around 0.5 Hz.

5 Conclusions

Two long range scanning lidars were operated concurrently at a fixed point to study the wake of a full-scale wind turbine. A new strategy was applied suitable to characterize the steady wake, in particular its downstream axis. A reasonable agreement was found between the evaluated direction of the wake and the downstream wind direction.

The developed measurement and analysis techniques are seen as a valid alternative to complex scanning pattern applied to study wake meandering. The higher sampling rate achieved staring the lidars at a fixed point, compared to a scanning measurement, makes this approach convenient to study the dynamic behaviour of

the wake. Spectral analysis of the lidar data show a non-homogeneous distribution of the frequency content of the wind LOS component which varies across the wake and in downstream direction. A discussion has been elaborated on the low frequency dynamics of the wake and on the interaction between the wake with the free atmosphere. The analysis technique can be further developed to characterize wake meandering in more detail and eventually validate and develop meandering models.

List of symbols

α	angle between the wake axis x' and the North axis y
β	azimuth angle of the laser beam
ABL	atmospheric boundary layer
A_i	parameters implemented in the model of LOS_{def}
D	rotor diameter [m]
DBS	Doppler beam swinging
DPM	disk particle model
DWM	dynamic wake meandering
CNR	carrier-to-noise ratio
FWHM	full-width-half-maximum
LOS	line of sight
LOS_{def}	line of sight profile deficit
NTP	network time protocol
ROI	region of interest
VAD	visual azimuth display
x, y, z	Cartesian axes identifying the East, North and vertical direction respectively
x', y', z'	Cartesian axes identifying the downstream wake axis, the transversal and the vertical directions
V_{av}	average horizontal wind speed
V_{LOS}	line of sight/radial velocity component

Acknowledgments

The authors thank the whole “Lidar and Wake” group at ForWind – University of Oldenburg which realized the measurement campaign and SENVION SE which made the anemometry data available for this research.

This research is part of the German joint project “GW Wakes” and it is supported by The Federal Ministry for Economic Affairs and Energy (BMWi) (Contract No 0325397A).

References

AINSLIE, J., 1988: Calculating the flowfield in the wake of wind turbines. – *J. Wind Engin. Indust. Aerodyn.* **27**, 213–224.

AITKEN, M., R. BANTA, Y. PICHUGINA, J. LUNDQUIST, 2014: Quantifying wind turbine wake characteristics from scanning remote sensor data. – *J. Atmos. Ocean. Technol.* **31**, 765–787.

ESPAÑA, G., S. AUBRUN, S. LOYER, P. DEVINANT, 2012: Wind tunnel study of the wake meandering downstream of a modelled wind turbine as an effect of large scale turbulent eddies. – *J. Wind Engin. Indust. Aerodyn.* **101**, 24–33.

FRANSEN, S., M. THØGERSEN, 1999: Integrated fatigue loading for wind turbines in wind farms by combining ambient turbulence and wakes. – *Wind Engineering* **23**, 327–339.

JUNGO, G.V., F. PORTÉ-AGEL, 2014: Volumetric scans of wind turbine wakes performed with three simultaneous wind lidars under different atmospheric stability regimes. – *J. Phys. Conference Series* **524**, 012164.

KÄSLER, Y., S. RAHM, R. SIMMET, M. KÜHN, 2010: Wake measurements of a multi-mw wind turbine with coherent long-range pulsed doppler wind lidar. – *J. Atmos. Ocean. Technol.* **27**, 1529–1532.

KATIC, I., J. HØJSTRUP, N. JENSEN, 1986: A simple model for cluster efficiency. – *EWEC 1986 Proceedings* **1**, 407–410.

LARSEN, G., H. MADSEN, K. THOMSEN, T. LARSEN, 2008: Wake meandering: a pragmatic approach. – *Wind Energy* **11**, 377–395.

MACHIELSE, L., P. EECEN, H. KORTERINK, S. VAN DER PIJL, J. SCHEPERS, 2007: ECN test farm measurements for validation of wake models. – *EWEC 2007*, http://www.ewea.org/ewec2007/allfiles2/64_Ewec2007fullpaper.pdf

MANN, J., J. CARIOU, M. COURTNEY, R. PARMENTIER, T. MIKKELSEN, R. WAGNER, P. LINDELÖW, M. SJLÖHOLM, K. ENEVOLDSEN, 2008: Comparison of 3D turbulence measurements using three staring wind lidars and a sonic anemometer – Risø-R-1660(EN). – Risø DTU.

SCHNEEMANN, J., D. TRABUCCHI, J. TRUJILLO, M. KÜHN, 2012: Comparison of measurements of the horizontal wind speed of a 2D multi lidar and a standard anemometer. – *The Science of Making Torque from Wind*, Oldenburg, October 9–11, 2012.

SMALIKHO, I.N., V.A. BANAKH, Y.L. PICHUGINA, W.A. BREWER, R.M. BANTA, J.K. LUNDQUIST, N.D. KELLEY, 2013: Lidar investigation of atmosphere effect on a wind turbine wake. – *J. Atmos. Oceanic Technol.* **30**, 2554–2570.

TAYLOR, J., 1997: An introduction to error analysis. – University Science Books.

TRUJILLO, J., M. KÜHN, 2009: Adaptation of a lagrangian dispersion model for wind turbine wake meandering simulation. – *Proc. of EWEC*, 16–19 March, Marseille, France.

TRUJILLO, J., F. BINGÖL, G. LARSEN, J. MANN, M. KÜHN, 2011: Light detection and ranging measurements of wake dynamics. part ii: two-dimensional scanning. – *Wind Energy* **14**, 61–75.

VASILJEVIC, N., G. LEA, M. COURTNEY, J. MANN, T. MIKKELSEN, 2013: The long range windscanner system – how to synchronously intersect multiple laser beams. – *European Wind Energy Conference & Exhibition 2013*, Vienna, Austria, 04/02/13, <http://www.ewea.org/annual2013/>

WERNER, C., 2005: Doppler Wind Lidar – Range-Resolved Optical Remote Sensing of the Atmosphere. – Springer, 325–354.

Chapter 4

Study of wake meandering by means of fixed point lidar measurements:

Spectral analysis of line of sight wind component

The content of this chapter consists of the

CONFERENCE JOURNAL ARTICLE

Journal of Physics: Conference Series 625 (2015) 012016

Main Author

©2015 The Authors

Reproduced under the Creative Commons Attributions-NonCommercial-
ShareAlike 3.0 Unported ([link](#))

presented at the Wake Conference, Visby, Sweden, May 2015.

Study of wake meandering by means of fixed point lidar measurements: Spectral analysis of line-of-sight wind component

Davide Trabucchi, Gerald Steinfeld, David Bastine, Juan-José Trujillo, Jörg Schneemann and Martin Kühn

ForWind-University of Oldenburg, Institute of Physics, Ammerländer Heerstr. 136, 26129 Oldenburg

E-mail: davide.trabucchi@uni-oldenburg.de

Abstract. The validation of dynamic wake meandering models by full field measurements is an important but challenging task. Recently a new approach has been proposed, where a long range lidar was employed to analyse the power spectral density of the line of sight wind component measured across the wake trajectory. The method is promising, but the number of useful time series within a measurement campaign depends to a large extent on a favourable geometrical setup of the lidar position and the wind direction. In the first part of the paper the approach is further investigated. To this avail, lidar simulations based on large eddy simulation results are analysed. In the second part, the approach is applied to real measurement data from a campaign with a long range lidar windscanner in the offshore wind farm »alpha ventus«. Eventually results about the wake dynamics are discussed.

1. Introduction

When a wind turbine is operating, it extracts energy from the wind passing through its rotor. In this process a wind deficit is generated which slowly recovers while it moves downstream. The area of the wind field affected by the wind deficit with increased local turbulence is commonly known as wake.

In a wind farm wind turbines often operate in the wake of other turbines. In these conditions, not only is the available energy of the wind less than in the free stream, but more severe turbulent fluctuations affect the turbine. A precise knowledge of the turbulence properties of the wake is therefore necessary to correctly predict the dynamic loading of the turbine structure in the design process. Hence, for instance, longer life-cycle or optimised structure design can derive from the reduction of the uncertainty on turbulence fluctuations in wakes.

The wake models applied in aero-elastic simulations can be divided in steady and dynamic models. The former consider a straight propagation of the wake where turbulence fluctuations are given by the combination of ambient and aero-dynamic turbulence [1]. The latter describe the wake as a series of deficit disks released at the turbine rotor and moving downstream transported by the atmospheric turbulent structures with scales larger than the rotor diameter [2; 3]. In these models the contribution of the so-called wake meandering, i.e. the lateral displacement of the wake deficit from the rotor axis, is taken into account along with the ambient and aero-dynamic turbulence.



A wind tunnel can be a suitable facility to study the dynamics of the wake [4; 5]. Synthetic wind fields generated by means of Large Eddy Simulation (LES) have been also applied to investigate the wake meandering [6; 7]. Nacelle based lidar have been implemented in full field experiments, for instance in [8; 9], to track dynamically the position of the wake center and to compare the results with the expectations from meandering models.

According to wake meandering models, the points near the lateral edges of the deficit are alternately inside and outside the wake. This results in a fluctuation of the wind component aligned with the rotor axis which is related to the wake dynamics. An approach to characterize the described fluctuations is proposed in [10], where long range lidar measurements are performed staring the laser beam at about hub height, diagonally across the wake. With this configuration, the necessity of an inclination about the axial wind direction has the drawback that only the wind turbulent fluctuations aligned with the lidar line of sight (LOS) can be measured. This aspect is investigated in the first part of this paper by means of lidar simulations, where a varying offset is applied between the LOS and the wind direction. In the central part, spectral characteristics of the LOS measurements previously simulated are evaluated for the study of the wake meandering. Eventually, fixed point lidar measurements collected in the offshore wind farm »alpha ventus« are considered. In particular, the power spectral density (PSD) of the data sampled across the wake of a wind turbine is analyzed.

2. Influence of the lidar beam inclination on the power spectral density of line of sight measurements

2.1. Lidar simulations

An unsteady, three dimensional wind field generated by the LES implementation PALM [11] is used as virtual environment for lidar simulations. The wake of a 2 MW Tjaereborg wind turbine with a rotor diameter D_T of 62 m and a hub height of 61 m is simulated by means of an actuator line (ACL) model [12]. The resulting wind field has a spatial and temporal resolution of 4 m and 0.4 s respectively.

The target of the lidar simulations was a point located at hub height in the wake of the described turbine, about $3 D_T$ downstream with a lateral offset from the rotor axis of about 1 rotor radius R_T . The measurements were simulated with a 0.4 s sampling time. Four different LOS inclinations from the mean wind direction were considered, namely from 0° to 60° with a 20° increment. The layout of the simulations is illustrated in figure 1. In order to only estimate the influence of projection of the wind vector on the LOS direction, the volume average of the lidar measurements was not applied to the lidar simulations.

2.2. The PSD of the LOS wind component across the wake

The PSD of the simulated LOS measurements was evaluated by means of the Welch algorithm, applying 90 % overlapping rectangular windows of about 3 min duration and is presented in

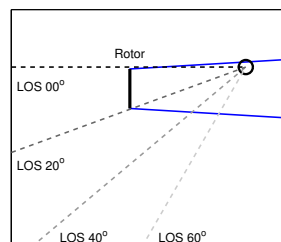


Figure 1. Layout of the lidar simulations (top view)

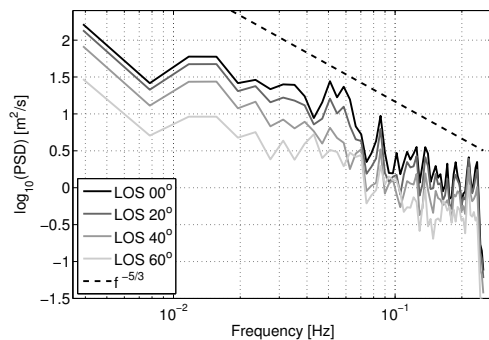


Figure 2. Power spectral density of the simulated LOS wind speed.

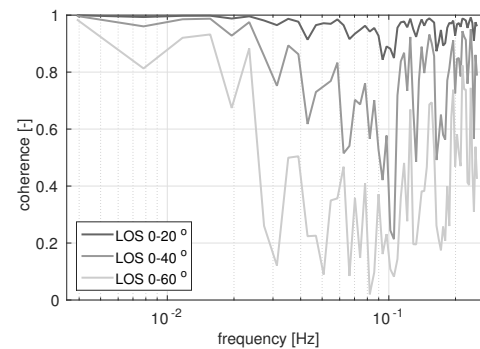


Figure 3. Variation of the spectral coherence between the simulated LOS measurements for an increasing angle of misalignment

figure 2. The 95 % confidence level conservatively estimated for this settings according to [13] corresponds to the range from -36% to $+79\%$ of the PSD value. From the graph it is evident that the energy content captured by the LOS projection decreases when the inclination angle increases. The spectral coherence function (SCF) can help to better interpret the results from the PSD analysis. It represents the normalized cross-spectral density between two signals [14] and indicates how well their spectral content is correlated. In particular, the SCF is constant and equal to 1 or 0 if the two considered signals are linearly correlated or completely uncorrelated. The SCF of the LOS simulated measurements aligned with the wind direction in relation to the the ones with an increasing offset is depicted on the graph of figure 3. A coherence close to one is found for a deviation angle of 20° . For larger deviations a coherence value above 0.8 characterizes only the low frequency region, up to 0.02 – 0.03 Hz. Then it progressively decays and eventually starts fluctuating randomly. This result indicates that for long time fluctuations the vertical and transverse wind components are only weakly affecting the LOS projection even for larger direction offset.

3. Application of fixed point lidar measurements to the study of the wake meandering

A wake tracking procedure [8] has been applied to the wind field at the cross-section $3 D_T$ downstream. The corresponding PSD of the lateral displacement of the wake deficit was evaluated to better understand whether a hidden relation exists between the lateral wake meandering and the fluctuations of the longitudinal wind speed at the lateral edge of the wake deficit. The normalized PSD of the wake lateral displacement and the one of the LOS measurements simulated with no offset with respect to the wind direction are compared in figure 4.

In both PSD curves, the energy is concentrated in the low frequency band and, at about 0.02 Hz, it starts decaying with a rate of about $-5/3$. While the PSD of the LOS simulations does not present any slope change in the high frequency range, the one of the wake lateral displacement sharply drops down. This may result from a low-pass filtering effect implicit in the wake-tracking procedure. Furthermore, the position of the wake center is supposed to be driven by the large-scale turbulent structures of the atmosphere.

It could be speculated on a resemblance to spectral peaks in the PSD of the LOS simulations near to 0.05 Hz and 0.09 Hz. This signature is not found in the spectral analysis of the wake tracking data, therefore no link with the wake meandering can be asserted. To better understand the nature of these possible peaks, further research will deal with longer datasets which could

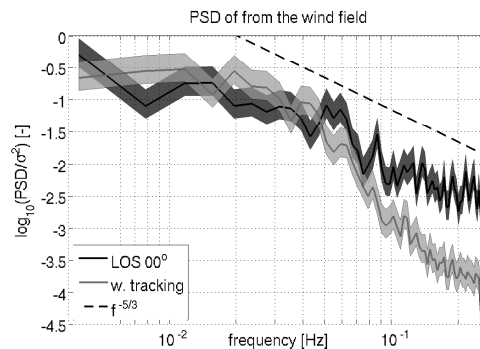


Figure 4. Normalized power spectral density and corresponding 95 % confidence level of the LOS simulations aligned with the wind direction and of the displacement of the wake center.

improve the statistical significance of the PSD.

4. Offshore lidar measurements of the wake meandering

Three long range scanning lidars Windcube WLS200S were deployed at the offshore wind farm »alpha ventus« in the German North Sea for one year from spring 2013. Twelve 5 MW wind turbines from two different manufacturers are installed as illustrated in figure 5 from West to East in rows of four units. The six turbines in the northern half of the wind farm are characterized by a rotor diameter D of 126 m mounted on a 92 m high tower, while the six in the southern half have a 116 m rotor at an hub height of 90 m. Two lidars were positioned on the platform of the meteorological mast FINO1, while the third unit was installed on the transformer station AV0 near the south-east corner of the wind farm.

Table 1. Technical sheet of the Windcube WLS200S.

Properties		Acquisition	
Wave length	1.54 μm	Photodiode sampling rate	250 MHz
Pulse length (FWHM)	0.1 – 0.4 μs	FFT length	64 – 128 – 256 points
Max laser power	5 mW	LOS component accuracy	0.2 m/s
Pulse repetition rate	10 – 20 kHz	max # range gates	250
Max range	6500 m		

Table 2. Measurement setup.

Setting	Value
Azimuth angle	-17.62°
Elevation angle	1.80°
Pulse length (Full Width Half Maximum)	0.20 μs
FFT points	64
Accumulation/Sampling time	0.60 s
Physical resolution in line of sight	~ 40 m

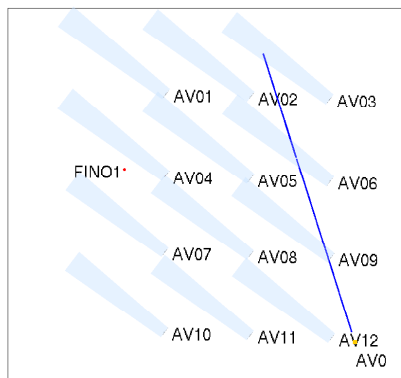


Figure 5. Position of the measurement beam (blue line) of the lidar installed on the transformer platform AV0 in the wind farm »alpha ventus«. Wakes are drawn downstream the turbines AV01-AV12 for a wind direction of 127° .

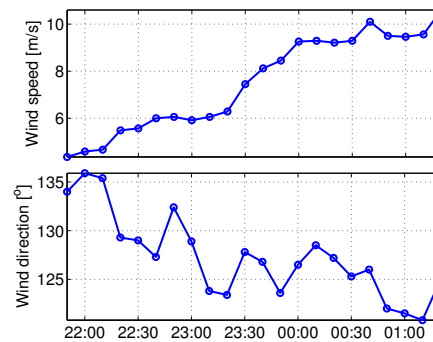


Figure 6. Ten-minute wind speed (top panel) and direction (bottom panel) collected by the top cup anemometer and the vane installed on the FINO1 meteorological mast at 100 m and 90 m respectively.

4.1. Measurement setup

Staring lidar measurements were performed with the lidar installed on the transformer station. The target point was located at hub height in the middle position among the four turbines in the north-east corner of the wind farm. The 244 range gates implemented in this experimental campaign were distributed equally every 15 m between 100 m and 2992 m. A finer separation of 5 m was applied along a $3 D$ distance centered to the aimed point. The objective of the measurements was to study the wake dynamics of the wind turbine AV06 by means of spectral analysis. The layout of the measurement is sketched in figure 5 for a wind direction of 127° , while the technical data and settings applied on the lidar are summarized in tables 1 and 2.

4.2. Dataset description

The measurements took place for about 3 hours on 17/12/2013 at night. The ten minute average of the wind speed and direction measured during the campaign by the top cup anemometer and the wind vane installed on FINO1 at 100 m and 90 m respectively [15] is reported in figure 6. Figure 7 shows the full dataset of measurements. The wake of the wind turbines AV06 and AV09 are clearly visible within the shorter and further ranges respectively. Since only the measurements which took place in the wake of AV06 are at about hub height, only the further ranges were considered. Among all the data, only six ten minute intervals were analysed for this study. For sake of concision only the interval measured on 18/12/2013 at 01:04 is presented here. Data with a carrier to noise ratio (CNR) below -25 dB or higher than -5 dB was filtered out. Before the analysis, also outliers identified with the Chauvenet criterion [16] were excluded from the filtered time series. The remaining data was re-sampled applying a linear interpolation with a constant time step of 0.6 s.

In order to represent the LOS measurements in the fixed frame of reference of the wake of AV06, the orientation of the wake axis was determined using the center of the average deficit measured by the lidar. The derived wind direction, i.e. 127° , has a 6° offset with respect to the wind direction provided by the FINO1 instrumentation. The fact that for this direction FINO1 is in the wake of the wind farm could explain this deviation. In figures 8 and 9 the position of the measurement points along with the data considered in this study are represented in the

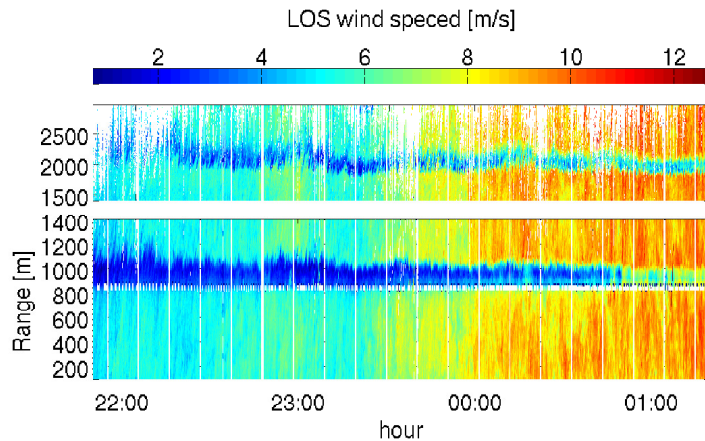


Figure 7. LOS measurements conducted on 17/12/2013 at night. In the top panel the measurements cross the wake of AV06, while in the bottom panel the one of AV09.

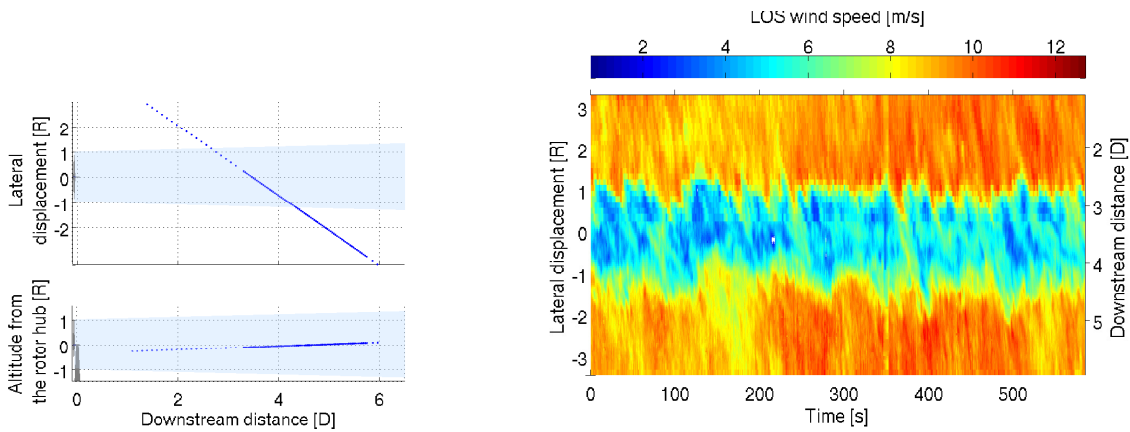


Figure 8. Top and side view of the measurement points represented in AV06 rotor frame of reference.

Figure 9. Ten minute time interval at 1:04 selected from the full dataset and represented in the AV06 rotor frame of reference.

reference frame of AV06 wake. Here, the x dimension is normalized with the rotor diameter D , while y and z with the corresponding radius R . Considering this setup, the inclination of the LOS from the wind direction is about 35° , which is an acceptable value according to the results of section 2.2.

4.3. Spectral analysis

The PSD of the lidar measurements was performed applying the same procedure described in section 2.2. The related results are illustrated in figure 10 where the lateral boundaries of the wake can be easily identified. In fact, in this region the energy content is particularly high in relation to other positions over the rotor, especially in the low frequency range. Around $2.7 D$ downstream, the area characterized by a higher level of the spectral energy covers a range of $\pm 0.5 R$ across the edge of the wake. At the opposite edge, about $4 D$ downstream, the range characterized by the increased PSD is almost twice as wide. This results are in accordance with [10], where a similar behaviour has been observed between $1.5 D$ and $4 D$ downstream. Figure 11 offers a closer view of the PSD of the LOS measurements evaluated at the center of

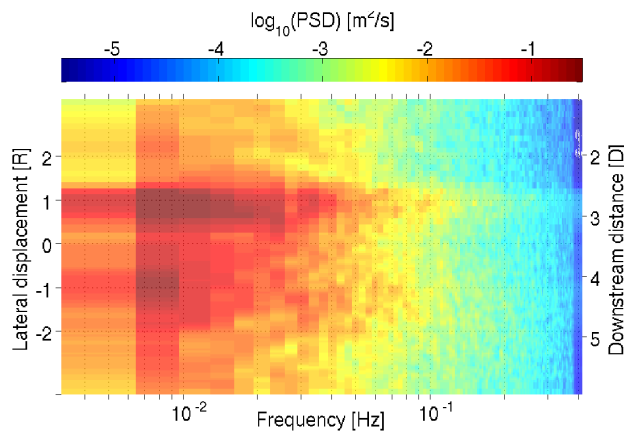


Figure 10. Power spectral density of the LOS wind component as a function of the frequency (abscissa), of the lateral displacement (left ordinate) and of the downstream position (right ordinate).

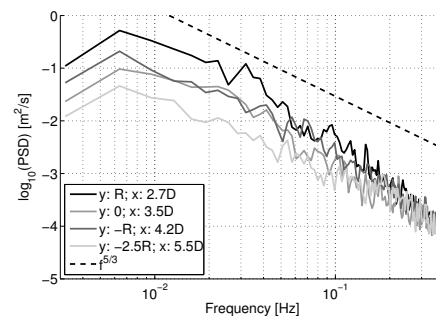


Figure 11. Power spectral density of the LOS wind component measured at different downstream distances, respectively at the lateral edges of the wake, in its center and in the free stream.

the wake $3.5 D$ downstream and at the two opposite sides of the wake located at $2.7 D$ and $4.2 D$ respectively. The same graphic includes the PSD calculated in the free stream.

A comparison of the curves confirms that the spectral energy content outside the wake is remarkably lower than in the area affected by it. Moreover, the diagram reveals that the PSD values in the center and at the edge of the deficit are very similar in the far wake, while they are considerably higher in the transition between the near and far wake. The high spectral energy content found in the near wake at the boundary of the deficit seems to spread radially towards the center of the wake and towards the free stream while moving downstream, until eventually a quite uniform and lower level of turbulent energy is reached.

Considering the wake meandering models, these effect could be in part related to the amplitude of the displacement of the wake deficit, which generates the alternation of the measurement point position between in and outside the wake. In the transition between near and far wake smaller horizontal displacements characterize the wake due to the short time characterized by lateral transport, while, further downstream, the displacements could be larger than $1 R$ as observed also in [17].

However, the increase of low frequency turbulence at the wake lateral boundaries could also be explained by turbulent diffusion. Only if an anti-correlation was found between the fluctuations measured at opposite sides of the wake, the relation between the fluctuations of the measurements at the edge of the wake and the wake meandering could be confirmed [5]. The applied measurement setup does not allow to perform the anti-correlation analysis for two points at the same downstream distance. The cross-correlation coefficient [14] has therefore been evaluated for the LOS time series sampled at the opposite edges of the wake deficit, but $2.8 D$ and $4.2 D$ downstream, respectively. The resulting curve visible in figure 12 as a function of the imposed time lag between the considered signals shows a minimum of -0.34 for a time lag of 26 s. The corresponding peak is not necessarily statistically significant, for this reason a moderate anti-correlation can only be assumed. This hypothesis is sustained by the delay which is in the order of the expected travelling time of the deficit between the two considered points.

A dominant peak was probably not found because of the large longitudinal distance between the two considered points. To support this explanation, the cross-correlation analysis was applied

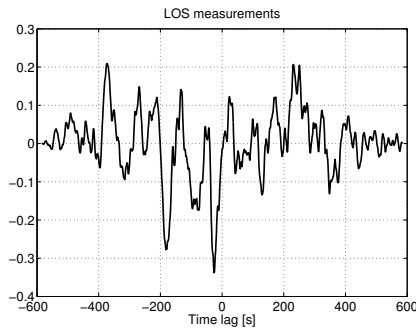


Figure 12. Cross-correlation of two LOS time series measured around hub height, at the opposite edges of AV06 wake deficit $2.8 D$ and $4.2 D$ downstream, respectively.

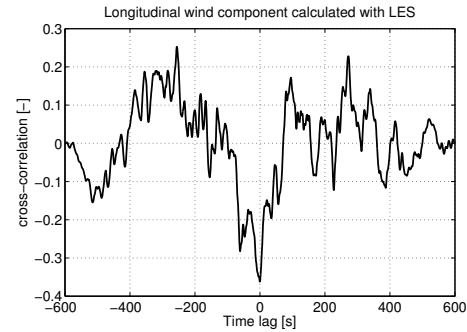


Figure 13. Cross-correlation of the longitudinal wind component sampled from the simulated wake of section 2.1 at hub height, at the opposite edges of the wake deficit, about $3 D$ downstream, respectively.

with no downstream offset to the longitudinal wind component of the simulated wind field described in section 2.1. Two points at hub height, about $3 D_T$ downstream and at opposite sides of the wake were considered. The related graph shown in figure 13 presents a clear evolution of the cross-correlation in which a negative peak and no time lag can be identified. This suggests that the results of the cross-correlation analysis from the full field lidar measurements could be improved if two points at the same downstream section were considered. Moreover, it indicates that the negative correlation found for the LOS measurements in figure 12 could be a real feature of the wind field and not just the outcome of an uncorrelated time series. For this reasons, a connection between the higher turbulence energy content at the edge of the wake and the wake meandering can be supposed.

5. Conclusion

In the first part of this work, simulations of lidar measurements at a fixed position in the wake of a wind turbine have been analysed to understand the influence of the misalignment between the LOS direction and the mean wind direction on the spectral analysis of the lidar measurements. It was demonstrated that LOS measurements at a fixed point can well represent the dynamic fluctuations of the main wind component at the edge of a wake deficit when they are oriented with a moderate offset with respect to the mean wind direction. The results suggest also that this constraint could be relaxed if only low-frequency fluctuations are considered.

To investigate the suitability of fixed point lidar measurements to the study of wake meandering, the normalized PSD of the lateral displacement of the wake center was compared with the one calculated for the LOS measurements simulated with no deviation from the wind direction. In both cases, the energy content mainly distributed within the low frequency range and then decays following a power law. No corresponding spectral peaks could be identified.

In the last part of the paper, full field data were considered. The measurement approach implemented in the simulations was reproduced in the offshore wind farm «alpha ventus» during an experimental campaign. In relation to other positions in the wake, a high level of spectral energy characterizes a well defined region around the lateral edges of the deficit in the transition between near and far wake. The meandering of the wake was suggested as possible explanation and a negative correlation between LOS measurements or simulations at opposite sides of the wakes supports this argument.

Fixed point lidar measurements showed to be a potential application for the study of the wake

dynamics by means of spectral analysis. This preliminary study indicates a possible relation between the wake meandering and the spectral characteristics of appropriate lidar measurements at the lateral boundaries of the wake. However, this hypothesis has to be confirmed by further research.

Acknowledgments

The authors thank the whole »Lidar and Wakes« group at ForWind - University of Oldenburg which made the measurement campaign possible.

The research in the offshore wind farm »alpha ventus» was carried out in the frame of the RAVE (Research at alpha ventus) research project »GW Wakes - Part A«, funded by the German Federal Ministry for Economic Affairs and Energy (BMWi) based on a decision of the Parliament of the Federal Republic of Germany (grant number 0325397A).

References

- [1] Frandsen S T and Thøgersen M 1999 *Wind Engineering* **23** 327–339 ISSN 0309-524X
- [2] Larsen G C, Madsen H A, Thomsen K and Larsen T J 2008 *Wind Energy* **11** 377–395 ISSN 1099-1824 URL <http://dx.doi.org/10.1002/we.267>
- [3] Trujillo J J and Kühn M 2009 *European Wind Energy Conference (EWEC)*
- [4] Medici D and Alfredsson P H 2008 *Wind Energy* **11** 211–217 ISSN 1099-1824 URL <http://dx.doi.org/10.1002/we.247>
- [5] España G, Aubrun S, Loyer S and Devinant P 2012 *Journal of Wind Engineering and Industrial Aerodynamics* **101** 24 – 33 ISSN 0167-6105 URL <http://www.sciencedirect.com/science/article/pii/S0167610511002157>
- [6] de Mare M, Mann J, Churchfield Matthew J and Patton Edward G 2013 *EWEA Offshore*
- [7] Bastine D, Björn W, Matthias W and Joachim P 2014 *Journal of Physics: Conference Series* **524**
- [8] Trujillo J J, Bingöl F, Larsen G C, Mann J and Kühn M 2011 *Wind Energy* **14** 61–75 ISSN 1099-1824 URL <http://dx.doi.org/10.1002/we.402>
- [9] Machefaux E, Larsen G C, Troldborg N, Gaunaa M and Rettenmeier A 2014 *Wind Energy* ISSN 1099-1824 URL <http://dx.doi.org/10.1002/we.1805>
- [10] Trabucchi D, Trujillo J J, Bitter M and Kühn M 2014 *Meteorologische Zeitschrift* – URL <http://dx.doi.org/10.1127/metz/2014/0610>
- [11] Raasch S and Schröter M 2001 *Meteorologische Zeitschrift* **10** 363–372 URL <http://dx.doi.org/10.1127/0941-2948/2001/0010-0363>
- [12] Troldborg N, Sorensen J N and Mikkelsen R 2010 *Wind Energy* **13** 86–99 ISSN 1099-1824 URL <http://dx.doi.org/10.1002/we.345>
- [13] Manolakis D G, Ingle V K and Kogon S M 2000 *Statistical and Adaptive Signal Processing* (McGraw-Hill) chap 5
- [14] Bendat J and Piersol A 2000 *Random data analysis and measurement procedures* (Wiley Interscience)
- [15] Beeken A, Neumann T and Westerhellweg A 2008 *DEWEK*
- [16] Taylor John R 1997 *An introduction to error analysis* (University Science Books)
- [17] España G, Aubrun S, Loyer S and Devinant P 2011 *Wind Energy* **14** 923–937 ISSN 1099-1824 URL <http://dx.doi.org/10.1002/we.515>

Chapter 5

Nacelle-based lidar measurements for the calibration of a wake model at different offshore operating conditions

The content of this chapter consists of the

CONFERENCE JOURNAL ARTICLE

Energy Procedia 137 (2017) 77-88

Main Author

©2017 The Authors

Reproduced under the Creative Commons Attribution-NonCommercial-NoDerivatives 4.0 International Public License ([link](#))

presented at the 14th EERA DeepWind Conference hold in Trondheim, Norwegen in January, 2017.

Available online at www.sciencedirect.com**ScienceDirect**

Energy Procedia 137 (2017) 77–88

Energy

Procediawww.elsevier.com/locate/procedia

14th Deep Sea Offshore Wind R&D Conference, EERA DeepWind'2017, 18-20 January 2017,
Trondheim, Norway

Nacelle-based Lidar Measurements for the Calibration of a Wake Model at Different Offshore Operating Conditions

Davide Trabucchi, Juan-José Trujillo, Martin Kühn

ForWind - University of Oldenburg, Küpkersweg 70, Oldenburg 26129, Germany

Abstract

Commonly, wake models are calibrated in wind tunnels or using flow simulations with a wide degree of physical details. In general, it is assumed that these methods cannot fully reproduce the real operating conditions of wind turbines. This research aims at investigating the calibration of an analytical single wake model in relation to full-scale measurements. Within this scope, we fitted the wake model to wake measurements realised with a lidar installed on the nacelle of an offshore wind turbine. We studied the parameters returned by the fit separating cases at different levels of atmospheric turbulence and thrust on the wind turbine rotor. Comparing the results with a published calibration based on few LES wind fields representative for partial load conditions, we achieved good agreement when the considered wind turbines operated in similar conditions. For other situations, i.e. at full load, we found different calibrations of the model parameters. Our results show that and how nacelle-based lidar measurements can be complementary in the development of wake models.

© 2017 The Authors. Published by Elsevier Ltd.
Peer-review under responsibility of SINTEF Energi AS.

Keywords: nacelle lidar, full field experiment, wake recovery, wake expansion, model verification

1. Introduction

In a wind farm, the upstream turbines slow down the wind to generate electrical energy thereby creating a wake flow with reduced wind speed behind their rotors. As a consequence, downstream turbines generally produce less energy and are subject to more severe fatigue loads [1].

To predict the energy yield of a wind farm, engineering wake models are applied to estimate the corresponding energy losses. These models need to have reasonable computational costs. Therefore, they describe the shape of the wake deficit using simplified analytical formulas based on few parameters. The drawback of this simplification is a reduced ability to fully resolve the turbulent structures composing the wake flow. It follows that engineering wake models have a much lower accuracy than more physically detailed models, but this is the price to pay to have simulation tools suitable for industrial applications.

E-mail address: davide.trabucchi@uni-oldenburg.de

Walker et al.[2] indicate that 50 % uncertainty is to be expected for the estimation of energy wake losses with current engineering wake models. In new offshore wind projects, the size and costs have increased fast leading to a strong impact of the uncertainty on the financial risk of the project and on the confidence of possible investors. For this reason, the accuracy of engineering wake models has become a main concern of the wind energy community.

More extensive and precise calibration of these models could reduce their uncertainty. For a long time their development and validation have relied on the indirect verification of the power production and not on the spatial description of the flow. Today, the advancement in simulations and full field measurements allow to develop and validate models using the flow itself.

Very detailed wake simulations, such as large eddy simulations (LES) with wind turbines modelled by means of an actuator line or an actuator disk model, can simulate the wind farm flow with a high degree of fidelity. For instance Niayifar and Porté-Agel[3], Trabucchi et al.[4] and Keck et al.[5] used LES for the evaluation and calibration of engineering wake models. This approach offers realistic wake data, but its results cannot always be generalised since often only few exemplary test cases are addressed due to the high computational costs of the simulations.

Measurements of scaled wind turbine wakes with different level of complexity have been widely used to study wakes [6–8]. The advantage of wind tunnel measurements is the possibility to well define the environmental conditions of the measurements. They could also be applied for the calibration of engineering wake models, however, it is not always possible to entirely reproduce the physics of the interaction between the wind turbine rotor and the atmospheric boundary layer in wind tunnels.

Full field experiments with remote sensing technology could partly compensate some limitations of wind tunnel experiments. Käsler et al.[9], Trujillo et al.[10] and Bingöl et al.[11] were among the first ones using lidars for wake measurements. In recent studies, Aitken et al.[12] and Iungo[13] applied long-range scanning lidars to study the wake recovery under different atmospheric conditions. Furthermore, Vollmer et al.[14] used offshore dual Doppler lidar measurements [15] to validate the implementation of a modified actuator disk model in LES [16].

Nonetheless, there is a strong demand for full-scale experiments to determine and verify the empirical rules implemented in codes for the estimation of wake losses. The present work aims to investigate an analytical wake model by means of full-scale offshore measurements. Specifically, we chose the model proposed by Bastankhah and Porté-Agel[17], which had been calibrated with wakes from an actuator disc model within an LES wind field. Our study addresses the development of the wake profile and is based on wake measurements taken with a long-range scanning lidar installed on the nacelle of a wind turbine during different atmospheric and operating conditions.

2. Measurements

The research of this paper is based on wind measurements in the wake of an offshore wind turbine performed with a long-range scanning lidar installed on the wind turbine nacelle. In the following we describe the setup of the instrumentation and how the data were prepared for the evaluation of the wake model.

2.1. Experimental setup

The measurement campaign was conducted in the offshore wind farm Nordsee Ost which is located 35 km north-west of the island Heligoland in the German North Sea. This wind farm consists of 48 turbines of type Sen-vion 6.2M126 (rotor diameter $D = 126$ m, hub height $z_H = 96.5$ m and rated power 6.15 MW) and shares its southern border with the wind farm Meerwind Süd/Ost (see Fig. 1a).

A long-range scanning lidar Leosphere WLS200S was deployed for a period of 7 months starting from November 2015 on the nacelle of the wind turbine NO48 (diamond in Fig. 1b). The lidar scanned downstream through the wake emitting 200 ns long laser pulses at 20 kHz, sampling the light back-scattered from the aerosol particles in the atmosphere using a so-called range gate window of about 256 ns. With these settings, the lidar physical range resolution was about 44 m in terms of full-width-half-maximum [18].

Each measurement cycle took about 200 s including five consecutive horizontal and one vertical scans, indicated as PPI (Plan Position Indicator) and RHI (Range Height Indicator) respectively; all scans covered a 30° sector. The trajectory patterns were scanned continuously at $1^\circ/\text{s}$ and the radial wind speed v_R , i.e. the wind speed component parallel to the pointing direction of the laser beam, was simultaneously measured every 15 m in the range between

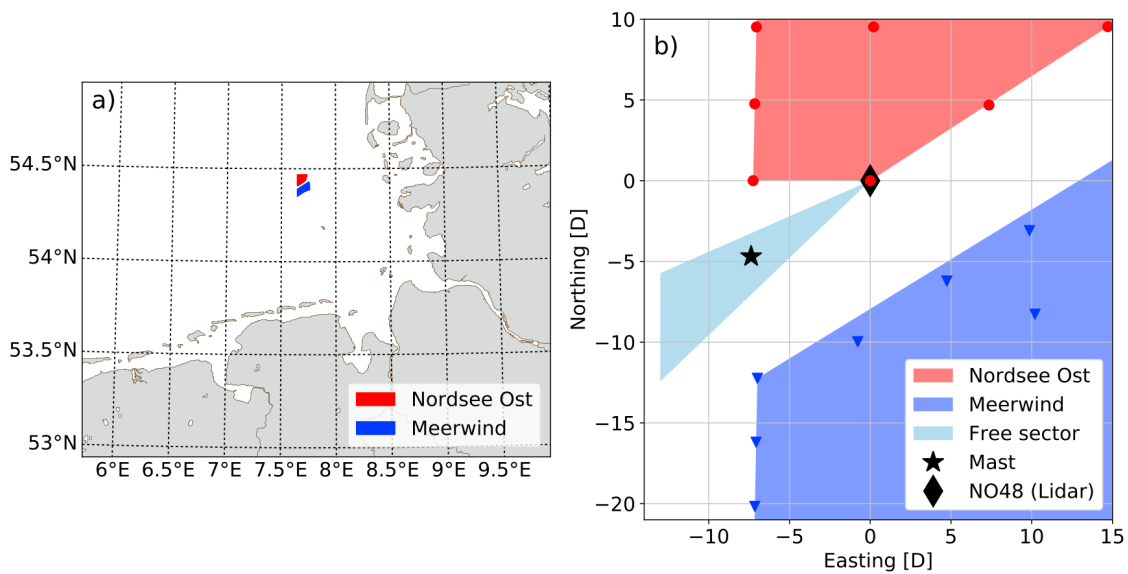


Fig. 1: Maps of the German North Sea including the position of the offshore wind farm Nordsee Ost where the experimental campaign took place (a); Layout of the experimental campaign including the position of instrumentation and the free sector considered in this research (b).

100 m and 1000 m with a sampling time of 0.5 s per beam. From December 12, 2015 the maximal range was extended to 2500 m and the resolution was changed to 25 m keeping the other settings unchanged.

The instrumentation on the nacelle was completed by three interconnected differential Global Navigation Satellite System (GNSS) devices Trimble SPS855/SPS555H. The GNSS antennas were mounted on the railing of the nacelle helicopter platform. With this system it was possible to measure accurately the nacelle tilt and yaw (ξ_{GPS} and γ_{GPS} respectively). These measurements were used to estimate the actual direction of the laser beam in a global reference system.

A meteorological mast is installed at the south-west corner of the wind farm (star in Fig. 1b). Data from the mast as well as from the Supervisory Control and Data Acquisition (SCADA) system were available as ten-minute statistics. Specifically, the average wind direction (ϕ_{87}) was estimated on the basis of three vanes mounted with 120° separation at 87 m height; the average wind speed (v_{96}) at 96 m height with the corresponding turbulence intensity (TI_{96}) were evaluated from the two cup anemometers installed at opposite sides on the top of the mast. These data are supposed to include a correction for the mast shadowing effect, but no detailed documentation was made available. Additionally, the power law exponent (α) of the wind speed vertical profile evaluated using values at 32 m and 96 m height and the potential temperature difference ($\Delta\theta$) evaluated between heights 25 m and 96 m were available. From the SCADA data, the nacelle yaw and the operational status of the wind turbine NO48 were provided.

From all the timeseries recorded during the campaign, we selected for this study only ten-minute intervals during which there was a fixed orientation of the nacelle with a maximal yaw misalignment of $|\phi_{87} - \gamma_{GPS}|$ of 3° and an availability of lidar data larger than 70 %. Moreover, to avoid any wake effect on the mast and to consider only lidar measurements of a single wake, we analysed time intervals characterised by a wind direction between 220° and 252° . This lead to a total of 213 intervals available for this study.

2.2. Lidar data processing

In this section we explain how we calculated the ten-minute horizontal wind speed within the sectors scanned by the PPI and RHI trajectory respectively.

Filtering

First, we collected all the data measured following the same scanning trajectory during the selected time interval and filtered out unreliable measurements by means of two different approaches: data with a poor signal quality,

i.e. a carrier to noise ratio (CNR) below -24 dB, or affected by hard targets and identified by a CNR above -5 dB were excluded from the dataset. Furthermore, outliers were detected and removed by statistical analysis using the Chauvenet criterion [19]. When more than 30 % of data had a CNR within -18 dB and -5 dB, the second approach was applied: the lowest CNR threshold was lowered to -27 dB and, referring to the statistics of the data included in the same CNR interval, only radial wind speeds within 2.56 standard deviation around the average were considered.

An additional filter was included into both approaches to remove the data corresponding to a spectral width of the Doppler peak outside of the range from 0.05 m s^{-1} to 6.0 m s^{-1} . These boundaries were based on own experience and suited all the cases well.

Time averaged horizontal wind field reconstruction

We assumed a homogeneous and uniform wind direction ϕ_{87} and a negligible vertical wind speed to calculate the ten-minute average horizontal wind speed \bar{v}_H from the average radial wind speed \bar{v}_R :

$$\bar{v}_H = \frac{\bar{v}_R}{\cos(\bar{\xi}) \cos(\bar{\gamma} - \phi_{87})} \quad (1)$$

In Eq. 1, the variables indicated with a bar refer to the average of data corresponding to the same scanner position approximated to the first digit and to the same range r . In our measurements, the scanner position is defined by the azimuth and elevation angles γ and ξ which indicate the direction of the laser beam projected on the horizontal and vertical plane respectively.

Before rounding and averaging, the azimuth angle γ_L provided by the lidar was transformed into the corresponding angle γ in the global reference system considering the nacelle yaw γ_{GPS} . With respect to the elevation ξ , we neglected the average tilt of the nacelle $\bar{\xi}_{GPS}$, which oscillated in the range from 358.27° to 359.07° during the time intervals considered. This approximation could introduce a maximal underestimation of \bar{v}_H lower than 0.05 %.

Finally \bar{v}_H was associated to the Cartesian coordinates \bar{x} , \bar{y} , \bar{z} derived with $\bar{\gamma}$, $\bar{\xi}$ and r , considering the average tilt rotation $\bar{\xi}_{GPS}$ only for the vertical coordinate \bar{z} :

$$[\bar{x}, \bar{y}, \bar{z}] = \left[\sin(\bar{\gamma}) \cos(\bar{\xi}), \cos \bar{\gamma} \cos(\bar{\xi}), \sin(\bar{\xi} + \bar{\xi}_{GPS}) \right] r \quad (2)$$

After screening the processed RHI measurements, we noticed some artefacts in the results and we therefore decided to exclude these data from the study to preserve the reliability of the research.

2.3. Uncertainty evaluation

To estimate the uncertainty associated to the calculation of the horizontal wind speed from the lidar measurements, we followed two approaches: the first is derived from the uncertainty propagation theory [20] considering uncertainties of type B only; the second one is based on a comparison with ten-minute cup anemometer data measured on the top of the meteorological mast.

In the application of the uncertainty propagation theory we disregarded the contribution of the elevation ξ which is negligible in comparison to the other terms in case of horizontal PPI scans. Accordingly, we evaluated the combined standard uncertainty (CSU) as

$$CSU = v_H \sqrt{(\tan(\bar{\gamma} - \phi_{87}))^2 (\delta_{\bar{\gamma}}^2 + \delta_{\phi_{87}}^2) + \frac{1}{\bar{v}_R^2} \delta_{\bar{v}_R}^2} \quad (3)$$

estimating the uncertainty of the azimuth and the one of the wind direction as $\delta_{\gamma} = \delta_{\phi_{87}} = 5^\circ$. Concerning the radial wind speed we considered the uncertainty $\delta_{\bar{v}_R} = 0.75 \text{ m s}^{-1}$ which is a reasonable value for lidar measurement taken in wakes with an identical device and filtered using a CNR threshold [21]. The combined standard uncertainty of the horizontal wind speed is exemplary reported for two time intervals in Fig. 2a-b. In both cases, the uncertainty is dominated by the contribution of the radial wind speed where the radial and the wind directions are aligned. The different azimuthal shading in the two examples is related to different offsets between the wind direction at the meteorological mast and the yaw of the nacelle. From this analysis, the uncertainty varies within 0.7 m s^{-1} and 1.1 m s^{-1} .

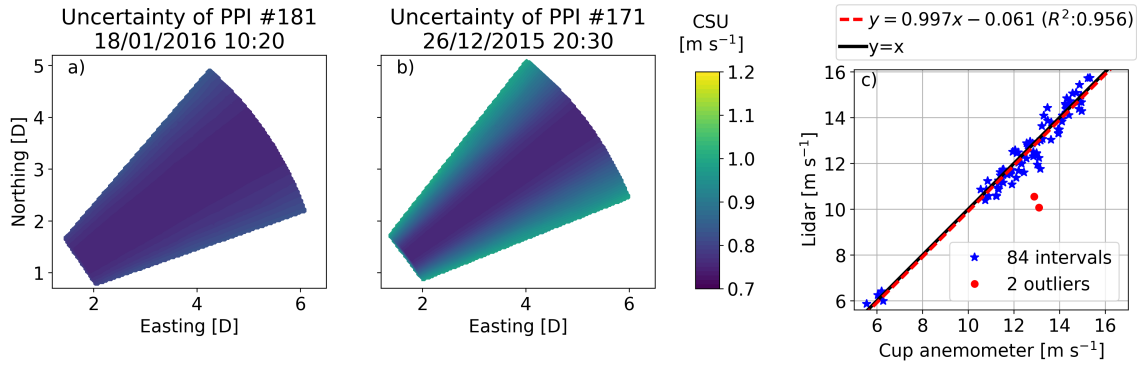


Fig. 2: Combined standard uncertainty (CSU) evaluated for the PPI scans included in the time intervals number 181 (a) and 151 (b); Linear regression between the horizontal wind speed at the top of the meteorological mast measured by a cup anemometer and evaluated from lidar measurements (c).

For the comparison with the top anemometer data, we considered the wind direction sector from 40° to 72° and averaged the lidar measurements taken about 0.5 m above the top of the mast within a 15 m radius around the anemometer. The good agreement of the two datasets is easily recognisable in the scatter plot of Fig 2c, is quantified by the regression line

$$y = 0.997x - 0.061 \quad (4)$$

and by the corresponding coefficient of determination which is very close to one ($R^2 = 0.956$). The small intercept of the regression line and the associated 0.3% underestimation of the horizontal wind speed measured with the cup anemometer suggest that the results from the uncertainty propagation analysis provide a conservative estimation of the uncertainty.

3. Wake model description and fit

The measurements described in the previous section are suitable for the evaluation of wake models. For instance, Trabucchi et al.[22] and Aitken et al.[12] used simple analytical models to estimate the main characteristics of wakes measured with lidars. In our study, we addressed the model proposed by Bastankhah and Porté-Agel[17]. We chose this model because it had been fully calibrated using LES and thus offers the possibility of a comparison with a calibration based on full field lidar measurements.

Bastankhah and Porté-Agel[17] developed the model to fulfill the basic physical principles of wakes applying a realistic shape of the wind speed reduction. More in detail, the model maps the wake deficit on the downstream cross sections $y_W - z_W$ with a Gaussian surface which expands linearly along the stream wise coordinate x_W and recovers respecting the mass and momentum conservation in relation to its width and to the thrust coefficient C_T :

$$v_{DM}(x_W, y_W, z_W, C_T) = \left(1 - \sqrt{1 - \frac{C_T}{8\sigma^2}}\right) \exp\left(-\frac{y_W^2 + z_W^2}{2\sigma^2}\right) \text{ with } \sigma = k^* x_W + \varepsilon \quad (5)$$

The normalised width of the wake is determined by the standard deviation σ of the Gaussian surface which increases proportionally to the wake expansion rate k^* from the initial value ε at $x_W = 0$.

Furthermore, Bastankhah and Porté-Agel[17] derived a theoretical relationship between the thrust coefficient and width of the wake immediately behind the rotor:

$$\varepsilon = 0.25 \sqrt{\beta} \text{ with } \beta = \frac{1}{2} \frac{1 + \sqrt{1 - C_T}}{\sqrt{1 - C_T}} \quad (6)$$

Similarly as in [12,22,23], we fit the model of Eq. 5 to the normalized wake deficit v_D obtained subtracting the average horizontal wind speed v_H from the corresponding inflow vertical profile v_{in} :

$$v_D(x_W, y_D, z_W) = \frac{v_{in}(\bar{z}) - v_H(\bar{x}, \bar{y}, \bar{z})}{v_{96}} \quad \text{with } v_{in}(\bar{z}) = v_{96} \left(\frac{\bar{z}}{z_{ref}} \right)^\alpha \quad \text{and } z_{ref} = 96 \text{ m} \quad (7)$$

In Eq. 5, x_W , y_W and z_W define the normalised position of the measurements relative to the rotor centre and parallel to the wake direction ϕ_W , therefore we apply a coordinate transformation before the fit to the wake deficit measurements:

$$[x_W, y_W, z_W] = \frac{1}{D} [\bar{x} \sin(\phi_W) + \bar{y} \cos(\phi_W), -\bar{x} \cos(\phi_W) + \bar{y} \sin(\phi_W), (\bar{z} - z_H) + g_Z \bar{x}_W] \quad (8)$$

The vertical gain g_Z is also included in the coordinate transformation to compensate for a possible misalignment of the PPI plane and for a possible variable vertical offset of the wake centre.

4. Results and discussion

For the evaluation of the wake model described in section 3, we fitted Eq. 5 to the measured ten-minute average wake deficit data. The fit was performed with a non linear least-square approach using the trust region reflective method implemented in the function *optimize.curve_fit* included in Scipy [24]. No weighting was applied to the data and constrained bounds were assigned to the parameters of the model. Namely we forced ε between 0.1 and 0.4; k^* within 0 and 1; g_Z in the range from -1 and 1; the wake direction ϕ_W in the sector from 0° to 90° .

To avoid phenomena not reproducible with this wake model, i.e. the effect of the rotor hub in the near wake and the deceleration of the flow within the induction zone of the next turbine which is located about eight diameters downstream the rotor, we only considered data in the range from two to six rotor diameters downstream. Furthermore, we excluded the undisturbed flow at the sides of the wake from the fitting procedure applying the wake deficit threshold of 2.83 % that Ainslie[25] used to define the wake radius.

The fit provided the best set of parameters which can represent the data for different atmospheric and operating conditions. The next three subsections deal with the quality of the fit, explain its results in relation to different operating conditions and finally show a comparison with results obtained implementing the calibration suggested by Bastankhah and Porté-Agel[17] and by Niayifar and Porté-Agel[3].

4.1. Evaluation of the analytical wake model fit

To assess the quality of the fit to the data of each time interval, we computed the associated root-mean-square error (RMSE). For this calculation, we included only the data where the modelled, normalised wake deficit values were above 2.83 %, that is the same threshold used to separate the wake from the free flow in the fitting procedure. This threshold is supposed to exclude from the analysis wind field areas where lower wind speed data are not the result of the wind turbine rotor, but of large scale turbulent structures. In terms of normalised wake deficit, we obtained a maximal value of the RMSE slightly below 0.16 as documented in Fig. 3a. These errors could appear unacceptable considering that common values of the normalised wake deficit are below 0.5; however, we think that the corresponding results could still be significant for this research if they are given the proper attention. In this sense, after a visual inspection of all cases we excluded only one time interval since the wake was hardly detectable in the corresponding measurements. Figure 4 shows an example which could facilitate the perception of the RMSE: Figure 4b and Fig. 4d provide examples of the wind fields reproduced by the analytical model using the parameters from a better and a poorer fit to the corresponding wake deficit data which are illustrated in Fig. 4a and Fig. 4c respectively.

To better understand the RMSE results, we divided the data in intervals at which the turbine operated above and below rated wind speed. With this, we assume distinct behaviors with respect to the rotor thrust in the two regions. Accordingly, we expect to observe low and high thrust coefficient conditions. In Fig. 3, the two groups are indicated with red bullets and blue stars respectively. This classification shows that the analytical model fits better wake deficits produced above rated wind speed. Below rated wind speed, the wake of Fig. 4c seems to expand faster than expected by the model (see Fig. 4d). In other studies [12,26], the radial growth of the wake downstream is described with a

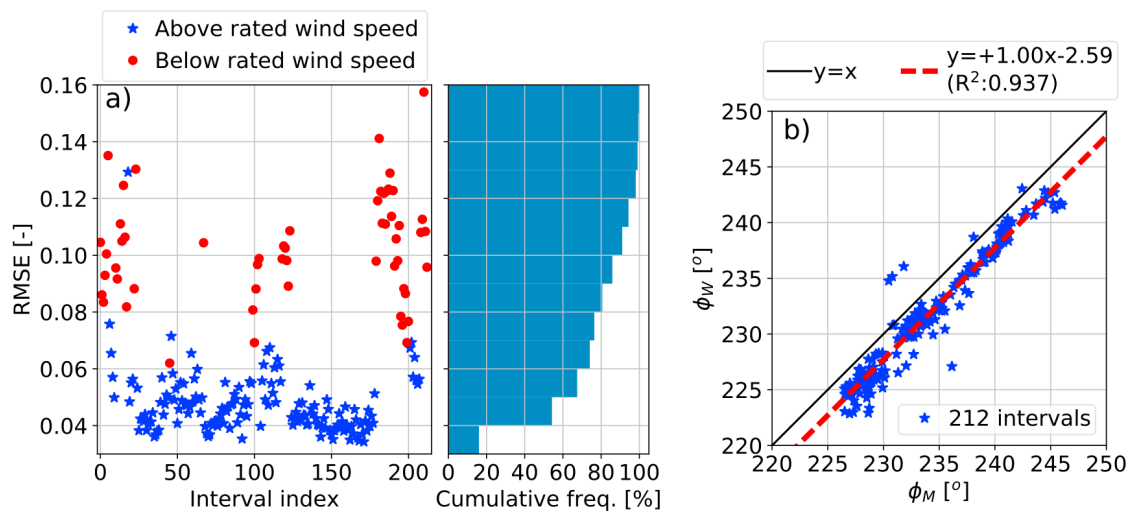


Fig. 3: Root-mean-square error (RMSE) of the least-square fit of the wake model to the data and corresponding number of occurrence (a); Linear regression between the wind direction measured near hub height at the meteorological mast and the wind direction evaluated from the wake model fit (b).

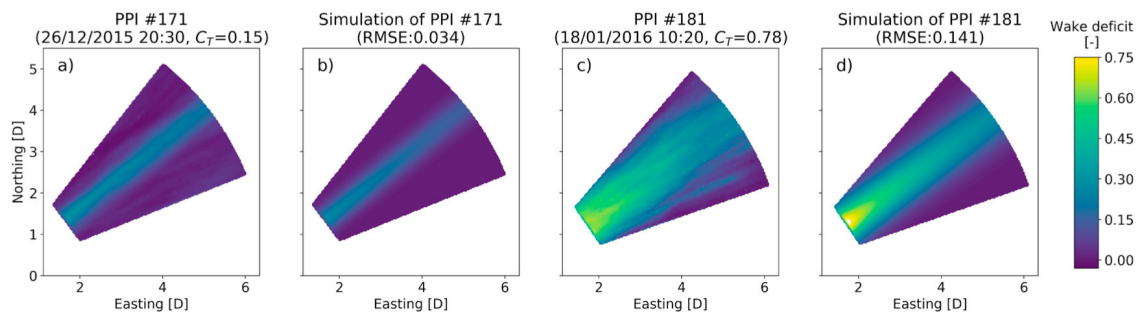


Fig. 4: Visual comparison between wake deficit data evaluated from the lidar measurements (a and c) and the wake deficit calculated with the corresponding fitted model (b and d) for different values of the associated root-mean-square error (RMSE).

power law. In this regard, a similar definition of the wake expansion could fit to wakes which propagate from turbines operating in these conditions better than a linear relationship. The fast expansion of the wake deficit is probably due to the high thrust coefficient applied to the rotor by the turbine operating below rated wind speed. In this condition, high shear characterises the edges of the wake deficit and intensifies the turbulent mixing. Consequently, the recovery and the expansion of the wake are faster.

Also the simple definition of the wake model could be partly responsible for the low RMSE values. In fact, the wake deficit is composed by spatial turbulent structure which cannot be resolved by the Gaussian surface implemented in the model.

As final check of the fit results, we performed a linear regression analysis of the wind and wake directions ϕ_{87} and ϕ_w measured at the mast and returned by the fit respectively. The results exhibit a fair agreement with the coefficient of determination $R^2 = 0.937$ and the slope of the regression line which indicates a perfect correlation. The intercept of the regression line identifies an offset of 2.59° , which is reasonable considering possible uncertainties linked to the vane orientation on the mast or the small yaw misalignment tolerated in this research. Although linear regression methods could be questionable when applied to circular variables, the results of our analysis are still qualitatively representative of the data.

4.2. Fit parameters describing the wake recovery and expansion at different operating conditions

In this section we describe first the results from the fit of the analytical model to the wake data and then we use them to calibrate the parameters implemented in the model.

The wake measurements described in this paper were conducted under different conditions. To better understand the parameters provided by the fit for the analytical wake model, we classified the time intervals according independently to the atmospheric stratification, to the turbulence intensity TI_{96} and to the thrust coefficient C_T . We collected the results in Fig. 5. In the analysis, the atmospheric stratification was defined neutral for values of the potential temperature difference $\Delta\Theta$ between -0.2° and 0.2° , while it was considered unstable and stable for values below and above this range respectively.

Looking at the expansion rate k^* in relation to the atmospheric stratification (Fig. 5, left column) one can notice a reduction moving from neutral to stable conditions. A comparable reduction was observed in the study by Abkar and Porté-Agel[27], who founded $k^* = 0.033$ and $k^* = 0.022$ for wakes reproduced with LES at neutral and stable stratification respectively. These results are in accordance with the expectations considering that stable conditions are characterised by lower turbulent mixing which tends to slow down the recovery and the expansion of the wake.

Following the same argument, we can explain the growth of the expansion rate k^* with increasing turbulence intensity TI (Fig. 5, central column). At higher turbulence levels ($TI > 8\%$), the expansion rate is discontinuous and then drops to an almost constant value. In this range, the scarce availability of data prevent from a generally valid interpretation. Nonetheless, we could relate the discontinuity in the trend to the variations of the corresponding inflow wind speed (Fig. 5, top panel). The comparison shows similar features; in particular, the strong variations are observed when the wind turbines operated near the cut in wind speed. In this conditions, wakes are particularly strong and generate high shear which favours the recovery and the expansion of the wake. This could be one reason of the steep increase of the expansion rate responsible for the discontinuous trend.

Regarding ε , i.e. the parameter defining the initial value of the wake width at $x_W = 0$, specific relationships with the atmospheric stratification or the turbulence intensity are not clearly evident (Fig. 5, left and central column). On the contrary, a much stronger link with the corresponding inflow wind speed (Fig. 5, top panels) can be noticed as in the case of the expansion rate. In fact, an inverse correlation seems to exist between the wind speed and the and the expansion rate when the turbulence intensity or especially the atmospheric stratification are regarded. This connection could be justified by the fact that, at higher wind speeds, as for instance at rated power, the thrust coefficient on the rotor is relatively low and, consequently, also the amplitude of the wake deficit immediately behind it. In this context, the conservation of mass is the reason of the inverse correlation between the wind speed and the initial wake expansion: to lower inflow wind speeds correspond higher amplitudes and larger width of the wake profiles. This explanation is confirmed by the almost monotonic development of ε for an increasing thrust coefficient C_T (Fig. 5, right column).

4.3. Parametrisation of the analytical wake model

After the general discussion about the results, here we address the width of the wake and its the amplitude at the centre of the rotor in relation to the analytical model of section 3 calibrated partly in [17] with LES and wake measurements from a wind tunnel experiment and partly in [3] using the same set of LES wind fields. In the former study, Eq. 6 was modified to better fit the data; in the latter a linear relationship to describe the wake expansion rate k^* as a function of the turbulence intensity TI was derived. Accordingly, the mentioned calibrations of the model prescribe:

$$\begin{aligned}\varepsilon &= 0.2 \sqrt{\beta} \\ k^* &= 0.3837 TI + 0.003678\end{aligned}\tag{9}$$

The wakes in the LES used for this calibration were simulated with an actuator disc model of a Vestas V80-2M (rated windspeed 12 m s^{-1}) wind turbine operating at an inflow wind speed of 9 m s^{-1} at hub height (thrust coefficient $C_T = 0.8$). A neutral atmospheric stratification was reproduced and four different aerodynamic surface roughness lengths were applied leading to different turbulence intensity levels between 4.5% and 13.5% .

Similarly, we analysed the parameters of the model fitted to the wake measurements. For the analysis, we classified our data into categories and considered their average values disregarding categories with less than five entries.

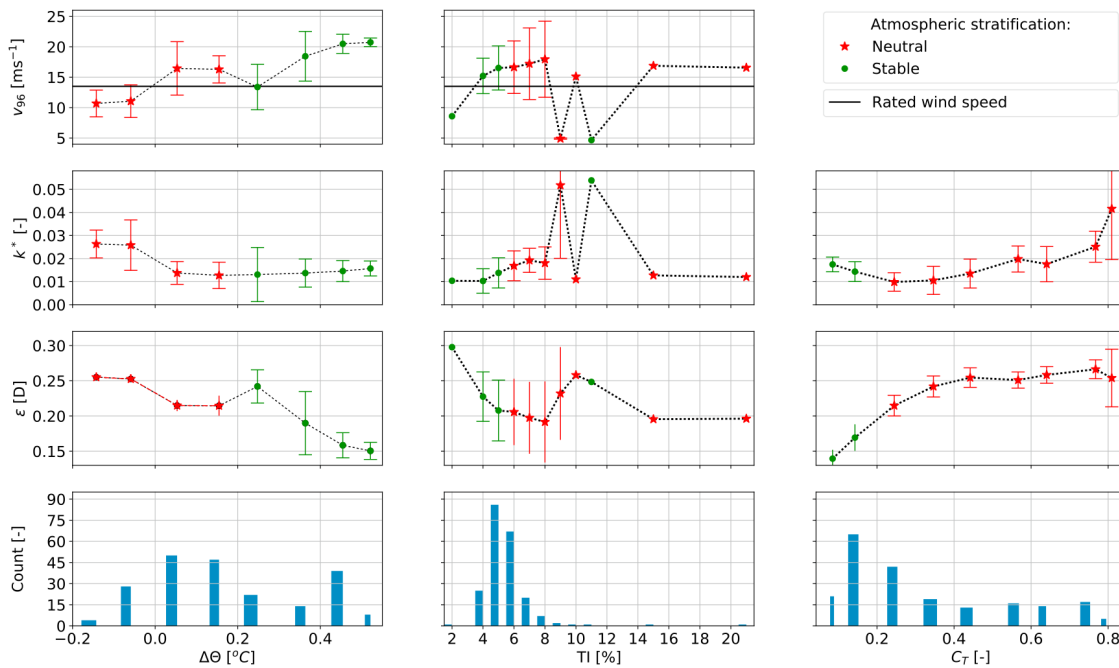


Fig. 5: Variation of the fit parameters as a function of the potential temperature difference ($\Delta\Theta$), of the turbulence intensity (TI) measured at the meteorological mast and of the thrust coefficient (C_T). The graphs report the binned statistics of the fit parameters, namely their average (bullet points), standard deviation (error bars) and number of items in the considered bin (histogram).

In particular, we grouped the results obtained for ε according to different values of $\sqrt{\beta}$ and searched for a linear relationship. As in Eq. 6 no offset was regarded. We considered first all the data; then we divided between cases above and below the rated wind speed V_R . The results are collected in Fig. 6a and in Table 1.

The straight lines passing through the origin fitted to the data are in fair agreement with Eq. 9, but the results seem to well represent the data only for conditions below rated wind speed. We suspect that at high wind speed values, the outer part of the blades is stalled causing the rotor to be effective only over a reduced radius. This could be the reason of the very low values observed for the initial wake width ε in the range $1.015 \leq \sqrt{\beta} < 1.045$, or in terms of thrust coefficient in the interval $0.11 \leq C_T < 0.26$. As shown in Fig. 6a, a two parameters line fits better the data in these operating conditions. For smaller values of $\sqrt{\beta}$, another curve should be considered since, according to Eq.6, β tends to one for C_T values approaching zero and none of the curves reported in this paper can match this behavior.

Using a similar approach, we looked for the linear dependence of the expansion rate k^* on the turbulence intensity. We summarised the results in Table 2 and in Fig. 6b considering, from top to bottom: all conditions, conditions above and conditions below rated wind speed respectively. For similar operating conditions, i.e. for data below rated wind speed, the linear fit results and the previous study calibration described by Eq. 9 are comparable. Considering data above rated wind speed, we found parameters lower than the ones of the previous calibration. This is a relevant results because it extends the applicability of the wake model to this specific operating conditions. The linear fit to all data provided intermediate results with respect to the other two cases.

In Fig. 7, we juxtaposed the amplitude of the wake deficit of Eq. 5 evaluated once with the above calibration and once with the results from our fit at increasing downstream distance at the centre of the wake ($y_W = 0, z_W = 0$). We analysed the calibrations obtained using all data (Fig. 7a) or selecting wind conditions above (Fig. 7b) and below (Fig. 7c) rated wind speed. In the calculations, we applied the corresponding average thrust coefficient and turbulence intensity. The curves visualise how different calibrations could influence the application of the model. Moreover, they confirm the better agreement between our calibration and the previous one for wind conditions below rated wind speed.

From these results, we conclude that the parameters found for situations above rated wind speed could provide a complementary calibration of the model.

Table 1: Results from the fit of the linear curves $\varepsilon = m \sqrt{\beta}$ or $\varepsilon = m \sqrt{\beta} + q$ to the initial wake width at $x_W = 0$ estimated from the lidar measurements.

	Time intervals	Slope (m)	Intercept (q)
All data	180	0.21	-
Above rated wind speed	148	0.21	-
Below rated wind speed	27	0.22	-
$1.015 \leq \sqrt{\beta} < 1.045$	125	2.68	-2.56
$\sqrt{\beta} \geq 1.045$	55	0.22	-

Table 2: Results of the linear fit $k^* = m TI + q$ to the expansion rate values estimated from the lidar measurements.

	Time intervals	Slope (m)	Intercept (q)
All data	205	0.2092	0.0031
Above rated wind speed	154	0.1894	0.0024
Below rated wind speed	50	0.2773	0.0047

5. Conclusion

In addition to more common wind tunnel scaled experiments or high fidelity simulations, the use of full-scale wake measurements performed with a lidar from the nacelle of a wind turbine could improve the accuracy of engineering wake models and of the corresponding wake losses, consequently reducing the uncertainty of a wind farm energy yield estimation.

This paper aims to verify an analytical wake model using full field nacelle-based lidar measurements. Specifically, we analysed the data from an offshore measurement campaign and addressed the model by Bastankhah and Porté-Agel[17] with the calibration by Niayifar and Porté-Agel[3].

Generally, the model fitted the wake measurements well. In terms of root-mean-square error (RMSE), we found relatively high values which reveal the limitation of engineering wake models in describing accurately the spatial turbulent variability of wakes. Nonetheless, even results with the lowest RMSE are meaningful and were used in this research. The RMSE analysis also showed that the wake model performed better for wind turbine operating above rated wind speed.

More in detail, we addressed the initial width of the wake right behind the rotor and its downstream expansion rate. Concerning the initial width in relation to the rotor loading, we found an overall agreement with the theoretical prediction and with the calibration by Bastankhah and Porté-Agel[17]. However, the data with the lowest thrust coefficients are not well represented by the results. For these cases, we described the unexpected width of the wake

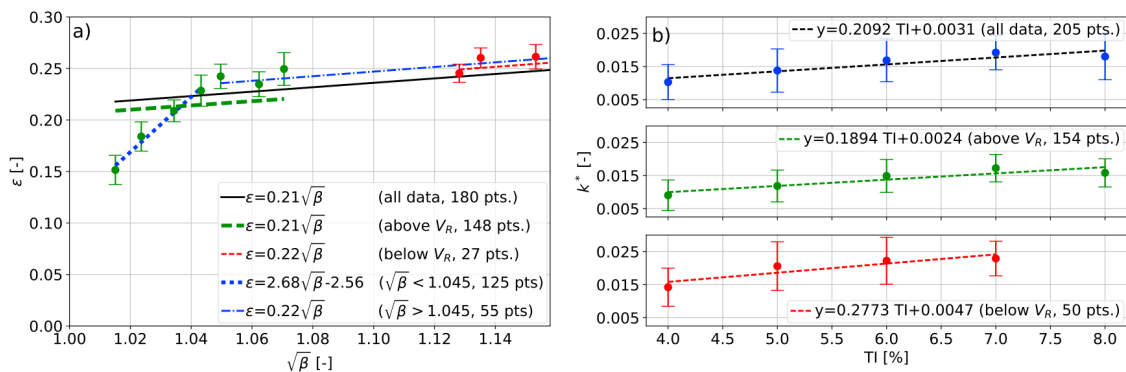


Fig. 6: Dependency of the initial wake width ε on the parameter β (a); Dependency of the wake expansion rate k^* on the turbulence intensity TI (b). The graphs consider operating conditions above and below the wind turbine rated wind speed V_R and report the binned statistics of the wake parameters, namely their average (bullet points) and standard deviation (error bars).

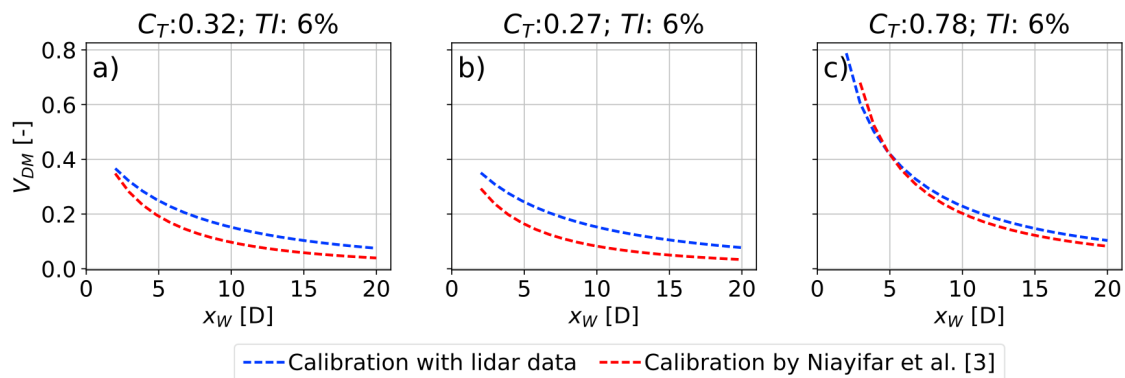


Fig. 7: Comparison between the centre-line wake deficit v_{DM} predicted by the analytical model previously calibrated by Niayifar and Porté-Agel[3] and the one calibrated using the results from the fit of the model and considering all data (a), wind conditions above (b) and below (c) rated wind speed. The curves describe the development of the wake deficit along the downstream coordinate x_w at the centre of the wake.

with a complementary calibration curve. The unforeseen behavior of the wakes in these operating conditions could be explained by the gradual dissolution of wakes occurring when the thrust coefficient approaches zero.

Regarding the expansion rate in relation to the turbulence intensity, we dealt with operating conditions below and above the rated wind speed of the wind turbine respectively. In the former case, we had a low availability of data, but our results are comparable with the linear calibration by Niayifar and Porté-Agel[3]. Since no reference was found for the latter case, our study provides a first calibration for wakes generated by wind turbines operating above rated wind speed. Differently from the other case, the reliability of this result is supported by a relatively large availability of data.

The paper shows that and how full field wake measurements with nacelle-based lidar could be complementary to LES wind fields in the calibration of analytical wake models. Although there might be limitations linked to their time-space resolution and data processing, experiments of this kind are a reliable source of information about the downstream evolution of the wake; they could provide data for a complete survey of real environmental conditions and extend the applicability of the model.

Acknowledgements

The authors would like to acknowledge Innogy for providing access to the wind turbine and the meteorological mast data, Senvion for the technical support during the measurement campaign and the colleagues from the University of Oldenburg who contributed to the realization of the experimental campaign. A particular thanks goes also to Katrin Ritter and Jorge Steiner who helped with the processing of the measurements.

The measurement campaign was funded by the European project FP7-Energy-2011 283145/ClusterDesign, while the German Federal Ministry for Economic Affairs and Energy (BMWi) based on a decision of the Parliament of the Federal Republic of Germany (grant number 0325397A) founded the analysis of the data.

References

- [1] Barthelmie, R.J., Jensen, L.E.. Evaluation of wind farm efficiency and wind turbine wakes at the nysted offshore wind farm. *Wind Energy* 2010;13(6):573–586. doi:10.1002/we.408.
- [2] Walker, K., Adams, N., Gribben, B., Gellatly, B., Nygaard, N.G., Henderson, A., et al. An evaluation of the predictive accuracy of wake effects models for offshore wind farms. *Wind Energy* 2016;19(5):979–996. doi:10.1002/we.1871; wE-14-0212.R2.
- [3] Niayifar, A., Porté-Agel, F. Analytical modeling of wind farms: A new approach for power prediction. *Energies* 2016;9(9):741. doi:10.3390/en9090741.
- [4] Trabucchi, D., Vollmer, L., Kühn, M.. Shear layer approximation of navier-stokes steady equations for non-axisymmetric wind turbine wakes: Description, verification and first application. *Journal of Physics: Conference Series* 2016;753(3):032030. doi:10.1088/1742-6596/753/3/032030.

- [5] Keck, R.E., de Maré, M., Churchfield, M.J., Lee, S., Larsen, G., Madsen, H.A.. Two improvements to the dynamic wake meandering model: including the effects of atmospheric shear on wake turbulence and incorporating turbulence build-up in a row of wind turbines. *Wind Energy* 2015;18(1):111–132. URL: <http://dx.doi.org/10.1002/we.1686>. doi:10.1002/we.1686; wE-12-0166.R2.
- [6] Hancock, P.E., Pascheke, F.. Wind-tunnel simulation of the wake of a large wind turbine in a stable boundary layer: Part 2, the wake flow. *Boundary-Layer Meteorology* 2014;151(1):23–37. doi:10.1007/s10546-013-9887-x.
- [7] Lignarolo, L., Ragni, D., Krishnaswami, C., Chen, Q., Ferreira, C.S., van Bussel, G.. Experimental analysis of the wake of a horizontal-axis wind-turbine model. *Renewable Energy* 2014;70:31 – 46. doi:<http://dx.doi.org/10.1016/j.renene.2014.01.020>; special issue on aerodynamics of offshore wind energy systems and wakes.
- [8] Chamorro, L.P., Porté-Agel, F.. A wind-tunnel investigation of wind-turbine wakes: Boundary-layer turbulence effects. *Boundary-Layer Meteorology* 2009;132(1):129–149. doi:10.1007/s10546-009-9380-8.
- [9] Käsler, Y., Rahm, S., Simmet, R., Kün, M.. Wake measurements of a multi-mw wind turbine with coherent long-range pulsed doppler wind lidar. *Journal of atmospheric and oceanic technology* 2010;27:1529–1532. doi:10.1175/2010JTECHA1483.1.
- [10] Trujillo, J.J., Bingöl, F., Larsen, G.C., Mann, J., Kühn, M.. Light detection and ranging measurements of wake dynamics. part ii: two-dimensional scanning. *Wind Energy* 2011;14(1):61–75. doi:10.1002/we.402.
- [11] Bingöl, F., Mann, J., Larsen, G.C.. Light detection and ranging measurements of wake dynamics part i: one-dimensional scanning. *Wind Energy* 2010;13(1):51–61. doi:10.1002/we.352.
- [12] Aitken, M.L., Banta, R.M., Pichugina, Y.L., Lundquist, J.K.. Quantifying wind turbine wake characteristics from scanning remote sensor data. *J Atmos Oceanic Technol* 2014;31(4):765–787. URL: <http://dx.doi.org/10.1175/JTECH-D-13-00104.1>. doi:10.1175/JTECH-D-13-00104.1.
- [13] Iungo, G.. Experimental characterization of wind turbine wakes: Wind tunnel tests and wind lidar measurements. *Journal of Wind Engineering and Industrial Aerodynamics* 2016;149:35–39. doi:10.1016/j.jweia.2015.11.009.
- [14] Vollmer, L., van Dooren, M., Trabucchi, D., Schneemann, J., Steinfeld, G., Witha, B., et al. First comparison of les of an offshore wind turbine wake with dual-doppler lidar measurements in a german offshore wind farm. *Journal of Physics: Conference Series* 2015;625:012001. doi:10.1088/1742-6596/625/1/012001.
- [15] van Dooren, M.F., Trabucchi, D., Kühn, M.. A methodology for the reconstruction of 2d horizontal wind fields of wind turbine wakes based on dual-doppler lidar measurements. *Remote Sensing* 2016;8(10).
- [16] Dörenkämper, M., Witha, B., Steinfeld, G., Heinemann, D., Kühn, M.. The impact of stable atmospheric boundary layers on wind-turbine wakes within offshore wind farms. *Journal of Wind Engineering and Industrial Aerodynamics* 2015;144:146 – 153. doi:<http://dx.doi.org/10.1016/j.jweia.2014.12.011>; selected papers from the 6th International Symposium on Computational Wind Engineering (CWE) 2014.
- [17] Bastankhah, M., Porté-Agel, F.. A new analytical model for wind-turbine wakes. *Renewable Energy* 2014;70:116 – 123. doi:<http://dx.doi.org/10.1016/j.renene.2014.01.002>; special issue on aerodynamics of offshore wind energy systems and wakes.
- [18] Cariou, J.P.. *Remote Sensing for Wind Energy*; chap. 6. Pulsed Lidar. DTU Wind Energy; 2015, p. 131–148.
- [19] Taylor John, R.. *An introduction to error analysis*. University Science Books; 1997. ISBN 093570275X.
- [20] JCGM WG1, . *Evaluation of measurement data — guide to the expression of uncertainty in measurement*. 2008.
- [21] Beck, H., Kühn, M.. Dynamic data filtering of long-range doppler lidar wind speed measurements. *Remote Sensing* 2017;9(6).
- [22] Trabucchi, D., Trujillo, J.J., Bitter, M., Kühn, M.. Application of staring lidars to study the dynamics of wind turbine wakes. *Meteorologische Zeitschrift* 2014;:557 – 564doi:10.1127/metz/2014/0610.
- [23] Keane, A., Aguirre, P.E.O., Ferchland, H., Clive, P., Gallacher, D.. An analytical model for a full wind turbine wake. *Journal of Physics: Conference Series* 2016;753(3):032039. doi:10.1088/1742-6596/753/3/032039.
- [24] Jones, E., Oliphant, T., Peterson, P., et al. *SciPy: Open source scientific tools for Python*. 2001–. URL: <http://www.scipy.org/>; [Online; accessed ;today;].
- [25] Ainslie J., F.. Calculating the flowfield in the wake of wind turbines. *Journal of Wind Engineering and Industrial Aerodynamics* 1988;27:213–224. doi:10.1016/0167-6105(88)90037-2.
- [26] Frandsen, S., Barthelmie, R., Pryor, S., Rathmann, O., Larsen, S., Højstrup, J., et al. Analytical modelling of wind speed deficit in large offshore wind farms. *Wind Energy* 2006;9(1-2):39–53. doi:10.1002/we.189.
- [27] Abkar, M., Porté-Agel, F.. Influence of atmospheric stability on wind-turbine wakes: A large-eddy simulation study. *Physics of Fluids* 2015;27(3):035104. URL: <http://dx.doi.org/10.1063/1.4913695>. doi:10.1063/1.4913695. arXiv:<http://dx.doi.org/10.1063/1.4913695>.

Chapter 6

3-D shear-layer model for the simulation of multiple wind turbine wakes

Description and first assessment

The content of this chapter consists of the

JOURNAL ARTICLE

Wind Energ. Sci. 2 (2017) 569-586

Main Author

©2017 The Authors

Reproduced under the Creative Commons Attributions-NonCommercial-
ShareAlike 3.0 Unported ([link](#))

included in the special issue dedicated to the Science of Making Torque from Wind
Conference hold in Munich, Germany, in October 2016.

Wind Energ. Sci., 2, 569–586, 2017
<https://doi.org/10.5194/wes-2-569-2017>
© Author(s) 2017. This work is distributed under
the Creative Commons Attribution 3.0 License.



3-D shear-layer model for the simulation of multiple wind turbine wakes: description and first assessment

Davide Trabucchi, Lukas Vollmer, and Martin Kühn

Institute of Physics, University of Oldenburg, ForWind, K pkersweg, 70, 26129 Oldenburg, Germany

Correspondence to: Davide Trabucchi (davide.trabucchi@uni-oldenburg.de)

Received: 2 January 2017 – Discussion started: 6 February 2017

Revised: 22 September 2017 – Accepted: 2 October 2017 – Published: 22 November 2017

Abstract. The number of turbines installed in offshore wind farms has strongly increased in the last years and at the same time the need for more precise estimations of the wind farm efficiency too. In this sense, the interaction between wakes has become a relevant aspect for the definition of a wind farm layout, for the assessment of its annual energy yield and for the evaluation of wind turbine fatigue loads. For this reason, accurate models for multiple overlapping wakes are a main concern of the wind energy community. Existing engineering models can only simulate single wakes, which are superimposed when they are interacting in a wind farm. This method is a practical solution, but it is not fully supported by a physical background. The limitation to single wakes is given by the assumption that the wake is axisymmetric. As an alternative, we propose a new shear-layer model that is based on the existing engineering wake models but is extended to also simulate non-axisymmetric wakes. In this paper, we present the theoretical background of the model and four application cases. We evaluate the new model for the simulation of single and multiple wakes using large-eddy simulations as reference. In particular, we report the improvements of the new model predictions in comparison to a sum-of-squares superposition approach for the simulation of three interacting wakes. The lower deviation from the reference considering single and multiple wakes encourages the further development of the model and promises a successful application for the simulation of wind farm flows.

1 Introduction

When the wind passes through the wind turbine rotor, kinetic energy is extracted from the wind and is converted into electrical power. The reduced kinetic energy is revealed by a wake deficit behind the rotor, i.e. a shear flow with lower speed and higher turbulent fluctuations than in the free flow upstream and sideways.

In this sense, wakes are the main cause of power losses in wind farms (Walker et al., 2016). In addition, wakes hitting a downstream turbine contribute to the increase in the fatigue loads of its components. For these reasons, wake modelling plays a major role in the definition of the layout of wind farms, in the evaluation of their annual energy yield and in the estimation of the lifetime of wind turbine components. Consequently, more accurate wake models can indirectly contribute to the cost-of-energy reduction thanks to more tailored design of wind turbines and wind farms.

Despite the large progress especially in the numerical modelling, Vermeer et al. (2003) still provide a comprehensive review of traditional wake modelling. Most of the engineering models described in their work evaluate the wind field of a single wake and combine the individual results in case of mutual interaction. More sophisticated computational fluid dynamics (CFD) such as Reynolds-averaged Navier–Stokes (RANS) equations or large-eddy simulations (LESs) can provide more realistic results because the physics of the flow is resolved up to more refined length and timescales. However, these alternatives have a much higher computational cost and can therefore become prohibitive for design applications.

Engineering tools for estimating wake effects in a wind farm often implement the steady-state, axisymmetric shear-layer approximation of the RANS equations, e.g. the one used in the Ainslie model (Ainslie, 1988). Due to the axial symmetry assumption, only the wind deficit of single

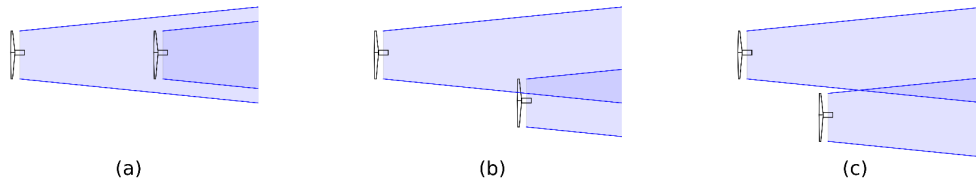


Figure 1. Different cases of merging wakes: (a) aligned wakes, (b) wake–turbine interaction and (c) wake–wake interaction.

wakes or wakes aligned on the same axis as those illustrated in Fig. 1a can be simulated with such models. For the case of wake–turbine or wake–wake interaction, shown in Fig. 1b and c, pragmatic methods are required. In the kinematic model by Katic et al. (1986), the square addition of the individual wake deficits is applied to deal with multiple wakes. In a previous study, Lissaman (1979) proposed the linear addition of the deficits; however, this method tends to overestimate the velocity reduction and could lead to unrealistic flow reversal when many wakes merge.

Machefaux (2015) compared the performance of the linear approach with the one of the square wake addition approach and noticed that the former is to be preferred for wakes of turbines operating at low thrust coefficients, while the latter returns better results in the opposite case. From this observation, he developed a wake superposition model that combines the linear and square additions of single wakes using a weighted average depending on the thrust on the rotor.

Crespo et al. (1999) declared that the classical wake superposition methods do not rely on a physical background and, if not handled properly, could lead to unrealistic results. This statement was motivation of this paper. In this regard, we aim to investigate whether a more detailed physical model could improve the simulation of multiple wakes. For this purpose, we pick up the suggestion by Ainslie (1988) to extend his model to the third dimension, dropping the hypothesis of an axisymmetric wake profile; accordingly, we develop the 3-D shear-layer (3DSL) model and test its performance in relation to Ainslie’s model and the square addition approach. For the assessment, we address four cases including a single wake, aligned wakes, and wake–turbine and wake–wake interaction; we use the wind fields extracted from LESs of the same wake conditions as reference and consider the section-average wind speed and the RMSE as figures of merit.

2 Model description

In the following the theoretical background of the 3DSL model is provided along with the description of its numerical implementation. Moreover, it is explained how to evaluate the parameters needed to apply the model.

2.1 Mathematical definition

The 3DSL model is meant to add the third dimension to the shear-layer approximation of the steady RANS equations for wind turbine wake simulations first described by Ainslie (1988), maintaining all his assumptions but the one of an axisymmetric wake profile. The 3DSL model is intended to simulate the development in the wake of the normalised wind velocity u_D , which can be defined as

$$u_D(x, y, z) = 1 - \frac{u_i(z) - u(x, y, z)}{u_H} \quad (1)$$

using a representative vertical profile of the inflow wind speed u_i , the corresponding hub height value u_H and the wind speed u at the desired position. For sake of brevity we will refer to u_D simply as wake velocity in the following. The 3DSL model is generally valid starting from a downstream distance at which the pressure gradient in the stream-wise direction is negligible. Moreover, the viscous term is not considered and no external forces are applied.

Different from other existing shear-layer models, our 3DSL approach is not formulated in a polar coordinate system, but considering a Cartesian frame of reference, i.e. the stream-wise wake velocity u_D , the cross-stream, and the vertical wind components v and w are defined along the downstream x , lateral y and upward z axes respectively. In the same way as u_D , the two latter wind components are also normalised by u_H .

Considering a dimensional analysis (Cebeci and Cousteix, 2005), the steady RANS equation for flows with a shear layer along the cross-stream and vertical component can be simplified to

$$\begin{cases} \frac{\partial u_D}{\partial x} + \frac{\partial v}{\partial y} + \frac{\partial w}{\partial z} & = 0 \\ u_D \frac{\partial u_D}{\partial x} + v \frac{\partial u_D}{\partial y} + w \frac{\partial u_D}{\partial z} & = - \left(\frac{\partial \overline{u'v'}}{\partial y} + \frac{\partial \overline{u'w'}}{\partial z} \right) \\ \frac{\partial p}{\partial y} = \frac{\partial p}{\partial z} & = 0 \end{cases} \quad (2)$$

The shear stress terms on the right-hand side of the second line of Eq. (2) can be modelled by means of an eddy viscosity closure introducing the eddy viscosities ϵ_y and ϵ_z and multiplying them by the corresponding cross-stream and vertical

gradients of u_D :

$$\begin{aligned} \overline{u'v'} &= -\epsilon_y \frac{\partial u_D}{\partial y} \\ \overline{u'w'} &= -\epsilon_z \frac{\partial u_D}{\partial z} \end{aligned} \quad (3)$$

Further details on the eddy viscosity model are provided in Sect. 2.4.

At this point, the system of Eq. (2) is still under-determined. To balance the unknown variables and the equations, we assume that the wind components v and w define a conservative vector field in all the cross sections $y-z$. A potential function Φ can therefore be defined such that

$$\begin{cases} \frac{\partial \Phi}{\partial y} = v \\ \frac{\partial \Phi}{\partial z} = w \end{cases} \quad (4)$$

Concerning multiple wakes, this assumption does not imply any limitation since a vector field resulting from the superposition of conservative vector fields is still conservative. However, this assumption limits the domain of possible solutions. For instance, swirling wakes in which the tangential velocity is inversely proportional to the distance from the rotation axis are accepted, while wakes rotating as a rigid body are not.

The hypothesis of a potential flow is implicit in the axial symmetry imposed by Ainslie. In his model, he considered a cylindrical coordinate system defined by the radial coordinate r , the angular coordinate θ and the axial coordinate x . The corresponding velocity vector field $\mathbf{V}(r, \theta, x) = (v_r, v_\theta, u)$ is conservative only if $\nabla \times \mathbf{V} = 0$. Considering the individual cross-section planes at a certain x coordinate, it implies that $\partial v_r / \partial \theta - \partial v_\theta / \partial r = 0$. This equation is always satisfied by the Ainslie model in which the tangential velocity v_θ is neglected and the radial velocity v_r does not vary along the angular coordinate θ when a constant radial distance r is considered.

The explanation above shows that, like the 3DSL model, the Ainslie model also assumes a potential flow and therefore no vorticity on the cross sections $y-z$. In the vortex cylinder model of the actuator disc (Burton et al., 2011), the flow field of a wind turbine wake is conservative everywhere but on the surface of the vortex cylinder that encloses the wake, along the root vortex and on the bound vortex sheet swept by the rotor blades. Accordingly, our approximation to a potential flow is reasonable for most of the simulation domain and, even if the real flow is not strictly conservative, the 3DSL model enables us to find one of the solutions for the under-determined, three-dimensional shear-layer problem that respects the conservation of mass and the momentum balance in the stream-wise direction.

Thanks to Eq. (4) and considering that, at each individual vertical cross section, $\partial u_D / \partial x$ depends only on y and z , the

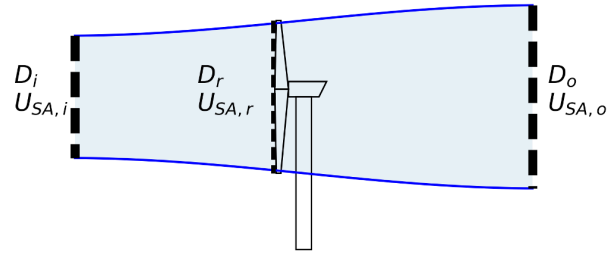


Figure 2. Sketch of the stream tube used to describe the disc actuator approach. The dashed lines represent the inflow, rotor and outlet cross sections, which are indicated with the subscripts i , r and o in the definition of the diameter D and the section-average wind speed U_{SA} .

conservation of mass (Eq. 2, first line) can be expressed as

$$\frac{\partial^2 \Phi}{\partial y^2} + \frac{\partial^2 \Phi}{\partial z^2} = -g, \quad (5)$$

where $g(y, z) = \partial u_D / \partial x$. This formulation is a second-order elliptic partial differential equation of the Poisson type, which can be solved numerically.

Considering the aforementioned assumptions, the final formulation of the 3DSL model can be summarised as

$$\begin{cases} \frac{\partial^2 \Phi}{\partial y^2} + \frac{\partial^2 \Phi}{\partial z^2} = -g \\ g = \frac{\partial u_D}{\partial x} \\ \frac{\partial \Phi}{\partial y} = v \\ \frac{\partial \Phi}{\partial z} = w \\ u_D \frac{\partial u_D}{\partial x} + v \frac{\partial u_D}{\partial y} + w \frac{\partial u_D}{\partial z} = \epsilon_y \frac{\partial^2 u_D}{\partial y^2} + \epsilon_z \frac{\partial^2 u_D}{\partial z^2} \end{cases} \quad (6)$$

2.2 Numerical implementation

The 3DSL model is implemented using finite difference schemes to obtain the numerical formulation of the physical model defined in Eq. (6). Stream-wise gradients are approximated with a forward finite difference scheme, while a central one is used for the gradient in the other directions. The solution of the wind field on each consecutive cross section is accomplished with the following steps:

1. approximation of the stream-wise gradient $g = \partial u_D / \partial x$ from the stream-wise momentum balance (Eq. 6, fifth line) evaluated on the previous cross section,
2. computation of the potential function Φ on the previous cross section solving the Poisson equation (Eq. 6, first line),

572

3. correction of v and w on the previous cross section with the values derived from the definition of Φ (Eq. 6, third and fourth lines),
4. reiteration of the cycle from step 2 until sufficient convergence of v and w is reached,
5. evaluation of u_D on the current section by means of numerical integration of Eq. (6), second line.

For the initial condition on the first cross section, a disc actuator model can be applied to estimate u_D , while v and w are set to zero. The vertical cross sections $y-z$ are defined by a regular grid with spacing $\Delta y = \Delta z = h$; the resolution Δx along the x axis is evaluated at each cross section. This is needed to accomplish the stability constraints of the numerical solution. In fact, the stream-wise momentum balance (Eq. 6, fifth line) is similar to the much simpler problem

$$\frac{\partial \zeta(y, z, t)}{\partial t} = \left(\frac{\partial^2 \zeta(y, z, t)}{\partial y^2} + \frac{\partial^2 \zeta(y, z, t)}{\partial z^2} \right) \mu. \quad (7)$$

The solution of this problem with a so-called forward-time central-space finite difference scheme is numerically stable only if $\mu \Delta t / h^2 \leq \frac{1}{4}$, where Δt and $h = \Delta y = \Delta z$ are the time and space discretisation increments respectively and μ is the diffusive parameter of the problem (Press et al., 2007, chap. 20.5). Inspired by this constraint, we conservatively define the downstream step size at each cross section as

$$\Delta x = \frac{\min(u_D) h^2}{4 \max(\epsilon_{y,z})}. \quad (8)$$

The boundary conditions are assigned in two different ways: periodic conditions are applied to solve the Poisson equation (Eq. 6, first line), while, for the solution of the stream-wise momentum balance (Eq. 6, fifth line), u_D is set as in the initial conditions on the boundaries.

2.3 Model initialisation

To run simulations with the 3DSL model it is necessary to initialise it with the wind field at the downstream outlet of the induction zone of the rotor, i.e. the region where the pressure field is influenced by the operation of the wind turbine. In fact, as explained in Sect. 2.1, the 3DSL model is not valid in the near field behind the rotor where the pressure gradients have a major influence on the flow.

Werle (2015) and Madsen et al. (2010) suggested possible methodologies suitable for this purpose. Here, we apply a classic disc actuator approach (Burton et al., 2011) to estimate the initial wake velocity $u_{D,o}$ at the outlet of the induction zone.

We consider the stream tube depicted in Fig. 2 and defined by the cross sections at the inlet, at the rotor and at the outlet of the induction zone. We indicate the corresponding diameters as D_i , D_r and D_o respectively. We use the same subscripts for the section-averaged wind speed U_{SA} and for the

D. Trabucchi et al.: 3-D shear-layer simulation model

stream-wise wind component u . Following the disc actuator theory, we assume that

- U_{SA} is homogeneous on each cross section of the stream tube,
- the induction factor a defined by the thrust coefficient C_T as in Eq. (16) regulates the evolution of U_{SA} through the stream tube such that

$$a = 1 - \frac{U_{SA,r}}{U_{SA,i}} = \frac{1}{2} \left(1 - \frac{U_{SA,o}}{U_{SA,i}} \right). \quad (9)$$

According to the conservation of mass of an incompressible flow across the stream tube (see Fig. 2), we can combine

$$U_{SA,i} D_i^2 = U_{SA,r} D_r^2 = U_{SA,o} D_o^2 \quad (10)$$

with Eq. (9) to calculate the inlet and the outlet cross-section diameters of the stream tube:

$$\begin{aligned} D_i &= D_r \sqrt{(1-a)} \\ D_o &= D_r \sqrt{\frac{(1-a)}{(1-2a)}} = D_i \sqrt{1-2a}. \end{aligned} \quad (11)$$

The initial conditions $u_{D,o}$ for the 3DSL model are calculated in three steps: first, we estimate the wind speed u_o at the outlet as

$$\begin{cases} u_o = u_i (1-2a) & \text{on the inlet cross section} \\ u_o = u_i & \text{outside the inlet cross section} \end{cases}, \quad (12)$$

applying the induction factor a to the inflow wind speed u_i on the inlet cross section of the stream tube homogeneously. Then, the wind field is expanded according to Eq. (11). Finally, the initial wake velocity $u_{D,o}$ is given, replacing u with u_o in Eq. (1).

To calculate the stream tube cross sections and the corresponding average wind speeds, this method needs to be applied iteratively until convergence. In fact, the induction factor a has to be known. Usually, it can be derived from the thrust coefficient C_T associated with the undisturbed wind speed at inlet of the stream tube according to the wind turbine specification. In the case described here, the undisturbed wind speed is defined as average over the inlet cross section by $U_{SA,i}$, which in turn is dependent on the induction factor a (see Eq. 11). For this reason, an iterative process is applied starting with the rotor diameter D_r as a first guess to approximate the diameter D_i of the inlet cross section.

As already mentioned, shear-layer wake models are valid only outside the induction zone. However, Madsen et al. (2010) noticed that the turbulent mixing influences the wake velocity profile already within this region. Therefore, they simulated wakes with their shear-layer model starting from the rotor position. To compensate for the effect of pressure gradients not included in their model but actually present in

D. Trabucchi et al.: 3-D shear-layer simulation model

573

reality until two to three rotor diameters downstream of the turbine, they applied a linear filter to the ambient eddy viscosity within this range. In the same way, the 3DSL model also first evaluates the wake velocity outside the induction zone to initialise the wake simulation, which in turn starts directly behind the rotor. Then, it applies the linear filter

$$\begin{cases} F_2 = \frac{x/D_r}{2.5} & \text{for } 0 < x \leq 2.5D_r \\ F_2 = 1 & \text{for } x > 2.5D_r \end{cases} \quad (13)$$

to the ambient eddy viscosity to mimic the effects of the pressure gradients within the near wake.

2.4 Eddy viscosity model

In the 3DSL model, the eddy viscosity is evaluated following the approach suggested by Ainslie (1988), who combined the contribution of the wake and of the atmosphere. Experimentally, he found that the proportionality coefficient $k = 0.015$ links the wake contribution to r_i and u_{ai} , which are the characteristic length and velocity scales of turbulent fluctuations within a wake in the cross-wise and vertical directions for $i = y, z$ respectively. Furthermore, he introduced the filter function¹

$$F_1 = \begin{cases} 0.65 + \left[\frac{(x/D_r - 4.5)^{1/3}}{23.32} \right] & 0 < x \leq 5.5D_r \\ 1 & x > 5.5D \end{cases} \quad (14)$$

to properly modulate the development of the turbulence generated by the shear layer within the wake.

To model the effect of the atmospheric conditions on the eddy viscosity, Ainslie used the momentum flux profile $\Phi_m(z_H/L_{MO})$ as a function of the wind turbine hub height z_H and of the Monin–Obukhov length L_{MO} (Dyer, 1974), the von Kármán constant κ and the friction velocity u_* .

Based on the definitions above, in the complete eddy viscosity model

$$\begin{aligned} \epsilon_i(x, y, z) &= \frac{F_1(x)k r_i(x) u_{ai}(x, y, z)}{\Phi_m(z/L_{MO})} \\ &+ \frac{F_2(x)\kappa u_* z}{\Phi_m(z/L_{MO})} \text{ for } i = y, z, \end{aligned} \quad (15)$$

the first and second addends represent the wake and atmospheric contributions respectively. As explained in Sect. 2.3, the filter function F_2 was added following the example by Madsen et al. (2010) to compensate for the pressure effect within the near wake when the 3DSL model is initialised at the rotor position.

In Eq. (15) we indicate the spatial dependence of the parameters because we want to stress the fact that, thanks to the three dimensions resolved by the model, the eddy viscosity does also not need to be axisymmetric anymore and can

¹In Eq. (14) the rational exponent 1/3 indicates the real cube root of the corresponding base.

be defined locally. For instance, it can vary linearly over the height z or depend on the local strain rates of the wind field, as it will be explained in Sect. 2.4.1.

2.4.1 Characteristic scales of turbulent fluctuations within wakes

In the 3DSL model, the characteristic turbulence length scales r_y and r_z are both approximated with a representative wake radius $r(x)$ derived as a function of the normalised downstream distance x and the thrust coefficient C_T using the analytical wake model by Frandsen et al. (2006) and revised by Rathmann et al. (2006) as

$$\begin{aligned} r(x) &= [\max(\beta, 0.7x/D_r)]^{0.5} \quad \text{where} \\ \beta &= \frac{1-a}{1-2a} \quad \text{and} \\ a &= \frac{1-\sqrt{1-C_T}}{2} \end{aligned} \quad (16)$$

In case of multiple wakes, only the turbine closest to the cross section considered is regarded in the evaluation of $r(x)$ within the overlapping area.

On each cross section, we define the local characteristic turbulence velocity scale u_{ai} as a function of the position $\mathbf{P} = (x, y, z)$. For this purpose, the local characteristic velocity scale is derived with the classic turbulence mixing length theory (Pope, 2000), similarly as in the model by Keck et al. (2012). Accordingly, the turbulent velocity scales

$$u_{ai}(\mathbf{P}) = u'_{Di}(\mathbf{P}) r(x) \text{ for } i = y, z \quad (17)$$

are modelled by means of the local strain rates of the wake velocity $u'_{Dy}(\mathbf{P}) = \left. \frac{\partial u_D}{\partial y} \right|_{\mathbf{P}}$ and $u'_{Dz}(\mathbf{P}) = \left. \frac{\partial u_D}{\partial z} \right|_{\mathbf{P}}$ together with the turbulence length scale approximated with $r(x)$ in the direction considered.

2.5 Multiple wakes

The 3DSL model is suited for simulation of multiple wakes and does not require the addition of individual wakes to resolve the wind field where wakes from different turbines are overlapping. Still, for simulations of multiple wakes it has to deal with the definition of the inflow wind field of a wind turbine hit by other wakes. This is a delicate matter because it generates a sort of conflict between the actuator disc model used for the initialisation of the 3DSL model and the recovery of the wake within the upstream induction zone of the downstream turbine.

The induction zone, that is, the region directly affected by the pressure gradients across the rotor, already begins in the inflow. For instance, the IEC 61400-12-1 standard for power performance measurements suggests measuring the wind speed of the free inflow at least two rotor diameters upstream from the wind turbine. Power performance measurements exclude the case of wind turbines operating in

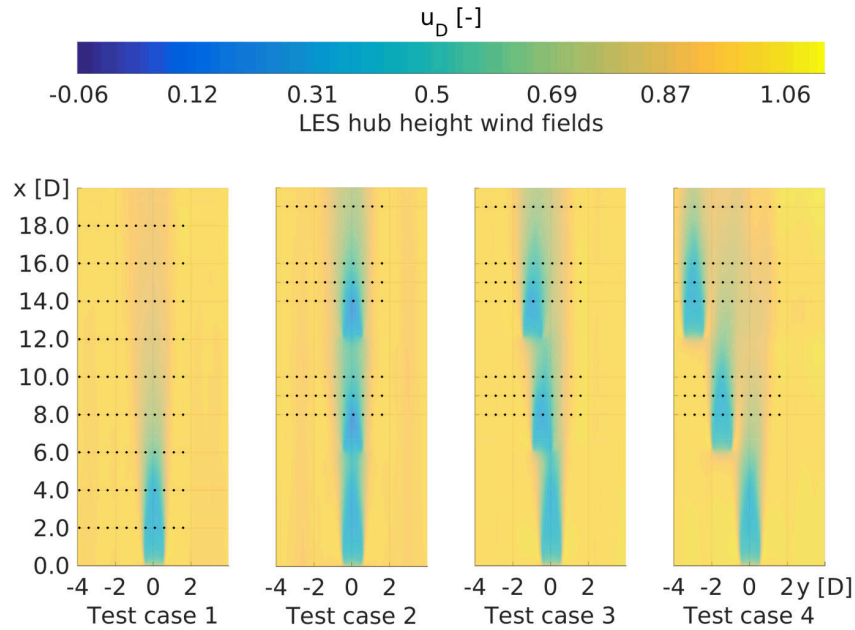


Figure 3. Colour map of the hub height wake velocity u_D evaluated for the test cases from the large-eddy simulations (LESs). The black dots indicate the position of the virtual turbine rotors used to compare the simulation results.

wakes. We could have followed this indication anyway, but we would have disregarded the recovery of the wake.

When a wind turbine operates within a wake, the 3DSL model uses the wind field on the rotor cross section as the inflow in the evaluation of the section-average wind speed $U_{SA,i}$. Doing this it neglects the effect of the induction zone upstream of the wind turbine, but this is necessary in order to consider the recovery of the wake. Recent studies that investigate how to model the induction zone upstream of the wind turbine rotor (Meyer Forsting et al., 2016) could provide tools to improve this pragmatic approach, but it is out of the scope of the present work.

3 Wake simulations

In this section we consider single and multiple wind turbine wakes from LES wind fields as a reference to evaluate and compare results from simulations carried out with the 3DSL model and with the Ainslie model as implemented in the wind farm layout software FLaP (Lange et al., 2003). In the latter case we apply the square addition approach to multiple wakes. Accordingly, the total wake velocity resulting from the overlapping of the consecutive wakes is assumed as

$$u_D = \sqrt{1 - \sum_i (1 - u_{D,sw_i})^2}, \quad (18)$$

where u_{D,sw_i} is the wake velocity of the i th single wake. The comparison includes three cases of multiple wakes (namely

aligned wakes and wake–turbine and wake–wake interactions), preceded by a single-wake simulation.

3.1 Test cases and reference wind fields

All the test cases are simulated with the same atmospheric conditions and as a reference consider wakes generated with the LES model implemented in PALM (Raasch and Schröder, 2001), whose solver is coupled with an actuator disc model (Calaf et al., 2010). These LES wind fields deal with wakes from the Siemens SWT-3.6-120 wind turbine (120 m rotor diameter D , 90 m hub height z_H). In the test cases two, three and four, the turbines are placed with a consecutive downstream displacement of $6D$ and a cumulative separation in the cross-stream direction of $0.0D$, $0.5D$ and $1.5D$ respectively. These layouts lead to the hub height maps of the wake velocity displayed in Fig. 3.

The wind field is evaluated on a uniform grid with a spatial resolution of 10 m ($0.083D$) and a total domain size of approximately 20, 5 and 3.5 km along the stream-wise, cross-stream and vertical axes respectively. The reference wind field results from the temporal average of 45 min simulations with a time step close to 1 s. With a roughness length $z_0 = 0.002$ m and a vertically constant potential temperature, the wind conditions should resemble a typical offshore boundary layer in neutral stratification ($\Phi_m(z_H/L_{MO}) = 1$). The friction velocity u_* evaluated fitting the logarithmic profile $u = (u_*/\kappa) \ln(z/z_0)$ to the average vertical profile of the wind speed on the inflow section is about 0.3 ms^{-1} . Un-

Table 1. Overall performance of the 3DSL model and FLaP (Ainslie model) in relation to the reference large-eddy simulation wind field. Namely, the average deviation $\bar{\Delta}_{\text{RAWS}}$ of the rotor-average wind speed, the total root mean square error \bar{E}_{RMS} , the coefficient of determination R^2 , the corresponding regression line slope A and intercept B are included.

		Test case 1		Test case 2		Test case 3		Test case 4	
		3DSL	FLaP	3DSL	FLaP	3DSL	FLaP	3DSL	FLaP
$\bar{\Delta}_{\text{RAWS}}$	[-]	0.20	0.20	0.17	0.23	0.17	0.38	0.17	0.29
$\bar{E}_{\text{RMS}}/u_{\text{H}}$	[-]	0.27	0.29	0.31	0.31	0.29	0.48	0.34	0.46
R^2	[-]	0.93	0.92	0.95	0.97	0.96	0.96	0.94	0.90
A	[-]	0.83	0.79	1.02	0.85	0.95	0.72	0.86	0.77
B	[ms ⁻¹]	1.31	1.57	-0.07	1.21	0.37	2.15	0.95	1.68

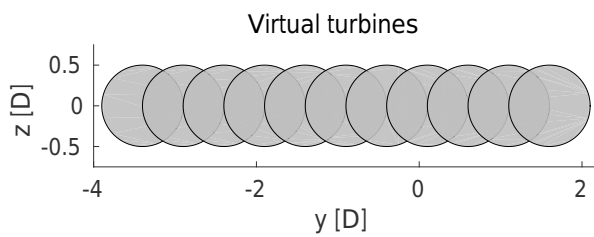


Figure 4. Illustrative sketch of the rotors of the virtual turbines considered to assess the performance of the engineering models in relation to the large-eddy simulations.

der these conditions, the hub height wind speed $3.3 D$ upstream of the first rotor is 8 m s^{-1} with 5 % turbulence intensity TI. According to this inflow wind speed, the wind turbines are operating in partial load with a thrust coefficient² $C_T = 0.858$.

3.2 Simulations with the shear-layer models

The simulation domains of the 3DSL and of the Ainslie model are different. In the first case, the cross sections are resolved with 111 and 81 points in the lateral and vertical directions respectively, extend from $y = -7$ to $y = +3 D$ and are $8 D$ high. The adaptive step in the downstream direction leads to 2291 points from $x = 0$ to $x = 20 D$. With these settings, the simulation of three wind turbine wakes takes about 11 s.

In FLaP, we impose the initial condition taking into account the turbulence intensity, the thrust coefficient and the tip speed ratio of the turbine according to Lange et al. (2003). Additionally, for test case 2 and test case 3, we consider the turbulence added by the wake following the empirical formula suggested by Hassan (1992) as reported in Burton et al. (2011).

For the simulation of a single wake with FLaP, 181 points are considered along the downstream direction from $x = 2$ to

²This value comes from a report generated by the software WindPRO 3.0.629 by EMD International A/S.

$x = 20 D$; the radial coordinate counts 20 000 points in the range from 0 to $7 D$. The enormous number of points in the radial direction is dictated to achieve a convergent result with a downstream step close the one of the LES wind field. This simulation set-up requires a computational time of about 6 s for a single wake.

The computational times reported above refer to simulations performed on one core of a 2.7 GHz standard processor with 16 GB of RAM available, using MATLAB R2016a for the 3DSL model and a compiled Fortran implementation of the Ainslie model for FLaP.

4 Results

For a quantitative assessment of the results, we sample the wind fields using several virtual turbines of the same type as the one used for the simulations; their rotors are centred on the black dots printed in the wind fields of Fig. 3. An illustrative sketch of a row of the virtual turbine rotors is given in Fig. 4.

With regard to the virtual turbine rotor j , to the corresponding N_j grid points and in relation to the reference stream-wise wind component u_{ref} , we analyse

- the relative deviation of rotor-average wind speed (RAWS)

$$\Delta_{\text{RAWS}, j} = \frac{\sum_{i=1}^{N_j} u_i}{\sum_{i=1}^{N_j} u_{\text{ref}, i}} - 1 \quad (19)$$

- the RMSE

$$\bar{E}_{\text{RMS}, j} = \sqrt{\frac{\sum_{i=1}^{N_j} (u_i - u_{\text{ref}, i})^2}{N_j}} \quad (20)$$

576

- the linear regression of the stream-wise wind component values on the grid points within the rotor area.

On the one hand, the first two figures of merit are individually considered for each virtual turbine. On the other hand, we calculate the overall values $\overline{\Delta}_{\text{RAWS}}$ and $\overline{E}_{\text{RMS}}$, averaging the absolute values $\Delta_{\text{RAWS}, j}$ for the former and considering all virtual turbines at once in the calculation of the RMSE for the latter. These overall values are collected in Table 1.

The three methods of evaluation are related, but each has its own specific character. The RAWS is often used as parameter to evaluate the operational state of a wind turbine. In this sense, it is very close to the application field. However, it cannot give precise information about the accuracy of the simulated wind field because inaccurate provisions of the wake velocity could cancel out in the averaging process. The RMSE does not suffer from this problem and can express the accuracy of the simulations with more confidence. Last, we also included the regression analysis in our study because in this way we could see how well the models are correlated to the reference in terms of the coefficient of determination R^2 , and of the corresponding regression line slope A and intercept B . These statistical parameters are included in Table 1 too.

To provide further information on the intermediate results of the simulations, we include figures describing the development of the horizontal and vertical profiles of the wake velocity at different cross sections in Appendix A.

4.1 Test case 1: single wake

In the first test case, we address a single wake to assess the general accuracy of the two shear-layer wake models and at the same time to have a term of comparison for the simulation of multiple wakes.

Looking at the results in Fig. 5, the 3DSL model and FLaP tend to have fair and very similar results with values of Δ_{RAWS} (top panels) and E_{RMS}/u_H (bottom panels) below 10% after $6D$ downstream. Higher errors occur in the preceding region, especially around the centre of the rotor ($y = 0D$) where the RAWS is overestimated. Here, the 3DSL model seems to perform slightly better, in particular from the graphics of E_{RMS} . In the far wake, starting from $12D$ the profiles of Δ_{RAWS} and E_{RMS} do not vary much moving downstream.

The difference between the results of the two models perceived in Δ_{RAWS} and E_{RMS}/u_H is not found in the overall RAWS $\overline{\Delta}_{\text{RAWS}}$ and in the average root mean square error $\overline{E}_{\text{RMS}}/u_H$. Similarly, the results of the regression analysis are essentially the same for the two models. The corresponding scatter plots in Fig. 6 and intercept B suggest that, in general, the two models tend to overestimate the wind speed values, i.e. to underestimate the wake effects.

D. Trabucchi et al.: 3-D shear-layer simulation model

4.2 Test case 2: multiple aligned wakes

Even though the simulation of consecutive aligned wakes with the Ainslie wake model does not require the square addition approach because the wake velocity profiles remain axisymmetric, we apply this approach to be consistent with the other test cases.

The main results are collected in Fig. 7, the top panels of which show that FLaP overestimates the RAWS relative deviation Δ_{RAWS} , particularly around the axis of the real turbine rotor ($y = 0D$) where the maximum of the deviation is reached. Moving sideways, the deviation decreases gradually.

Differently, the 3SDL model underestimates the RAWS around the axis of the real turbine rotor and overestimates it around the boundaries of the wakes ($y = \pm 1D$). Also in this case, the highest absolute deviation from the reference is around the axis of the real turbine rotors.

In general, the results give the impression that the 3DSL model simulations are a little more accurate in terms of RAWS. The same conclusion is not evident in the values of the RMSE drawn in Fig. 7c, d. Since in both figures of merit the two models have a very similar behaviour, it is hard to draw a clear conclusion from the comparison.

Contrary to the previous test case, the overall statistics $\overline{\Delta}_{\text{RAWS}}$ and $\overline{E}_{\text{RMS}}/u_H$ sustain the impression suggested by Fig. 7: the former indicates that 3DSL simulations have a deviation from the reference on average six percentile points lower than FLaP. In contrast, the latter suggests that the two models have the same accuracy in terms of overall RMSE.

The slope and the intercept from the regression analysis (Table 1) show that the 3DSL model approaches an almost perfect regression line. FLaP does not have such good results in these terms, but it is characterised by a lower spread of the data as indicated by the higher coefficient of determination R^2 . This outcome can be explained with the different distribution of the deviation from the reference of the two models (see Fig. 8): on the one hand, the 3DSL model tends to underestimate the lower values of the wind speed, i.e. in the near wake especially in the region around the axis of the real turbine rotor. On the other hand, it tends to overestimate the higher wind speed values around the boundaries of the wake at a further downstream distance. The resulting uneven distribution leads to an almost perfect regression line. Differently, FLaP mainly overestimates the wind speeds in the whole domain, causing a higher intercept and a lower slope of the regression line. The same arguments explain the results of Δ_{RAWS} described before.

Considering all these results, we conclude that the two models simulate the wake of this test case differently, but they have very similar overall performance.

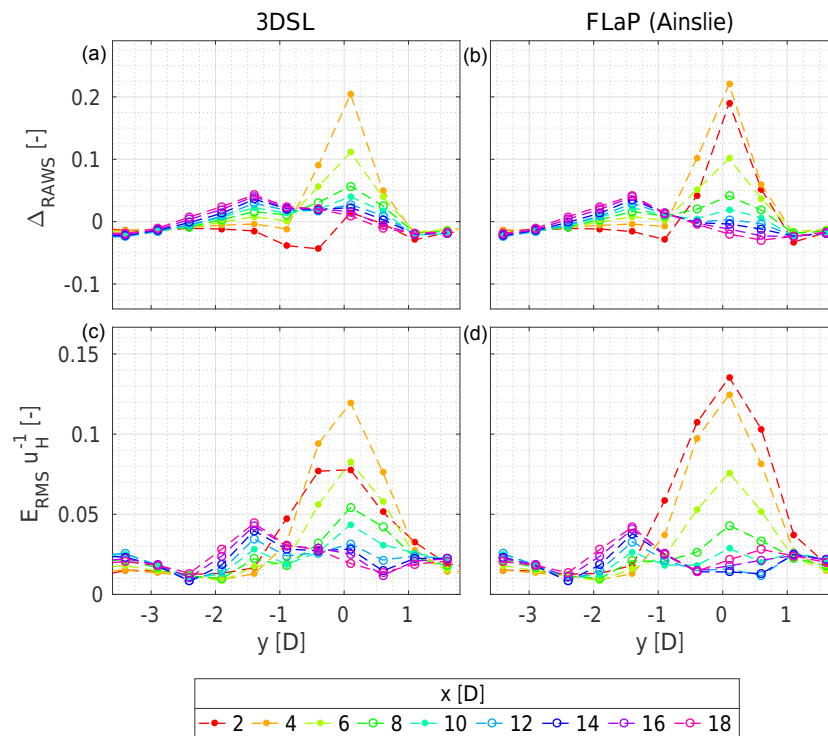


Figure 5. Test case 1 (single wake). Deviation of the rotor-average wind speed Δ_{RAWS} (a, b) and of the root mean square error E_{RMS} (c, d) evaluated in relation to the large-eddy simulation wind field for the simulation with the 3DSL model and with FLaP.

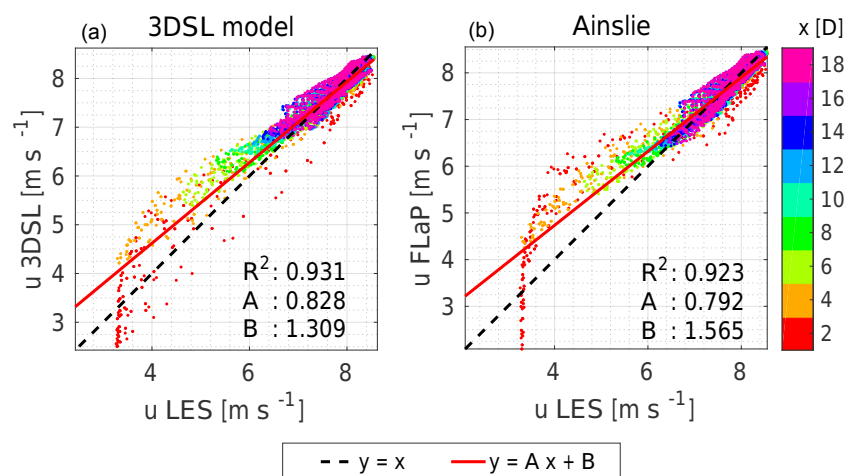


Figure 6. Test case 1 (single wake). Scatter plot and corresponding regression line of the wind speed derived from the 3DSL model (a) and from the FLaP wake simulations in relation to the reference wind field calculated with large-eddy simulations (LESs).

4.3 Test case 3: multiple wakes with 0.5D lateral separation

The simulation of multiple wakes with offset provided more pronounced differences between the two models. Concerning

the RAWS plotted in the top panels of Fig. 9, the values of Δ_{RAWS} evaluated with the 3DSL simulations are contained within $\pm 10\%$, with negative peaks around the centre line of the turbines at the corresponding first downstream cross

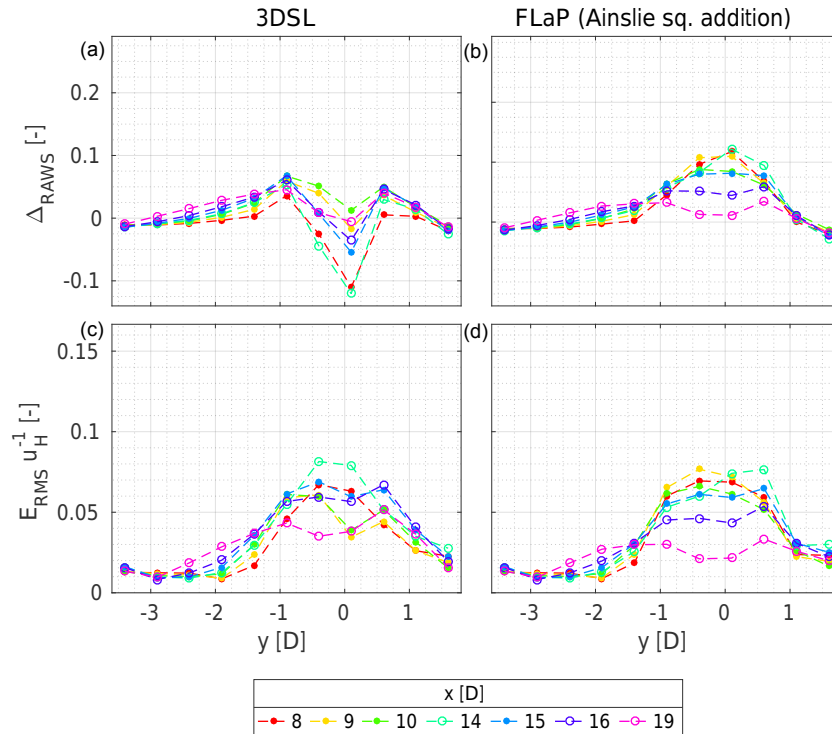


Figure 7. Test case 2 (multiple aligned wakes). Deviation of the rotor-average wind speed Δ_{RAWS} (a, b) and of the root mean square error E_{RMS}/u_H (c, d) evaluated in relation to the large-eddy simulation wind field for the simulation with the 3DSL model and with FLAP.

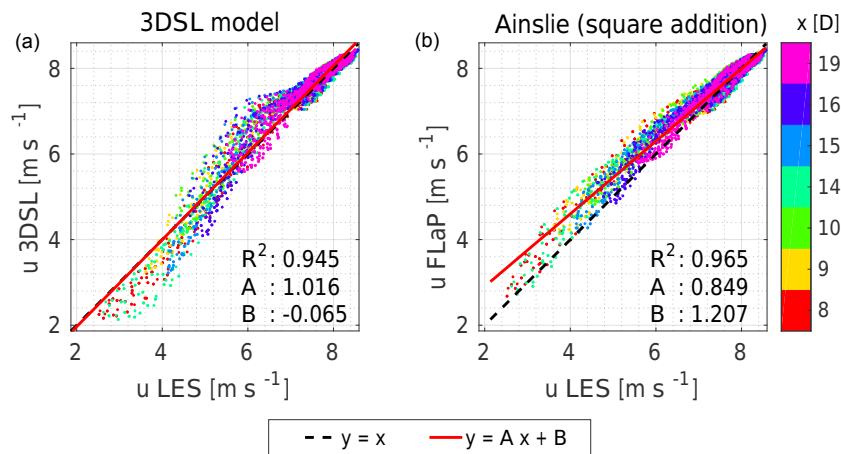


Figure 8. Test case 2 (multiple aligned wakes). Scatter plot and corresponding regression line of the wind speed derived from the 3DSL model (a) and from the FLAP wake simulations in relation to the reference wind field calculated with large-eddy simulations (LES).

section ($x = 8$, $y = -0.5 D$ and $x = 14$, $y = -1.0 D$); otherwise the 3DSL model overestimates the Δ_{RAWS} .

The wakes predicted with FLAP and the square addition rule overestimate the rotor equivalent wind speed values almost everywhere and are higher than in the case of the sim-

ulation with the 3DSL model. In the results from FLAP, we also notice that the maximal deviation of the RAWs at each cross section is higher than in test case 2 in which the aligned wakes are supposed to be axisymmetric. Furthermore, it increases passing through the third turbine. Conversely, we do

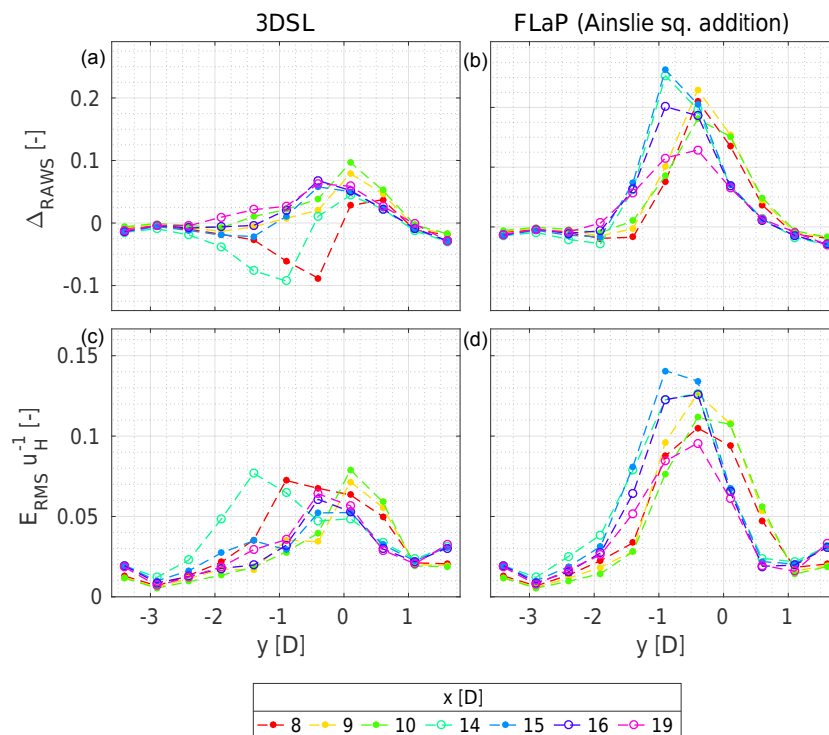


Figure 9. Test case 3 (multiple wakes with $0.5 D$ lateral separation). Deviation of the rotor-average wind speed Δ_{RAWS} (a, b) and of the root mean square error E_{RMS} (c, d) evaluated in relation to the large-eddy simulation wind field for the simulation with the 3DSL model and with FLaP.

not observe such behaviour in the 3DSL model, in which the maximum peaks of Δ_{RAWS} have a similar level as in test case 2 on all cross sections. This difference between the two models might be due to the three-dimensional, non-axisymmetric character of the multiple wakes simulated in this test case, which is better reproducible by the 3DSL model.

The results of the RMSE (Fig. 9c, d) are derived from a different point of view; however, they lead to the same observations.

The overall statistics provide a quantitative summary of the results mentioned above; in particular, the 3DSL model achieves a deviation from the reference RAWS ($\overline{\Delta_{\text{RAWS}}}$) 21 percentile points lower than FLaP. Considering the overall RMSE, the spread between the two models is even more acute: in the simulations with the 3DSL model, $\overline{E_{\text{RMS}}}$ is almost 20 percentile points lower than in FLaP simulations.

Here, the regression analysis (see Fig. 10) replicates the results of test case 2, with the difference that, for the 3DSL model simulations, the slope A and the intercept B of the regression line are not so close to their ideal values 1 and 0 respectively. In turn, the coefficient of determination R^2 is a little higher indicating less scatter of the data. For the simulations with FLaP we observe a remarkable increase in

the intercept, which indicates a larger overestimation of the wind speed, meaning a larger underestimation of the wake effects.

4.4 Test case 4: multiple wakes with $1.5 D$ lateral separation

Due to the increased cross-stream separation between the three turbines considered in this test case, the flow seems composed by single wakes. The results presented in Fig. 11 are therefore comparable with those of test case 1, but with an amplified difference between the performance of the two models. In fact, with regard to the reference, both the deviation of the RAWS and the RMSE evaluated for FLaP are clearly higher than the ones evaluated for the 3DSL model.

The corresponding overall values give a measure of this difference: both the deviation $\overline{\Delta_{\text{RAWS}}}$ of FLaP and the average root mean square error $\overline{E_{\text{RMS}}}/u_H$ are more than 10 percentile points larger than the ones of the 3DSL model.

The regression analysis displayed in Fig. 12 provides results close to those of test case 1 for both models, apart from the intercept, which in test case 4 is lower for the simulation with the 3DSL model, while it is higher for the FLaP simulation.

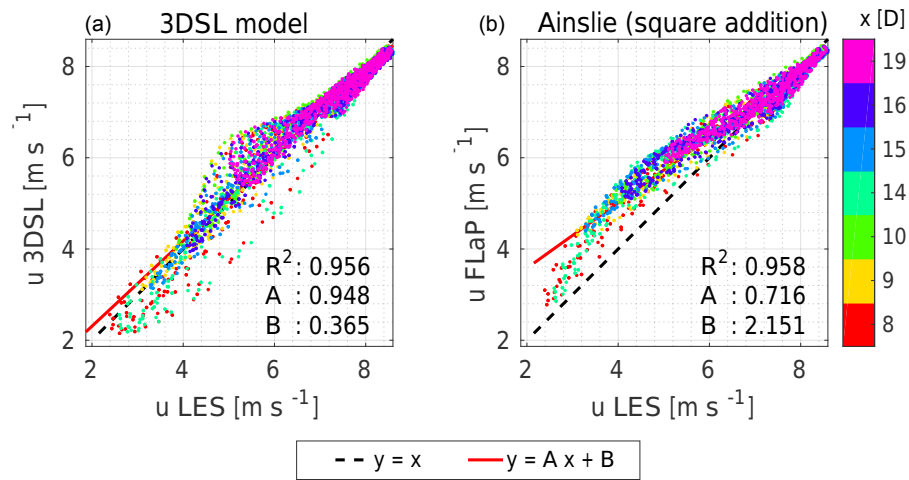


Figure 10. Test case 3 (multiple wakes with a $0.5 D$ lateral separation). Scatter plot and corresponding regression line of the wind speed derived from the 3DSL model (a) and from the FLaP wake simulations in relation to the reference wind field calculated with large-eddy simulations (LESs).

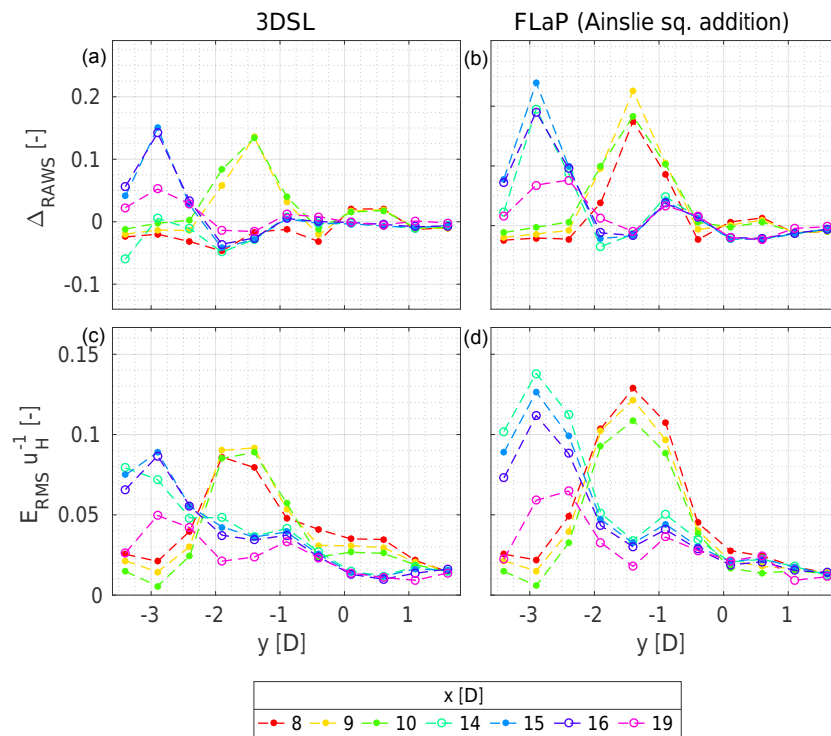


Figure 11. Test case 4 (multiple wakes with $1.5 D$ lateral separation). Deviation of the rotor-average wind speed Δ_{RAWS} (a, b) and of the root mean square error E_{RMS} (c, d) evaluated in relation to the large-eddy simulation wind field for the simulation with the 3DSL model and with FLaP.

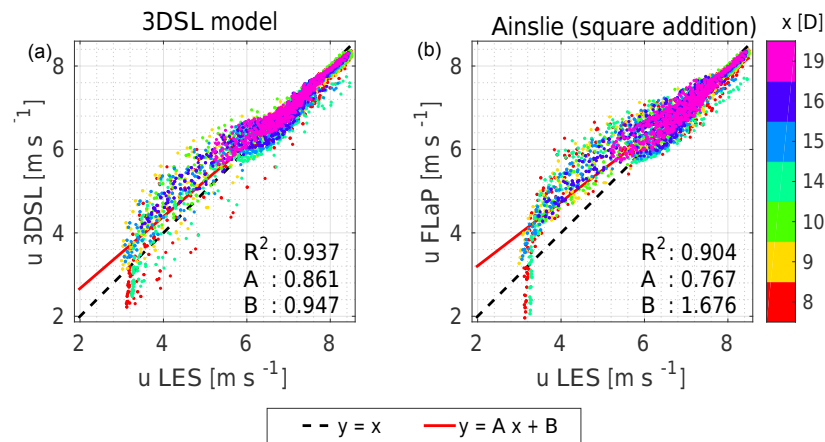


Figure 12. Test case 4 (multiple wakes with a $1.5 D$ lateral separation). Scatter plot and corresponding regression line of the wind speed derived from the 3DSL model (a) and from the FLaP wake simulations in relation to the reference wind field calculated with large-eddy simulations (LESs).

5 Discussion

In Sect. 4, we compared two shear-layer wake models with a different level of detail in the physical description of the flow. The results are not always easy to interpret because in some cases one model was accurate where the other was not and vice-versa. We dealt with this problem by estimating different figures of merit that are generally in agreement. This temporarily solves the conflict between the applicative point of view of the RAWS and the more wind-field-oriented approach of the RMSE.

The object of comparison was the performance of the two models in the simulation of multiple wakes. In this regard, the figures of merit are generally in favour of the 3DSL model. This is a positive outcome of our research and encourages the further development of this new model. Nonetheless, the two models provided similar results for axisymmetric wakes (test case 1 and test case 2). This points out the advantage given by the third dimension resolved by the 3DSL model. In fact, in the other test cases, i.e. when multiple wakes have a lateral separation, the additional details in the physical description of the flow implemented in the 3DSL model seem to improve the results.

Despite the different performances, we found similar deficiencies in the two models. This particularly regards the flow of single wakes near the rotor cross section as indicated by the results of test case 1 and in test case 4. Furthermore, the regression analysis and the scatter plot indicate the tendency to overestimate the wind velocity in the same cases. More in detail, it is possible to notice that the lowest wind speed in single wakes near the rotor was underestimated, while further downstream there was a general overestimation of the wind speed in the wake. This indicates that single wakes might have recovered in the transition between near and far wake

too fast. The analysis of the individual wake profiles could help to understand this interpretation and at the same time could provide hints about how to deal with this issue. In many cases, a possible solution could be provided by different eddy viscosity models. In this sense, the three-dimensional domain of the 3DSL model offers the possibility to develop proper spatial distributions of these quantities, while the axisymmetric two-dimensional models would have more limits in the accomplishment of this task.

6 Conclusions

This paper investigated the possibility of improving the simulation of multiple wakes with engineering wake models such as the commonly used Ainslie model (Ainslie, 1988), implemented for instance in the wind farm layout software FLaP (Lange et al., 2003). In this regard, the paper presented a new wake shear-layer model (3DSL) that can deal with non-axisymmetric flows and is therefore suitable to simulating multiple wakes at once. Differently, when the Ainslie model is applied in a wind farm, the flow of multiple wakes is evaluated, superimposing the deficit of the individual wakes according to a linear or square addition approach. To allow the simulation of multiple wakes without the superposition of the individual wakes, the 3DSL model abandons the hypothesis of an axisymmetric wake assumed by Ainslie (1988) and adds a third dimension to the simulation domain. In order to do this, it assumes a potential flow on the vertical cross sections.

In a benchmark with LESs as a reference case, we considered four test cases and compared wake simulations performed with FLaP and with the 3DSL model. The assessment was based on the average wind speed on the rotor of

582

D. Trabucchi et al.: 3-D shear-layer simulation model

several fictive turbines and on the corresponding RMSE. The two models provided similar results when they simulated axisymmetric wakes, but the 3DSL model performed better in the test cases including non-axisymmetric wakes. In part, this might be one of the advantages of the third dimension included in the 3DSL model.

Since only a few test cases using wakes simulated within LESs were addressed here, these results cannot be generalised. For the same reason, we cannot make any statement about how these results could affect the estimation of the annual energy yield of a wind farm. Nevertheless, we are confident that the additional details in the physical description of the wake flow implemented in the 3DSL model can in general offer new possibilities for improving the simulation of single and multiple wakes at an affordable computational cost.

Data availability. The wind field data and the model implementation code could be made available in the framework of a cooperation agreement. Please contact the corresponding author for further information.

Appendix A: Normalised wake wind velocity profiles

The comparison of the 3DLS model and of FLaP with the reference wind field from large-eddy simulations (LESs) reported in this paper deals with figures of merit representative for integral results and therefore cannot provide detailed results about the output of the two models at specific positions in the simulation domain. For this reason we show the downstream development of the wake velocity for the test cases analysed in this paper in this appendix.

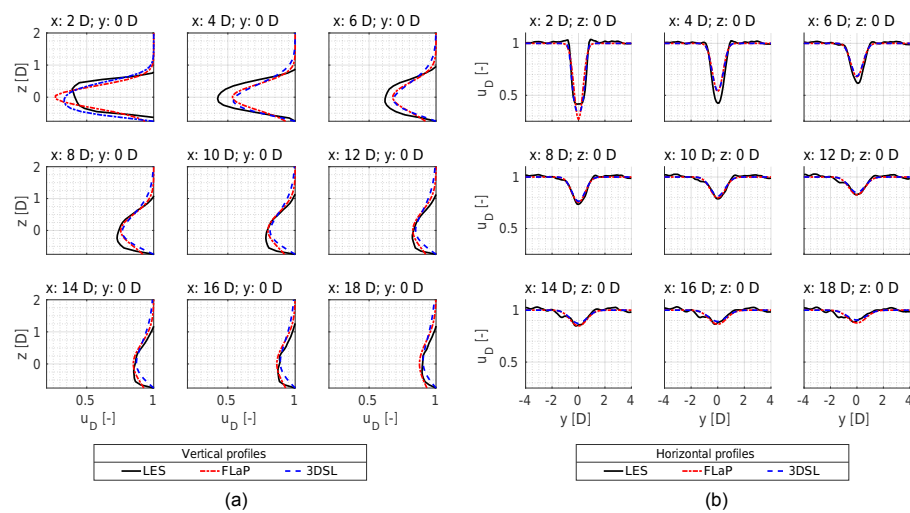


Figure A1. Test case 1 (single wake). Downstream development of the vertical (a) and horizontal (b) profiles of the wake velocity evaluated along the wind turbine rotor axis from the 3DSL model and from the FLaP simulations and from the reference large-eddy simulation (LES) wind field.

584

D. Trabucchi et al.: 3-D shear-layer simulation model

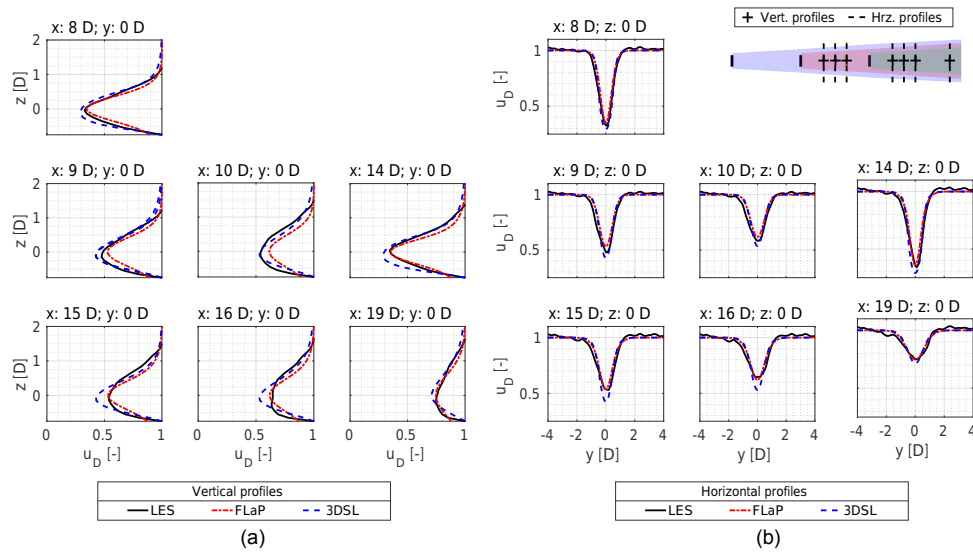


Figure A2. Test case 2 (multiple aligned wakes). Downstream development of the vertical **(a)** and horizontal **(b)** profiles of the wake velocity evaluated along the common axis of the wind turbines from the 3DSL model and FLaP simulations and from the reference large-eddy simulation (LES) wind field. The position of the profiles considered is illustrated in the top right corner of **(b)**.

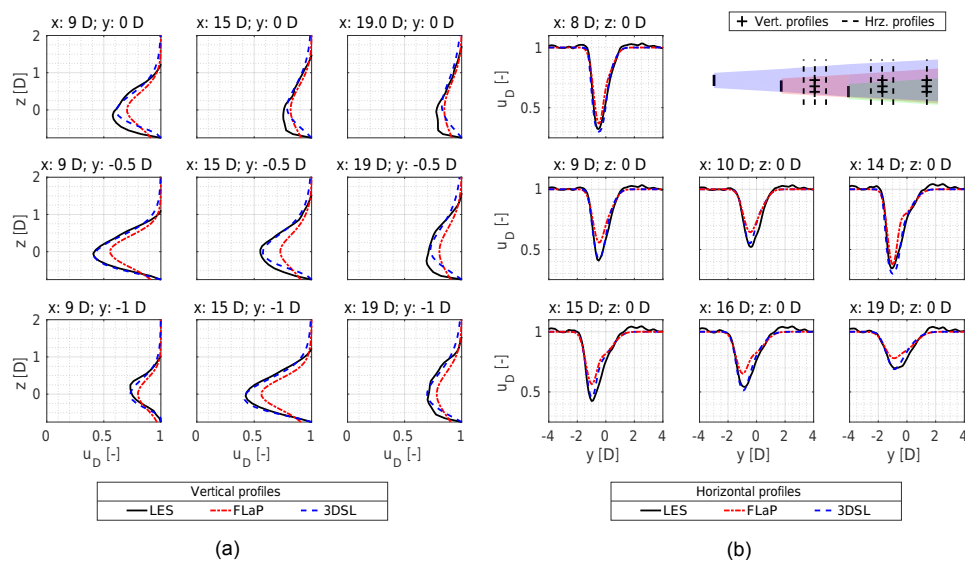


Figure A3. Test case 3 (multiple wakes with $0.5 D$ lateral separation). Downstream development of the vertical **(a)** and horizontal **(b)** profiles of the wake velocity evaluated along the common axis of the wind turbines from the 3DSL model and FLaP simulations and from the reference large-eddy simulation (LES) wind field. The position of the profiles considered is illustrated in the top right corner of **(b)**.

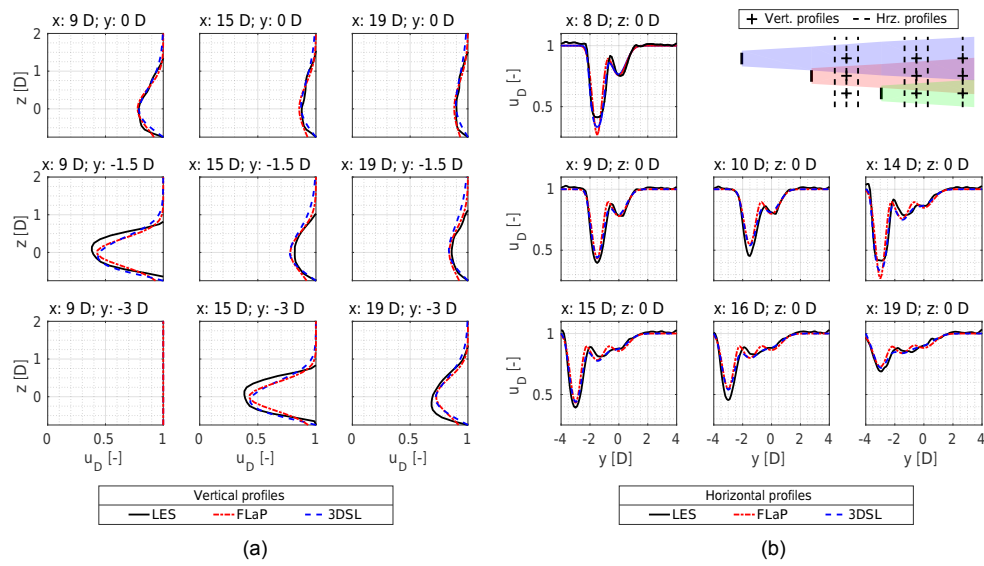


Figure A4. Test case 4 (multiple wakes with $1.5 D$ lateral separation). Downstream development of the vertical (a) and horizontal (b) profiles of the wake velocity evaluated along the common axis of the wind turbines from the 3DSL model and FLaP simulations and from the reference large-eddy simulation (LES) wind field. The position of the profiles considered is illustrated in the top right corner of (b).

584

D. Trabucchi et al.: 3-D shear-layer simulation model

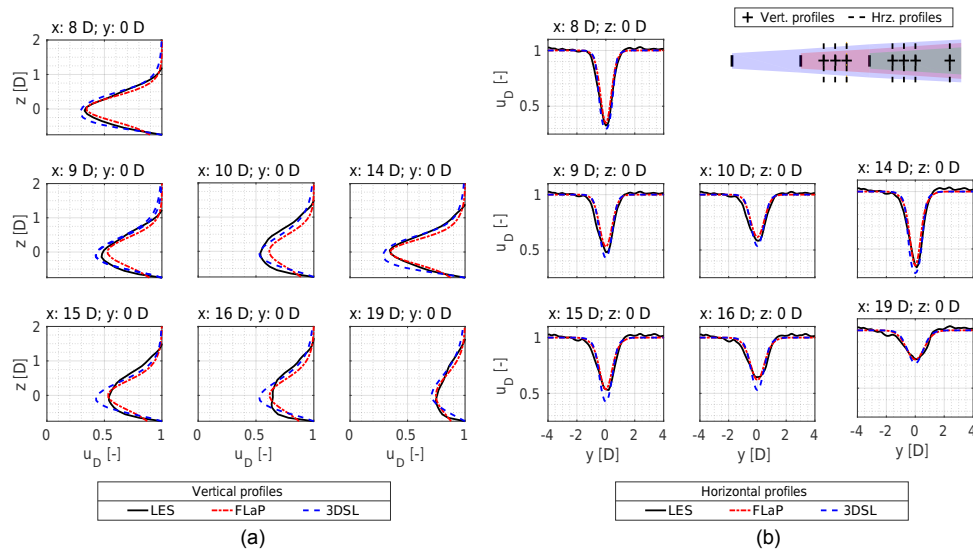


Figure A2. Test case 2 (multiple aligned wakes). Downstream development of the vertical **(a)** and horizontal **(b)** profiles of the wake velocity evaluated along the common axis of the wind turbines from the 3DSL model and FLaP simulations and from the reference large-eddy simulation (LES) wind field. The position of the profiles considered is illustrated in the top right corner of **(b)**.

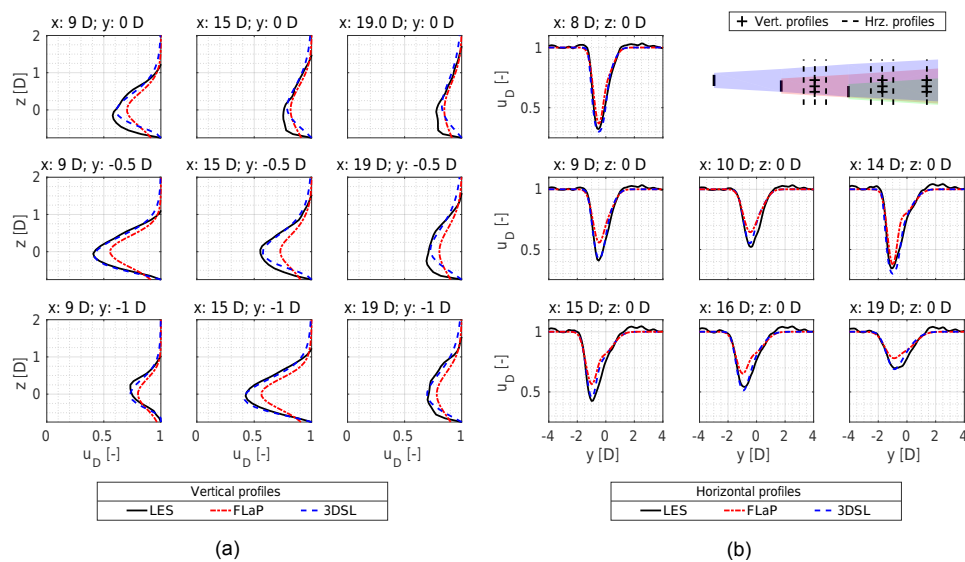


Figure A3. Test case 3 (multiple wakes with $0.5 D$ lateral separation). Downstream development of the vertical **(a)** and horizontal **(b)** profiles of the wake velocity evaluated along the common axis of the wind turbines from the 3DSL model and FLaP simulations and from the reference large-eddy simulation (LES) wind field. The position of the profiles considered is illustrated in the top right corner of **(b)**.

3-D shear-layer model for the simulation of multiple wind turbine wakes

Further development, calibration and assessment

7.1 Introduction

This chapter elaborates the general formulation of the 3-D shear-layer (3DSL) model illustrated in Chapter 6 for the simulation of non-axisymmetric wakes. In particular, it deals with the streamwise pressure gradient in the vicinity of the rotor. This term was previously approximated as a reduction of the wake turbulent diffusion. The model is then calibrated and verified using both full-field wake measurements and synthetic wakes reproduced with LES.

7.1.1 Basic formulation of the 3DSL model

In a Cartesian domain, the non-dimensional wind speed components u , v and w can be defined along the non-dimensional axes x , y and z in the streamwise, cross-stream and vertical directions, respectively. The coordinates and the wind speed components are normalised by the rotor diameter D of a well-defined wind turbine and by the streamwise wind component u_{HH} at hub-height, upstream in the undisturbed flow. In this space, the wind deficit on a downstream cross-section can be calculated subtracting u from the corresponding values in the undisturbed flow. Considering u_D as the difference of the wind speed deficit from one, the basic formulation of the 3DSL model consists of:

- The continuity equation

$$\frac{\partial u_D}{\partial x} + \frac{\partial v}{\partial y} + \frac{\partial w}{\partial z} = 0 \quad (7.1)$$

- The shear-layer approximation of the Reynolds averaged Navier-Stokes (RANS) equations

$$u_D \frac{\partial u_D}{\partial x} + v \frac{\partial u_D}{\partial y} + w \frac{\partial u_D}{\partial z} = \epsilon_y \frac{\partial^2 u_D}{\partial y^2} + \epsilon_z \frac{\partial^2 u_D}{\partial z^2} \quad (7.2)$$

- The assumption that the potential field Φ can be defined on vertical cross-sections as

$$\frac{\partial \Phi}{\partial y} = v \quad , \quad \frac{\partial \Phi}{\partial z} = w \quad . \quad (7.3)$$

The initial conditions of the of wake simulations are imposed at the rotor section where the wind deficit is calculated by means of the actuator disc mode (Burton et al., 2011). The initial deficit is propagated downstream by diffusion. The contribution of ambient turbulence to the diffusive process depends on atmospheric variables such as the friction velocity u_* , the non-dimensional shear profile Φ_m function of the physical height Z normalised by the Monin-Obukov length L_{MO} . The streamwise pressure gradient expected in the near-wake development range is not addressed by the 3DSL model directly, but it is included here as reduction of the wake turbulent diffusion by means of a filter function. The diffusion due to the wake can be assumed proportional to the turbulence velocity scale $u_{a,y,z}$ and to the corresponding length scales σ_r at the considered wake cross-section. In scaled experiments, Ainslie, (1988) observed that in the near-wake development region the turbulent mixing grows slower than the turbulence scales. For this reason he introduced the following eddy-viscosity model

$$\epsilon_{y,z} = \frac{F_1 k \sigma_r u_{a,y,z}}{\Phi_m(Z/L_{MO})} \frac{F_2 \kappa u_* z}{\Phi_m(Z/L_{MO})} \quad (7.4)$$

where the wake and the ambient turbulence contributions are given by the first and second addends, respectively. Each term is based on a proportionality constant: $k=0.015$ is the proportionality constant suggested by Ainslie, (1988) for the wake contribution and κ is the von Karman constant applied to estimate the ambient turbulence diffusion. Last, the two filter functions

$$F_1 = \begin{cases} 0.65 + \left[\left(\frac{x-4.5}{23.32} \right)^{1/3} \right] & \text{for } 0 < x \leq 5.5 \\ 1 & \text{for } x > 5.5 \end{cases} \quad (7.5a)$$

$$F_2 = \begin{cases} \frac{x}{x_{F2}} & \text{for } 0 < x \leq x_{F2} \\ 1 & \text{for } x > x_{F2} \end{cases} \quad (7.5b)$$

are included in the eddy-viscosity model. The former reduces the wake turbulent diffusion in order to balance the turbulence production. The latter is a surrogate for the effects of the streamwise pressure gradients and linearly scales the ambient turbulent diffusion from 0 to 1 according to the filter parameter x_{F2} .

7.1.2 Objectives

This chapter aims to improve the 3DSL model and to verify its implementation. These overall goals are fragmented into smaller objectives that are addressed separately in the next sections and can be summarised as follows:

1. Model the gradient of the pressure field p within the rotor induction zone and include it into the right hand side of Eq. 7.2 such that the streamwise momentum balance equations can be re-written as

$$u_D \frac{\partial u_D}{\partial x} + v \frac{\partial u_D}{\partial y} + w \frac{\partial u_D}{\partial z} = -\frac{1}{\rho} \frac{\partial p}{\partial x} + \epsilon_y \frac{\partial^2 u_D}{\partial y^2} + \epsilon_z \frac{\partial^2 u_D}{\partial z^2} \quad (7.6)$$

where ρ denotes the air density.

2. Calibrate the turbulence length scale σ_r of a single wind turbine wake.
3. Revise the numerical implementation.
4. Verify the 3DSL model for single and multiple wakes with full-field measurements and large-eddy simulations (LES).

7.2 Model of the streamwise pressure gradient

A possible way to consider the effect of the pressure field within the induction zone of a wind turbine rotor is to prescribe a proper pressure gradient. This approach is inspired by Schepers, (2012), who assigns the pressure gradient on the basis of results from simulations with a free vortex wake model, executed in advance and saved as look-up tables. To include the near-wake region into the domain valid for the 3DSL model, the pressure contribution is estimated from the analytical solution of a vortex-cylinder wake model.

The wake of a wind turbine can be described by the system of three type of vortices including a straight root vortex, one bound lifting line vortex per rotor blade and one helicoidal vortex filament shed from the tip of each blade. All mentioned vortex filaments are characterised by constant circulation. As the number of blades tends to infinity, the vortex system reduces to the root vortex Γ_r , a bound vortex sheet Γ_b at the rotor disc and a continuous cylindrical vortex sheet along the wake which includes the tangential and longitudinal components Γ_t and Γ_l . (Burton et al., 2011). This decomposition is explained in Fig. 7.1 where, for simplicity, the case of a finite number of blades is illustrated.

To model the streamwise pressure gradient, only the contribution by the tangential vortex is considered because it is the only one which directly affects the streamwise wind velocity.

Branlard et al., (2015) provide an analytical solution for the streamwise and radial wind velocity components $u_{x,\gamma_t}(x, r)$ and $u_{r,\gamma_t}(x, r)$ induced by the tangential vortex introduced before (see Fig. 7.1c). The solution is expressed as

$$\begin{aligned} u_{x,\gamma_t}(x, r_V) &= \frac{\gamma_t}{2} \left[\frac{R_V - r_V + |R_V - r_V|}{2|R_V - r_V|} + \frac{x q(x)}{2\pi\sqrt{r_V} R_V} \left(K(q^2(x)) + \frac{R_V - r_V}{R_V + r_V} \Pi(q^2(0), q^2(x)) \right) \right] \\ u_{r,\gamma_t}(x, r_V) &= -\frac{\gamma_t}{2\pi} \sqrt{\frac{R}{r_V}} \left[\frac{2 - q^2(z)}{q(z)} K(q^2(x)) - \frac{2}{q(z)} E(q^2(x)) \right] \end{aligned} \quad (7.7)$$

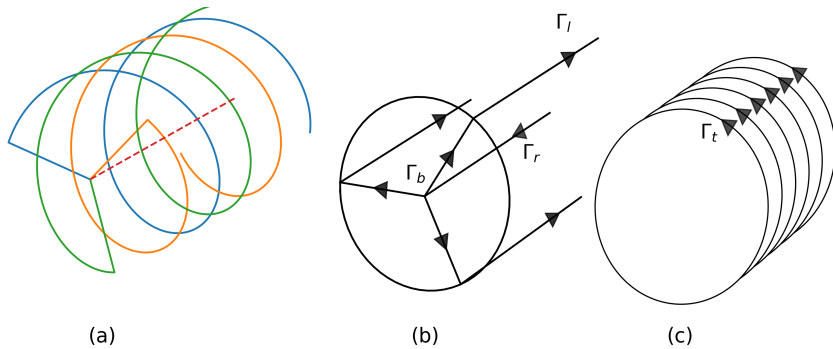


Figure 7.1: Helicoidal vortex system of a wind turbine wake (a) decomposed into its linear components (b), i.e. the bound, root and trailing edge longitudinal vortices and its tangential component (c).

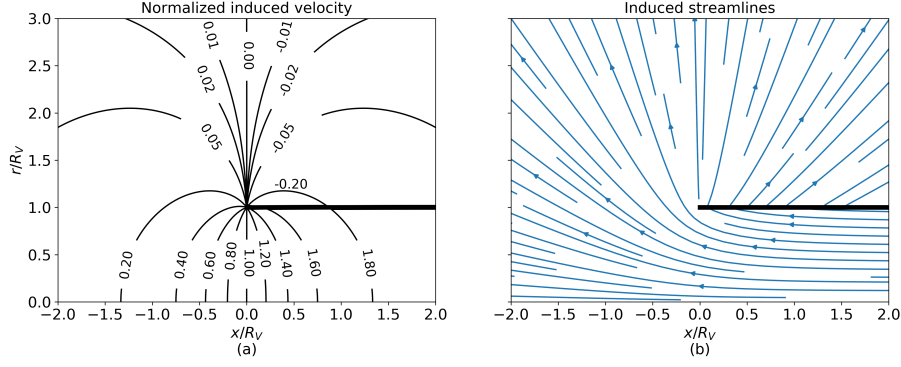


Figure 7.2: Wind field induced by a semi-infinite vortex-cylinder (a). The streamwise velocity contour is normalised by $2R_V/\gamma_t$ and the streamlines are evaluated for $\gamma_t = -1 \text{ m s}^{-1}$ (b).

where the complete elliptic integrals K , E and Π of the first, second and third kind are functions of the elliptic parameter

$$q^2(x) = m(x) = \frac{4r R_V}{(R_V + r)^2 + x^2}. \quad (7.8)$$

In Eq. 7.7, x and r_V stand for the distances from the rotor and from its axis, respectively; R_V denotes the radius of the vortex-cylinder and γ_t is the intensity of the tangential vortex. According to the disc actuator theory, γ_t can be related to the thrust coefficient C_T of a rotor with homogeneous loading and inflow velocity u_{HH} by

$$\gamma_t = (\sqrt{1 - C_T} - 1) u_{HH}. \quad (7.9)$$

The wind field defined by $u_{x,\gamma_t}(x, r)$ and $u_{r,\gamma_t}(x, r)$ is depicted with contour levels and streamlines in Fig. 7.2

For $x > 0$, u_{γ_t} has a discontinuity at the surface of the cylinder vortex, i.e. when $r_V = R_V$. Along this surface the induced velocity reduces to

$$u_{\gamma_t}(x, r_V = R_V) = \frac{\gamma_t}{4} + \frac{\gamma_t}{2} \frac{x q(x)}{2\pi\sqrt{r_V} R_V} (K(q^2(x))). \quad (7.10)$$

The wind field resulting from the vortex-cylinder model can be used to estimate the deceleration imposed by the turbine on the flow. Assuming that this flow is (i) non-viscous and (ii) composed by the streamwise and radial wind speed components only, the steady momentum balance equation can be simplified to

$$u_{x,\gamma_t} \frac{\partial u_{x,\gamma_t}}{\partial x} + u_{r,\gamma_t} \frac{\partial u_{x,\gamma_t}}{\partial r_V} = -\frac{1}{\rho} \frac{\partial p_{\gamma_t}}{\partial x} \quad (7.11)$$

and, with a finite difference approximation of Eq. 7.11, it is possible to calculate the entity of the streamwise pressure gradient numerically from the solution of the vortex-cylinder model (Eq. 7.7 and Eq. 7.10).

Because of the discontinuous wind field, the pressure gradient has a singularity at the rotor tip. As a consequence, numerical instabilities can arise in its vicinity and lead to non-physical negative values of the kinetic energy. In the implementation of the 3DSL model, such values are replaced by the lowest positive value of the kinetic energy over the considered vertical cross-section.

Before applying the results of the vortex-cylinder model to Eq. 7.6, some considerations are required. Differently from the 3DSL model, the vortex-cylinder model does not include turbulent diffusion. If the contribution of the pressure gradient is implemented into Eq. 7.6, part of its energy is recovered by turbulent diffusion and the resulting wind deficit is lower than expected. To compensate for this inconvenient, the factor G_γ is introduced to scale the pressure gradient in the near-wake development range as required:

$$\frac{\partial p}{\partial x} = G_\gamma \frac{\partial p_{\gamma t}}{\partial x}. \quad (7.12)$$

For the same reason, the filter function F_2 (Eq. 7.5b) is still considered to reduce the diffusion of the ambient eddy-viscosity. Suitable values for G_γ and for the filter parameter x_{F2} are discussed in Section 7.4.

Another aspect to consider is the application of the pressure gradient model to multiple wakes. The heterogeneous flow downstream of a wind turbine and the wake generated turbulence reduce the aerodynamic efficiency of a wind turbine rotor operating in wakes. To take into account these effects, (Iungo et al., 2018) suggest to apply the correction factor C_{aero} which can be estimated as

$$C_{aero} = a_{aero} \exp(b_{aero} + \epsilon_{inc}^{0.5}) + d_{aero} \quad (7.13)$$

where ϵ_{inc} indicates the incoming eddy-viscosity averaged over the rotor and the parameters a_{aero} , b_{aero} and d_{aero} depend on the aerodynamics of the blade. In the 3DSL model C_{aero} is estimated empirically from case to case and it is applied to reduce the thrust coefficient.

7.3 Numerical implementation

The 3DSL model describes the fluid mechanics of a wake with parabolic partial differential equations. This means that the solution can be estimated with a finite difference approximation of the physical problem marching forward step by step from the initial conditions. This section summarises briefly the numerical implementation of the 3DSL model, explains the revisions with respect to the version of Chapter 6 and includes a flow chart Fig. 7.3 of the algorithm applied to solve flow.

Simulations with the 3DSL model are initiated with a known, three-dimensional wind vector field $\mathbf{V}_i = [u_{Di} \ v_i \ w_i]^T$ on the cross-section at the downstream distance x_i . Next, the 3DSL model estimates the streamwise wind component $u_{D,i+1}$ at the next cross-section from the momentum balance equation (Eq. 7.2). Then, the cross-stream and vertical wind components v and w are evaluated from the implementation of the potential flow assumption (Eq. 7.3) into the continuity equation (Eq. 7.1).

Differently from the methodology explained in Chapter 6, here Eq. 7.2 is solved with a fractional method applied to a staggered grid (Ferziger et al., 2008). This approach is based on an implicit numerical scheme (the Crank-Nicolson method) that demands a little more computational resources than the explicit method implemented before, but it is stable regardless of the resolution of domain discretisation.

Following the example by Seibold, (2008), the solution of Eq. 7.2 is divided into two steps. In the first one (Block 1 in Fig. 7.3), only the transport terms and the pressure gradient are estimated

with the vortex-cylinder model:

$$u_D \frac{\partial u_D}{\partial x} = -\frac{1}{\rho} \frac{\partial p}{\partial x} - v \frac{\partial u_D}{\partial y} - w \frac{\partial u_D}{\partial z}. \quad (7.14)$$

In accordance with partial derivation rules, Eq. 7.14 can be conveniently rewritten as

$$\frac{\partial \left(u_D^2 + \frac{p}{\rho} \right)}{\partial x} = - \left(\frac{\partial (u_D v)}{\partial y} + \frac{\partial (u_D w)}{\partial z} \right). \quad (7.15)$$

From known conditions at the downstream position x_i , u_D^2 can be calculated with an explicit method at an intermediate step $x_{i+1/2}$.

From the results at $x_{i+1/2}$, u_D is calculated at x_{i+1} (Block 2 in Fig. 7.3). Because of the non-linearity of the equation, an iterative process is applied until convergence of u_D . For this purpose, the iteration variable \tilde{u}_D is estimated as the average of u_D at $x_{i+1/2}$ and x_{i+1} . Then, at each iteration, the Crank-Nicolson method is applied to the diffusive terms of Eq. 7.2:

$$\tilde{u}_D \frac{\partial u_D}{\partial x} = \epsilon_y \frac{\partial^2 \tilde{u}_D}{\partial y^2} + \epsilon_z \frac{\partial^2 \tilde{u}_D}{\partial z^2}. \quad (7.16)$$

To solve Eq. 7.16, the general boundary condition $u_D=1$ is imposed to the domain. An additional condition on the first derivative is applied such that $\frac{\partial u_D}{\partial y}=0$ and $\frac{\partial u_D}{\partial w}=0$ on the lateral and top sides, respectively. Differently, an additional condition on the second derivative forces $\frac{\partial^2 u_D}{\partial z^2}=0$ on the bottom side.

At this point, three passages are left to calculate also v and w at x_{i+1} (Block 3 Fig. 7.3). An upwind approximation of $\frac{\partial u_D}{\partial x}$ at x_{i+1} can be calculated from u_D evaluated at x_{i+1} and x_i . Then, Eq. 7.1 can be rewritten as Poisson equation leveraging the potential flow assumption (Eq. 7.3):

$$\frac{\partial^2 \Phi}{\partial y^2} + \frac{\partial^2 \Phi}{\partial z^2} = -\frac{\partial u_D}{\partial x}. \quad (7.17)$$

Here, the boundary conditions are set to have no mass flow across the lower boundary and, at the same time, to balance the overall variation of the mass flow $\Delta Q = \rho \left(\int_{A_{i+1}} u_D dydz - \int_{A_i} u_D dydz \right)$ between two consecutive cross-sections A_{i+1} and A_i with the mass flow across the boundaries of the upstream cross-section at A_i . To achieve these conditions, the values on the boundaries of the domain, y_b and z_b , are calculated by means of a twin pair of potential flow source elements:

$$\phi(y_b, z_b) = \frac{-\Delta Q/2}{2\pi\rho} \ln \left(\sqrt{y^2 + z^2} \right) \quad (7.18)$$

one placed at the centroid of the streamwise variation of the mass flow evaluated over the vertical upstream cross-section, one at the opposite side with respect to the lower boundary.

Now, the potential function Φ can be calculated solving the linear system given by the finite difference formulation of Eq. 7.17.

In the last passage, of the numerical solution, v and w are derived from Eq. 7.3 at x_{i+1} .

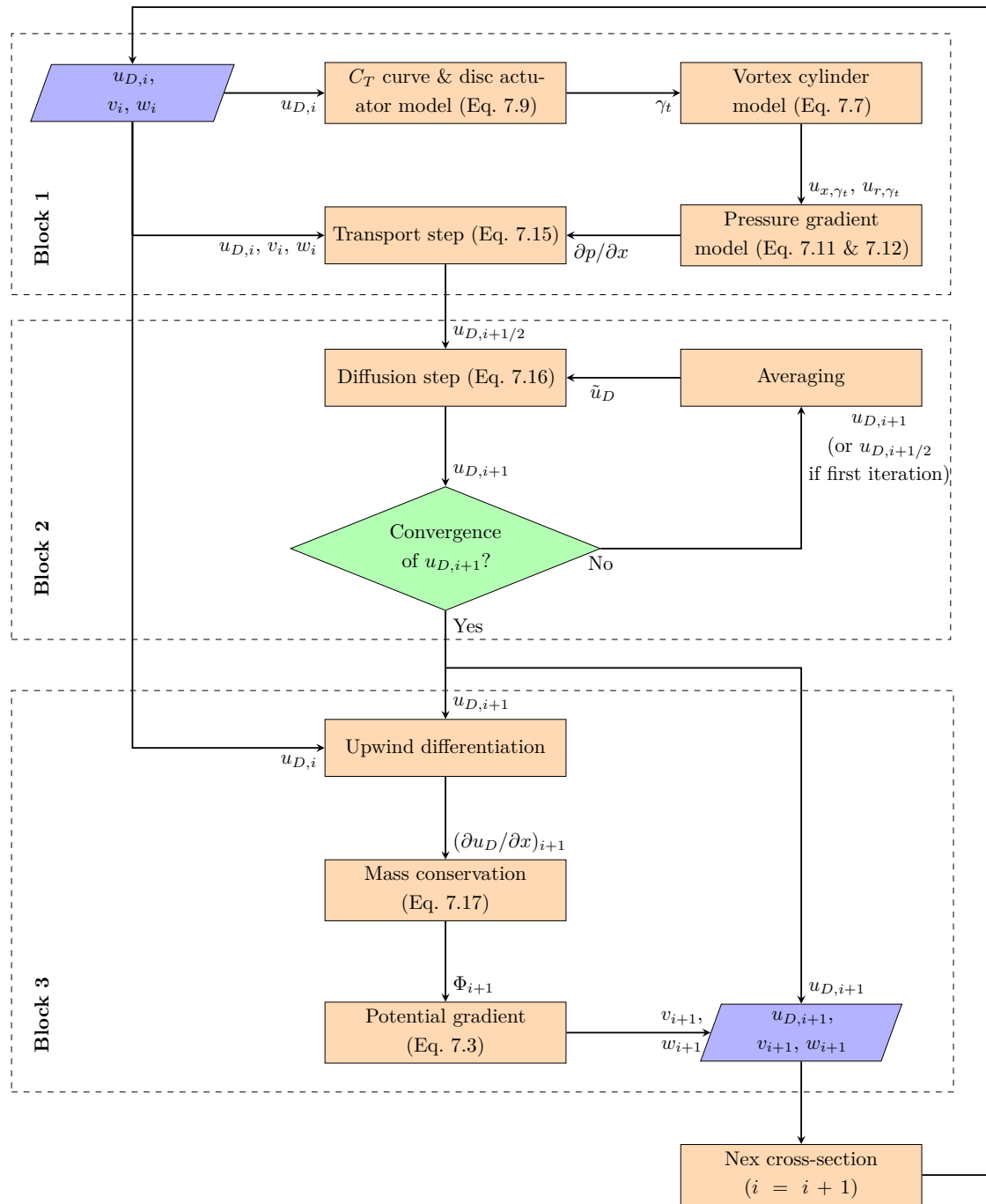


Figure 7.3: Flowchart of the algorithm implemented in the 3DSL model to solve the wind field on the vertical cross-section $i + 1$ from the known wind field on the upstream cross-section i .

7.4 Calibration of the turbulence length scale in a single wake

This section addresses the calibration of the wake width used to approximate the turbulence length scale σ_r in the eddy-viscosity model (see Eq. 7.4). First, the wind deficit profiles measured during a full-field experimental campaign are introduced. Then, a linear expansion model is fitted to the width of the measured profiles.

7.4.1 Profiles of the wind deficit in the wake from nacelle-based lidar measurements

For the calibration of the 3DSL model, the 10 min average data measured during the experimental campaign described in Section 5.3 are available. The dataset consists of time-series from a meteorological tower and measured by a long-range lidar installed on the nacelle of an offshore wind turbine. In that experiment, the lidar performed horizontal scans of the wake downstream of the rotor.

The average atmospheric conditions at the mast during the measurements of the wind deficit profiles in the wake are defined by the friction velocity u_* and by the momentum flux profile $\Phi_m(Z/L_{MO})$. The former is evaluated as

$$u_* = \frac{TI/100\% u_{HH}}{2.4} \quad (7.19)$$

where the turbulence intensity TI is expressed in per cent and u_{HH} indicates the undisturbed hub-height wind speed (Lange et al., 2003). The momentum flux profile is calculated according to Dyer, (1974) as a function of the physical height Z normalised by the Monin-Obukhov length L_{MO} . An estimation of L_{MO} is obtained using the bulk Richardson number derived from the vertical gradients of wind speed, temperature and pressure (Stull, 2017).

To analyse separately different load conditions on the rotor, the measurements are collected in classes of thrust, considering six intervals of the thrust coefficient C_T from 0.25 to 0.85 with an incremental step of 0.1.

A second classification is based on the turbulence intensity considering 1% bins. Due to the scarce amount of data, only one turbulence intensity range is available for all C_T classes (see Fig. 7.4a). For this reason, the following calibration includes only 10 min intervals with a turbulence intensity TI between 5% and 6% and is therefore not representative of all turbulence conditions.

Considering Eq. 7.19, an additional filter is applied to have a rather homogeneous friction velocity distribution in the class; specifically, only a $\pm 1 \text{ m s}^{-1}$ hub-height wind speed interval is considered for each C_T class.

The average profiles of the wind deficit in the wake are evaluated in terms of deficit at six downstream positions x_i where the corresponding wind speed is subtracted from the free-flow. The results are collected in the C_T classes and are averaged within each interval $x_i \pm 0.1 D$ considering 0.05 D bins along the cross-stream axis at hub-height. Table 7.1 summarises the results of the classification described above and Fig. 7.4b provides an example of the wind deficit measurements and average profile at $x_i = 3 D$ downstream of the rotor.

Table 7.1: Average atmospheric conditions and data availability for the thrust coefficient (C_T) classes, considering the corresponding interval of the hub-height wind speed u_{HH} and the turbulence intensity range from 5% to 6% .

C_T class	(± 0.05)	0.3	0.4	0.5	0.6	0.7	0.8
u_{HH} interval	($\pm 1 \text{ m s}^{-1}$)	15.5	14.5	13.5	12.5	10.5	9.5
Available intervals	[-]	13	13	9	9	4	6
u_{HH}	[m s^{-1}]	15.7	14.3	13.4	12.1	10.9	9.3
u_*	[m s^{-1}]	0.35	0.33	0.31	0.28	0.25	0.21
α	[-]	0.140	0.089	0.056	0.071	0.050	0.035
Φ_m	[-]	1.62	1.62	0.87	0.88	0.64	0.49

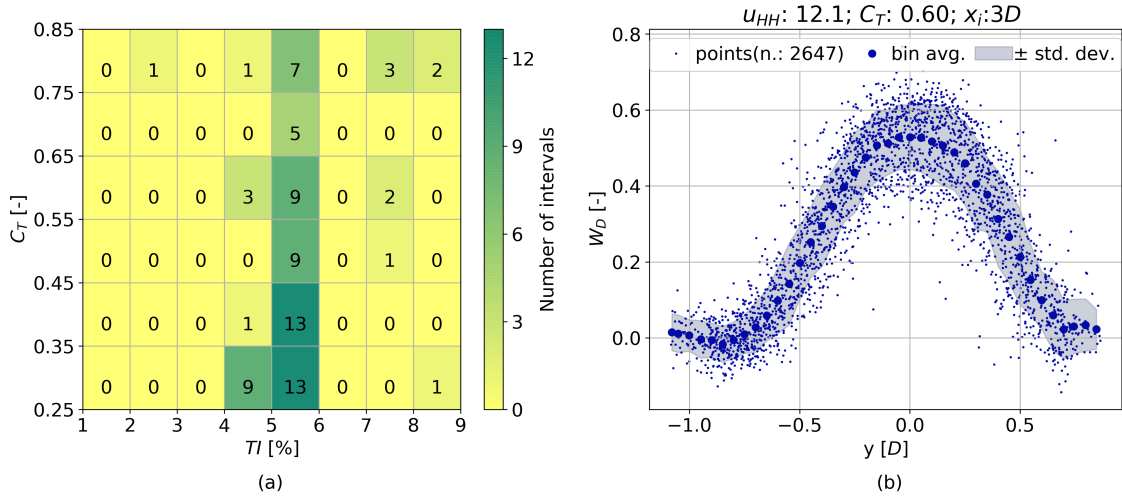


Figure 7.4: Number of 10 min intervals available classified according to the thrust coefficient C_T and the turbulence intensity TI (a). Exemplary wake profile W_D obtained for the C_T class 0.6 at the cross-section $x_i = 3D$ (b).

7.4.2 Turbulence length scale of a single wake

In one of the first shear-layer wake models, Ainslie, (1988) defined the turbulence length scale as the width σ_r of the Gaussian shape which describes the wake wind profile u_D normalised by the inflow wind speed at hub-height u_{HH} . This study, deals with the same definition, considering the wake deficit profile function

$$W_{DF} = 1 - u_D = u_o + D_M \exp\left(-3.56 \left(\frac{r}{\sigma_r}\right)^2\right) \quad (7.20)$$

where D_M is the magnitude of the wake centre-line wind deficit and r is the radial distance from it. Differently from Ainslie's original Gaussian shape, Eq. 7.20 includes also the variable offset u_o accounting for possible local variations of the free-flow from the upstream reference wind speed u_{HH} .

Comparing Eq. 7.20 with the wind speed deficit profiles of the wakes described in Section 7.4.1, it is possible to derive how the turbulence length scale σ_r scales varying the thrust coefficient C_T

and the downstream distance from the rotor. To accomplish this task, Eq. 7.20 is fitted to the deficit profiles and the results about the expansion of the wake – i.e. the downstream development of σ_r – can be observed in Fig. 7.5a with respect to rotor thrust.

Considering separately the different C_T cases, σ_r can be modelled using the linear function

$$\sigma_r = k' x_i + \epsilon' \quad (7.21)$$

defined by the expansion rate of the wake k' and of the corresponding initial width ϵ' . The results for each C_T case are summarised in Table 7.2 and in Fig. 7.5b.

Noting that (i) the expansion rate k' grows linearly with the thrust coefficient C_T and (ii) that the initial wake width ϵ' varies in a similar fashion, these two parameters can be approximated with the functions

$$\begin{aligned} k' &= 0.17C_T - 0.04 \\ \epsilon' &= 0.71C_T + 0.45. \end{aligned} \quad (7.22)$$

In conclusion, the turbulence length scale σ_r of a single wake can be estimated with Eq. 7.21. For the case of turbulence intensity around 5%, the parameters k' and ϵ' can be estimated Eq. 7.22 which was calibrated with respect to nacelle-based lidar measurements of a single wake.

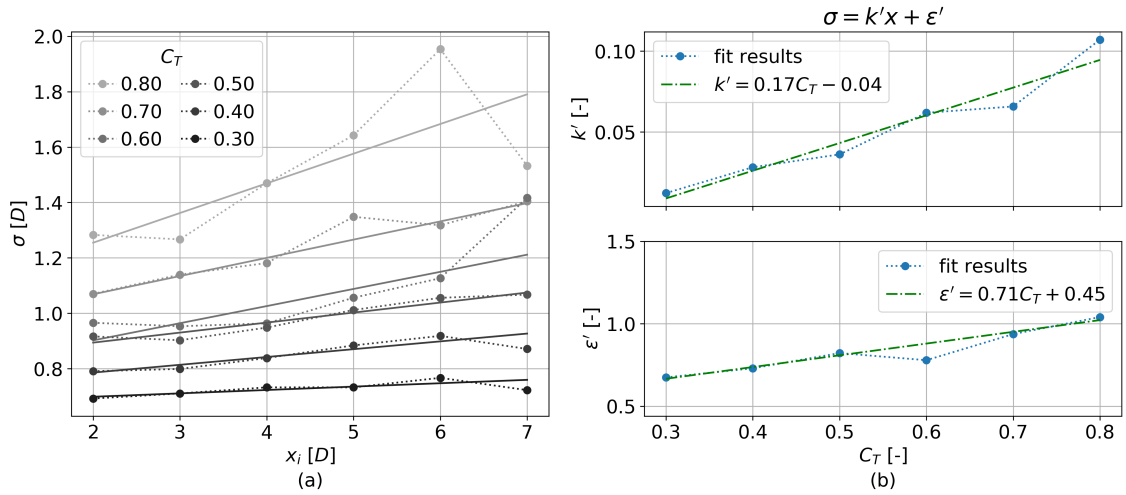


Figure 7.5: Downstream evolution of the wake width σ_r evaluated from the profile function of the wind speed deficit fitted to full-field wake measurements.

Table 7.2: Expansion rate k' and initial wake width ϵ' evaluated from the profile function of the wind speed deficit fitted to full-field wake measurements.

	C_T					
	0.3	0.4	0.5	0.6	0.7	0.8
k'	0.012	0.028	0.036	0.062	0.066	0.107
ϵ'	0.674	0.730	0.822	0.779	0.937	1.041

Table 7.3: Main characteristics of the reference datasets used for the assessment of the parameters of the pressure gradient model.

	Unit	Symbol	LES	Lidar measurements
Turbine manufacturer	-	-	Siemens	Senvion
Turbine model	-	-	SWT-3.6-120	6.2M126
Rotor diameter	[m]	D	120	126
Hub-height	[m]	z_H	90.0	96.5
Hub-height inflow wind speed	$[\text{m s}^{-1}]$	u_{HH}	8.1	9.3
Hub-height turbulence intensity	[%]	TI	5	5
Friction velocity ^(*)	$[\text{m s}^{-1}]$	u_*	0.17	0.21
Non-dimensional shear profile	[-]	Φ_m	1.00	0.49
Thrust coefficient	[-]	C_T	0.86	0.75

(*) Here friction velocity was estimated with Eq. 7.19 considering TI , not as in Section 6.3 fitting the vertical profile of the streamwise average wind speed.

7.5 Parameter assessment for the pressure gradient model

In the Section 7.2, the 3DSL model was further developed including the streamwise pressure gradient close to the rotor, namely within its induction range. In the actual implementation, the induction range extends from 1 D upstream to 2.5 D downstream. In that region, the streamwise pressure gradient is approximated scaling the results from a vortex-cylinder model with the factor G_γ and reducing the turbulent diffusion with the linear filter function F_2 which grows from 0 to 1 while moving downstream from the rotor up to x_{F2} .

Suitable values for these parameters are investigated in this section, first on the base of a single wake simulated with LES, then using lidar measurements as a reference. The two reference cases are extracted from Chapter 6 (Test case 1) and Section 7.4 (C_T class 0.8). Their main characteristics are summed up in Table 7.3.

While considering F_2 the same value $x_{F2}=5.5$ could be applied to reproduce the wakes of both the LES and the lidar measurements, only with different values of G_γ – namely 1.15 and 1.25 for the former and the latter case, respectively – a fair agreement with both reference cases could be achieved (see Figures 7.6 and 7.7).

As shown in Fig. 7.6, the 3DSL model simulations with the combination of parameters $x_{F2}=5.5$, $G_\gamma=1.125$ (red dash-dot line) are in fair agreement with the LES reference (blue circles). In general, the hub-height deficit is matched well, sometimes with a little overestimation. In the lower part of the wake, the wind deficit recovers faster, in particular between 8 D and 12 D (Fig. 7.6a, central line). The same can be observed for negative y . The black dash lines indicate the simulation with the parameters obtained from the comparison with the lidar measurements, i.e. $x_{F2}=5.5$, $G_\gamma=1.25$. With these settings, the agreement with the reference is poor at $x=2$ D where the deficit is clearly overestimated. However, the exceeding deficit has almost completely recovered at $x=4$ D.

For the comparison of the 3DSL model with the wake profiles from the lidar measurements the same notation as in Fig. 7.6 is applied to Fig. 7.7. At the first two sections downstream of the rotor ($x=2.3$ D), the 3DSL model simulations with $G_\gamma=1.25$ (black dash line) match the reference

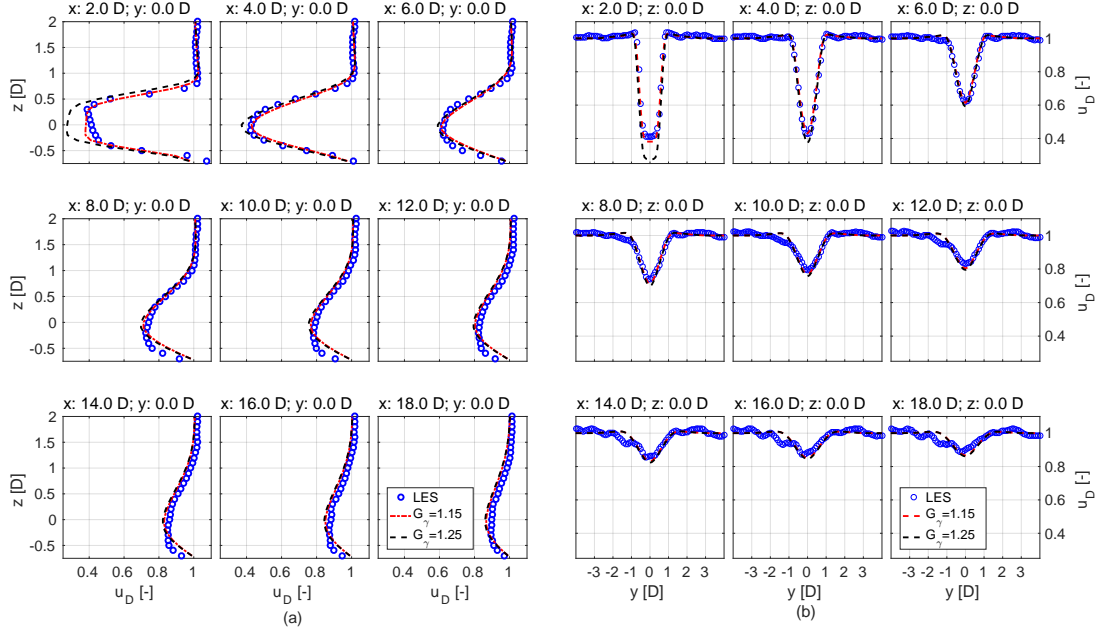


Figure 7.6: Horizontal (a) and vertical (b) profiles of the normalised streamwise wind component simulated with the 3DSL model applying $x_{F2}=5.5$ in combination with $G_\gamma=1.15$ (red dash-dot line) and $G_\gamma=1.25$ (black dash line). The results are compared to the reference profiles from the large-eddy simulation (LES) wind field at different downstream position (blue circles).

(blue circles) almost perfectly, while with $G_\gamma=1.25$ (red dash-dot line) they underestimate the wind deficit. From $x=4D$ the two values of G_γ produce very similar profiles, with the centre-line wind deficit very close to the reference. However, the wind speed in the wake is overestimated at its flanks, where the wind speed deficit recovers faster.

While close in the near-wake development range the two comparisons show opposite results, the same tendency was observed further downstream. This means that the far-wake is not very sensitive to the initial conditions. The disagreement in the near-wake could be explained by the different atmospheric conditions of the two reference cases. In fact, the LES are characterised by lower diffusive conditions than the lidar measurements (compare u_* and Φ_m in Table 7.3). It follows that, in the LES, less energy from the pressure gradient budget is recovered than in the lidar measurements. Therefore a lower G_γ is needed to compensate the recovery effects not considered by the vortex-cylinder model on which the pressure gradient model is based.

The results show also the limitations of the eddy-viscosity model implemented in the 3DSL model. First, the common value $x_{F2}=5.5$ for both comparisons indicates that the diffusion due to ambient turbulence is overestimated in the near-wake and needs to be scaled down beyond the range affected by the streamwise pressure gradient. Second, the diffusion in the far-wake at the flanks of the wind deficit seems also to be little overestimated by the eddy-viscosity model.

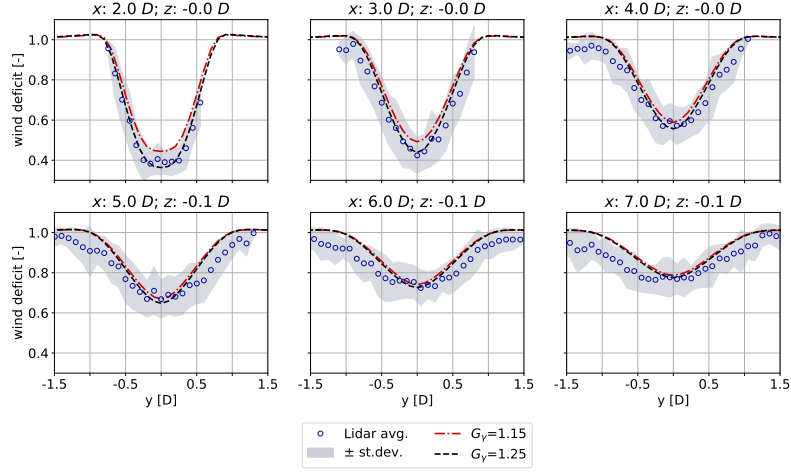


Figure 7.7: Horizontal profiles of the normalised streamwise wind component simulated with the 3DSL model applying $x_{F2}=5.5$ in combination with $G_\gamma=1.15$ (red dash-dot line) or $G_\gamma=1.25$ (black dash line). The results are compared to the reference profiles measured with a nacelle-based lidar at different downstream positions (blue circles).

7.6 Evaluation of the 3DSL model: Simulation of multiple wakes

In the assessment of Section 7.5, single wakes simulated with the elaborated version of the 3DSL model compared well with LES and lidar measurements. In this section, the focus is on multiple wakes. Accordingly, the 3DSL model is applied to simulate the wakes generated by three turbines with 6 D streamwise separation, applying a cumulative cross-stream displacement of 0.0 D, 0.5 D and 1.5 D in three different cases, respectively. In the first case, the downstream rotors are in full-wake conditions, in the second one in partial-wake conditions and in the last case the rotors are alongside the wakes. The layout of the three conditions is illustrated in Fig. 7.8.

The correction factors $C_{aero}=0.45$ and $C_{aero}=0.25$ are applied to simulate the lower aerodynamic efficiency of the rotor blades in wakes in the first and second layout, respectively. In these two cases, the filter function F_1 is applied to all turbines considering the downstream distance from the first rotor because the downstream turbines are in full and partial-wake, respectively. In these conditions, the eddy-viscosity can already be considered fully developed. These settings do not

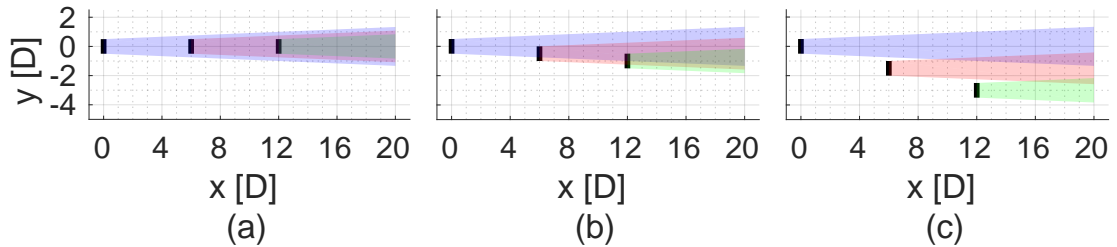


Figure 7.8: Layout of the simulated turbines with the rotor in different wake conditions: full-wake (a), partial-wake (b) and alongside-wake (c) rotor conditions.

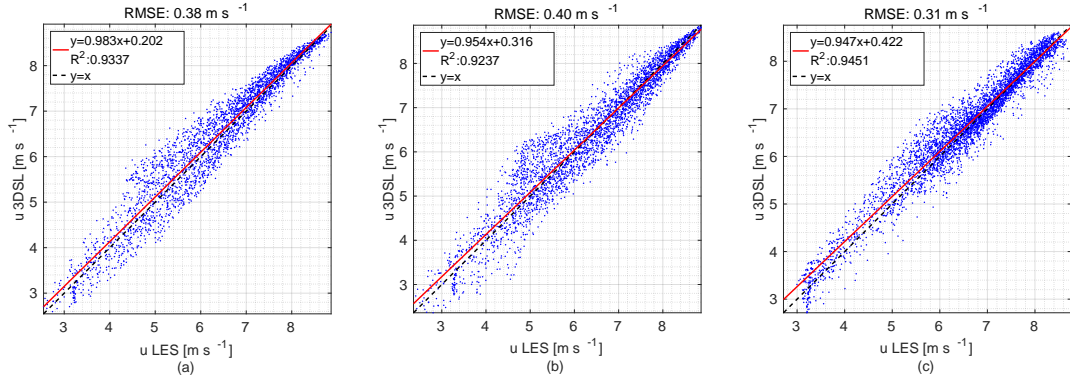


Figure 7.9: Scatter plot and corresponding regression line and root-mean-square error (RMSE) of the streamwise wind component derived from the 3DSL model in relation to the reference field calculated with large-eddy simulations (LES) for (a) full-wake, (b) partial-wake and (c) alongside-wake rotor conditions.

apply to the third case in which there is not a direct wake-turbine interaction.

The assessment is based on LES with the inflow conditions described in Table 7.3. The same LES wakes as in Section 6.4.2 to Section 6.4.4 are applied here as a reference too. While in Section 6.4 the assessment considers the points within the rotor area of virtual turbines in the wakes, this section considers the streamwise wind speed simulated at nine distances downstream of the upfront turbine. The nine cross-sections are equally spaced from 2D to 18D.

In Fig. 7.9, the regression analysis of the wind speed values on the nine cross-sections provides a quantitative evaluation of the 3DSL model simulations. Panels (a), (b) and (c) present the full-wake, partial-wake and alongside-wake rotor conditions, respectively. To avoid a possible bias from the undisturbed flow outside of the waked areas, only wind speed values below or equal 98% of the free hub-height wind speed u_{HH} were analysed.

The results of the three wake situations considered show a decent correlation between the 3DSL model and LES wind. A larger scatter characterises the intermediate wind speed range.

Figures 7.10 to 7.12 juxtapose the streamwise wind speed simulated with the 3DSL model and with LES for the cases of full-wake, partial-wake and alongside-wake rotor conditions. The rotor of the nearest turbine is drawn with a solid black line to help to orientate on the cross-sections. From a qualitative comparison, the fair correlation of the regression analysis between the two simulation models is confirmed. Considering the same selection of points, the absolute deviation $|\Delta u_D|$ between the 3DSL model and LES is on average around 3.5% of the upstream hub-height wind speed u_{HH} . High deviations around 18% of u_{HH} are observed at the boundary of the wake in correspondence to the cross-sections of the downstream rotors (6D and 12D). In the alongside-wake condition (Fig. 7.12), such differences are also observed close to the lower boundary at all sections downstream of the second turbine. There, the coalescing wakes measured with the 3DSL model mix slower than in the reference case. These differences might correspond to the large scatter observed in the intermediate wind speed range of the regression analysis.

The distribution of the vertical and lateral wind speed components v and w on the vertical cross-sections gives some hints to discuss the results. Similar aspects can be observed in all the wake

situations; however, only the full-wake condition is addressed in the following for sake of summary. In this respect, Figures 7.13 and 7.14 compare the results in terms of v and w , respectively.

In the former, a change of sign of v can be identified along the vertical coordinate z . This is clear evidence of vertical veer. In this condition, the wind deficit of wakes tends to have a skewed shape. With little abstraction, this distortion of the deficit can be intuited in the results of Figures 7.10 to 7.12.

Looking at w on the vertical cross-sections in Fig. 7.14 non-homogeneous convective structures can be identified. Not only is convection source of turbulence, but it also plays an important role to balance the mass flow.

Vertical veer and convection are not modelled into the 3DSL model yet; they can be a reason of the deviation from the LES, together with the limits of the eddy-viscosity model mentioned analysing single wakes in Section 7.5.

7.7 Summary and discussion of the results

The structure of this chapter is two-folded. In the first part, it focused on a few improvements of the 3DSL model, in the second one on its application to single and multiple wakes.

Concerning the further development of the model, the actuator disc model used to initialise the simulations was replaced by a more sophisticated streamwise pressure gradient model based on a vortex-cylinder potential flow. Then, a more robust and stable numerical formulation was implemented. Last, the turbulence length scale was calibrated using wake measurements sampled with a scanning lidar from the nacelle of an offshore turbine.

With respect to the application of the 3DSL model, simulations of single and multiple wakes were compared with the nacelle-based lidar measurements mentioned before and with large-eddy simulations. A reasonable agreement with the two sources of reference was found in all comparisons. At the same time, the comparisons exposed some limitation of the pressure gradient model and of the eddy-viscosity model. In particular, it was found that: (i) the pressure gradient model depends on the ambient eddy-viscosity and (ii) the width of the wakes simulated with the 3DSL model reduces faster than in the reference cases analysed. From the first observation, it can be concluded that a calibration of the pressure gradient model with respect to different diffusive condition is required. The second point suggests that the length scale applied to model the turbulent diffusion driven by the wake shear may lack in detail. A refined model could improve the results. For instance, the formulation suggested by Iungo et al., (2018) could be a possible alternative. Its main advantage is to consider also the reduction of turbulent kinetic energy due to dissipation along with the generation by ambient turbulence and by the shear layer of the wake which are already included in the current implementation.

Other possible improvements could consider to include the wake rotation and to chose more sophisticated boundary conditions, for instance including vertical veer.

The observed limitations are a drawback of assumptions and simplifications implemented in the 3DSL model. Nevertheless, in the test cases analysed in this chapter, the 3DSL model was able to match the reference wind fields with discrete accuracy. This is an indication that those assumptions and simplifications are reasonable.

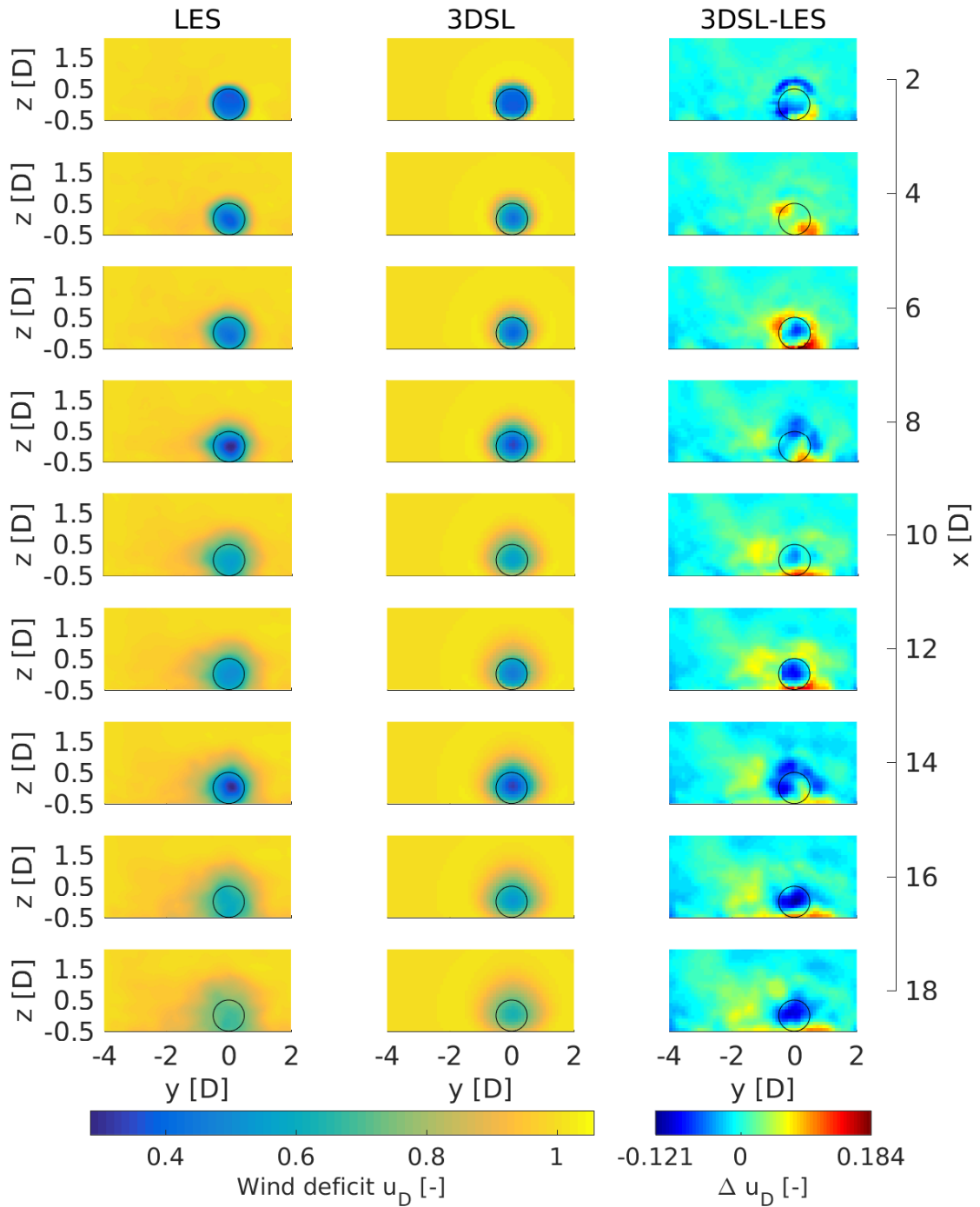


Figure 7.10: Juxtaposition (left and central columns) and difference (right column) of the results from large-eddy (LES) and 3DSL model simulations with respect to the normalised streamwise wind speed component estimated on nine downstream cross-sections for the full-wake rotor conditions. The solid black lines delineate the area of the closest upstream rotor.

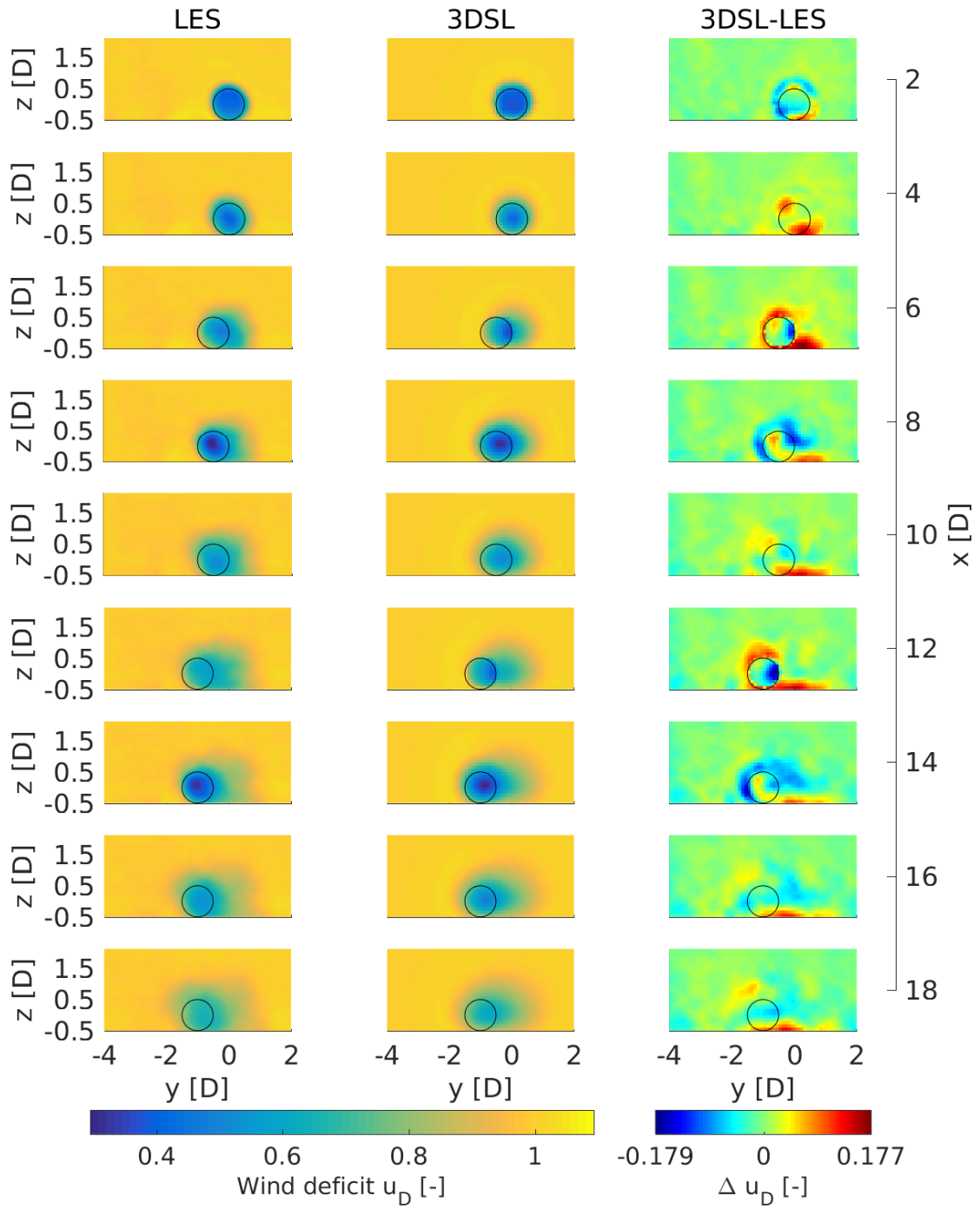


Figure 7.11: Juxtaposition (left and central columns) and difference (right column) of the results from large-eddy (LES) and 3DSL model simulations with respect to the normalised streamwise wind speed component estimated on nine downstream cross-sections for the partial-wake rotor conditions. The solid black lines delineate the area of the closest upstream rotor.

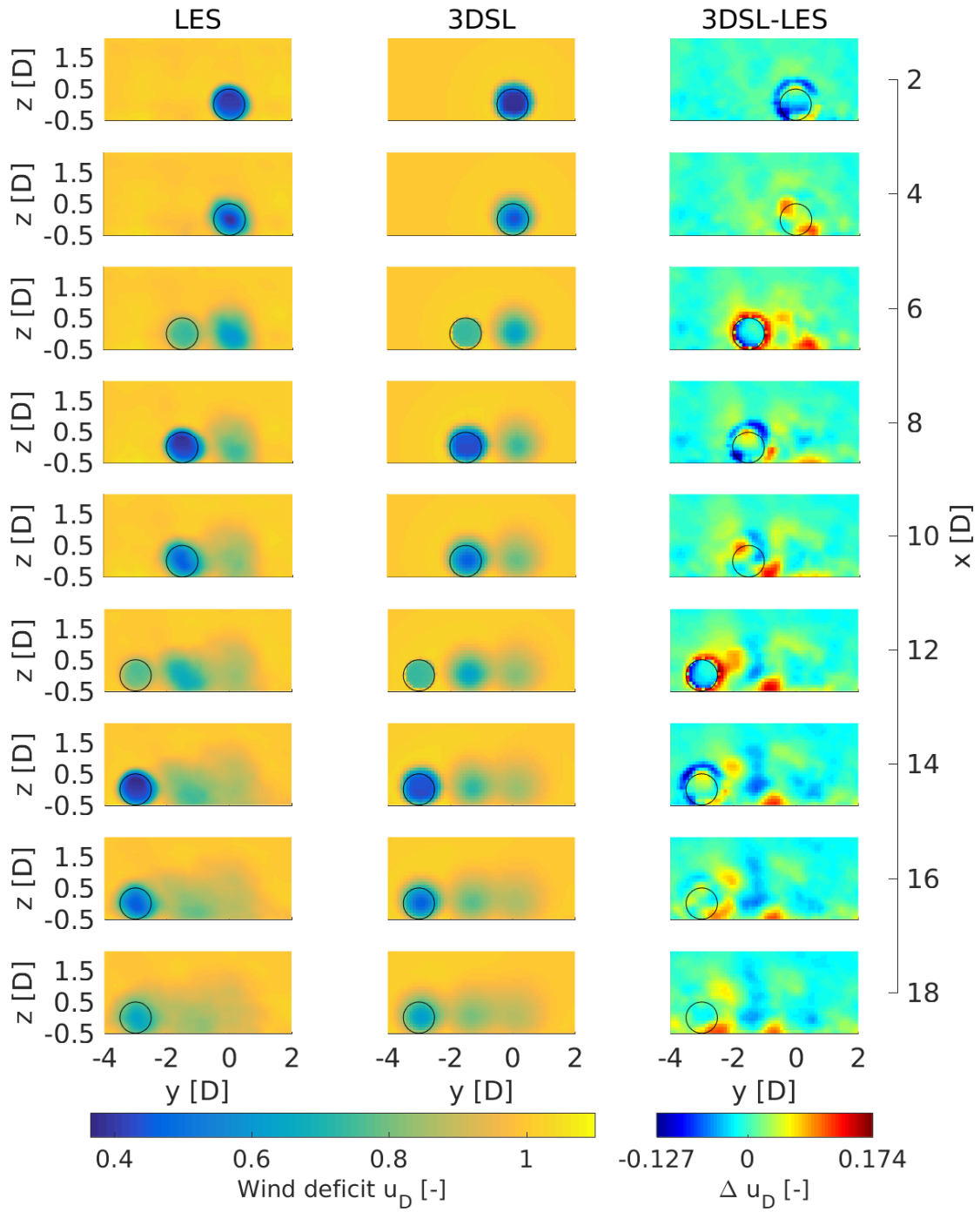


Figure 7.12: Juxtaposition (left and central columns) and difference (right column) of the results from large-eddy (LES) and 3DSL model simulations with respect to the normalised streamwise wind speed component estimated on nine downstream cross-sections for the alongside-wake rotor conditions. The solid black lines delineate the area of the closest upstream rotor.

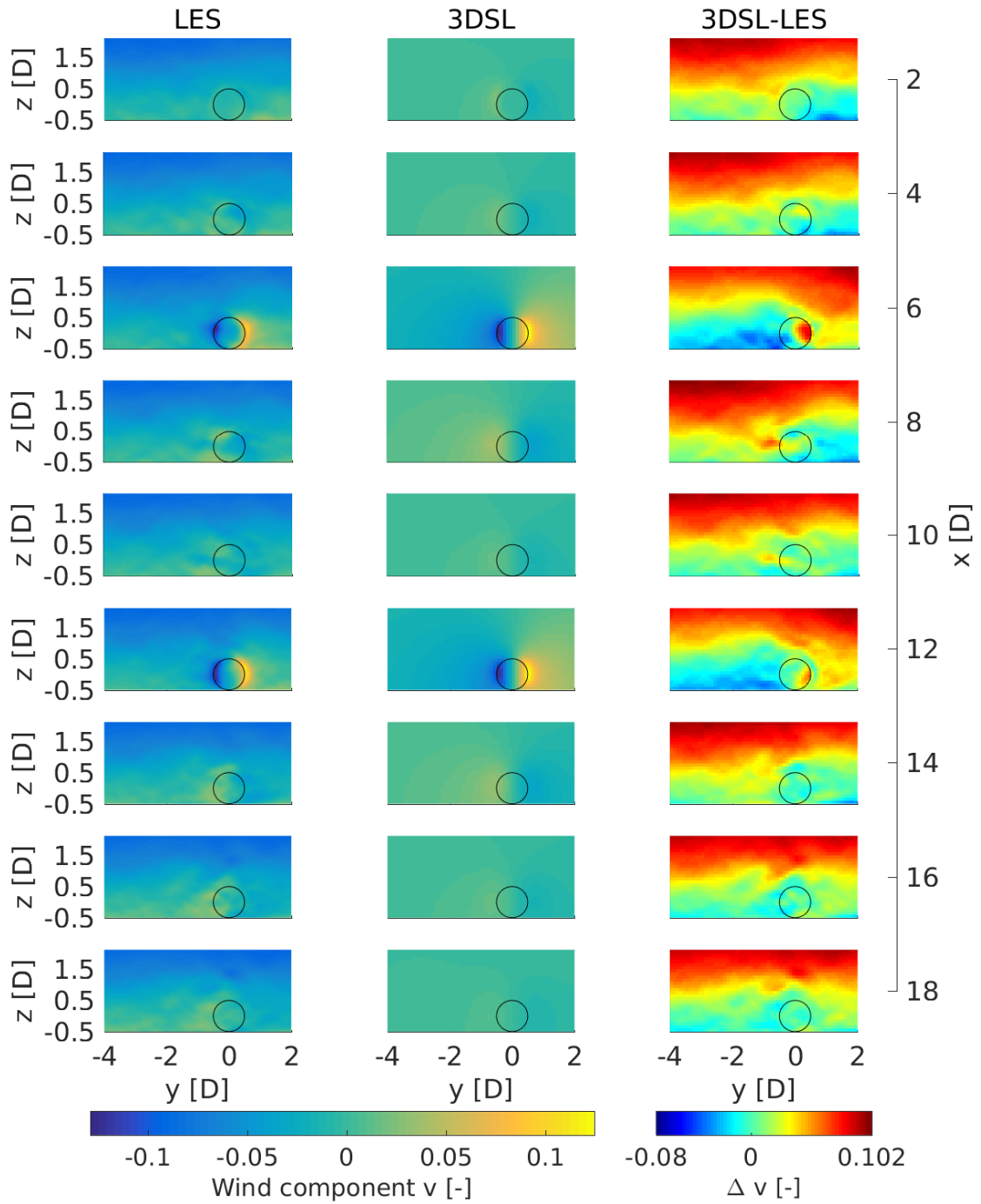


Figure 7.13: Juxtaposition (left and central columns) and difference (right column) of the results from large-eddy (LES) and 3DSL model simulations with respect to the normalised cross-stream wind speed component estimated on nine downstream cross-sections for the full-wake rotor conditions. The solid black lines delineate the area of the closest upstream rotor.

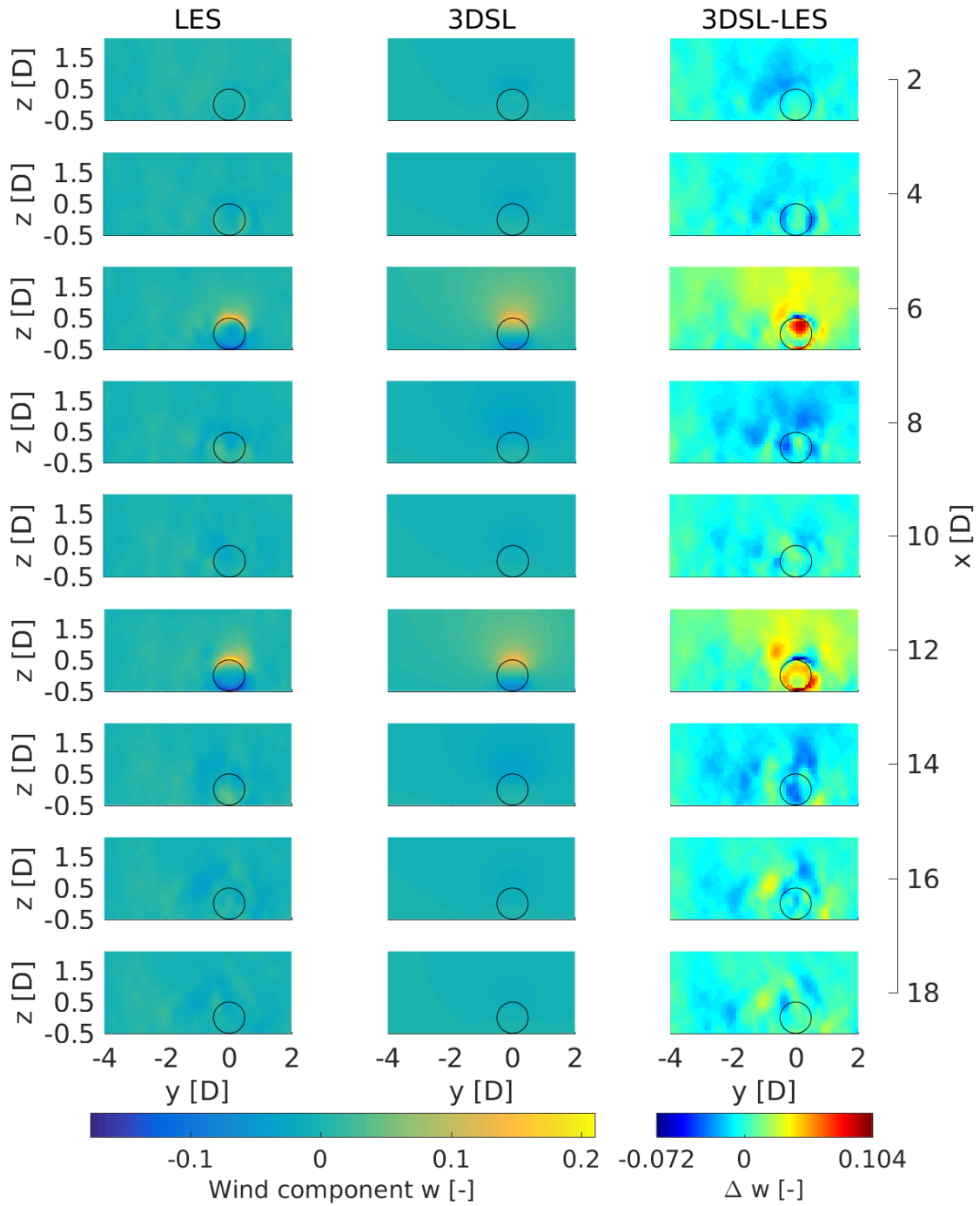


Figure 7.14: Juxtaposition (left and central columns) and difference (right columns) of the results from large-eddy (LES) and 3DSL model simulations with respect to the normalised vertical wind speed component estimated on nine downstream cross-sections for full-wake rotor conditions. The solid black lines delineate the area of the closest upstream rotor.

Conclusion

8.1 Summary and final remarks

The overall objective of this thesis was to develop an engineering model for multiple wakes, i.e. the flow propagating downstream when a wake passes through a turbine rotor or close alongside it. On the one hand, the methodology was based on the combination, simplification and elaboration of existing flow models; on the other hand, the calibration and verification of the resulting flow model were done with lidar wake measurements and large-eddy simulations (LES). In this respect, the overall objective was reformulated as two sub-objectives:

1. Develop methodologies for the assessment of wakes with lidar measurements.
2. Develop an engineering wake model which abandons the idea of single wakes to consider multiple wakes as a whole.

Accordingly, a large part of the research was dedicated to the experimental investigation of wakes using lidars. Some approaches to study the average wind profile in a wake or its dynamic were tested in a virtual environment (Chapter 2). The results confirmed that lidar measurements are not always reliable in wakes. However, it was shown that simulations of lidar wake measurements can give insight into the distortion introduced into the measurements by the lidars itself. A new approach was developed to measure the frequency content of the wake meandering. The approach was implemented in full-field experiments and lidar simulations were applied as proof-of-concept (Chapter 3 and 4). The results showed that the low-frequency energy content of turbulent fluctuations is higher at the boundary of the wake than around the wake axis. Furthermore, the findings from an exemplary analysis suggested that the increased level of energy content could be related to the wake meandering. Lidar wake measurements were subsequently applied to wake modelling (Chapter 5). Based on the experience gathered studying wake measurements with lidar, an experimental campaign was designed to capture the average shape of a single wake. The measurements were taken from the nacelle of an offshore wind turbine. The wind field reconstruction model applied to the lidar data was verified against wind measurements from a meteorological tower close to the turbine and the results were used to calibrate an analytical wake model.

The results summarised above were obtained applying lidar measurements to assess average and dynamic features of wakes. In this respect, not only is the first of the two sub-objectives accomplished: The research activity on which the results are founded also addressed a more general question:

How to deal with the limitations of lidar technology being applied to wake measurements?

The temporal and spatial averaging of lidar measurements is indeed a huge concern for lidar measurements in wakes. However, lidar's weaknesses are known and can be mitigated by applying the following approach: (i) Define the objective of the measurements – e.g. the average shape of the wake, or its position. (ii) Develop a methodology (measurement setup, scanning trajectory, wind field reconstruction model) which minimises the impact of the lidar measurements on the results – for instance, multi-lidar configurations or fixed-point measurements. (iii) Apply lidar simulations to verify the methodology, estimate errors and possibly optimise the methodology to minimise the errors.

In parallel to the research about lidar wake measurements, a new engineering wake model for multiple wakes was developed. The model is based on a shear-layer approximation of the equations governing the flow in the wake. Common shear-layer models applied to wake simulations assume an axisymmetric flow. This assumption is not always valid for multiple wakes. In these situations, the wakes are simulated individually and their effects are cumulated in the overlapping areas. The new model is three-dimensional, hence it does not assume axisymmetric wakes and it can also directly simulate multiple wakes. In some exemplary simulations of multiple wakes, the three-dimensional shear-layer (3DSL) model performed better than a common two-dimensional implementation with respect to LES used as reference (Chapter 6). After some improvements to the near-wake module implemented in the initial formulation, the 3DSL model was first calibrated for single wakes using lidar measurements and LES; then, it was applied to simulate multiple wakes and finally, the results were evaluated against LES of the same upstream wake conditions (Chapter 7). The 3DSL model could reproduce the main features of the wakes, however, some limitations were identified. In particular, different setting points were found for the near-wake module and the eddy-viscosity model underestimated turbulent diffusion at the outer boundaries of the wake. Nevertheless, considering the simplifications included in the 3DSL model an overall good agreement with LES can be stated.

With this achievement, also the second of the sub-objectives introduced at the beginning can be considered accomplished. However, looking back at the development process of the 3DSL model someone may still want to ask:

How far is it possible to conveniently improve the physics of engineering wake models?

During the development of the 3DSL model, a wide range of options was investigated with respect to the numerical implementations, the wake and ambient eddy-viscosities and the rotor model. Often proportionality parameters, efficiency coefficients, length scales or constant quantities were required. Sometimes, the same combinations of their values could be found for different verification cases, sometimes not. In the end, the settings provided positive results, but it had been a long journey. This means that it is possible to simplify the physical description of wakes with a reasonable fidelity of the results to reality. However, a refined tuning process may be required; furthermore, it must be

considered that the results of the tuning may not be valid overall. In this respect, a large number of parameters implemented into an engineering model is a barrier to its application. This is one of the main limitations of reducing physical complexity and also explains the broad diffusion of axisymmetric wake models.

8.2 Outlook

Lidar measurements of wakes were studied in this work. An engineering wake model for multiple wakes was developed and several verification tests were conducted, some of them based on lidar measurements. The next steps could follow two natural directions: further testing and further development.

Considering testing activity, two important points were not fully addressed by the presented research. The first one is the calibration and verification of single wake simulations at different turbulence intensity values. The calibration could be carried out on the basis of new large-eddy simulations taking advantage of the possibility to set the required atmospheric conditions; the results could then be verified against measurements from full-field experiments. The second point deals with the verification of multiple wakes simulations against full-field experimental data. The measurement campaign presented in Chapter 5 was supposed to provide a useful dataset for both points. Unfortunately, no suitable measurements were available because of external issues (e.g. visibility, wind speed and direction, operational conditions of the turbines, measurement quality and lidar functionality). This shortage should be addressed next.

Moving on from verification tests, the 3DSL model could be applied to estimate the power production of wind turbines in a wind farm. For this purpose, round-robin exercises could be considered, for instance the "Lillgrund 360 Efficiency" benchmark (IEA Wind Task 31, 2011). This test case was issued by the Wake bench community in the framework of the International Energy Agency Implementing Agreement Wind Task 31. The objective is to estimate the efficiency of the wind farm (48 wind turbines) for every 5° sector as the total power produced by the wind farm, normalised by the power of specific turbines facing the undisturbed flow.

In terms of development, a revision of the eddy-viscosity model could remedy the too fast recovery observed at the flanks of the wakes simulated with the 3DSL model. The implementation suggested by Iungo et al., (2018) is a possible example to follow.

Until now the focus has been on the average wake flow. Next, the wake dynamics could be implemented into the 3DSL model too. Wake meandering models assume that the wake off-axis displacement is driven by large scale structures of atmospheric turbulence. The challenge for the simulation of multiple wakes is to understand the evolution and correlation of these turbulence structures within a wind farm. Lidar or more generally remote sensing experimental activity could be applied here to track parallel or consecutive wakes in a wind farm and to study the cross-correlation between their meandering paths.

Even if the framework of wind energy has been changing in the last years and the interest towards mesoscale models to estimate the overall effects of the wakes propagating from entire wind farms has increased, engineering wake models are going to remain an important subject of investigation motivated for instance by wind farm control applications, which need fast and accurate models to simulate the interaction among wakes and turbines to define the optimal control strategy.

References

Since Chapters 3, 4, 5 and 6 consist of scientific publication, they already include the references of the cited literature. For this reason, the following list considers only publications cited in Chapters 1,2, 7 and 8.

- Ainslie J., F. (1988). “Calculating the Flowfield in the Wake of Wind Turbines”. In: *Journal of Wind Engineering and Industrial Aerodynamics* 27, pp. 213–224. DOI: 10.1016/0167-6105(88)90037-2.
- Aitken, M. L., R. M. Banta, Y. L. Pichugina, and J. K. Lundquist (2014). “Quantifying Wind Turbine Wake Characteristics from Scanning Remote Sensor Data”. In: *J. Atmos. Oceanic Technol.* 31.4, pp. 765–787. ISSN: 0739-0572. DOI: 10.1175/JTECH-D-13-00104.1.
- Archer, C. L., A. Vassel-Behagh, C. Yan, S. Wu, Y. Pan, J. F. Brodie, and A. E. Maguire (2018). “Review and evaluation of wake loss models for wind energy applications”. In: *Applied Energy* 226, pp. 1187–1207. ISSN: 0306-2619. DOI: 10.1016/j.apenergy.2018.05.085.
- Banakh, V. and C. Werner (2005). “Computer simulation of coherent Doppler lidar measurement of wind velocity and retrieval of turbulent wind statistics”. In: *Optical Engineering* 44. DOI: 10.1117/1.19551670.
- Barthelmie, R. J., P. Doubrawa, H. Wang, and S. C. Pryor (2016). “Defining wake characteristics from scanning and vertical full- scale lidar measurements”. In: *Journal of Physics: Conference Series* 753.3, p. 032034. URL: <http://stacks.iop.org/1742-6596/753/i=3/a=032034>.
- Bastine, D., L. Vollmer, M. Wächter, and J. Peinke (2018). “Stochastic Wake Modelling Based on POD Analysis”. In: *Energies* 11.3. ISSN: 1996-1073. DOI: 10.3390/en11030612.
- Bendat, J. S. and G. Piersol A. (2000). *Random data analysis and measurement procedures*. Wiley Interscience. DOI: 10.1002/9781118032428.
- Bilbro, J., G. Fichtl, D. Fitzjarrald, M. Krause, and R. Lee (1984). “Airborne Doppler Lidar Wind Field Measurements”. In: *Bulletin of the American Meteorological Society* 65.4, pp. 348–359. DOI: 10.1175/1520-0477(1984)065<0348:ADLWFM>2.0.CO;2.
- Bodini, N., D. Zardi, and J. K. Lundquist (2017). “Three-dimensional structure of wind turbine wakes as measured by scanning lidar”. In: *Atmospheric Measurement Techniques* 10.8, pp. 2881–2896. DOI: 10.5194/amt-10-2881-2017. URL: <https://www.atmos-meas-tech.net/10/2881/2017/>.

- Boquet, M., P. Royer, J.-P. Cariou, M. Machta, and M. Valla (2016). “Simulation of Doppler Lidar Measurement Range and Data Availability”. In: *Journal of Atmospheric and Oceanic Technology* 33.5, pp. 977–987. DOI: 10.1175/JTECH-D-15-0057.1.
- Branlard, E. and M. Gaunaa (2015). “Cylindrical vortex wake model: right cylinder”. In: *Wind Energy* 18.11, pp. 1973–1987. ISSN: 1099-1824. DOI: 10.1002/we.1800. URL: <http://dx.doi.org/10.1002/we.1800>.
- Burton, T., N. Jenkins, D. Sharpe, and E. Bossanyi (2011). *Wind Energy Handbook, 2nd Edition*. John Wiley & Sons, Ltd., Publication.
- Carbajo Fuertes, F., C. D. Markfort, and F. Porté-Agel (2018). “Wind Turbine Wake Characterization with Nacelle-Mounted Wind Lidars for Analytical Wake Model Validation”. In: *Remote Sensing* 10.5. ISSN: 2072-4292. DOI: 10.3390/rs10050668. URL: <http://www.mdpi.com/2072-4292/10/5/668>.
- Cherukuru, N. W., R. Calhoun, R. Krishnamurthy, S. Benny, J. Reuder, and M. Flügge (2017). “2D VAR single Doppler lidar vector retrieval and its application in offshore wind energy”. In: *Energy Procedia* 137. 14th Deep Sea Offshore Wind R&D Conference, EERA DeepWind’2017, pp. 497–504. ISSN: 1876-6102. DOI: 10.1016/j.egypro.2017.10.378.
- Churchfield, M., Q. Wang, A. Scholbrock, T. Herges, T. Mikkelsen, and M. Sjöholm (2016). “Using High-Fidelity Computational Fluid Dynamics to Help Design a Wind Turbine Wake Measurement Experiment”. In: *Journal of Physics: Conference Series* 753.3, p. 032009. URL: <http://stacks.iop.org/1742-6596/753/i=3/a=032009>.
- Clifton, A., P. Clive, J. Gottschall, D. Schlipf, E. Simley, L. Simmons, D. Stein, D. Trabucchi, N. Vasiljevic, and I. Würth (2018). “IEA Wind Task 32: Wind Lidar Identifying and Mitigating Barriers to the Adoption of Wind Lidar”. In: *Remote Sensing* 10.3. ISSN: 2072-4292. DOI: 10.3390/rs10030406. URL: <http://www.mdpi.com/2072-4292/10/3/406>.
- Crespo, A., J. Hernández, and S. T. Frandsen (1999). “Survey of modelling methods for wind turbine wakes and wind farms”. In: *Wind Energy* 2.1, pp. 1–24. ISSN: 1099-1824. DOI: 10.1002/(SICI)1099-1824(199901/03)2:1<1::AID-WE16>3.0.CO;2-7.
- Crespo, A., F. Manuel, D. Moreno, E. Fraga, and J. Hernández (1985). “Numerical analysis of wind turbine wakes”. In: *Delphi Workshop on Wind Energy Applications*, pp. 15–25.
- Dörenkämper, M., B. Witha, G. Steinfeld, D. Heinemann, and M. Kühn (2015). “The impact of stable atmospheric boundary layers on wind-turbine wakes within offshore wind farms”. In: *Journal of Wind Engineering and Industrial Aerodynamics* 144. Selected papers from the 6th International Symposium on Computational Wind Engineering CWE 2014, pp. 146–153. ISSN: 0167-6105. DOI: 10.1016/j.jweia.2014.12.011.
- Doubrawa, P., R. J. Barthelmie, H. Wang, and M. J. Churchfield (2017). “A stochastic wind turbine wake model based on new metrics for wake characterization”. In: *Wind Energy* 20.3, pp. 449–463. DOI: 10.1002/we.2015.
- Drechsel, S., G. J. Mayr, M. Chong, and F. K. Chow (2010). “Volume Scanning Strategies for 3D Wind Retrieval from Dual-Doppler Lidar Measurements”. In: *Journal of Atmospheric and Oceanic Technology* 27.11, pp. 1881–1892. DOI: 10.1175/2010JTECHA1495.1.
- Dyer, A. (1974). “A review of flux-profile relationships”. In: *Boundary-Layer Meteorology* 7.3, pp. 363–372. ISSN: 0006-8314. DOI: 10.1007/BF00240838.
- España, G., S. Aubrun, S. Loyer, and P. Devinant (2011). “Spatial study of the wake meandering using modelled wind turbines in a wind tunnel”. In: *Wind Energy* 14.7, pp. 923–937. ISSN: 1099-1824. DOI: 10.1002/we.515.

- (2012). “Wind tunnel study of the wake meandering downstream of a modelled wind turbine as an effect of large scale turbulent eddies”. In: *Journal of Wind Engineering and Industrial Aerodynamics* 101, pp. 24–33. ISSN: 0167-6105. DOI: 10.1016/j.jweia.2011.10.011.
- European Union (2019). URL: https://ec.europa.eu/clima/sites/clima/files/long_term_strategy_brochure_en.pdf.
- Ferziger, J. H. and M. Perić (2008). *Numerische Strömungsmechanik*. Springer. DOI: 10.1007/978-3-540-68228-8.
- Frandsen, S. T. (2007). “Turbulence and turbulence-generated structural loading in wind turbine clusters (Risoe-R.1188(EN))”. PhD thesis. Risoe - DTU.
- Frandsen, S. T., J. B. Rebecca, S. Pryor, O. Rathmann, S. Larsen, J. Højstrup, and M. Thøgersen (2006). “Analytical modelling of wind speed deficit in large offshore wind farms”. In: *Wind Energy* 9.1-2, pp. 39–53. ISSN: 1099-1824. DOI: 10.1002/we.189.
- Frehlich, R. (1996). “Simulation of coherent Doppler lidar performance in the weak signal regime”. In: *Journal of Atmospheric and Oceanic Technology* 13, pp. 646–658. DOI: "10.1175/1520-0450(2000)039<0245:SOCCLP>2.0.CO;2".
- (2001). “Estimation of Velocity Error for Doppler Lidar Measurements”. In: *Journal of Atmospheric and Oceanic Technology* 18.10, pp. 1628–1639. DOI: 10.1175/1520-0426(2001)018<1628:EOVEFD>2.0.CO;2.
- García, L., M. Vatn, F. Mühle, and L. Sætran (2017). “Experiments in the wind turbine far wake for the evaluation of an analytical wake model”. In: *Journal of Physics: Conference Series* 854.1, p. 012015. DOI: 10.1088/1742-6596/854/i=1/a=012015.
- Gerke, N., I. Reinwardt, P. Dalhoff, M. Dehn, and W. Moser (2018). “Validation of turbulence models through SCADA data”. In: *Journal of Physics: Conference Series* 1037.7, p. 072027. DOI: 10.1088/1742-6596/1037/7/072027.
- Hancock, P. E. and F. Pascheke (2014). “Wind-Tunnel Simulation of the Wake of a Large Wind Turbine in a Stable Boundary Layer: Part 2, the Wake Flow”. English. In: *Boundary-Layer Meteorology* 151.1, pp. 23–37. ISSN: 0006-8314. DOI: 10.1007/s10546-013-9887-x.
- Hassan, U. (1992). “A wind tunnel investigation of the wake structure within small wind turbine farms”. In: *E/5A/CON/5113/1890*.
- Herbert-Acero, J. F., O. Probst, P.-E. Réthoré, G. C. Larsen, and K. K. Castillo-Villar (2014). “A Review of Methodological Approaches for the Design and Optimization of Wind Farms”. In: *Energies* 7.11, pp. 6930–7016. ISSN: 1996-1073. DOI: 10.3390/en7116930. URL: <http://www.mdpi.com/1996-1073/7/11/6930>.
- Herges, T. G., J. C. Berg, J. T. Bryant, J. R. White, J. A. Paquette, and B. T. Naughton (2018). “Detailed analysis of a waked turbine using a high-resolution scanning lidar”. In: *Journal of Physics: Conference Series* 1037.7, p. 072009. DOI: 10.1088/1742-6596/1037/7/072009.
- IEA (2018). *Global Energy & CO2 Status Report 2018*. Tech. rep. International Energy Agency. URL: <https://webstore.iea.org/global-energy-co2-status-report-2018>.
- IEA Wind Task 31 (2011). *Website*. URL: <https://windbench.net/lillgrund-360-efficiency>.
- IEC (2005). *Wind turbines – Part 1: Design requirements*.
- (2017). *Wind energy generation systems - Part 12-1: Power performance measurements of electricity producing wind turbines*.
- Intergovernmental Panel on Climate Change (2018). *Global Warming of 1.5°C*. Tech. rep. URL: <https://www.ipcc.ch/sr15/>.

- Iungo, G. V. and F. Porté-Agel (2014). “Volumetric Lidar Scanning of Wind Turbine Wakes under Convective and Neutral Atmospheric Stability Regimes”. In: *Journal of Atmospheric and Oceanic Technology* 31.10, pp. 2035–2048. DOI: 10.1175/JTECH-D-13-00252.1.
- Iungo, G. V., V. Santhanagopalan, U. Ciri, F. Viola, L. Zhan, M. A. Rotea, and S. Leonardi (2018). “Parabolic RANS solver for low-computational-cost simulations of wind turbine wakes”. In: *Wind Energy* 21.3, pp. 184–197. DOI: 10.1002/we.2154.
- Jensen, N. O. (1983). *A note on wind generator interaction (Risoe-M-2411)*. Tech. rep. Risoe - DTU. URL: <http://130.226.56.153/rispubl/VEA/veapdf/ris-m-2411.pdf>.
- Jones, D., A. Sakhel, M. Buck, and P. Graichen (2019). *The European Power Sector in 2018: Up-to-date analysis on the electricity transition*. Tech. rep. Agora Energiewende and Sandbag. URL: https://www.agora-energiewende.de/fileadmin2/Projekte/2018/EU-Jahresauswertung_2019/Agora-Energiewende-European-Power-Sector-2018_WEB.pdf.
- Käsler, Y., S. Rahm, R. Simmet, and M. Kün (2010). “Wake Measurements of a Multi-MW Wind Turbine with Coherent Long-Range Pulsed Doppler Wind Lidar”. In: *Journal of atmospheric and oceanic technology* 27, pp. 1529–1532.
- Katic, I., J. Højstrup, and N. O. Jensen (1986). “A simple model for cluster efficiency”. In: *EWEC Proc. '86*, pp. 407–10.
- Lange, B., H.-P. Waldl, A. G. Guerrero, D. Heinemann, and R. J. Barthelmie (2003). “Modelling of offshore wind turbine wakes with the wind farm program FLaP”. In: *Wind Energy* 6.1, pp. 87–104. DOI: 10.1002/we.84.
- Larsen, G. C. (1988). *A Simple Wake Calculation Procedure*. English. ISBN: 87-550-1484-4. URL: http://orbit.dtu.dk/files/55567186/ris_m_2760.pdf.
- Larsen, G. C., H. A. Madsen, K. Thomsen, and T. J. Larsen (2008). “Wake meandering: a pragmatic approach”. In: *Wind Energy* 11.4, pp. 377–395. ISSN: 1099-1824. DOI: 10.1002/we.267.
- Lissaman P, B. S. (1979). “Energy effectiveness of arbitrary arrays of wind turbines”. In: *Journal of Energy* 3.6, pp. 323–328.
- Lundquist, J. K., M. J. Churchfield, S. Lee, and A. Clifton (2015). “Quantifying error of lidar and sodar Doppler beam swinging measurements of wind turbine wakes using computational fluid dynamics”. In: *Atmospheric Measurement Techniques* 8.2, pp. 907–920. DOI: 10.5194/amt-8-907-2015. URL: <http://www.atmos-meas-tech.net/8/907/2015/>.
- Machefaux, E. (2015). “Multiple Turbine Wakes”. PhD thesis. DTU Wind Energy. ISBN: 978-87-93278-21-9.
- Madsen, H. A., G. C. Larsen, T. J. Larsen, N. Troldborg, and R. Mikkelsen (2010). “Calibration and Validation of the Dynamic Wake Meandering Model for Implementation in an Aeroelastic Code”. In: *Journal of Solar Energy Engineering* 132.4, pp. 041014–041014. ISSN: 0199-6231. DOI: 10.1115/1.4002555.
- Martínez-Tossas, L. A., M. J. Churchfield, and C. Meneveau (2016). “A Highly Resolved Large-Eddy Simulation of a Wind Turbine using an Actuator Line Model with Optimal Body Force Projection”. In: *Journal of Physics: Conference Series* 753, p. 082014. DOI: 10.1088/1742-6596/753/8/082014.
- MEASNET (2016). *Evaluation of site-specific wind condition*. URL: http://www.measnet.com/wp-content/uploads/2016/05/Measnet_SiteAssessment_V2.0.pdf.
- Medici, D. and P. H. Alfredsson (2008). “Measurements behind model wind turbines: further evidence of wake meandering”. In: *Wind Energy* 11.2, pp. 211–217. ISSN: 1099-1824. DOI: 10.1002/we.247.

- Meyer Forsting, A. R., N. Troldborg, and A. Borraccino (2017). “Modelling lidar volume-averaging and its significance to wind turbine wake measurements”. In: *Journal of Physics: Conference Series* 854.1, p. 012014. URL: <http://stacks.iop.org/1742-6596/854/i=1/a=012014>.
- Moon, J. S., L. Manuel, M. J. Churchfield, S. Lee, and P. S. Veers (2018). “Toward Development of a Stochastic Wake Model: Validation Using LES and Turbine Loads”. In: *Energies* 11.1. ISSN: 1996-1073. DOI: 10.3390/en11010053.
- Muller, Y.-A., S. Aubrun, and C. Masson (2015). “Determination of real-time predictors of the wind turbine wake meandering”. In: *Experiments in Fluids* 56.3, p. 53. ISSN: 1432-1114. DOI: 10.1007/s00348-015-1923-9.
- Ott, S., J. Berg, and M. Nielsen (2011). *Linearised CFD Models for Wakes*. English. Danmarks Tekniske Universitet, Risø Nationallaboratoriet for Bæredygtig Energi. ISBN: 978-87-550-3892-9.
- Panofsky, H. and J. Dutton. *Atmospheric turbulence: Models and Methods for Engineering Applications*.
- Peña, A., C. Bay Hasager, B. Merete, J. B. Rebecca, F. Bingöl, J.-P. Cariou, S. Emeis, T. S. Frandsen, M. Harris, I. Karagali, S. Larsen, J. Mann, T. Mikkelsen, M. Pitter, C. P. Sara, A. Sathe, D. Schlipf, C. Slinger, and R. Wagner (2015). *Remote Sensing for Wind Energy*. Denmark: DTU Wind Energy.
- Pitter, M., S. Chris, and H. Michael (2015). “Remote Sensing for Wind Energy”. In: ed. by A. Peña. DTU Wind Energy. Chap. 4 Introduction to continuous-wave Doppler lidar, pp. 72–103.
- Quarton D, C. and F. Ainslie J (1989). “Turbulence in wind turbine wakes.” In: *European Wind Energy Conference EWEC’89*. Glasgow, 10-13 June 1989.
- Raach, S., D. Schlipf, and P. W. Cheng (2017). “Lidar-based wake tracking for closed-loop wind farm control”. In: *Wind Energy Science* 2.1, pp. 257–267. DOI: 10.5194/wes-2-257-2017.
- Raasch, S. and M. Schröter (2001). “PALM - A Large-Eddy Simulation Model Performing on Massively Parallel Computers”. In: *Meteor. Z.* 10, pp. 363–372. DOI: 10.1127/0941-2948/2001/0010-0363.
- Réthoré, P.-E., P. Fuglsang, G. C. Larsen, T. Buhl, T. J. Larsen, and H. A. Madsen (2013). “TOPFARM: Multi-fidelity optimization of wind farms”. In: *Wind Energy* 17.12, pp. 1797–1816. DOI: 10.1002/we.1667.
- Rettenmeier, A. (2015). “Remote Sensing for Wind Energy”. In: ed. by A. Peña. DTU Wind Energy. Chap. 8. Nacelle-based lidar systems, pp. 157–170.
- Rockel, S., J. Peinke, M. Hölling, and R. B. Cal (2016). “Wake to wake interaction of floating wind turbine models in free pitch motion: An eddy viscosity and mixing length approach”. In: *Renewable Energy* 85, pp. 666–676. ISSN: 0960-1481. DOI: 10.1016/j.renene.2015.07.012. URL: <http://www.sciencedirect.com/science/article/pii/S0960148115301087>.
- Rothermel, J., C. Kessinger, and D. L. Davis (1985). “Dual-Doppler Lidar Measurement of Winds in the JAWS Experiment”. In: *Journal of Atmospheric and Oceanic Technology* 2.2, pp. 138–147. DOI: 10.1175/1520-0426(1985)002<0138:DDLMO>2.0.CO;2.
- Sanderse, B., S. van der Pijl, and B. Koren (2011). “Review of computational fluid dynamics for wind turbine wake aerodynamics”. In: *Wind Energy* 14.7, pp. 799–819. ISSN: 1099-1824. DOI: 10.1002/we.458.
- Schepers, G. (2003). *ENDOW: Validation and improvement of ECN’s wake model*. Tech. rep. ECN.
- Schepers Jan, G. (2012). “Engineering models in wind energy aerodynamics. Development, implementation and analysis using dedicated aerodynamic measurements”. PhD thesis. ECN.

- Schlipf, D., F. Haizmann, N. Cosack, T. Siebers, and P. W. Cheng (2015). “Detection of Wind Evolution and Lidar Trajectory Optimization for Lidar-Assisted Wind Turbine Control”. In: *Meteorologische Zeitschrift* 24.6, pp. 565–579. DOI: 10.1127/metz/2015/0634.
- Schlipf, D., J.-J. Trujillo, V. Basterra, and M. Kühn (2009). “Development of a wind turbine lidar simulator”. In: *EWEC 2009*. Parc Chanot, Marseille, France 16-19 March 2009. DOI: 10.18419/opus-3914.
- Schmidt, J. and B. Stoevesandt (2014). “Wind farm optimisation with wakes from fluid dynamics simulations”. In: *EWEA Annual event*. DOI: 10.13140/2.1.2544.3847.
- Segalini, A. (2017). “Linearized simulation of flow over wind farms and complex terrains”. In: *Philosophical Transactions of the Royal Society A: Mathematical, Physical and Engineering Sciences* 375.2091, p. 20160099. DOI: 10.1098/rsta.2016.0099.
- Seibold, B. (2008). *A compact and fast Matlab code solving the incompressible Navier-Stokes equations on rectangular domains*. Tech. rep. Massachusetts Institute of Technology. URL: http://math.mit.edu/~gs/cse/codes/mit18086_navierstokes.pdf.
- Smalikho, I. N., V. A. Banakh, Y. L. Pichugina, W. A. Brewer, R. M. Banta, J. K. Lundquist, and N. D. Kelley (2013). “Lidar Investigation of Atmosphere Effect on a Wind Turbine Wake”. In: *J. Atmos. Oceanic Technol.* 30.11, pp. 2554–2570. ISSN: 0739-0572. DOI: 10.1175/JTECH-D-12-00108.1.
- Stull, R. (2017). *Practical Meteorology: An Algebra-based Survey of Atmospheric Science*. Ed. by U. of of British Columbia. version 1.02b. Sundog Publishing, LLC. ISBN: 978-0-88865-283-6.
- Thøgersen Morten, L., T. Sørensen, P. Nielsen, A. Grötzner, and S. Chun (2011). *WIndPro/Park. Introduction to Wind Turbine Wake Modelling and Wake Generated Turbulence*. EMD International A/S.
- Trabucchi, D., L. Vollmer, and M. Kühn (2017a). “3-D shear-layer model for the simulation of multiple wind turbine wakes: description and first assessment”. In: *Wind Energy Science* 2.2, pp. 569–586. DOI: 10.5194/wes-2-569-2017.
- Trabucchi, D., G. Steinfeld, D. Bastine, J.-J. Trujillo, J. Schneemann, and M. Kühn (2015a). “Study of wake meandering by means of fixed point lidar measurements: Spectral analysis of line-of-sight wind component”. In: vol. 625. 1, p. 012016. DOI: 10.1088/1742-6596/625/1/012016.
- Trabucchi, D., J.-J. Trujillo, and M. Kühn (2017b). “Nacelle-based Lidar Measurements for the Calibration of a Wake Model at Different Offshore Operating Conditions”. In: *Energy Procedia* 137. 14th Deep Sea Offshore Wind R&D Conference, EERA DeepWind’2017, pp. 77–88. DOI: 10.1016/j.egypro.2017.10.335.
- Trabucchi, D., J.-J. Trujillo, J. Schneemann, M. Bitter, and M. Kühn (2015b). “Application of staring lidars to study the dynamics of wind turbine wakes”. In: *Meteorologische Zeitschrift*, pp. 557–564. DOI: 10.1127/metz/2014/0610.
- Trabucchi, D., J.-J. Trujillo, G. Steinfeld, J. Schneemann, M. Machtaa, J. P. Cariou, and M. Kühn (2011). “Numerical assessment of performance of lidar WindScanners for wake measurements”. In: *EWEA Annual event*. Vortrag. URL: <http://www.ewea.org/annual2011/conference/conference-programme/> (visited on 04/10/2016).
- Troldborg, N. (2008). “Actuator Line Modeling of Wind Turbine Wakes”. PhD thesis. Technical University of Denmark - Department of Wind Energy, Risø Campus.
- Troldborg, N., J. N. Sorensen, and R. Mikkelsen (2010). “Numerical simulations of wake characteristics of a wind turbine in uniform inflow”. In: *Wind Energy* 13.1, pp. 86–99. ISSN: 1099-1824. DOI: 10.1002/we.345.

- Trujillo, J.-J., F. Bingöl, C. L. Gunner, J. Mann, and M. Kühn (2011). “Light detection and ranging measurements of wake dynamics. Part II: two-dimensional scanning”. In: *Wind Energy* 14.1, pp. 61–75. ISSN: 1099-1824. DOI: 10.1002/we.402.
- Trujillo, J.-J., K. S. J, I. Würth, D. Schlipf, and M. Kühn (2016). “Full-field assessment of wind turbine near-wake deviation in relation to yaw misalignment”. In: *Wind Energy Science* 1.1, pp. 41–53. DOI: 10.5194/wes-1-41-2016.
- van Dooren, M. F., D. Trabucchi, and M. Kühn (2016). “A Methodology for the Reconstruction of 2D Horizontal Wind Fields of Wind Turbine Wakes Based on Dual-Doppler Lidar Measurements”. In: *Remote Sensing* 8.10, p. 809. ISSN: 2072-4292. DOI: 10.3390/rs8100809.
- Vollmer, L., G. Steinfeld, D. Heinemann, and M. Kühn (2016). “Estimating the wake deflection downstream of a wind turbine in different atmospheric stabilities: an LES study”. In: *Wind Energy Science* 1.2, pp. 129–141. DOI: 10.5194/wes-1-129-2016.
- Werner, C. (2005). “Doppler Wind Lidar - Range-Resolved Optical Remote Sensing of the Atmosphere”. In: ed. by D. C. Weitkamp. Springer. Chap. 12, pp. 325–354. URL: http://dx.doi.org/10.1007/0-387-25101-4_12.
- Wildmann, N., S. Kigle, and T. Gerz (2018). “Coplanar lidar measurement of a single wind energy converter wake in distinct atmospheric stability regimes at the Perdigão 2017 experiment”. In: *Journal of Physics: Conference Series* 1037.5, p. 052006. DOI: 10.1088/1742-6596/1037/5/052006.
- WindEurope (2018). *Wind energy in europe-outlook to 2022*. URL: <https://windeurope.org/about-wind/reports/wind-energy-in-europe-outlook-to-2022/#download>.
- (2019). *Wind energy in Europe 2018*. URL: <https://windeurope.org/about-wind/statistics/european/wind-energy-in-europe-in-2018/>.
- Witha, B., G. Steinfeld, M. Dörenkämper, and D. Heinemann (2014). “Large-eddy simulation of multiple wakes in offshore wind farms”. In: *Journal of Physics: Conference Series* 555, p. 012108. DOI: 10.1088/1742-6596/555/1/012108.

Publications

Peer-reviewed publications on which this thesis is based

Trabucchi, D., J.-J. Trujillo, J. Schneemann, M. Bitter, and M. Kühn (2015). “Application of staring lidars to study the dynamics of wind turbine wakes”. In: *Meteorologische Zeitschrift* 24.6, pp. 557–564. DOI: 10.1127/metz/2014/0610.

D.T. developed a new method for wake measurements with lidar, analysed the measurements and wrote the manuscript included in Chapter 3; J.S. had a main role in the execution of the measurement campaign; J.-J.T. discussed the result with D.T.; M.B. and M.K. contributed to the formulation of the results in the manuscript and had a supervising role.

Trabucchi, D., G. Steinfeld, D. Bastine, J.-J. Trujillo, J. Schneemann, and M. Kühn (2015). “Study of wake meandering by means of fixed point lidar measurements: Spectral analysis of line-of-sight wind component”. In: *Journal of Physics: Conference Series* 625.1, p. 012016. DOI: 10.1088/1742-6596/625/1/012016.

D.T. conducted the research, analysed the data and wrote the manuscript included in Chapter 4; G.S. simulated the wind turbine wake; D.B. and J.-J.T. discussed the results of the research with D.T.; J.S. had a main role in the design and execution of the measurement campaign; M.K. analysed the content of the manuscript and had a supervising role.

Trabucchi, D., J.-J. Trujillo, and M. Kühn (2017). “Nacelle-based Lidar Measurements for the Calibration of a Wake Model at Different Offshore Operating Conditions”. In: *Energy Procedia* 137. 14th Deep Sea Offshore Wind R&D Conference, EERA DeepWind’2017, pp. 77–88. DOI: 10.1016/j.egypro.2017.10.335.

D.T. defined the objective of the research and the measurement settings, analysed the data and wrote the manuscript included in Chapter 5; J.-J.T. coordinated the measurement campaign and discussed the results of the research with D. T.; M.K. contributed with new ideas on presentation and had a supervising role.

Trabucchi, D., L. Vollmer, and M. Kühn (2017). “3-D shear-layer model for the simulation of multiple wind turbine wakes: description and first assessment”. In: *Wind Energy Science* 2.2, pp. 569–586. DOI: 10.5194/wes-2-569-2017.

D.T. developed the model, dealt with its evaluation and wrote the manuscript included in Chapter 6; L.V. simulated the wind turbine wakes; M.K. provided guidance in the definition of the scope and had a supervising role.

Further peer-reviewed publications

- Bastine, D., M. Wächter, J. Peinke, D. Trabucchi, and M. Kühn (2015). “Characterizing Wake Turbulence with Staring Lidar Measurements”. In: *Journal of Physics: Conference Series* 625.1, p. 012006. URL: <http://stacks.iop.org/1742-6596/625/i=1/a=012006>.
- Clifton, A., P. Clive, J. Gottschall, D. Schlipf, E. Simley, L. Simmons, D. Stein, D. Trabucchi, N. Vasiljevic, and I. Würth (2018). “IEA Wind Task 32: Wind Lidar Identifying and Mitigating Barriers to the Adoption of Wind Lidar”. In: *Remote Sensing* 10.3. ISSN: 2072-4292. DOI: 10.3390/rs10030406. URL: <http://www.mdpi.com/2072-4292/10/3/406>.
- Mittelmeier, N., J. Allin, T. Blodau, D. Trabucchi, G. Steinfeld, A. Rott, and M. Kühn (2017). “An analysis of offshore wind farm SCADA measurements to identify key parameters influencing the magnitude of wake effects”. In: *Wind Energy Science* 2.2, pp. 477–490. DOI: 10.5194/wes-2-477-2017. URL: <https://www.wind-energ-sci.net/2/477/2017/>.
- Schneemann, J., D. Trabucchi, J.-J. Trujillo, and M. Kühn (2014). “Comparing measurements of the horizontal wind speed of a 2D Multi-Lidar and a cup anemometer”. In: vol. 555. 1, p. 012091. DOI: 10.1088/1742-6596/555/1/012091.
- Trabucchi, D., G. Steinfeld, D. Bastine, J.-J. Trujillo, J. Schneemann, and M. Kühn (2015). “Study of wake meandering by means of fixed point lidar measurements: Spectral analysis of line-of-sight wind component”. In: vol. 625. 1, p. 012016. DOI: 10.1088/1742-6596/625/1/012016.
- Trabucchi, D., L. Vollmer, and M. Kühn (2016). “Shear-layer approximation of Navier-Stokes steady equations for non-axisymmetric wind turbine wakes: Description, verification and first application”. In: *Journal of Physics: Conference Series* 753.3, p. 032030. URL: <http://stacks.iop.org/1742-6596/753/i=3/a=032030>.
- van Dooren, M. F., D. Trabucchi, and M. Kühn (2016). “A Methodology for the Reconstruction of 2D Horizontal Wind Fields of Wind Turbine Wakes Based on Dual-Doppler Lidar Measurements”. In: *Remote Sensing* 8.10. ISSN: 2072-4292. DOI: 10.3390/rs8100809. URL: <http://www.mdpi.com/2072-4292/8/10/809>.
- Vollmer, L., M. van Dooren, D. Trabucchi, J. Schneemann, G. Steinfeld, B. Witha, J.-J. Trujillo, and M. Kühn (2015). “First comparison of LES of an offshore wind turbine wake with dual-Doppler lidar measurements in a German offshore wind farm”. In: *Journal of Physics: Conference Series* 625.1, p. 012001. DOI: 10.1088/1742-6596/625/1/012001.

Conferences and colloquia

- Beck, H., A. Rott, D. Trabucchi, and M. Kühn (2016). “Reconstruction of volumetric wind turbine wakes in complex terrain by long-range lidar measurements”. In: *EUROMECH Colloquium 576: Wind Farms in Complex Terrains*. Stockholm.
- Beck, H., J. J. Trujillo, D. Trabucchi, J. Schneemann, and M. Kühn (2015). “Full-field observation of dynamic wakes by means of long-range LIDAR measurements”. In: *Large Wind-Power Plants Colloquium: Interaction, Control and Integration*. Leuven.
- Rott, A., J. Schneemann, D. Trabucchi, J. J. Trujillo, and M. Kühn (2017). “Accurate deployment of long-range scanning lidar on offshore platforms by means of sea surface levelling”. In: *WindTech Conference*. Poster. URL: http://windtechconferences.org/wp-content/uploads/2018/01/Windtech2017_AnRott-Poster.pdf.

- Schlipf, D., D. Trabucchi, O. Bischoff, M. Hofsäß, J. Mann, T. Mikkelsen, A. Rettenmeier, J.-J. Trujillo, and M. Kühn (2010). “Testing of Frozen Turbulence Hypothesis for Wind Turbine Applications with a Scanning Lidar System”. In: *ISARS - 15th International Symposium for the Advancement of Boundary Layer Remote Sensing*. Paris. DOI: 10.18419/opus-3915.
- Schneemann, J., D. Bastine, H. Beck, M. van Dooren, J. Hieronimus, G. Steinfeld, D. Trabucchi, J. J. Trujillo, L. Vollmer, M. Kühn, and J. Schmidt (2015a). “Investigation of flow conditions and turbulence characteristics in large offshore wind farms by remote sensing experiments and simulations”. In: *Offshore Wind R&D conference*. Oral presentation. Bremerhaven.
- Schneemann, J., D. Bastine, H. Beck, M. van Dooren, G. Steinfeld, D. Trabucchi, J. J. Trujillo, J. Schmidt, and M. Kühn (2015b). “GW Wakes: Measurements of Wake Effects in alpha ventus with Synchronised Long Range LiDAR Windscanners”. In: *12th German Wind Energy Conference DEWEK*. Bremen.
- Schneemann, J., D. Brickwell, B. Stoevesandt, J. J. Trujillo, D. Trabucchi, G. Steinfeld, M. Wächter, H. Beck, and M. Kühn (2012a). “GW Wakes: Measuring wake effects and wake turbulence characteristics of very large offshore wind farms with synchronized long-range lidar windscanners”. In: *11th German Wind Energy Conference DEWEK*. Bremen.
- Schneemann, J., D. Trabucchi, J. J. Trujillo, and M. Kühn (2012b). “Comparison of measurements of the horizontal wind speed of a 2D multi Lidar and a standard anemometer”. In: *TORQUE - The Science of Making Torque from Wind*. Oldenburg. URL: <https://iopscience.iop.org/article/10.1088/1742-6596/555/1/012091/pdf>.
- Schneemann, J., J. J. Trujillo, D. Trabucchi, H. Beck, R. Unguran, S. Voß, and M. Kühn (2013). “GW Wakes - Measuring wake effects in "alpha ventus" using a long-range multi lidar”. In: *FINO Conference*. Kiel.
- Schneemann, J., S. Voss, G. Steinfeld, D. Trabucchi, J. J. Trujillo, B. Witha, and M. Kühn (2012c). “Lidar simulations to study measurements of turbulence in different atmospheric conditions”. In: *EUROMECH Colloquium 528: Wind Energy and the impact of turbulence on the conversion process*. Oldenburg. URL: https://link.springer.com/chapter/10.1007/978-3-642-54696-9_19.
- Trabucchi, D., H. Beck, J. Schneemann, J. J. Trujillo, R. Ungurán, S. Voss, and M. Kühn (2013). “Offshore wind farm flow characteristics measured by a long-range multi-lidar system: development and preliminary results”. In: *EWEA Offshore*. Frankfurt.
- Trabucchi, D., J. Schneemann, J. J. Trujillo, and M. Kühn (2012). “Full-field study of wind turbine wake dynamics by means of two long-range lidars”. In: *TORQUE - The Science of Making Torque from Wind*. Oldenburg.
- Trabucchi, D., J. J. Trujillo, J. Schneemann, M. Bitter, and M. Kühn (2014). “Application of staring lidars to study the dynamics of wind turbine wakes”. In: *ISARS - 17th International Symposium for the Advancement of Boundary Layer Remote Sensing*. Aukland.
- Trabucchi, D., J.-J. Trujillo, G. Steinfeld, J. Schneemann, and M. Kühn (2011a). “Simulation of measurements of wake dynamics with nacelle- and ground-based lidar wind scanners”. In: *Book of Abstracts Wake Conference*. Gotland University. Gotland, pp. 170–174. URL: http://space.hgo.se/wake_conference/?q=system/files/bookabstract2011_update_1.pdf (visited on 04/11/2016).
- Trabucchi, D., J.-J. Trujillo, G. Steinfeld, J. Schneemann, M. Machtaa, J. P. Cariou, and M. Kühn (2011b). “Numerical assessment of the performance of lidar WindScanners for wake

- measurements”. In: *EWEA Annual event*. Vortrag. URL: <http://www.ewea.org/annual2011/conference/conference-programme/> (visited on 04/10/2016).
- Trujillo, J. J., D. Trabucchi, O. Bischoff, M. Hofsäß, J. Mann, T. Mikkelsen, A. Rettenmeier, D. Schlipf, and M. Kühn (2010). “Testing of Frozen Turbulence Hypothesis for Wind Turbine Applications with a Staring Lidar”. In: *European Geosciences Union General Assembly, Wind Power Meteorology*. Vienna.
- Trujillo, J. J., D. Trabucchi, D. Schlipf, and M. Kühn (2012). “Numerical Simulation of Detailed Lidar Measurements in the Near Wake of a Wind Turbine”. In: *ISARS - 16th International Symposium for the Advancement of Boundary Layer Remote Sensing*. Boulder.
- Trujillo, J.-J., W. Friedrichs, J. Schneemann, D. Trabucchi, and M. Kühn (2017). “Robust and systematic analysis of lidar data for wake research”. In: *Wind Energy Science Conference*.
- van Dooren, M. F., D. Trabucchi, H. Beck, J. Schneemann, W. Friedrichs, and M. Kühn (2015). “Assessment of the global wind and the local wake direction at »alpha ventus« using long range scanning LiDAR”. In: *EWEA Offshore*. Copenhagen.

Curriculum vitae

Personal data

Name Davide Trabucchi
Born 1983 in Sondalo, Italy

Industrial experience

04/2018 - today **Deutsche WindGuard Consulting GmbH**
Remote sensing test laboratory
Calibration of remote sensing instruments for wind speed measurements
Power curve assessment
Wind measurements

Academical career

04/2010 - 03/2018 **Oldenburg University**
Research scientist
Participation to national and international research projects (GW Wakes, CompactWind, Windscanner.eu, CLUSTERDESIGN)
Conceptual design and monitoring of lidar experiments
Project management and advisory board member in the framework of IEA Wind Energy Task 32
Teaching tasks (lecture and tutorials)
Supervision of student projects (internships, bachelor theses and master theses)

09/2006 - 06/2010 **Technical University of Milan (Politecnico Milano)**
Master of Science in aeronautical engineering
Master thesis at the Technical University of Stuttgart:
Testing Taylor's frozen turbulence hypothesis for wind turbine application
Exchange year at the Technical University of Munich

09/2002 - 06/2006 **Technical University of Milan (Politecnico Milano)**
Bachelor of Science in aerospace engineering

Eidesstattliche Erklärung

Hiermit versichere ich, die vorliegende Arbeit selbstständig verfasst, keine anderen als die angegebenen Quellen und Hilfsmittel verwendet und die Leitlinien guter wissenschaftlicher Praxis der Carl von Ossietzky Universität Oldenburg befolgt zu haben.

Die Arbeit hat weder in ihrer Gesamtheit noch in Teilen einer anderen Hochschule zur Begutachtung in einem Promotionsverfahren vorgelegen und im Zusammenhang mit dem Promotionsvorhaben wurden keine kommerziellen Vermittlungs- oder Beratungsdienste in Anspruch genommen.

Teile der Arbeit sind bereits veröffentlicht.

Oldenburg, 30.05.2019

Daide Trabucchi
Daide Trabucchi